Monitoring the Variable Stellar Universe

Thesis

Monitoring the Variable Stellar Universe

Meredith Vivian Morrell MSci

A thesis submitted for the degree of

Doctor of Philosophy

in Astrophysics

Supervisors: Dr Ulrich Kolb and Dr Andrew Norton

School of Physical Sciences

The Open University

October 2020

Abstract

Monitoring the Variable Stellar Universe is a demonstration of the use of a small aperture, autonomous telescope as a tool to follow up transient variable stars. I used the Open University robotic telescope PIRATE, a relatively low cost facility built with off-the-shelf components, located in Tenerife, to observe targets selected from the Gaia Science Alerts stream which uses Gaia space observatory observations to identify potential transient objects. A total of 45,000 images were collected by me for over 2,700 hours of exposure time. A subset of 22,000 of those observations are discussed here.

To match the pace of data acquisition of the automated telescope, I used Python to construct both a data reduction pipeline, and a data analysis pipeline which uses ensemble photometry and string length minimisation to generate photometric light curves. I compared the light curves generated by my data analysis pipeline to the those generated using the Cambridge Photometry Calibration Server, which produced similar results.

The largest single data set for a target was Gaia16aye, a binary microlensing event which began in July 2016, and peaked five times over the next 18 months. The data I collect was part of a collaborative effort by over 100 observatories to follow up and model the system. I used the PIRATE data to investigate the colour index variation over time, and found that the event was achromatic as expected for a microlensing event. In addition to Gaia16aye, 77 other targets were observed during the main acquisition period between May 2017 and January 2019, including microlensing events, supernovae, cataclysmic variables, active galactic nuclei and several targets with unknown classification. The light curves generated for these targets are also discussed here.

PIRATE proved to be an effective example of a small, autonomous telescope collecting a large quantity of data for a relatively small investment of staff time and financial resource. The Gaia Science Alerts stream used in conjunction with PIRATE proved to be a slight mismatch, with many alerts being too faint for PIRATE to follow. A larger telescope would be preferable to exclusively follow the Gaia alerts stream, and regular data quality monitoring through daily light curve generation would make PIRATE target selection for longer term follow up better. But PIRATE as it is now is very capable of transient follow up and would be used more effectively by branching out to other alert streams such as ASAS-SN, which is more closely matched to current PIRATE setup in terms of observing magnitude.

Acknowledgements

I could not have asked for better supervisors in Ulrich Kolb and Andrew Norton, whose patience and guidance were immensely important in helping me finish this project.

I would like to thank OpenSTEM Labs and the PIRATE team, and Sybilla Technologies for their work with PIRATE.

My friend Dean Roberts helped me a lot, both with PIRATE operations and maintenance, and with discussions of many aspects of my project, especially when I was just getting started. The other people I met at the open university: Mark Parker, Joe Cooper and Heidi Thiemann made every day more enjoyable. Outside the university: Alex Miles, Marisa Wood and Terry Jin all of whom helped me both before I began, and during my PhD.

Most of all I need to thank my mum, Margaret for always helping me through everything big and small and my dad, Darius, who I miss very much.

Contents

List of Figures

List of Tables

1 Introduction

To gain a full understanding of the universe and our place in it, it should be the aim of humankind to be capable of observing the whole night sky, to all depths and on all timescales. There is a huge variety of variable stellar phenomena which are important to observe so we can expand our knowledge, intrinsic variables such as pulsating, flaring and rotating stars, and geometric variables such as eclipsing binaries and microlensing events. These events cover a vast range of timescales, from events which last a few seconds in the case of some flaring stars, and events which cover months and years such as Mira variables which pulsate periodically over the course of hundreds of days.

With the likes of the Zwicky Transient Facility publishing 0.6 - 1.2 million new variable targets every day, there is already need for a large quantity of telescope time to follow up some of these targets, and that is only going to increase in the near future with the Large Synoptic Survey Telescope (LSST) predicted to find even more transients each night.

Follow up can range from a single observation per night for a few nights, to multiple observations per night for months or years, and occur at all source brightness depending on the variable.

Photometric follow up has two important parameters which must be considered when choosing how to follow them up, the brightness of the source and the timescale over which an event occurs. There is a need for follow-up from the brightest and quickest events, to the faintest, slowest targets and not all instruments are well suited to all events. The biggest telescopes in use today are useful for the fainter targets, but time spent following a single target by these kinds of instruments is limited, as high demand for exposure time makes them expensive. Smaller, automated systems are well suited to follow-up at most timescales for bright targets, and longer term follow up for fainter targets. A large quantity of data can be acquired each night and requires no human intervention, so long term follow up can be achieved relatively cheaply.

This project aims to demonstrate the use of the small aperture autonomous robotic telescopes for long term photometric monitoring of variable and transient systems.

The telescope PIRATE, owned and operated by The Open University, is a prime example of a small aperture, automated system, and will be used for all the observations made during this project. The PIRATE system is easily replicable, using off-the-shelf, commercial hardware and software.

To match the acquisition speed, data reduction and analysis also needs to be auto-

mated such that an observer can go from picking a target to looking at a light curve without using valuable time. Construction of a pipeline to achieve this will be an important part of this project.

Targets will be selected from the list published by the Gaia Science Alerts team, which aims to publish alerts between a few hours and days after the Gaia observation that triggered it. Although PIRATE is capable of follow up of targets within minutes of publishing for time-sensitive targets, this project will not focus on that aspect and as such the GSA list time delay is not an issue.

In Chapter 2 I will begin by introducing the telescope PIRATE, which was used for all the data acquisition in this project. I will put it in context by discussing other similar telescopes in use today, discuss maintenance tasks which I have been involved in, and the signal-to-noise limitations of PIRATE in the terms of this project.

Chapter 3 looks at variable stars, with the aim to develop an understanding of the different types of variable which may be observed during this project. They are split into: rotating variables, eclipsing variables, pulsating variables, eruptive variables, explosive and novalike variables (including cataclysmic variables), microlensing events and active galactic nuclei.

Chapter 4 is an introduction to the Gaia satellite and the Gaia Science Alerts project, which was used to choose variable targets for observation. It also contains discussion of the Cambridge Photometry Calibration Server, which was used to aid light curve generation, magnitude calibration and collaboration between observatories in making target light curves. The filters PIRATE uses are also compared to the filters used by the various catalogues which the photometry server uses in it's cross-matching system for magnitude calibration.

Chapter 5 describes the pipelines I created for data reduction and light curve generation through ensemble photometry and string length minimisation.

Chapter 6 discusses the difference between the light curves generated by the Cambridge Photometry Calibration Server and the Ensemble Photometry Pipeline I created.

Chapter 7 introduces binary microlensing, the target Gaia16aye, the contribution of PIRATE observations to the collaborative effort made to follow up the target, and my own investigation of the colour index of the target as it was lensed.

Chapter 8 contains light curves and discussion of all the rest targets I observed which successfully produced a light curve.

Chapter 9 is a summary of the work presented and discusses possible improvements

and future work which could be carried out.

2 Autonomous Robotic Telescopes

A robotic telescope is one which can be controlled remotely by a human. An automated telescope is one which can carry out a list of observations without human intervention. An autonomous observatory can reliably keep track of sunrise, sunset, weather conditions and use this information to open and close the dome and start and stop observations as necessary. Since the late 1960s, astronomers have gradually made the steps necessary towards making a fully autonomous, robotic telescope.

The University of Wisconsin developed the first automated photoelectric telescope (APT) in 1968 using a digital computer, the PDP-8. It followed a fixed sequence of observations of bright stars, which were fed to it by Paper Tape (McNall et al. 1968).

In 1975 the first successful robotic telescope was run, a 0.75m telescope built by the New Mexico Institute of Mining and Technology, primarily to search for supernova events in distant galaxies. It was successfully remotely controlled from 30km away using a microwave link (Colgate and Moore and Carlson 1975).

In 1983 Boyd and Genet began running a 0.25m telescope in Arizona, one of the first successful APTs to run without the need for any human intervention barring input of a list of targets to observe (Genet 1986). The telescope calculated the position of the sun to decide whether or not it was time to observe, then it could move to a given target, centre it and make observations in U, B and V filters using the photoelectric detectors, making it an autonomous telescope (Genet et al. 1987).

The Carlsberg Automatic Meridian Circle was a 0.18cm telescope which began operating in 1984 in La Palma, a fully autonomous observatory and automated telescope. The autonomous observatory was capable of monitoring weather conditions and could cease telescope operations without human intervention in addition to starting and stopping observations based on the position of the sun (Helmer et al. 1985).

More modern robotic telescopes no longer rely on photoelectric devices with the invention of the CCD in the late 1960s. The wide-spread adoption of CCD technology in the 1980s and its decreasing cost to produce in the 1990s meant that it would not be long before autonomous robotic telescopes started using the technology. The Bradford Robotic Telescope (BRT) was one of the first robotic autonomous telescopes to use a CCD rather than a photoelectric device. It began operating from El Observatorio Del Teide in Tenerife in 1993, was controllable through the internet and was primarily used for educational purposes (Baruch et al. 2007).

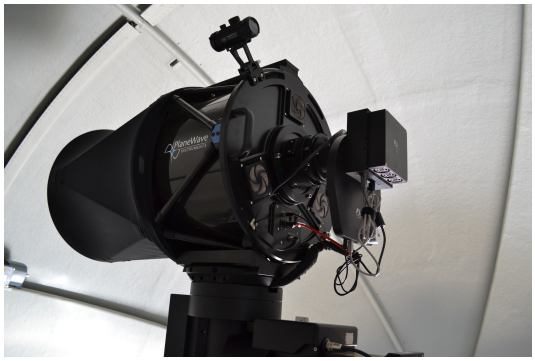

(a) PIRATE

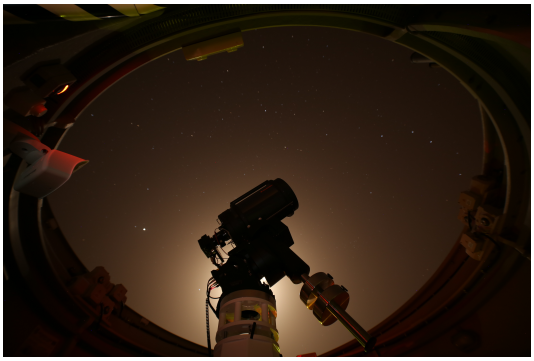

(b) COAST

Figure 1: Figure 1a is PIRATE as imaged by Dean Roberts in 2016. Figure 1b is COAST as imaged by Meredith Morrell in 2018.

2.1 PIRATE & COAST

PIRATE and COAST are two robotic autonomous telescopes owned and operated by the Open University (figure 1). Based in El Observatorio del Teide in Tenerife since August 2016, the telescopes are computer controlled through software called ABOT designed by Sybilla Technologies (Sybilski et al. 2014), and can be used to control the telescope remotely over the internet. If no-one is in real-time control of the telescope it carries out observations from a pre-defined schedule set by observers. The telescopes are also equipped with weather sensors and are capable of closing the dome and suspending operation should poor weather arise. Table 1 gives specifics on the telescopes which remained the same throughout the project, the cameras which changed on COAST on 12/05/2019 and the filters which were changed on 20/05/2018.

Due to the flexibility of the robotic control and autonomous functions, the telescopes have several primary uses, from education and public outreach to research for professional astronomers.

One key aspect of robotic autonomous telescopes is that they can be used to quickly respond to alerts of fleeting transient events, such as gamma ray bursts or gravitational wave alerts. Removing the need for human intervention means that the first follow up images after an alert can be taken within minutes. Some alerts systems such as the one the Laser Interferometer Gravitational-Wave Observatory (LIGO) uses can typically send out the important information for follow up observations on the order of minutes after identifying an event (Abbott et al. 2016). While this aspect is important in the field of robotic autonomous telescopes, it is less important in this project which focusses on the follow up of Gaia Science Alerts.

The Gaia alerts system looks for variable stars and usually does not alert for days

Telescope	PIRATE	COAST
OTA	17" Cassegrain Plainwave CDK17	14" Schmidt-Cassegrain Celestron C14-A XLT
Focal Length (mm)	2939	3910
Focal Ratio	f/6.8	f/11
Camera/CCD	FLI Proline PL16803/ KAF-16803	SBIG STL1001E/ KAF-1001E
		Proline PL090000/ KAT-090000
CCD size (pixels)	4096 x 4096	1024 x 1024
		3056 x 3056
Pixel Size (microns)	9	24
		12
Field of View (arcminutes)	43 x 43	21.5 x 21.5
		32.2 x 32.2
Resolution (per pixel)	0.63"	1.27"
		0.63"
Filters (Before 20/05/2018)	Baader(B, G, R), Hα, OIII, SII, Luminance	Johnson(B, V, R, I), Hα, OIII, SII, Luminance
Filters (After 20/05/2018)	Johnson(U, B, V, R, I), Hα, OIII, SII, Luminance	Johnson(B, V, R), Hα, OIII, SII, Luminance

Table 1: Details of both telescopes remotely operated by the Open University in Tenerife. COAST had a camera change on 12/05/2019 so details for both are given, with the earlier camera given above, and the later below. Both telescopes are housed in Baader all sky domes and on 10 Micron GM4000 HPS German equatorial mounts.

after the first identification. Gaia is only visible to the ESA controlled downlink locations (Cebreros in Spain and New Norcia in Australia) for roughly 8 hours per day, and then the Gaia Data Processing and Analysis Consortium (DPAC) pre-processes the data and passes it to the alerts pipeline. The process of sending out an alert can take anything up to 48 hours after the data has been downlinked, meaning that following up within minutes of the alert is not as important as with LIGO (Wyrzykowski et al. 2012a).

Monitoring of photometric variables is a task well suited to robotic autonomous telescopes, and is key in this project. Many transient variable events take place over periods ranging from a few days to several hundred days, and periodic variables are constantly varying in brightness with periods similarly ranging from hours to years. Constant monitoring every night can be a challenge if a single astronomer has to manually take multiple pictures every night for hundreds of days. Autonomous telescopes only need to be told once to observe something until it is told to stop. For this project, the automatic acquisition of data is already possible thanks to PIRATE and COAST, the challenge is to automate the post-processing of the data.

2.2 Small Aperture Autonomous Robotic Telescopes Currently Observing in Optical Wavelengths

PIRATE and COAST have 43cm and 36cm apertures respectively, observe in optical wavelengths and their primary use is in monitoring of photometric variables, asteroid monitoring and educational use for university undergraduates. There are many other telescopes currently operating which are similar in size and are looking for variable stars of different kinds.

F.V. Hessman created a list of robotic telescopes which are currently, or soon to be in operation (Hessman 2016)[1], though it is worth noting that the list hasn't been updated since August 2016 and there have been some changes at least to Open University operated telescopes which have not been updated. For example the Bradford Robotic Telescope which was also situated at the Teide observatory was taken over by the Open University, and after investigation into its viability as an educational tool, it was decommissioned and replaced by COAST. The list also features PIRATE Mk.2 in the Mallorca observatory, though that telescope has been decommissioned and some of the systems used have now become COAST, such as the Celestron 14" telescope itself.

[1] accessed January 2019

Despite that, the list does include lots of telescopes which do appear to be operational, along with their aperture sizes and what their primary scientific purpose appears to be.

Below is a list of some of the currently operational automated telescope facilities as of February 2020 which are a similar size to PIRATE or are performing photometric follow up and monitoring of variable stars and transient events.

- The Katzman Automatic Imaging Telescope (KAIT), a 0.76m robotic autonomous telescope at Lick observatory on Mount Hamilton in San Jose, California, took first light in 1998 to search for nearby supernovae, and still operates today observing around 1000 galaxies a night (Filippenko et al. 2001).

- In 2003 the SuperWASP project was put together at two sites, El Observatorio del Roque de los Muchachos on the island of La Palma in the Canary Islands, and at the Sutherland Station of the South African Astronomical Observatory. Each site had 8 200mm telephoto lenses put together to create a super wide angle all sky survey in the search for extrasolar planets. SuperWASP could cover the entire night's sky every 40 minutes, accruing huge quantities of data (Pollacco et al. 2006).

- The Liverpool telescope located in El Observatorio del Roque de Los Muchachos, which took first light in 2004. A 2m fully autonomous telescope dedicated to both monitoring of variable objects and rapid follow up of unpredictable phenomena such as gamma ray bursts (Steele et al. 2004).

- The TRAnsiting Planets and PlanetesImals Small Telescopes (TRAPPIST) are two 0.6m robotic telescopes located in the ESO La Silla Observatory in Chile and at Oukaïmden Observatory in Morocco which search for extrasolar planets (Gillon et al. 2011) and recently published work detailing the discovery of 7 terrestrial planets orbiting a nearby dwarf star (Gillon et al. 2017).

- The Optical Gravitational Lensing Experiment (OGLE) team has been looking for variable stars since 1992 and are currently in their fourth phase which uses the 1.3m Warsaw robotic telescope in Las Campanas observatory, with a 1.5° field of view with 32 detector mosaic with 2048x4102pix CCDs (Udalski et al. 2015).

- The Panchromatic Robotic Optical Monitoring and Polarimetry Telescopes (PROMPT) are six 0.41m robotic telescopes which have been operational since

2006. Based in Cerro Tololo Inter-American Observatory (CTIO) in Chile PROMPT is set up primarily for the rapid follow up of gamma ray bursts in multiple photometric bands simultaneously, from near IR to UV (Reichart et al. 2005).

- pt5m is a 0.5m robotic telescope located in Roque de los Muchachos Observatory which has been observing since 2012 and is primarily used for transient follow up and time based photometry (Hardy et al. 2015). This telescope regularly follows up Gaia alerts transients and at the time of writing has submitted more observations to the Cambridge Photometry Server than any other telescope with more than 30,000 data points.

- The Catalina Sky Survey uses three telescopes with apertures 1.5m, 1.0m and 0.7m located in the Santa Catalina Mountains in Arizona. Typically the 1.0m telescope is used for observational follow up of Near Earth Objects (NEO), though the 0.7m telescope has been used for a real-time sky survey since 2009 (Drake et al. 2009).

- The Zwicky Transient Facility has been operational since 2018 and covering Northern skies every three nights. It uses the 1.2m Samuel Oschin telescope in the Palomar Observatory which is specifically looking for transients which are rapidly changing in brightness such as supernovae and gravitational wave counterparts (Graham et al. 2019).

- The All Sky Automated Survey for SuperNovae (ASAS-SN) current operates 24 telescopes located in Hawaii, Chile, South Africa, Texas and China. All the sites use 14cm telescopes and surveys the entire night sky each night between 8 and 18 magnitude. Although the primary use of the telescope is to look for supernova, it does also pick up some other types of transients. (Shappee et al. 2014).

2.3 Tenerife

The Canary Islands are located in the Atlantic ocean to the West of Morocco. El Observatorio del Teide is located on Tenerife, the largest of the Canary Islands and is one of two observatories along with el Observatorio del Roque de los Muchachos on La Palma which is run by the Instituto de Astrofisica de Canarias (IAC). Between the two observatories, instruments from over 60 institutions are set up including solar

and nocturnal optical instruments, some of which are also robotic like PIRATE and COAST.

El Observatorio del Teide is located 2390m above sea level in Teide national park (a UNESCO world heritage site), not far from Mount Teide volcano. The first telescope installed there was owned by the university of Bordeaux in 1964 to observe zodiacal light. As the observatory is located in a protected area, special attention is paid to maintaining the landscape as much as possible, so PIRATE and COAST both have a minimal footprint in an area close to the residencia with other robotic telescopes such as one of the Mobile Astronomical System of Telescope-Robots (MASTER) telescopes (Lipunov et al. 2012) (figure 2).

Aside from the excellent meteorological conditions of Tenerife in general, there are other reasons why Teide is one of the best observatory sites in the world. In 1988 the Spanish government established a law aimed at protecting the astronomical quality of the IAC observatories ('Ley del Cielo' - law 31/1988), and a group called La Officina Tecnica para la Proteccion de la Calidad del Cielo (OTPC) to facilitate and advise on the application of the new sky law. The law protects the observatories on the Canary Islands from light pollution, radio-electrical pollution, atmospheric pollution and aviation routes. This demonstrates that the Spanish government has an interest in maintaining astronomical research.

Varela et al. 2002 presented the results of meteorological and seeing measurements taken by Differential Image Motion Monitors (DIMMs) run by the IAC. The results indicate 78% of nights in summer, and 49% of nights in winter were useful in a several year period beginning in November 1992 at Teide observatory and continuing in el Roque de los Muchachos Observatory from May 1994, though the 49% of winter nights was likely an under-estimate of the average due to some unusual frost in the measurement period. The majority of the time lost (84%) was either due to high humidity, high cloud cover or high winds. The average seeing value in Teide over that period was 0.76", with lows of 0.2" and highs of 1.2" at different positions in the observatory at different times.

2.4 PIRATE maintenance

Over the course of this project I was part of the PIRATE group at the Open University and helped with maintenance and repairs to PIRATE and COAST. The maintenance tasks for PIRATE and COAST can be split into those tasks which could be carried out

Figure 2: El Observatorio del Teide as seen from above. PIRATE and COAST are indicated in red, and the residencia is indicated in green. Image taken from Google maps in August 2020, image copyright GRAFCAN, Maxar Technologies 2019.

remotely, and those which would require a team to go to Tenerife and perform hands-on maintenance. In-person maintenance trips occur roughly two or three times a year depending on how the telescopes have been performing, and whether any emergency situations have arisen, and I personally have travelled to Tenerife on two occasions to assist.

During the early operational stages of PIRATE in late 2016 we noticed that the

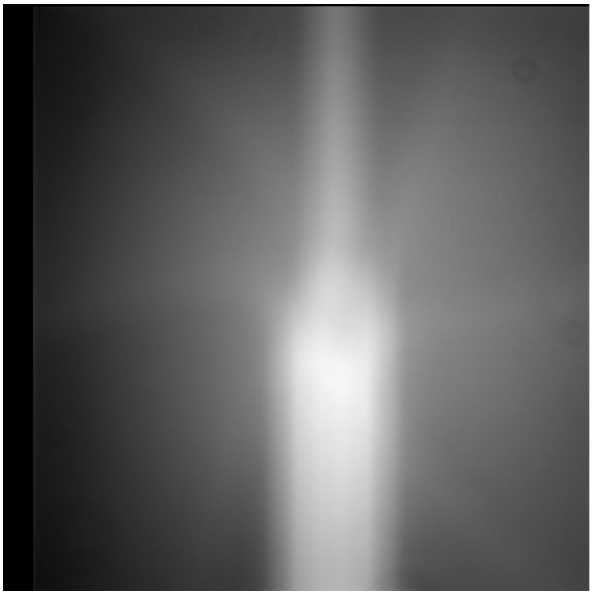

Figure 3: SII flat from PIRATE taken on 2017/02/02. The bright streak down the centre of the frame comes from the shutter being stuck open and pixels continuing to be exposed as they are read out.

flats being taken had a large bright spots in the centre of the frame. I spent some time trying to figure out what was causing the issue and whether or not it could be fixed remotely. The fault was identified to be the shutter installed on the FLI ProLine PL16803. The shutter would not close completely at the end of some exposures, which lead to flat images such as the example in figure 3. Although the effect was very obvious on some flats, some science frames were also discovered to have bright streaks. The sticking was also inconsistent, meaning it didn't always get stuck open and it didn't always stick open the same amount meaning it couldn't be accounted for easily, and lead to quite a lot of scientifically unsuitable data being acquired.

To fix this issue, a replacement iris shutter was acquired from the manufacturer and I flew to Tenerife along with other members of the PIRATE group. We dismantled the camera and replaced the defective part. This particular trip also had us complete other less-vital tasks such as cleaning the all-sky camera which had become a prime spot for birds to perch.

In 2018 COAST images started to come in which were very out of focus. After several nights of attempting to refocus COAST remotely, it became apparent that something was physically wrong with the focusser and another trip to the telescope would be required. I travelled to Tenerife and joined a member of the Baader team. The primary task here was to replace a broken bearing in the focusser, and to recentre the focusser so it has plenty of travel distance in the future.

Additional tasks included adjusting the mirror focus on COAST after the repaired focusser had been installed, ensuring that PIRATE and COAST could optimally get in focus, installing new software which would be capable of automatically creating a new pointing model and ensuring that the new pointing models were working.

Typically updating the pointing model for the telescope mount is done remotely. The mount needs to be told how accurately it is pointing at the RA/DEC coordinates given to it. To do this the mount would slew to a bright star by giving it coordinates, an image would be taken which should have the star at least somewhere near the centre of the frame, and then adjustments were made to the mount position until the target is in the precise centre of the frame. By calculating the difference in position from where it thought the star was to where it has been adjusted to, the mount has a reference point for how far off it was from finding the star initially. A pointing model is a mathematical algorithm which is used to calculate the error between where the telescope mount thinks it's pointing and where it actually points in the sky, and is typically based on 20-100 reference points across the sky.

Initially the pointing model had to be carried out using a computer controlled version of the mount handset and was only as accurate as the observer could be in centering a known star. After this second trip to Tenerife the pointing model is much more automated.

The new pointing model software is called Model Creator[2] and rather than pointing at known stars and making adjustments until it is centred, the software takes single images of a number of star fields defined by the user and plate solves the resulting images. The difference from expected position and actual position is then calculated by the software to give the correction necessary. The model creation can still be started remotely, though initial installation required someone to be in Tenerife.

Figure 4 shows the raw data from two targets. The top plot uses data from one night of observations of a microlensing event in November 2017 which used the pointing model that was created using the older manual method, and the bottom plot is one night of observations of eclipsing binary V354 UMa (taken by undergraduate students) in March 2020 which uses a pointing model created using the Model Creator software.

The important information in these graphs are the x and y positions of the target on the CCD in each observation. The target clearly drifts from it's initial position in

[2]Model Creator manual, accessed March 2020 - https://www.astromi.ch/Files/ModelCreator2/ModelCreator%20Manual.pdf

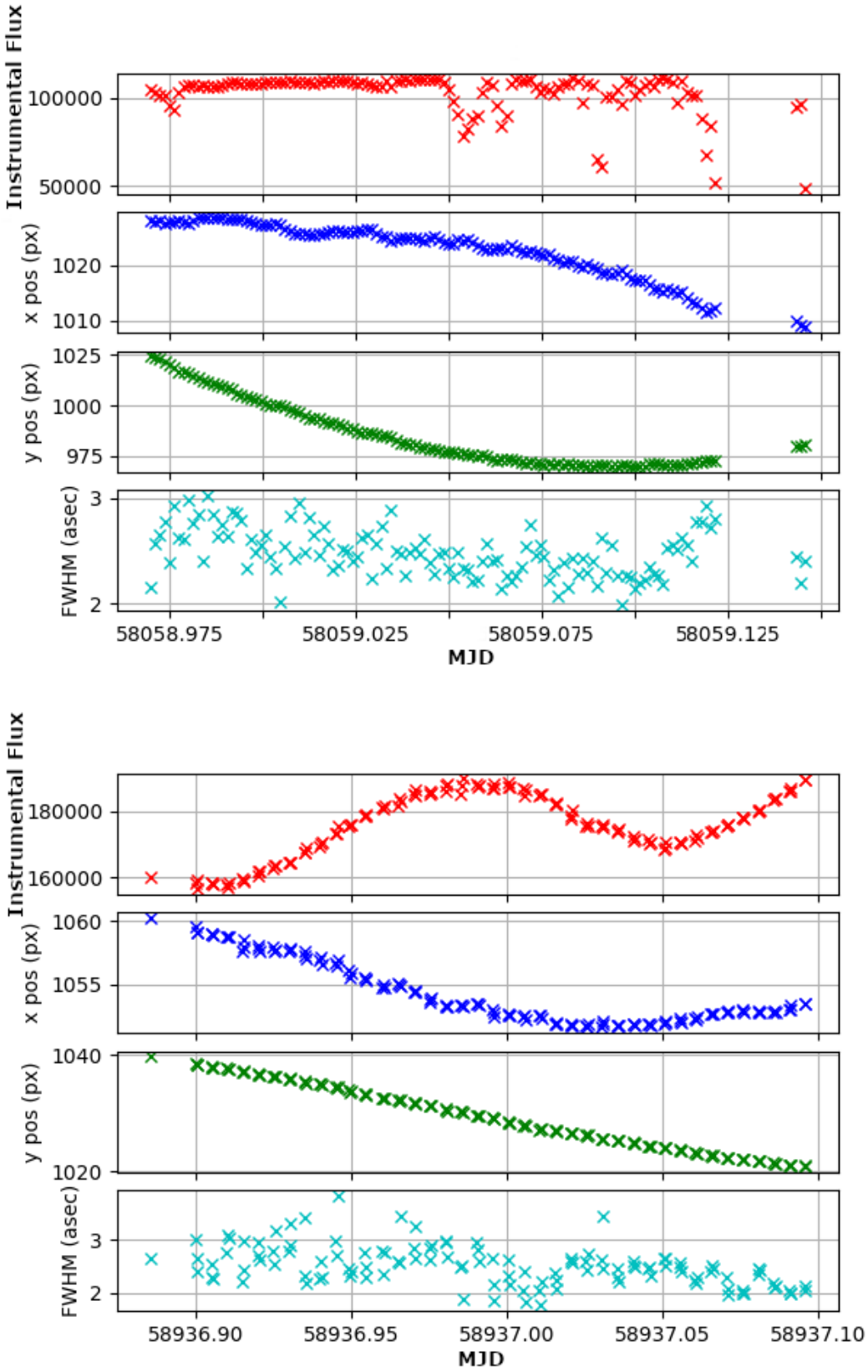

Figure 4: Raw data for the Kojima microlensing event on 02/11/2017 at the top, and the raw data for V354 UMa taken on 28/03/2020. X pos and Y pos indicate the position of the target on the PIRATE CCD in pixels.

both cases, but the pixel drift per hour in table 2 shows that the drift with the new method is significantly lower.

Pointing Model	**x position (pixels/hour)**	**y position (pixels/hour)**
Manual	4.4	18.3
Model Creator	2.0	3.4

Table 2: Pixel drift of the target on the PIRATE CCD before and after the installation of the Model Creator software.

An example of a remote maintenance task required for PIRATE was the adjustment of the logic for how it acquires flat fields.

A good flat field requires a uniform surface which is also uniformly illuminated, for dome flats this can be acquired by shining a lamp onto a flat surface and taking images of that. Since PIRATE does not have the facilities necessary to take dome flat fields, sky flats have to be taken instead. This means the telescope needs to be pointed at the sky while it is not so bright that the CCD is immediately over-exposed, but it is brighter than the night sky which does not illuminate the CCD very much. For a short time each day during dawn and dusk the sky is just bright enough to acquire flat fields for about 30 minutes.

Each flat takes between 1 to 30 seconds to expose, each filter ideally requires a minimum of of three well-exposed flat frames per night so that median combining flats can be used effectively to remove bright points such as stars, and each filter needs flats in both binning 1 and 2. This is a lot of frames which need to be taken in a relatively short amount of time. ABOT is capable of calculating how long the CCD should be exposed for to get a flat frame which is exposed to around the limit required, but it has to be told which filters to get flat frames for and how many.

The narrowband flats (Hα, SII, OIII) can be acquired while the sky is still relatively bright, as they block a large portion of the incident light. The binning 2 narrowband flats can all be taken in the first 15 minutes of dusk, and the last 15 minutes of dawn without issue. Dawn and dusk here are the times determined by ABOT, which calculates nautical twilight each day and uses when nautical twilight begins as the beginning of dusk, and when nautical twilight ends as the beginning of night time.

Deciding when the flats should be taken exactly is a matter of balancing how much time is available between when the sun is low enough in the sky that the CCD isn't flooded with photons immediately, and when the sun is still high enough that the sky

is bright enough to get a flat field as opposed to an astronomical image.

To decide how the filters should be arranged during the dusk twilight to get the best flats, I set ABOT to take flats in only a single filter per night - all B flats one evening, then all R flats another evening for example - then plotted the average counts across each frame against the times when the flats were taken. In addition, the frames were run through source extractor to see how many stars were present in each frame, the idea being that as the sky gets darker, more faint stars will be visible. The aim was to give a range of times relative to ABOTs dusk and night time for each filter when the conditions were most favourable to give flats close to the average counts we wanted (around 45000 counts).

The most useful indicators from this testing proved to be the length of the exposure which is chosen by ABOT automatically to attempt to get the flats to the counts requested and is therefore related to the average number of counts, and the number of sources found by source extraction of the frames. The data for the Johnson B flats are plotted in figure 5. All the frames taken before 19:00:29 on the graph have exposure time 0.05-0.5s which are test exposures taken by ABOT and are all too bright, its only after the exposure time gets longer that the sky begins to get dark enough to get lower sky counts. Surprisingly the first few dozen frames also find a lot of sources, but after inspection of the source extractor results it becomes apparent that the sources found before it reaches a minimum just before 19:03:22 are artifacts in the overexposed frames. From this graph the best time for B flats on 02/10/2018 was chosen to be between 19:03:00 and when night time begins (12 minutes), with the understanding that later flats would contain more stars.

The overall result of this testing indicated that the broadband flats (Baader B, G, R, Johnson U, B, V, R, I, and Luminance) can only be acquired during a very short period of time, around 10-15 minutes at the end of dusk and 10-15 minutes at the beginning of dawn, and it was best to take the flats in the order U, B, V, R, I to maximise the number of counts per second of exposure. But the narrowband filter flats could be acquired for about 45-15 minutes before the end of dusk.

With only three narrowband filters and about half an hour per night to get the necessary flats, the narrowband flats proved no problem and a significantly large number of flats could be acquired without impeding on the time needed to acquire broadband flats.

While the Baader filters were installed, there were only 4 broadband filters and

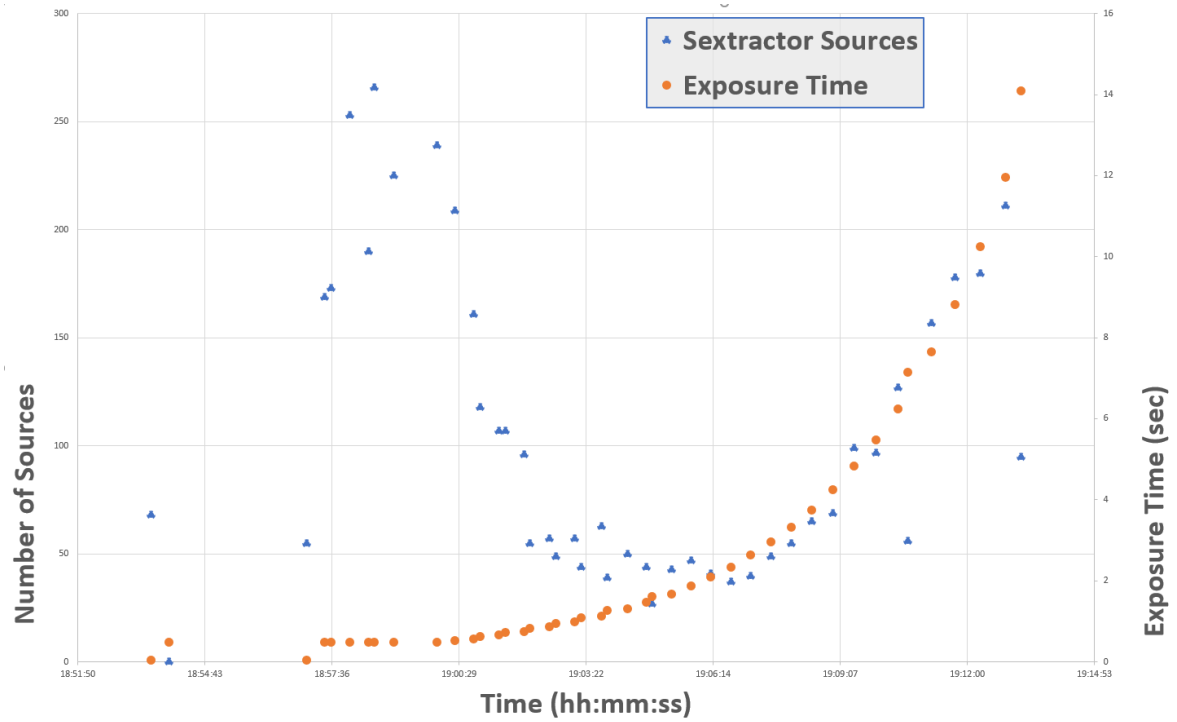

Figure 5: Measurements of the flat exposure time in orange, and the number of sources extracted from PIRATE Johnson B flat frames taken at dusk on 02/10/2018.

the flats could just barely be acquired during the 15 minutes. Around the same time the Johnson filters were installed, I was advised that it would be advantageous for ABOT to implement dithering between the flats. Dithering are small motions made by the mount between exposures to ensure any celestial objects in the frame are on a different position on the CCD, or out of frame between exposures meaning they are easily removed in the flat stacking procedure. Dithering takes time, as the mount has to slew to a new position, which means each flat takes more time when you add in the time for the dithering. Around 15-30s were added to the time taken for each flat.

The increased time required to take the flats, in combination with the increase from four to six broadband filters meant that all the broadband flats could no longer be taken every night.

I implemented a new strategy where U, V and I filters were taken on one night, then B, R and Luminance were taken the next night, rotating constantly, with binning 2 flats taken at dusk and binning 1 flats taken during the dawn. Table 3 illustrates the flat schedule over 2 consecutive nights.

Johnson Filter	U	B	V	R	I	L
Night 1	X		X		X	
Night 2		X		X		X

Table 3: The schedule for broadband flats taken by PIRATE over two nights, which repeats every two nights. L is the Luminance filter.

2.5 Signal to Noise of PIRATE

With a scientific telescope it is important to understand how much noise we expect to see at various apparent magnitudes, so we can decide whether or not to observe a target. In the following section I will try to measure how well PIRATE performs by calculating the signal to noise we expect.

VaST (Variability Search Toolkit) is a program developed by Sokolovsky et al. 2018 which can take as an input a series of calibrated images of the same field and generate light curves for every star which appears in every frame. VaST calculates several statistical measures of variability for each star in a series of frames of the same field, vs the instrumental magnitude for the star which is taken from the first image in the series fed to it. The instrumental magnitude can be calibrated to the apparent magnitude in VaST with some stars of known magnitude.

One of the statistical variability measures is the weighted standard deviation of each stars light curve. The plot of standard deviation vs apparent magnitude is a useful indication of the noise level in the light curve data; although most stars do vary to some degree, many do so only at a low amplitude of variation due to, e.g. sun spots rotating in and out of sight of the observer, or relatively small flare events. For stars that only undergo this low amplitude variation their standard deviation will be due to this, and random noise or detector noise. These stars are the majority of the data and as expected, the fainter stars have more random noise than the brighter ones.

Stars which vary with larger amplitudes will appear to have larger standard deviation than other stars at the same magnitude. This means VaST can be used to pick out variable stars from a set of data. For example in figure 6 there is a data point at ~ 13.75 mag and standard deviation ~ 0.15 mag which is much larger than other stars at the same magnitude which have standard deviation closer to ~ 0.01 mag. This is likely a variable star. Although this is a useful application for VaST, in this chapter we are more concerned with understanding the random noise in the data.

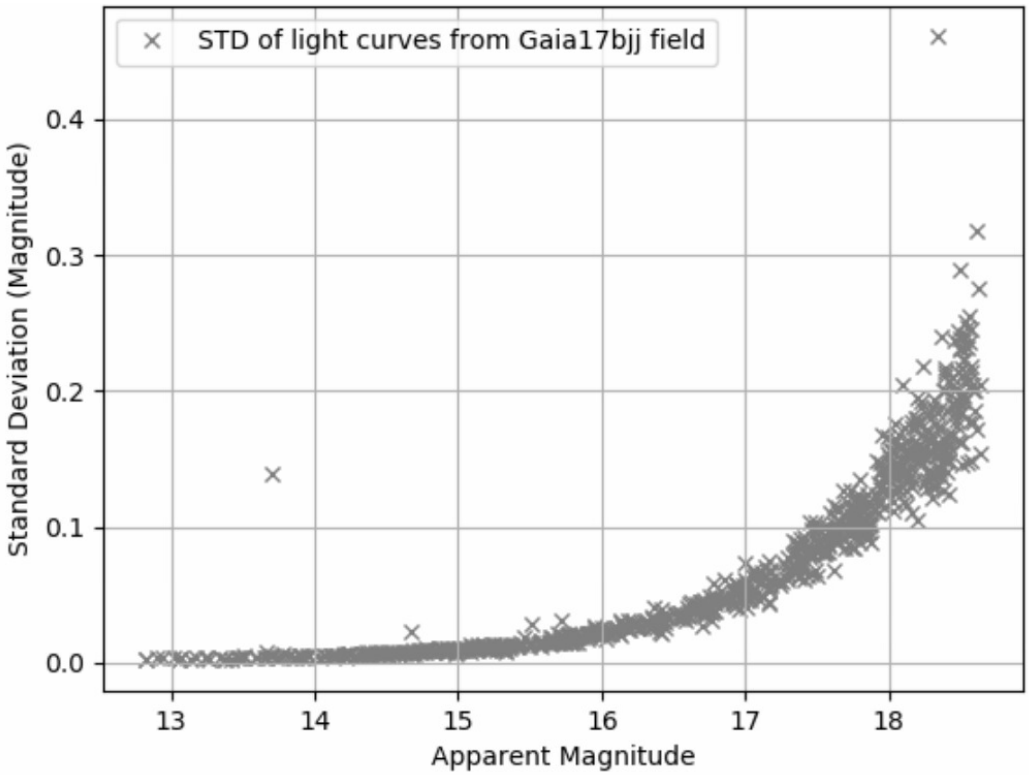

Figure 6: The clipped standard deviation of Baader R filter light curves generated for all the stars in a field which is centred on Gaia17bjj, plotted against the targets apparent magnitude as taken from the first frame in the series given to VaST. Data calculated by VaST.

The equation used by VaST to calculate the standard deviation (σ_{clip})

$$\sigma_{clip} = \sqrt{\frac{1}{N-1}\sum_{i=1}^{N}(x_i - \bar{x})^2} \tag{1}$$

uses average magnitude ($\bar{x}$) of the data set (x_i) which contains N measured magnitudes x_i where 5% of the brightest and 5% of the faintest measured magnitudes in each light curve are clipped up to a maximum of 5 points each side. The writer of VaST claims this is a useful method for removing photometrically corrupted data points which appear as outliers in light curves which affect the variability metrics used without actually identifying variability (Pashchenko et al. 2018).

In order to compare this measured scatter in the light curves to what should be expected for PIRATE, the CCD equation is used

$$SNR = \frac{gN_*}{\sqrt{gN_* + n_{pix}(gN_{Sky} + gN_{Dark} + N_R^2)}} \tag{2}$$

where SNR is the signal to noise ratio, N_* in ADU is the measured signal of the target, g (e^-/ADU) is the camera gain, N_{Sky} (ADU) is the number of photons per pixel due to sky background, N_{Dark} (ADU) is the number of electrons per pixel due to

dark current and N_R (e^-) is the number of electrons per pixel due to readout noise. N_{Sky}, N_{Dark}, and N_R are all given as values for a single pixel, whereas N_* is the counts in all the pixels which a star covers, so n_{pix} is the number of pixels N_* is counted for.

To convert to the logarithmic scale, we note that (Howell 2006, Birney et al. 2006)

$$\Delta m = 2.5log(\frac{S+N}{S}) = \frac{2.5}{ln10}ln(1+\frac{N}{S})$$
$$\Delta m \approx 1.0875(SNR)^{-1}$$

Where $ln(1+SNR^{-1})$ has been Taylor expanded and only the first term has been kept. Hence we use

$$\sigma_{mag} = 1.0875(SNR)^{-1} \tag{3}$$

The different terms in equation (2) need to be calculated, in the following I will explain how each value was calculated.

- N_R - the number of electrons per pixel due to readout noise is calculated by taking all the bias frames in the same binning as the data and median combining them, then taking the difference between that median frame and each of the bias frames used to make the median frame.

  The result are a set of median subtracted bias frames. Each of those median subtracted bias frames has the standard deviation of the counts in the pixels calculated.

  The resulting standard deviation for each of those frames are averaged together to give a single value for the readout noise in counts for one night.

  The process was repeated for six nights spread out over the course of the data, giving six values for the readout noise. Those values were averaged together to give a single value for the readout noise over the whole data collection run.

- N_{Dark} - the number of electrons per pixel due to dark current was calculated in a similar way to the readout noise. The bias frames from a particular night were combined to give a single median bias frame, and multiple dark frames of the same exposure length were also medianed together into a single median dark frame.

The median bias frame was subtracted from the median dark frame, and the resulting counts in the dark frame were scaled down by dividing by the dark exposure time.

The standard deviation of the counts in each pixel of the resultant dark frame is the dark noise for that night.

The process was repeated for the same six nights as the bias data and averaged to get a single value for the dark noise. Both this method and the read out noise method come from Holmes et al. 2011.

- N_{Sky} - the sky background per pixel was calculated by running source extractor on a night of data for the field.

  The BACKGROUND parameter in source extractor gives a value for the sky background in the central position of each source found in the frame (Holwerda 2005). The CCD equation uses the total number of background photons per pixel, so the average of all those values should be Representative of the whole frame.

  The process was repeated for all the frames in a night and then averaged, and then for the same six nights as the dark and read out noise and averaged again.

The expected values for the above categories of noise are calculated for targets with a range of counts and then the appropriate apparent magnitude for those counts are calculated by comparing the apparent magnitude of a star in the Gaia17bjj images to values in APASS catalogues. The particular star used for the magnitude calibration was used because it was not too bright or faint, and it had measured values in the three Johnson filters which approximately correspond to the same passband as the Baader filters. The same star was also used to calibrate the VaST magnitudes seen in figures 6 and 8, but even so there are a few different sources of uncertainty in using this method to position the magnitude scale of the signal to noise data.

- The value for the magnitude of the reference star has its own uncertainty in the APASS catalogues.

- The counts for the star in the PIRATE images also varies between exposures, both over the course of the night and over several nights. This means there is uncertainty in the counts being used as well.

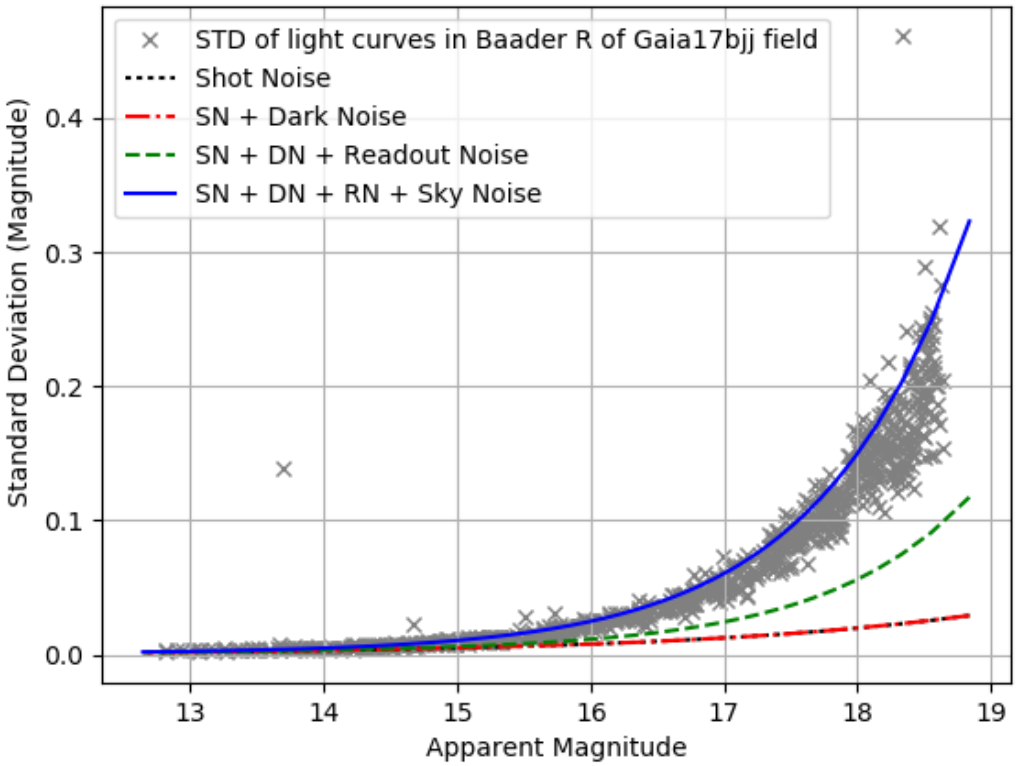

Figure 7: Contribution of the noise sources in equation (2). Each line represents the addition of another source of noise, eg. the black line only includes the shot noise, but the green line includes shot noise, dark noise and readout noise.

- The Baader filters do not exactly match any Johnson filters, they are only a rough match at best.
- The calibration may also vary depending on the colour of the star, so the calibration which applies to the chosen star with known magnitude may not apply exactly to another star in the field which has significantly different colour.

In figure 7 is an example of the contributions from the noise categories above. In this figure each noise source is added to the previous in the order shot noise, dark noise, readout noise and sky noise. The dark noise contributes the least, practically overlapping with the shot noise, which is the next largest contribution, followed by readout noise and sky noise which are the main contributors over all. The sky noise here uses the average of the sky background contributions over the time series processed by VaST.

In figure 8 the same data as in figure 6 is plotted, along with the expected value for the noise given by the CCD equation. Out of the four sources of noise in the CCD equation, the sky background provided the most variation of standard deviation. The

maximum, minimum and average sky background for the whole observing run have been plotted to show the variation which occurs over an observing run. Some nights the sky is much brighter than others due to factors such as a bright moon, or thin clouds moving into the view of the telescope. Although the CCD equation is expected to give a lower bound for the noise, we can see that the average sky noise is not below most of the VaST data points.

It is not clear why the calculated minimum expected noise is not below the majority the data from VaST. The difference is mostly likely related to the calculated sky background, as when the minimum value found on a single night for sky background is used, as displayed in figure 8, the noise does appear to be a lower bound for the majority of the comparison points. This may point to some detail in the method used to calculate the sky noise which leads to a higher value than expected, or perhaps the comparison of the value for minimum calculated noise with the standard deviation values calculated in VaST is not appropriate.

In addition to the Baader R filter graphs for Baader G, B, and Johnson R, V, B were calculated. And Johnson R, V and B were calculated for different exposure lengths as well. See appendix A.

Each night of the Gaia17bjj R data has three images, in figure 9 both the average for each night (blue crosses) and the median of each night (orange points) are plotted. The average and median for each night mostly appear to overlap, though it is possible that in some data something may affect the sky background between observations, such a thin cloud moving into view, so it would be better to use the median of each night as opposed to the average. Figure 9 also demonstrates that the sky background is highly variable between nights, and using either an average or a median may not be a good representation of the minimum sky background.

In addition to the above, to get a single value for the sky background over the whole observation series the background per night needs to be combined in some way. For the data in figure 8 (and the figures in appendix A) the average was used, but by looking at the average and median lines in red and green in figure 9 it seems that the median is more likely a better representation, due to the last two nights having significantly higher background than the previous nights, which increases the average value.

Figure 10 shows the difference between the average or median lines in figure 9 when used to calculate the CCD equation for Gaia17bjj R filter data. Although there is a difference between using the average and median, the difference is minimal.

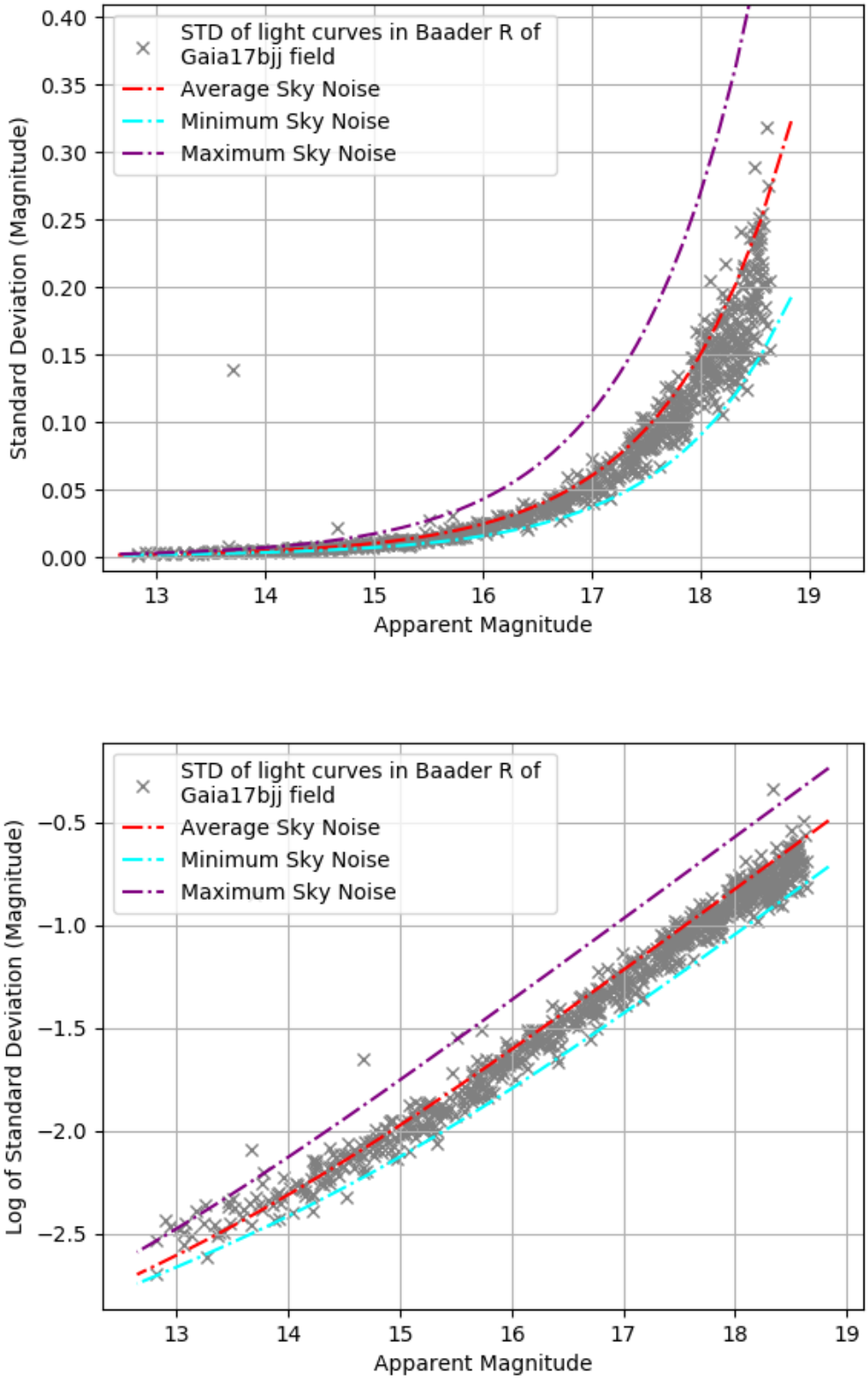

Figure 8: The same data of Gaia17bjj through Baader R filter included in the top figure, and also an estimation of the expected noise given by equation 3. The lower plot is the same data again plotted on a log scale to easier see what is going on at the bright end of the magnitude.

For any set of light curve data there will be an expected minimum level of noise which are those sources in equation 2. There will be a minimum quantity of shot noise, sky noise, dark noise and readout noise which in combination will account for a minimum level of scatter which we would expect to see even in an ideal star which is completely constant over the course of the measurements. This in turn can be used to understand what level of uncertainty we should expect to see in a set of data. For example in figure 8, measurements of a star through the Baader R filter with apparent magnitude 18, a 1σ result would expect 68% of measured results to be within ~ 0.15mag of 18 mag.

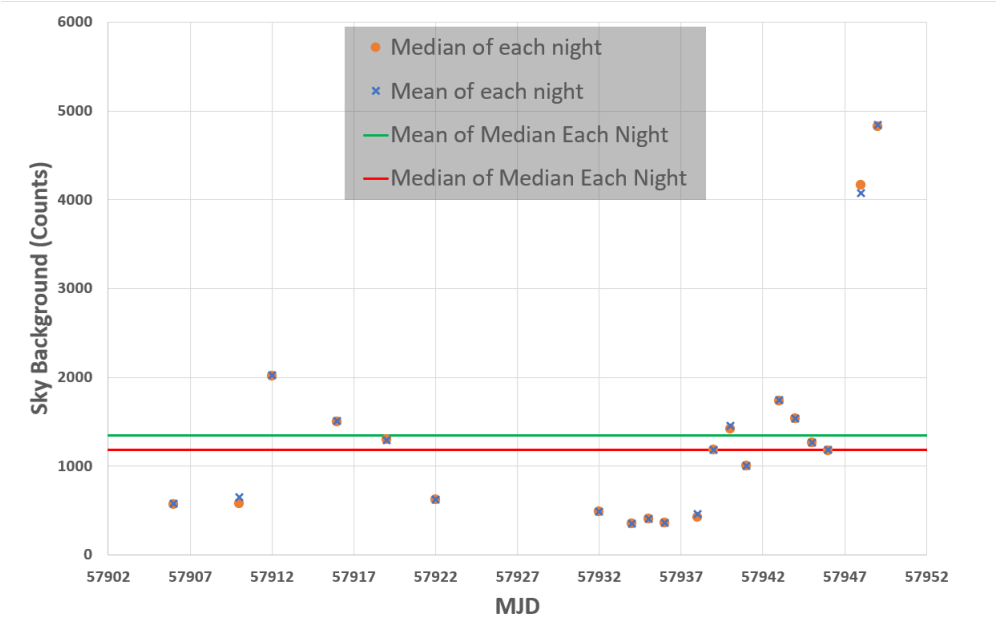

Figure 9: The sky background each night for Gaia17bjj through the Baader R filter between 01/06/2017 and 14/07/2017. The data points represent either the average background per night (blue crosses), or the median background per night (orange points). The two lines represent the average (green) and median (red) of the orange data.

The first reason for calculating the expected signal to noise ratio for PIRATE observations is to give an estimate of the quality of light curves which would be generated for targets at a particular magnitude before observations begin. For example, for a target around magnitude 15 in the Baader R filter we should expect relatively low uncertainty in the data at 0.01 mag, compared to a target at magnitude 18 which should have uncertainty 0.15 mag. This information means we can make more quantitatively informed decisions about how to spend telescope time based on the magnitude of the target. The magnitude 18 target in this case may not be worth observing if the type of variation expected is typically lower than the uncertainty expected.

The second reason for calculating these values is to determine whether variations

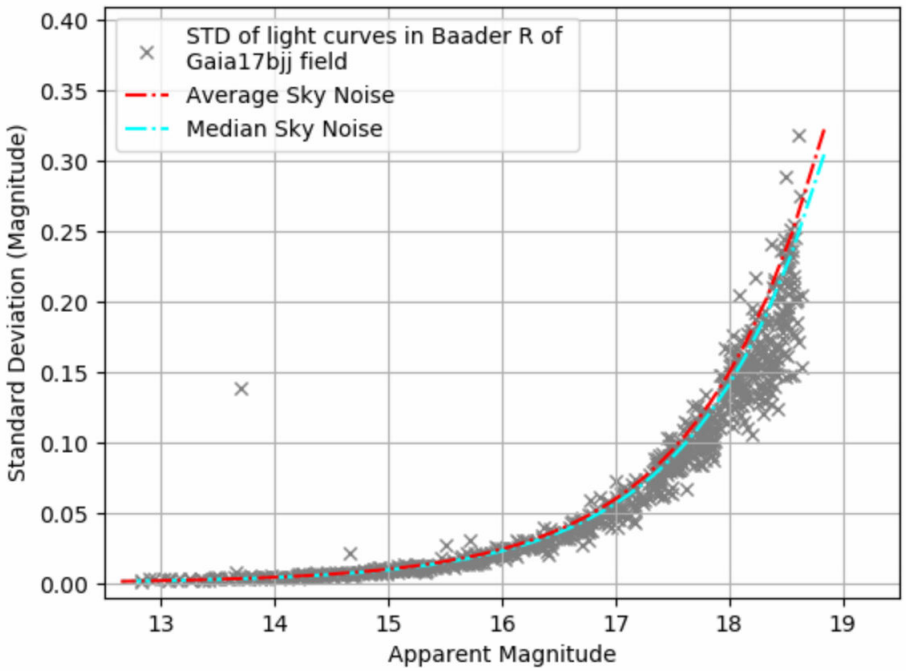

Figure 10: The CCD equation for Gaia17bjj in R using the average of every nights data in red, and the median of every nights data in cyan.

seen in an already observed target are likely due to noise, or due to some real variation due to the target. For example, if in the observations of the magnitude 15 star we see data which is varies by 0.05 magnitude, we know that that is higher than the 0.01 magnitude variations expected due to noise and therefore may be worth further investigation. Whereas if we see that same 0.05 magnitude variation in the magnitude 18 target, it is likely dismissable as variation due to noise.

The use of the minimum values calculated here are complicated by the fact that the minimum values do not appear to be below the data points from VaST. This discrepancy deserves further investigation, as the actual lower bound for the variability measured by VAsT would be reproduced by using the minimum sky background. The sky background is highly variable from night to night and the value I calculated using the method described on page 21 may not be representative of the minimum, but likely is some value higher than that. Going forward I will still refer to the uncertainty values calculated through this process, with the knowledge that the lower bounds of expected uncertainty due to noise may actually be lower than the calculated values, and so borderline variations should be considered more closely before dismissal.

2.6 PIRATE and Monitoring Variables

PIRATE presents an opportunity to perform long term follow up of variable and transient stars without the need for constant upkeep through human intervention, with only occasional maintenance trips required once or twice a year. It fits in with a host of other robotic autonomous telescopes which are currently observing variable targets of many different types and can be used well to contribute to collaborative photometric data in the astronomy community.

The figures presented in appendix A along with figure 8 give some indication of the level of uncertainty which should be expected in PIRATE data for targets of various magnitude, by using the CCD equation to account for several sources of noise.

The next chapter will go over different types of variable and transient stars which may be observed in this project.

3 Variable and Transient Stars

All stars change in brightness to some degree at some point throughout their lifetime, though the degree of variation in a lot of cases is too small to be visible from the Earth. Some stars are constantly varying with a particular period, like pulsating Cepheid variables which physically expand and contract, constantly varying in brightness as they do. Some stars undergo transient variability, such as supernova which increase in brightness, reaching a peak in absolute magnitude between -16 and -20 after just a few days, before slowly decreasing in brightness at ~ 0.1 mag per day. One way this variation can be detected is by measuring the light from stars arriving at the Earth over time; stars which have an increase or decrease in flux reaching the Earth are classified as variable. The kind of variable depends on the amount of time spent varying, the amplitude and manner of the variation and the physical properties of the star doing the varying (North et al. 2014).

The first variable star discovered was over 400 years ago, a Mira variable called Omicron Ceti in 1596 by David Fabricius. Over the course of the next 250 years only a handful of variables were recorded, but since 1850 advances in astronomical technology and techniques have meant that many more variables have been observed (Percy 2007). As of writing the most recent version of the General Catalogue of Variable Stars (GCVS 5.1) contains a list of 52,011 known variables within the Milky Way (Samus, N. and Kazarovets, E. and Durlevich, O. and Kireeva, N. and Pastukhova, E. 2017).

During the nineteenth century Friedrich Argelander began a naming system for variable stars where the first variable star found within a constellation would be given the designation R constellation (for example R Cygni). The next star would be named S constellation and so on. The tenth variable star would be named RR constellation, the eleventh would be RS constellation and so on up to ZZ constellation. After ZZ the names began AA constellation and so on. After letters of the alphabet run out for a constellation, variables are commonly named V335 onwards. Typically the class of variable is named after the first documented case of that type of variable, RR Lyrae for example (Kulkarni 2016, North 1997).

Since 1946 Lomonosov Moscow State University has kept the GCVS. In March of 2017 edition 5.1 was published, which lists 52,011 known variables within the Milky Way, and the most recent version of the New Catalogue of Suspected Variable Stars published in February 2017 contains a further 14,811 entries. GCVS uses its own experimental nomenclature and classification system for variable stars. The class name

is usually a shortened version of the common name (stars of type FK Comae Berenices for example are known as FKCOM in the GCVS) (Samus, N. and Kazarovets, E. and Durlevich, O. and Kireeva, N. and Pastukhova, E. 2017).

The American Association of Variable Star Observers (AAVSO) also has a catalogue of variable star in The International Variable Star Index (VSX) which currently[3] contains 1,438,172 variables. The catalogue was created with the aim to keep up to date information on variable stars using information from many sources (Watson et al. 2006).

The ASAS-SN group also keeps a database of variable stars with ASAS-SN light curves for over 666,000 targets[4] (Shappee et al. 2014, Jayasinghe et al. 2019).

In this section, variables will be described using the GCVS naming and classification system, though the common name will be used as well where available.

There are many different categories of variable stars, each with their own mechanisms for variation and their own distinguishing features. Even the Sun varies; dark star spots appear making the surface fainter, then disappear returning the surface to its original brightness. Solar flares occasionally erupt which when seen from far enough away that they are unresolvable from the disc of the Sun would cause the Sun to appear as though it had increased in brightness for a short period (Albrecet et al. 1969).

Variable stars are broadly split into two different categories and six different subcategories. Intrinsic variables are stars which vary in brightness over time due to some physical process, for example Cepheid variables periodically physically contract and expand causing an increase and decrease in brightness. Intrinsic variables can be broadly split into three subgroups: pulsating variables, eruptive variables and cataclysmic variables.

Extrinsic variables only appear to vary in brightness due to some external mechanism, such as eclipsing binaries where two stars orbiting one another appear to change in brightness as they pass in front of and behind one another. They can also be split into three subgroups: rotating variables, eclipsing variables and microlensing events (North et al. 2014).

GCVS does not include a list of microlensing events which I will describe here, but it does also include X-ray variable sources.

For this project the types of variables which I chose to follow up in particular were microlensing events and supernovae. Along the way I observed some variables which

[3]Accessed September 2020

[4]Accessed September 2020

were of unknown type at the time, so in the following chapter I will briefly discuss the main types of intrinsic and extrinsic variables with a particular focus on microlensing events and cataclysmic variables.

It is worth noting that some stars vary exclusively in bands of the electromagnetic spectrum outside the visible, and some vary in multiple different bands. For example GCVS includes X-ray variables such as X-ray binaries (XJ) where a usually optically visible star donates matter to a compact companion star such as a neutron star or a black hole, and as matter accretes to the companion or an accretion disc surrounding it, X-ray photons are released (Verbunt 1993). Another example are radio pulsars first discovered by Hewish et al. 1968, spinning neutron stars which emit beams of electromagnetic radiation, which lead to "pulsing" radio waves being received on Earth. Although pulsars radiate in other bands of the electromagnetic spectrum, the period of variation is typically on the scale of a few milliseconds to a few seconds and are not ideal targets for this project. I have excluded these from the following discussion as I am exclusively interested in targets which can be observed by PIRATE which is specifically an optical instrument.

3.1 Rotating Variable Stars

Rotating variables are distinct from other types in that the period of their variability is linked to the period of rotation of the star. The variability itself is due to some non-uniformity with their surface brightness such as star spots or in some cases because it has an ellipsoidal shape, which means as the star rotates, the changing aspect causes a variation in brightness.

Any star which rotates around an axis which is not parallel to the observer's line of sight and which has surface features that are either non-uniform around the axis of rotation or appear and disappear over time, will appear to vary in brightness to some degree.

In addition to the actual physical difference in brightness of different parts of the ellipsoidal star, depending on the axial rotation of a star, more or less of the disc of the star may appear at different times due to it appearing circular, or elliptical at different times.

Rotation makes stars ellipsoidal in shape due to centrifugal forces, which also leads to 'gravity darkening'. The ellipsoidal shape leads to the poles of the star appearing brighter than the equator, as the lower radius at the poles leads to higher surface

gravity, and by Von Zeipel's theorem the radiative flux of a uniformly rotating star is proportional to the local surface gravity (Tassoul 2000).

This variation in surface brightness cannot be seen in single stars, but is typically seen in binary pairs where the gravitational pull of the companion in addition to the centrifugal forces also has the effect of making the star appear ellipsoidal. This kind of variability is a type of binary variable rather than rotating variable. GCVS has both ELL which are a close binary pair of rotating ellipsoidals which are not eclipsing but vary in brightness due the change in emitting area visible to the observer during their orbits, and a sub-classification of eclipsing binaries RS (RS Canum Venaticorum) where one of the binary pair is also a rotating variable (Percy 2007, Percy 1978).

FK Comae Berenices is an example of a rotating star which varies both due to effects of gravity darkening and also due to the presence of many star spots. FK Com is a giant star which is rotating very rapidly (νsini $\sim$100km/s), and it is the prototype for FKCOM type variable stars, first identified by Bopp et al. 1981. In 1993 Jetsu, Pelt and Tuominen described star spot activity flip-flopping from one hemisphere to the other on FK Comae using photometric measurements made over 25 years (Jetsu et al. 1993).

3.2 Eclipsing Variable Stars

For a closely orbiting binary pair of stars, if one star passes between the observer and the other star, then the system is an eclipsing variable system. Most close binaries are not 'visual binaries', they are too close together compared to their distance from the observer to be resolved individually with current optical systems and techniques.

The eclipsing itself leads to a variable light curve, but the proximity of the stars to one another also leads to some other interesting effects. One such effect of some eclipsing binaries is reflection, where the light from one of the pair irradiates the other being absorbed and re-emitted by the reflector. This leads to a noticeable effect in the light curve, usually a slight dip just before an eclipse.

GCVS classifies "Eclipsing binaries" using several different properties, the first of which uses the shape of the binary light curve. Generally the light curve of a binary system has two minima, one when the brighter of the two stars passes behind the fainter (primary minima) and a second when the fainter star passes behind the brighter star (secondary minima).

EA (Algol) binaries have predominantly flat light curves, and the beginning and

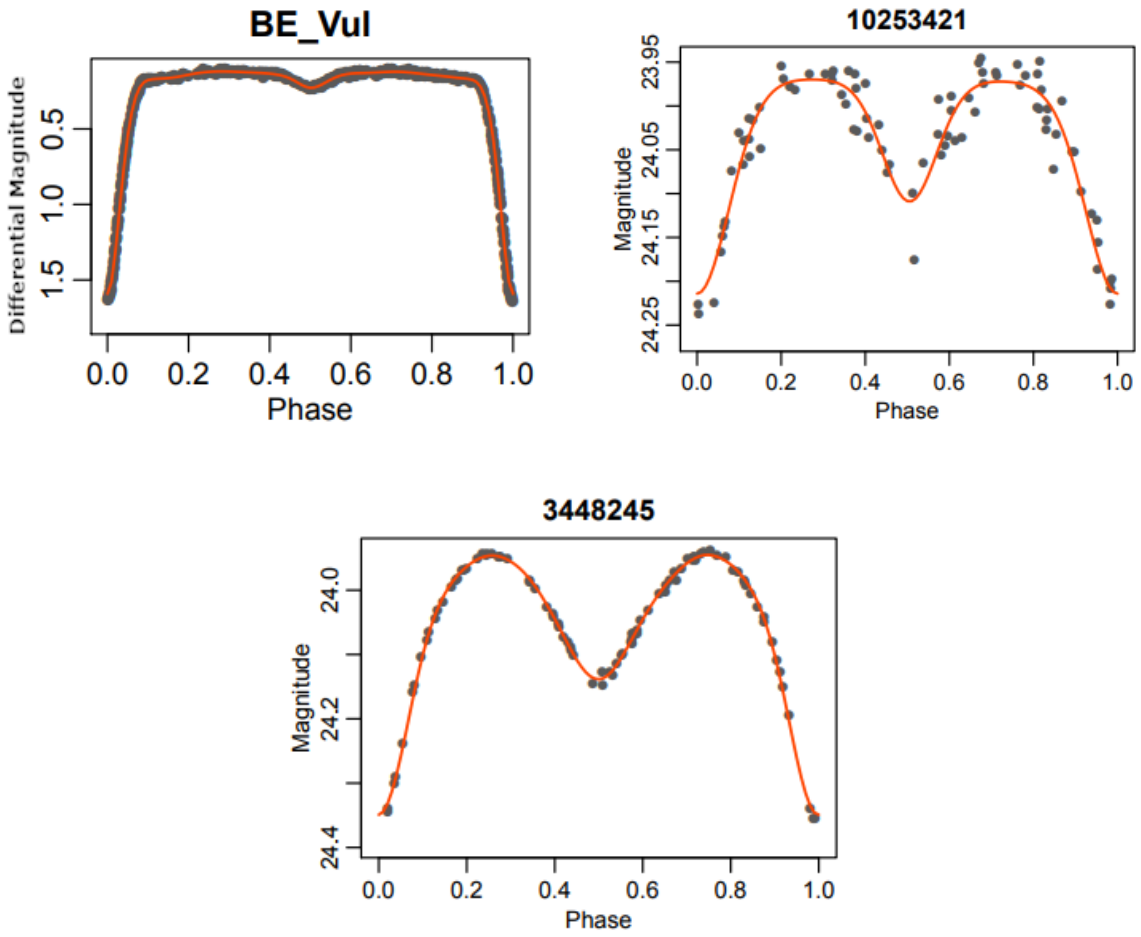

Figure 11: Example light curves of eclipsing binary systems. Top left is CALEB BE Vul, an example of an EA binary; top right is Kepler 10253421, an example of an EB binary; the bottom is Kepler 3448245, an example of an EW binary (Süveges et al. 2017).

end of the primary eclipse minima are easily identifiable, the secondary eclipse minima may be absent or extremely small relative to the primary minima (top left of figure 11). EB (β Lyrae) binaries have slightly harder to identify primary minima beginning and end points, and the secondary minima are very small relative to the primary if they are present at all (top right of figure 11). EW (W Ursae Majoris) binaries have continuous light curves where the beginning and end points of primary and secondary minima are indistinguishable, and the secondary minima are a significant portion of the depth of the primary minima (bottom of Figure 11). Kepler 10253421 and Kepler 3448245 in figure 11 also demonstrate why it is sometimes difficult to distinguish between EB and EW light curves.

The light curve morphology is a simple, but not necessarily the best way to distinguish these binaries. GCVS uses the position of the component stars in the HR diagram, Lagrange surfaces and the Roche Lobe concept alongside the light curve classification system.

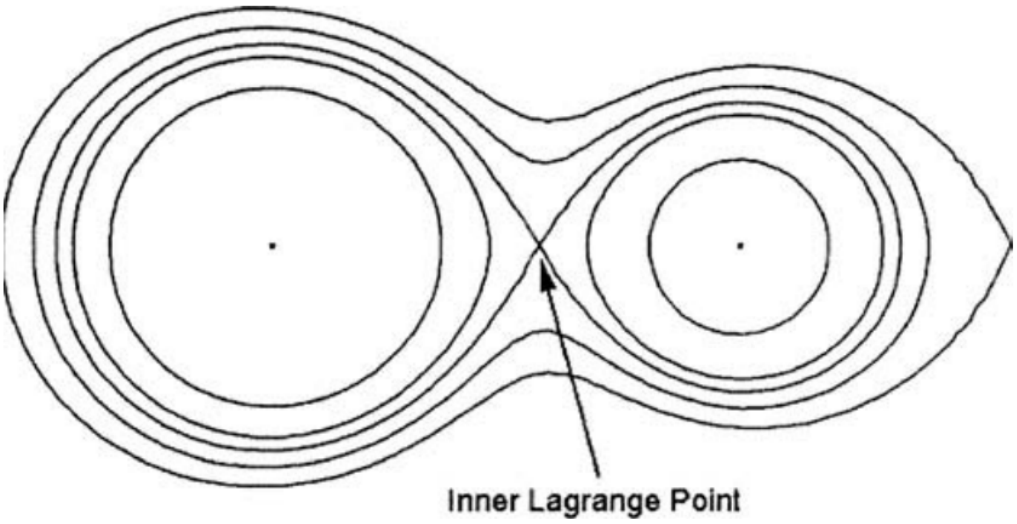

Figure 12: Illustration of surfaces of gravitational equipotential surrounding two stars as seen from the co-rotating reference frame as described by the Roche Model. Where the surface of each star is distorted enough to form an hour-glass shape with the other star the surfaces are called the Roche Lobes. (Percy 2007).

Around single stars the surfaces of constant gravitational potential energy are described by spheres which change proportionally to $1/r$, where r is the distance to the centre of the star.

For binary systems these surfaces are not simple spheres, as the equipotential surfaces of the two stars interfere with one another. By taking the co-rotating frame of the binary pair, we can model how these surfaces look. This model is called the Roche Model and figure 12 illustrates what the surfaces of constant gravitational potential look like in a binary system. Close to each star the surfaces are nearly spherical, and surfaces further out surround both stars. Between these two sets of surfaces, there is a critical surface which passes through the L1 Lagrange point for the system forming an hourglass shape around the two stars. These are the Roche Lobes for the system, and depending on how large each star is compared to its own Roche Lobe can be used to distinguish Eclipsing binary systems.

If we consider a binary pair in which both stars are initially much smaller than their respective Roche Lobes and still mostly spherical, then we have a *detached binary* with two stars orbiting one another.

At some point during the life time of the binary, one star may start to expand as part of its natural life cycle and as it does so the star will start to become more elliptical as the gravitational attraction of the companion becomes too large for the gravity of the expanding star to remain spherical. If the star continues to expand

until it reaches the size of its Roche Lobe while the other remains smaller than its own Roche Lobe it becomes a *semi-detached binary*. In this situation the combination of the expanding star's hydrostatic pressure and the gravitational attraction of the companion will overcome the gravity of the expanding star and matter may begin to pass to the companion, passing through the L1 Lagrange point. As the matter must conserve angular momentum the matter will spiral around the companion and either form an accretion disc or fall directly to the surface of the companion.

A third situation would have both stars expand to the point of filling their respective Roche Lobes, this would be a *contact binary* as the two stars would essentially be in contact (Kopal, Zdeněk 1989).

GCVS uses EA, EB and EW to classify binary systems by light curve, and roughly correspond to detached, semi-detached and contact respectively but these correspondances are not exact. Basic Roche Lobe classifications by GCVS are labelled D, SD and K for detached, semi-detached and contact respectively. The link between the two system is imprecise because the light curve morphology is not always easy to distinguish. The luminosity of the stream of matter passing between stars in a semi-detached system may be very high, while the luminosity of the matter stream of a detached system which is only passing very small amounts of matter between the two stars may be relatively low, leading to SD systems being labelled as EW for example.

On top of this classification, GCVS has two other sub-classification systems. Eclipsing binaries are classified first by their light-curve (E, EA, EB or EW). Then they are classified by either how they fill their Roche Lobes (AR, D, DM, DS, DW, K , KE, KW, SD), or by the physical characteristics of the stars (GS, PN, RS, WD, WR). See Table 4.

For example:

- EA/GS – An Algol binary where one or both of the stars is a supergiant
- EW/K – A W Ursae Majoris binary where the stars are in physical contact
- EB/WD/SD – A β Lyrae binary where one of the components is a white dwarf and the system is semi-detached

Eclipsing binaries are relatively abundant, the GCVS lists over 7000 E, EA, EB and EW stars without even including any of the sub-classified varieties. Using spectroscopic and photometric measurements and simple geometry the masses and radii of the stars

Sub-classification (physical)	**Description**
GS	Either one or both stars are a giant or supergiant
PN	One of the stars contains the nuclei of a planetary nebulae
RS	One of the stars is also a rotating variable (RS Canum Venaticorum)
WD	One of the stars is white dwarf
WR	One of the stars is a Wolf-Rayet star
Sub-classification (Roche Lobe)	**Description**
AR	Detached, both subgiants not filling their Roche-Lobes (AR Lacertae)
D	Detached
DM	Detached, both stars main-sequence
DS	Detached, one star is a subgiant not filling its Roche-Lobe
DW	Similar to KW (W UMa), but not in contact
K	Contact System
KE	Contact System, early O-A spectral type close to Roche Lobe size
KW	Contact, ellipsoidal, F0-K, primarily MS secondary below and to the left of the main sequence (W UMa)
SD	Semi-Detached

Table 4: Sub-classifications used by GCVS for eclipsing binary systems. Physical sub-classifications refer to the type of stars which form the binary pair, and Roche Lobe sub-classifications refer to the stars physical size compared to their Roche Lobes.

involved in a binary eclipsing event can be calculated relatively easily (Southworth 2012).

3.3 Pulsating Variable Stars

The most commonly known type of pulsating variable stars are Cepheid variables, well known as an important rung on the cosmic distance ladder due to the Period-Luminosity relationship discovered in 1912 by Henrietta Leavitt (Leavitt et al. 1912).

But Cepheids are just one type of pulsating star out of many; in fact GCVS lists 35 different kinds of pulsating star.

Pulsating variables increase and decrease in brightness due to expansion and contraction of the outer layers of the star. The type of expansion and contraction is usually referred to as either radial or non-radial, though some astronomers consider radial to just be a special case of non-radial. Radial pulsation is spherically symmetric, meaning the whole surface moves together as it expands and contracts. Non-radial pulsation means the shape of the star changes as well because different parts of the outer layer expand and contract at different times.

Stellar pulsation is analogous to oscillation, in that radial expansion can occur at a fundamental frequency and with higher harmonics. In the fundamental frequency the entire star expands and contracts together, while the first harmonic has a spherical surface of material which remains stationary. Material outside the sphere expands and material within the surface contracts, higher harmonic modes have multiple spheres of stationary material.

Non-radial pulsation does not expand and contract the entire star, but instead only a portion of the star expands, leading to the star changing shape with the pulsations. Non-radial pulsations also have modes of oscillation, in fact there are infinitely many along each coordinate axis. Typically stars which non-radially pulsate do so with a smaller amplitude than the radial pulsators, and many of the pulsating variables with relatively large amplitudes, such as the the Cepheids and Mira variables are radial pulsators. (Percy 2007).

For a star to radially pulsate, the gravity acting on the outer layers of the star must not be balanced by the pressure forcing those layers outwards. Some outer layer of the star needs to collapse inwards towards the core due to gravity and overshoot the point of hydrostatic equilibrium, where gravity and pressure are balanced. Then some mechanism is required to allow that layer to be forced back outwards by the interior pressure of the star, beyond the hydrostatic equilibrium point again, at which point gravity can again take over.

The κ mechanism describes the process in which star matter collapses inwards and compresses particular layers of gas which increases the amount of ionisation in that layer. This increase in ionisation in turn increases the opacity (κ), whereas typically an increase in temperature would decrease the opacity; the opaque layer created by this ionisation acts as a dam for the inner layers of the star. The increased thermal pressure

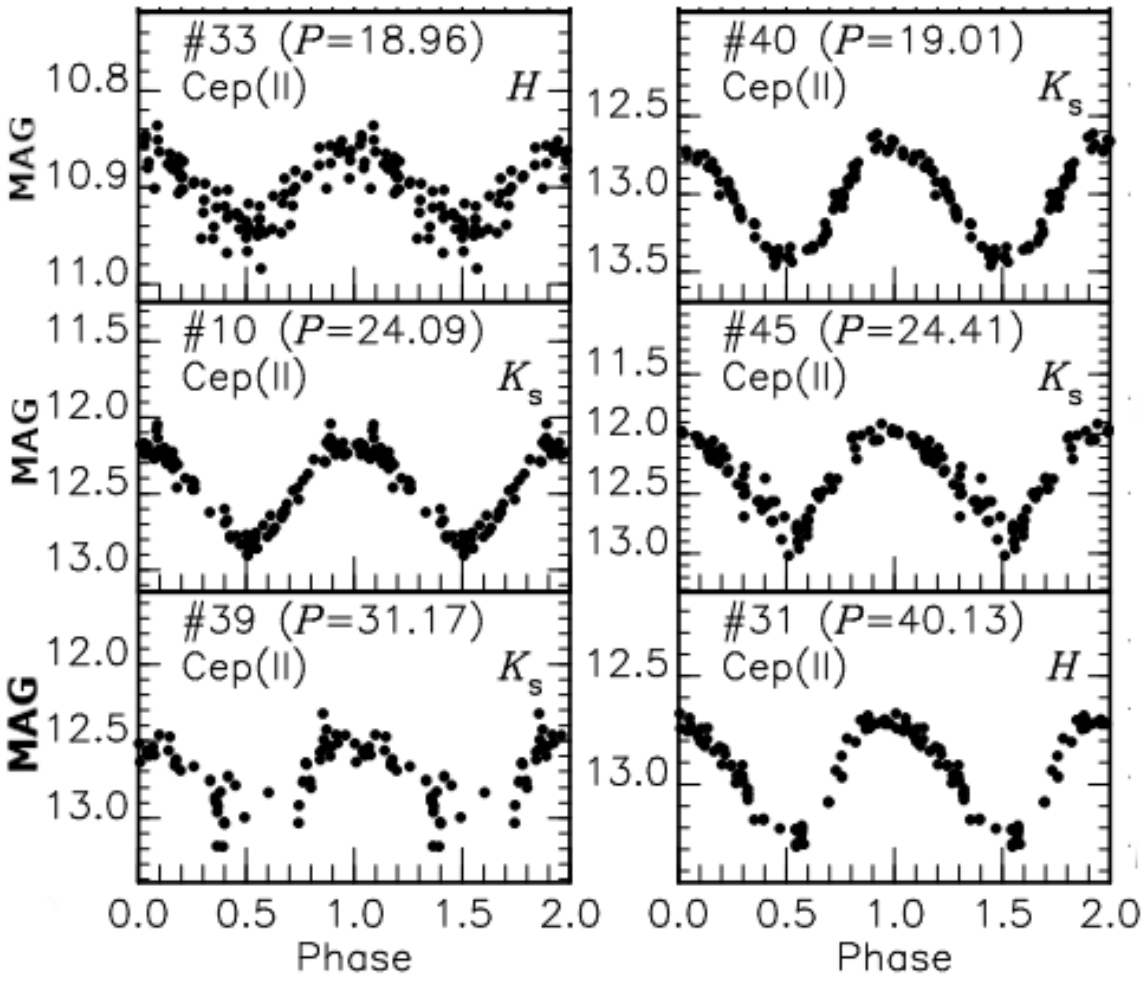

Figure 13: Example phase-folded light curves of multiple pulsating variables observed towards the galactic centre. Observed in the infrared using the IRSF 1.4 m telescope between 2001 and 2008 (Matsunaga et al. 2013). All of the pulsating variables pictured are type 2 Cepheid variables, where P indicates the calculated period of rotation in days, and H and K_s are the filters in which the targets were observed.

causes that layer to be forced outwards, decreasing in opacity as ions recombine with free electrons and as it does so, releasing some of the thermal energy and allowing the star to collapse under gravity again. The ionisation which causes the increased opacity comes from different elements in different types of pulsators, such as Mira variables which pulsate due to the ionisation of hydrogen and RR-Lyrae are due to the second ionisation of helium.

Many types of pulsating variables lie in the instability strip, a region of the Hertzsprung-Russell diagram off the main sequence, but not all pulsating stars lie in the instability strip. Figure 14 illustrates many different types of pulsating variables on an H-R diagram, including the cepheid instability strip (Ceph), Mira variables, beta-cephei and several types of pulsating white dwarfs along the white dwarf cooling track (DOV,

DBV, DAV). As some stars evolve they pass through the instability strip and the conditions inside the star become right for this process to occur (Zeilik et al. 1998).

The κ mechanism is a cyclic process, where the brightness of the star decreases as the opaque layer increases in opacity. This leads to light curves like that of δ Cephei,the prototype classical Cepheid variable DCEP (δ Cepheid), and many other examples found since that prototype, such as in Figure 13. Cepheids are typically yellow supergiant stars which are split into type 1 which are young massive stars, and type 2 which are old stars which are less massive than the Sun.

Cepheids were the first type of pulsating star to be observed to obey a luminosity-period relationship in 1912 when Henrietta Leavitt was working on observations of Cepheids in the Large Magellanic Cloud. Given how large the LMC is compared to the distance between us and the LMC, all the stars can be approximated to be at the same distance from us. Henrietta Leavitt found that Cepheids in the LMC with longer periods appear to be more luminous, and since the stars are all a similar distance from us the relationship must be intrinsic to the Cepheids themselves. The median luminosity of a Cepheid is directly related to its pulsation period, and with observations of the pulsation period of Cepheid variables can be used to calculate the median absolute magnitude, and therefore its distance from us.

RR (RR Lyrae) variables are another type of pulsating variables, with approximately 1.5 mag amplitude in the V band over the course of less than 1 day. They are typically stars which have moved on from the hydrogen burning phase to the helium burning phase of their evolution. They appear to all have the same absolute magnitude within a few tenths of a magnitude, regardless of period of oscillation which means they do not strictly follow a period-luminosity relationship in the same way as Cepheid variables, though astronomers have noticed a kind of PL relationship only in K filter of the Johnson-Cousins-Glass system which relies on the metallicity of the RR Lyrae variables (Catelan et al. 2004).

3.4 Eruptive Variable Stars

Eruptive variable stars typically involve some violent outburst of energy which take place in the chromosphere or coronae, and which also interact with the surrounding interstellar medium in some cases. There are a few different causes for these variations, some, such as UV Ceti variables (UV in GCVS), are strongly flaring stars which can increase in brightness by 6 magnitudes in seconds, then return to normal after a few

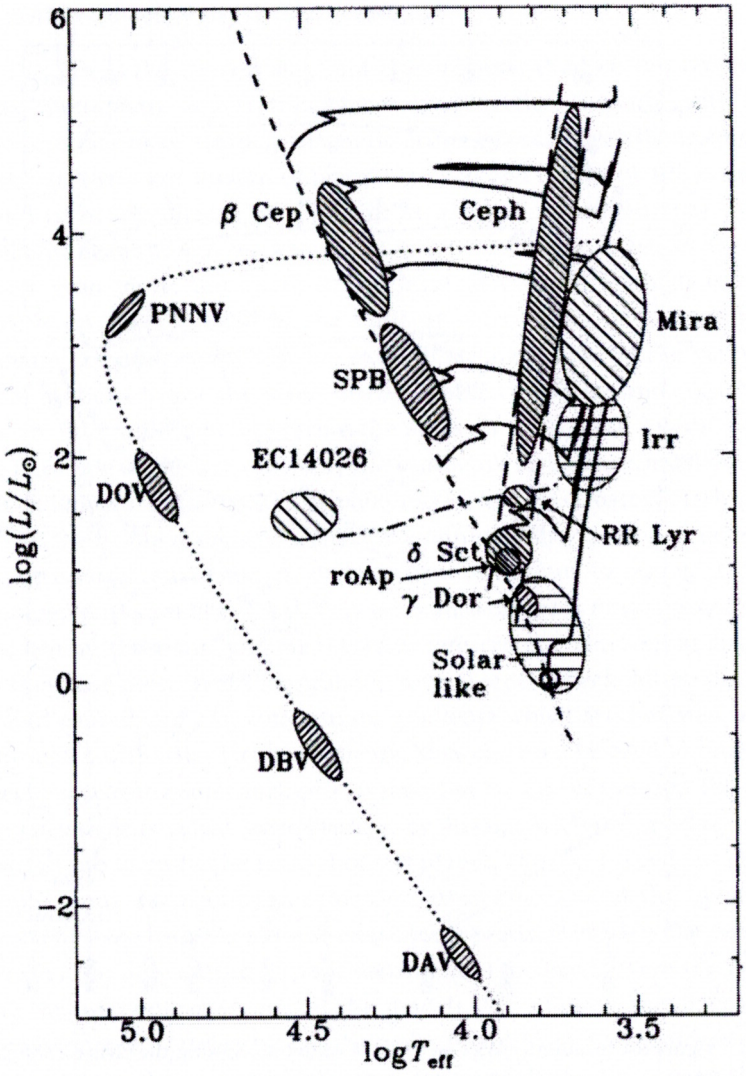

Figure 14: Regions of the H-R diagram where various types of pulsating star can be found, including the cepheid instability strip (Ceph) (Percy 2007).

minutes or hours.

T Tauri stars (INT,IT) are pre-main sequence stars found in star forming regions of gas and dust, which are above the main sequence in an HR diagram and evolving towards it. Although they are named for a photometrically variable example they are defined through spectroscopic features such as a strong Li γ6707 line. Photometric variability in these stars is often irregular and can be due to both activity on the rotating surface of the star, and the continued accretion of matter on to the surface of the star (Percy et al. 2010).

FU Orionis variables (FU) steadily increase in brightness over days or months reaching around 6 magnitudes brighter than before the outburst event, then slowly fades again. The prototypical example, FU Orionis, is fading very slow, having declined less than 1 magnitude since it's outburst in 1937, whereas V1057 Vygni which brightened by

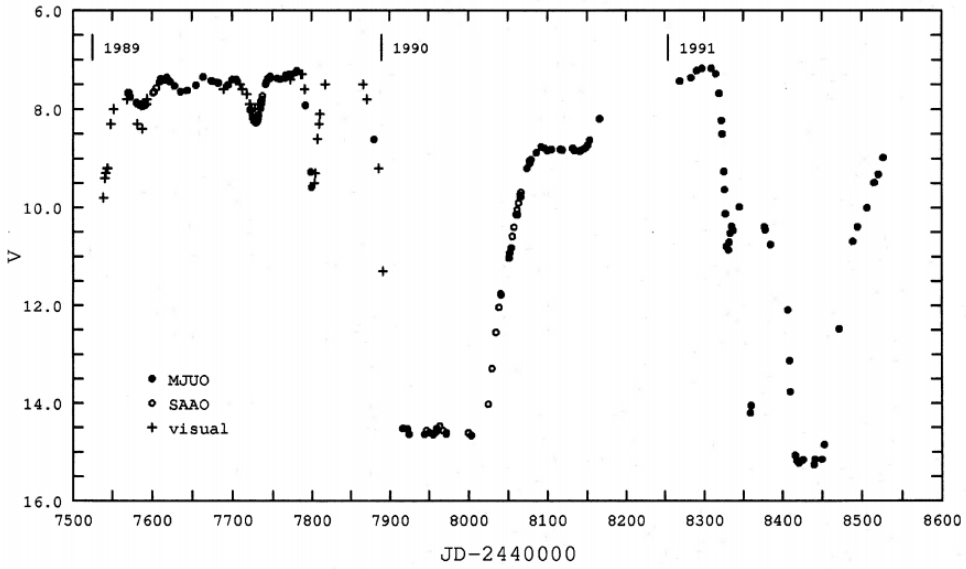

Figure 15: Light curve of an RCB star, in this case V854 Cen, data taken between 1989 and 1991 shows the star dipping up to ~ 8 mag irregularly (Clayton 1996).

6 magnitudes in 1969 faded by around 2 magnitudes in the 5 years after the outburst. FU Orionis stars are currently believed to be an evolutionary stage of some T Tauri stars, V1057 was identified as a T Tauri star prior to its outburst. The current understanding for what causes this outburst has a T Tauri star which is steadily accreting matter from a surrounding disc at a rate around $\sim 10^{-7}$ $M_\odot$ yr^{-1}. Occasionally the rate of accretion increases due to an outburst of the the inner accretion disc, resulting in an increased accretion rate of $\sim 10^{-4}$ $M_\odot$ yr^{-1} depositing as much as 0.01 $M_\odot$ onto the T Tauri star, and heating of the disc causes it to radiate optically. (Hartmann et al. 1996, Herbig 1977).

Another type of eruptive variable are the R Coronae Borealis (R Cor or RCB) irregular variables. These stars experience a significant dip in brightness of up to 9 magnitudes for irregular periods between a few weeks to a few months, before returning to their original brightness. This process is thought to be due to absorption of light by condensed dust grains in the stellar atmosphere ejected from the star. They then get brighter again when the dust grains disperse due to radiative pressure (Howell et al. 2013). Figure 15 shows an example light curve of an R Cor, V854 Cen.

3.5 Explosive and Novalike Variables (Including Cataclysmic Variables)

In the GCVS there are five groups of explosive and novalike variables: novae (N) and subdivisions (NA, NB, NC, NR), supernovae (SN) and subdivisions (SNI, SNII), dwarf novae (UG) and subdivisions (UGSS, UGSU, UGZ), symbiotic Z-Andromedae (ZAND) and novalike stars (NL).

Cataclysmic variables (CVs) have a more explicit definition which doesn't include all of the types listed above. They are interacting binary systems where a low-mass star has filled its Roche Lobe and is transferring hydrogen-rich matter to a white dwarf companion, which typically forms an accretion disc around the white dwarf. The accretion disc in a cataclysmic variable system is often brighter than the component stars. As matter spirals through the disc and releases gravitational energy which heats the disc to $\sim 3000 - 100,000$ K with luminosity $\sim 0.001 - 10$ $L_{\odot}$ (Patterson 1984).

In the case of a white dwarf with a significantly high magnetic field, the formation of an accretion disc can be prevented, and matter will fall directly onto the magnetic poles of the white dwarf forming a Polar, or an AM Her star. One such example is EU Cancri which was observed to have a magnetic field strength of 41 MG (Williams et al. 2013).

Most of the variables labelled as explosive and novalike variables in the GCVS are CVs, but GCVS does include some types which do not fit into the definition. For example GCVS includes all supernovae in the category, and while current models for type Ia supernovae suggest a progenitor system which may fit into the CV definition, all other types of supernovae including types Ib/c and type II, appear to originate from a single star undergoing core collapse and are therefore not cataclysmic variables.

In a typical system which experiences a nova event there is a white dwarf which is accreting matter onto its surface from an accretion disc which has formed from matter which has overflowed the Roche lobe of a cool companion K or M type dwarf star. As hydrogen in the accretion disc loses energy through friction and radiating gravitational potential energy, it eventually settles onto the surface of the white dwarf, which is mostly composed of carbon and oxygen due to the way white dwarfs form.

As hydrogen keeps falling to the surface forming a layer of hydrogen-rich nuclear fuel, the lowest layers of hydrogen are compressed by the surface gravity of the WD until electron degenerate matter forms. Heating from compression and nuclear fusion in the form of hydrogen burning, and later the CNO cycle cause the degenerate layer

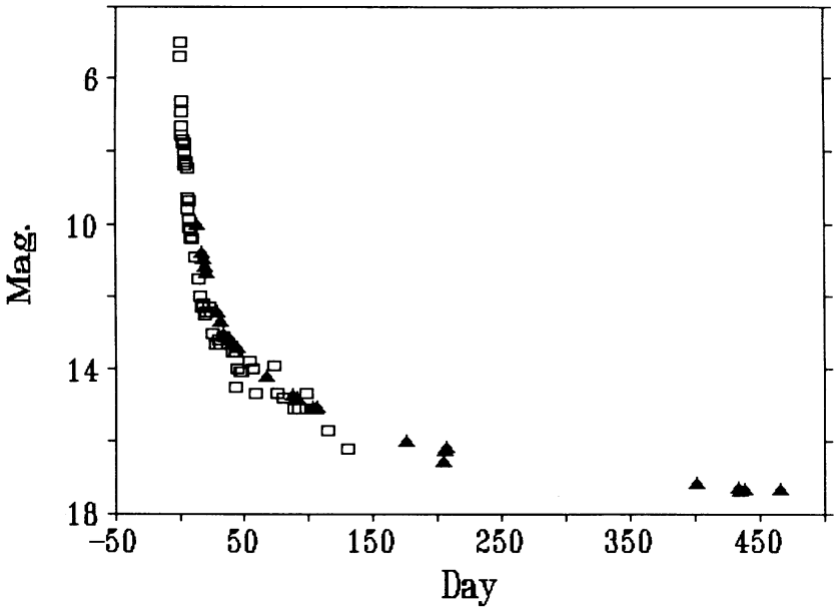

Figure 16: Light curve of V838 Her, a bright fast nova (NA) observed in March of 1991. The light curve has been caught after the peak brightness (above 5mag), but displays the star fading back to it's original brightness (around 17mag) over around 500 days. The squares are visual observations reported in International Astronomical Union (IAU) circulars, and triangles are observations made by the WISE observatory. Day 0 is March 24 1991 (Leibowitz 1993).

of hydrogen to heat, but as it is degenerate it is prevented from expanding until it reaches $\sim 7 \times 10^7$ K, but at that point the heat is increasing rapidly enough to initiate thermonuclear runaway (TNR).

The result of the TNR is an expanding shell of material puffing off of the white dwarf, and it can be very bright, on the order of $10^3 - 10^6$ $L_\odot$ brighter than the original system, corresponding to an increase of about 10-15 magnitude. But as the matter moves away from the star it eventually starts decrease in luminosity. This rising in brightness and then fading back towards the systems original brightness is characteristic of novae events, and the rate of increase and decrease leads to the various subdivisions mentioned earlier (Starrfield et al. 2016).

Classical novae are typically the NA (fast) and NB (slow) types, which rise in brightness quickly over the course of a few days and then fade back to the original brightness of the system at a rate of about three magnitudes in less than 100 days (NA), or more than 100 days (NB). NC novae are very slow, they typically remain close to their maximum brightness decades before eventually fading away. Figure 16 is an example of an NA type nova called V838 Her.

The nova process releases a huge amount of energy, on the order of 10^{37} J. It is not typically enough to destroy the system though, and hydrogen can eventually begin to

accrete again onto the surface of the white dwarf and begin another nova event. A binary system which goes nova more than once is a recurrent nova (NR); outbursts in recurrent novae have been seen to occur on a time scale of decades. It is possible that all novae are in fact recurrent nova on timescales longer than we have been observing them, but whether or not that is actually the case is unknown. Whether or not the mechanism for novae and recurrent novae are the same is still unclear (Hellier 2001, Good 2003).

Dwarf Novae (UG) and sub-classes are systems where the cooler star is a dwarf star or subgiant. Dwarf novae do not undergo thermonuclear reactions on the surface of the star; mass is not ejected. The variability is due to thermal instabilities in the accretion disk surrounding the white dwarf. As gas in the accretion disk heats up it undergoes a viscosity change which in turn causes mass flow to increase and heats up the entire disk, making it increase in luminosity. This leads to a much smaller peak in luminosity and an event which takes place over a few days or weeks, rather than hundreds of days (Idan et al. 2010).

Supernova (SN) light curves appear similar to novae though much more luminous, reaching $10 - 20$ mag brighter than baseline. A quick brightening event is followed by a slow decline, but unlike novae there is no chance for a recurrent supernova. The process is an irreversible transformation of the progenitor which ejects most of its stellar material at up to 10% the speed of light, which causes a shock wave that interacts with the surrounding interstellar medium to form to a supernova remnant, leaving behind a neutron star or a black hole.

A typical supernova event will brighten over the course of a few hours to a few days and then fade away at different rates, dependent on type. Light curves for type I supernovae (SNI) will decline at about 0.1mag per day for the first 20-30 days after maximum, then slow to approximately 0.01mag per day. Type II supernovae (SNII) light curves have more variation than type I, but typically the rate of decline at 40-60 days after maximum will be about 0.1mag per day.

The primary distinction between SNI and SNII is the presence of hydrogen absorption lines in the spectra of SNII at peak brightness, and the lack of hydrogen in SNI. These two types are further split into sub-types dependent on the presence or lack of other chemical absorption lines, and the light curves of each type can have distinct features, which can help with classification at least into type I, type II-L or type II-P. Beyond that light curves alone are usually not enough to make a distinction.

Type Ia supernovae have no helium absorption feature and strong silicon features in their spectra, and are a result of thermonuclear runaway as opposed to core-collapse which all other supernova originate from.

Type Ib supernovae have strong helium lines, but weak or absent silicon features, indicating that the star before going supernova had lost its hydrogen shell, but retains the helium shell. Type Ic supernovae spectra have no helium or silicon features, meaning they have lost both their hydrogen and helium shells before going supernova.

Type II-L and II-P are mostly distinguished from one another by the presence of a plateau (II-P) in their post-peak light curves, where the star seems to level off in brightness for a period of a few days to weeks before it begins declining in brightness again. This occurs as a shock wave caused by the collapsing core of the star propagates to the outer envelope of the star, ionising hydrogen and increasing its opacity. After a few days to weeks, the hydrogen layer begins to cool again, recombining and allowing photons from the inner layers of the star to reach us. II-L light curves on the other hand decline relatively linearly likely due to smaller envelopes of hydrogen. The distinction between the two types can be somewhat blurred as there is likely a continuum of stars which fit between the most II-L like and the most II-P light curves.

Type II-n are distinct from type II-L/II-P due to the presence of narrow hydrogen emission lines in their spectra. This likely arises when the supernovae event interacts with material surrounding the star, and the narrow lines come from that material as opposed to the star itself. Type II-b usually begin their supernova events with hydrogen lines present in their spectra, but eventually evolve to a more type Ib spectra. This appears to be due to a stripping of the hydrogen layer which surrounds the star, possibly by a companion star, leaving the star with very little hydrogen for the supernova to interact with.

Figure 17 are examples of light curves of the different supernovae types, as imaged by the Lick telescope.

Core-collapse occurs at the end of a stars nuclear fuel burning stages. Low mass main sequence stars fuse hydrogen through one of two nuclear reactions, either the proton-proton (PP) chain or the carbon-nitrogen-oxygen (CNO) cycle. Which reaction is dominant depends on the temperature of the star, with the PP chain dominating below about 2×10^7 K. Both are exothermic reactions, and release about 4.3×10^{-12}J of energy per overall reaction and produce Helium nuclei.

Once a main sequence star runs out of hydrogen and is not hot enough to fuse

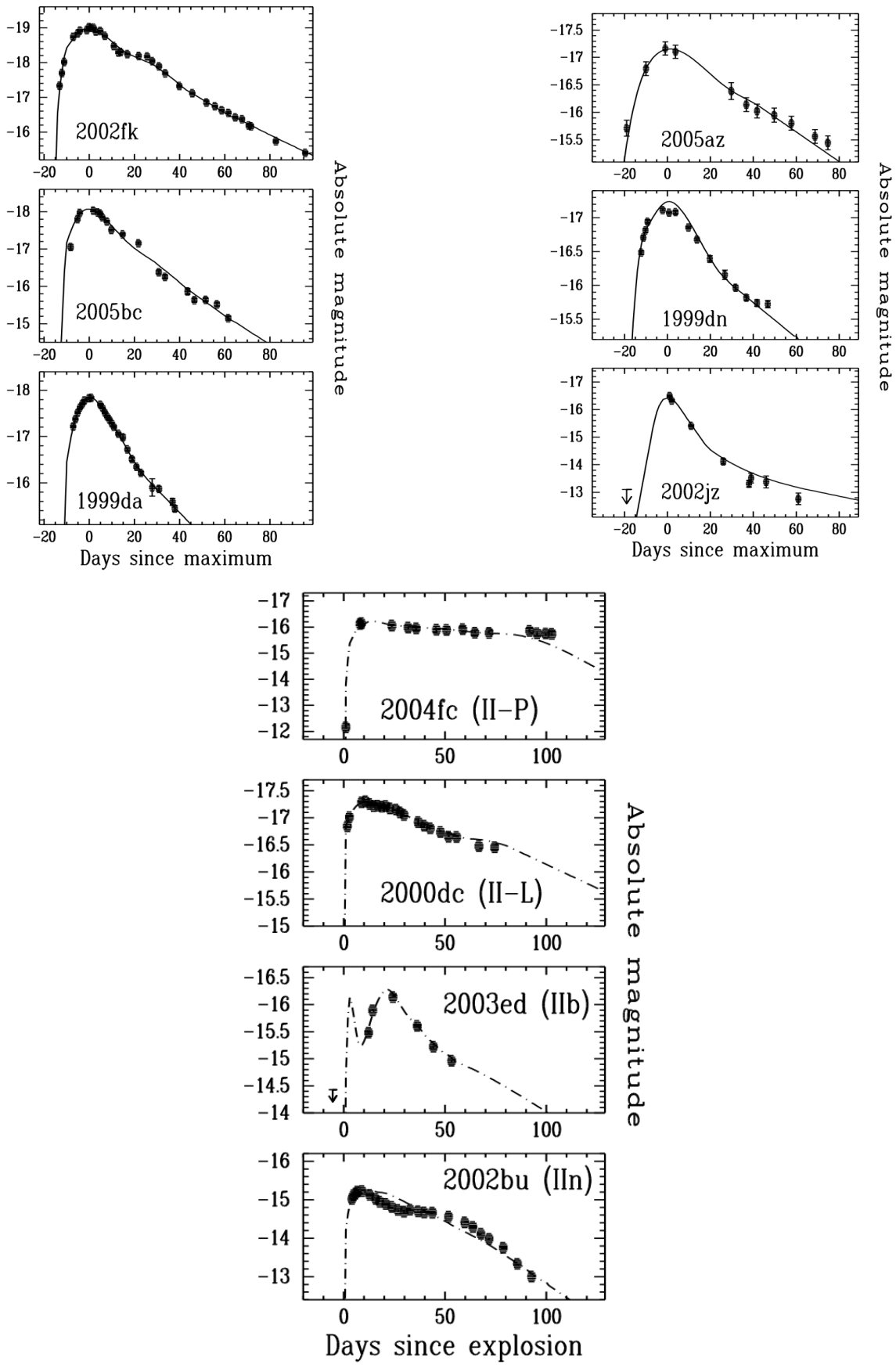

Figure 17: The three light curves in the top left (2002fk, 2005bc, and 1999da) are all type Ia supernovae. The three light curves in the top right (2005az, 1999dn, and 2002jz) are all type Ibc. The bottom four light curves (2004c, 2000dc, 2003ed, and 2002bu) are all type II, with their various sub-types listed on the light curve (Li et al. 2011b).

helium, the core will contract due to the lack of outward pressure to counteract gravity, raising the core temperature until it is high enough that helium fusion can begin. The triple-alpha process produces carbon and oxygen nuclei though helium fusion. This process only releases only about 1.2×10^{-12} J per reaction, much less than hydrogen fusion.

For low mass stars, once helium runs out the fusion process ends as there is not enough mass for gravity to contract the core further and produce the temperatures required to fuse carbon nuclei. The star puffs off its outer layer forming a planetary nebula, and the carbon-oxygen core which can no longer undergo fusion remains. Further gravitational collapse is prevented by electron degeneracy pressure, leaving a carbon-oxygen white dwarf.

More massive stars ($\gtrapprox 10$ $M_\odot$) can be massive enough that core collapse can continue, creating the temperatures needed to fuse higher and higher mass elements. But the culmination of this process is when silicon fuses into nickel which will decay into iron. The fusion process can go no further than iron, as the binding energy required for iron is the highest of all elements; fusing iron is an endothermic reaction, requiring energy input to fuse.

An iron core will build up as there is nowhere else for it go, until the mass exceeds the Chandrasekhar limit (~ 1.44 $M_\odot$). At which point electron degeneracy pressure is no longer enough to prevent further collapse. Electrons and protons combine to form neutrons, and at this point if the star is not too massive it will suddenly stop collapsing due to neutron degeneracy pressure, bouncing back slightly and creating a shock wave which ejects the outer layers of the star. Due to photodisintegration the shock wave stalls, and matter accretes onto the remains of the core for a short time, as it releases around $\sim 10^{46}$ J s^{-1} worth of neutrinos and forms a neutron star. A star with even greater initial mass ($\sim 20M_\odot$) will not be able to stop the accretion of material in this phase, and the core would condense to form a black hole. Whatever is left over, this collapse is usually observed by the vast amounts of energy released during the collapse process, as it blows away any remaining outer layers (Janka 2012, Sukhbold et al. 2016).

Currently the exact model or models for systems which lead to type Ia supernova is uncertain, but it is likely they are the result of thermonuclear runaway of white dwarfs in binary systems, rather than the core collapse model which other types of supernovae follow.

At the time of writing there are primarily two suggested models, the first is a carbon-oxygen white dwarf star with a binary companion which undergoes accretion onto its surface sometimes called a single degenerate system. Typically C-O white dwarfs for with a mass lower than ~ 1.1 $M_\odot$, but if accretion pushes the mass of the white dwarf past the Chandrasekhar mass (1.44 $M_\odot$) then the core temperature and pressure of the white dwarf can rise high enough to initiate carbon fusion, and subsequently oxygen fusion. This in turn further increases the pressure and temperature, but the white dwarf has no means to expand and cool as a main sequence star might due to electron degeneracy meaning that the core will continue to rise in temperature rapidly until there is enough energy for the star to either detonate or deflagrate.

The second model has a pair of C-O white dwarfs with a combined mass above the Chandrasekhar mass closely orbiting one another, sometimes called a doubly degenerate system. As the two stars orbit one another they radiate gravitational energy, spiralling inwards towards one another until they come into contact. Once they are in contact they merge into a single star, briefly surpassing the Chandrasekhar mass.

Neither model is fully satisfactory, the accretion model requires a fine tuning of the accretion rate from companion star and the interaction of the explosion with the donor star does not appear in measurements often enough. White dwarf binary mergers on the other hand are not frequent enough to account for all type Ia supernovae observed (Antoniadis et al. 2020, Wang et al. 2017, Nomoto et al. 1984, Khokhlov et al. 1993).

The first recorded observation of what was likely a supernova occurred as far back as 185AD and was recorded by Chinese astronomers (SN 185). Since then there have been many examples of naked eye supernovae observed, another in 1054AD by Chinese astronomers (SN 1054), Tycho Brahe observed a "new star" in 1572 (SN 1572), Kepler observed another in 1604 (SN 1604). Given how bright these were observed to be in the records of the time and remnants seen in the positions described, they were likely supernovae which occurred within the Milky Way.

The distinction between Nova and Supernova was only made in the 1930s, and was prompted by discussion of the first extra-galactic supernova observed, S Andromedae in 1885 which was almost as bright as the nebula it was observed in (M31 - the Andromeda galaxy). Fritz Zwicky who used the term "supernova" to describe these events and began a campaign to observe them.

Since the advent of CCDs and robotic autonomous telescopes, hundreds of supernovae are discovered each year, with an expected rate of around 1 supernova event in

a galaxy like the Milky way every 100 years (Percy 2007).

With the increased number of supernova observations it was discovered that SNIa appear to have a uniform peak brightness, perhaps due to their unique formation process. This was used by Perlmutter et al. 1999 to use SNIa as standard candles to deduce the distance to distant galaxies and from there discover the acceleration of the expansion rate of the universe. The 2011 Nobel prize in physics was awarded for this discovery. Recently there have been suggestions that the SNIa peak luminosity may not be as uniform as initially assumed, but may depend on the metalicity of the progenitor star (Moreno-Raya et al. 2016).

The All-Sky Automated Survey for Supernovae (ASAS-SN) team employ 20 automated telescopes around the globe to search for supernova events. Although the goal of the ASAS-SN team is to observe supernovae, the telescopes they employ are capable of imaging the entire night sky to a depth of about $V \approx 18$ mag around once per night. As of April 2017 they had a catalogue of 949 supernovae with peak brightness $m_{peak} < 17$ which they have observed since they began operations in 2013. The split of SN types along with their monthly observation rates are shown in table 5 (Holoien et al. 2019).

Supernova type	**Observed**	**Detection Rate (per month)**
Ia	655	14.9
Ib/Ic	58	1.3
II	233	5.3

Table 5: The number and rate of supernovae observed by the ASAS-SN group in 44 months between 2014 and 2017.

The Zwicky Transient Facility (ZTF) uses a 48" Schmidt optical telescope located at the Palomar Observatory, it can observe the entire Northern skies multiple times per night, to a depth of 20.5 mag and was built with time-domain astronomy in mind. Between May and December of 2018 the facility obtained photometric data an average of 46 nights each for 127 type Ia supernovae. This puts them at a detection rate of 15.9 SNIa per month (Yao et al. 2019).

Between March 1998 and December 2008 the Lick observatory conducted the Lick Observatory Supernova Search (LOSS) using the 0.75m Katzman Automatic Imaging Telescope (KAIT). The full sample of supernovae collected in this period is 929, and the supernova type rates has been calculated using subsets of this sample. Several

culls were made to the full sample including limiting the data set to only optimal and seasonal data, and a magnitude-limited sample. The percentage of each type in the magnitude-limited sample puts type Ia at 79%, types Ib/Ic at 4% and type II at 17% (Li et al. 2011a).

3.6 Microlensing Events

In 1801 Johann Georg von Soldner, using Newton's laws of motion and gravitation and the assumption that light behaves like particles, suggested that the mass of the Sun should be sufficient to change the trajectory of light. He proposed light from distant stars would be deflected when passing close by the surface of the Sun (Jaki 1978). The theory of general relativity set out by A. Einstein in 1916 predicted that not only would light be deflected by massive objects as von Soldner proposed, but the angle of deflection would be twice the value von Soldner calculated using Newtonian physics (Einstein 1936).

In 1919 British groups sponsored by the Royal Society and the Royal Astronomical Society observed a small patch of the sky during a solar eclipse, and compared the position of stars near the edge of the Sun to their positions later in the year when the Sun was not in the way. The experiment verified not only that the light of a star was deflected as it passed close to the Sun, but that the angle of deflection was closer to the value expected from General Relativity than the value from Newtonian physics (Dyson et al. 1920).

Gravitational lensing is the deflection of light rays as they pass through curved space-time created by the presence of massive objects. In astronomy gravitational lensing can occur any time a sufficiently massive object acting as a lens passes between a source of light and an observer. In general the effect of gravitational lensing is to create "images" of the source for the observer as demonstrated in Figure 18.

There are three regimes considered for gravitational lensing.

- Strong lensing - images of the source are clearly distinguishable, sometimes forming an Einstein ring around the source. Usually the lens and source are galaxies or quasars.

- Weak lensing – which may not produce distinguishable images of the source, but only distorts the shape of the background source and can usually only be identified through statistical methods looking for patterns in a large number of

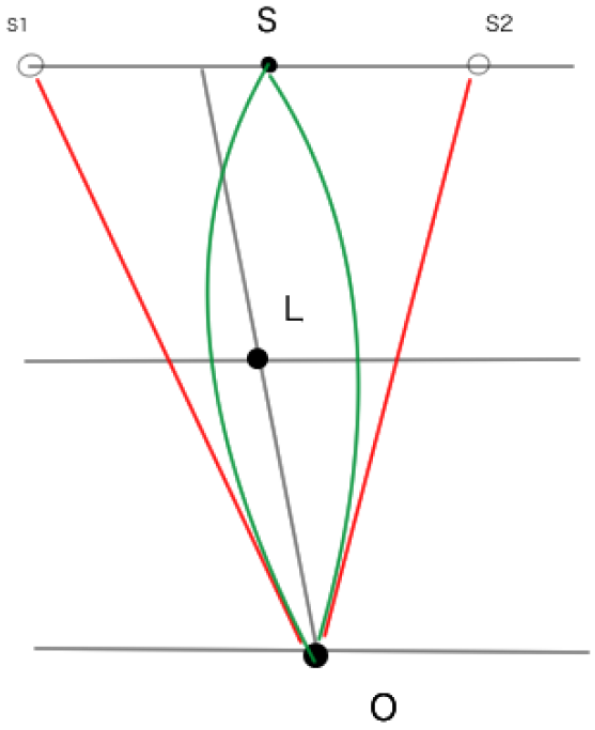

Figure 18: Demonstration of gravitation lensing. The observer at O sees two images S_1 and S_2 of the source S as the light is deflected by a lensing mass L (Lambourne 2010).

background sources.

- Microlensing – during a microlensing event images of a source star are produced due to the relative motion of the source and a lensing star with respect to the observer. Usually the images are not resolvable from the source itself using current astronomical techniques and equipment. Despite this, the images of the source make it appear up to several magnitudes brighter, meaning that photometric techniques can be used to make a light curve of the source star which will brighten, and then fade away due to the relative motion of the lens. These events are more typically seen with stars rather than galaxies and are within the Milky Way (De-Paolis et al. 2016).

When describing microlensing events, it is easiest to start with the simple case of a single point-like star lensing another single point-like source, this is demonstrated in Figure 19. Here a lensing mass L is somewhere between an observer O and a source star S which is radiating light - the dashed red lines. The radiated light is deflected by the angle θ towards the observer once it reaches a two dimensional surface at D_L which is perpendicular to the line between observer and the lens (L), the lensing plane. This causes θ_+ which is an image of the source star on the two dimensional surface at D_S which is perpendicular to the line between observer and lens (L), the source plane.

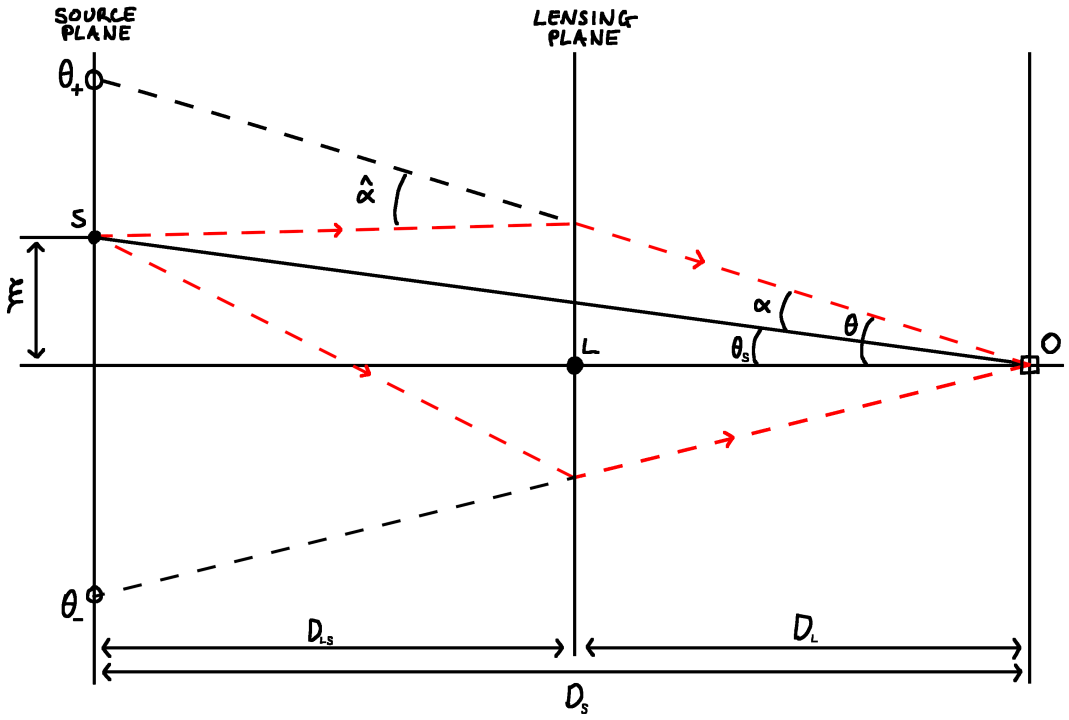

Figure 19: Schematic of a microlensing situation with point-like lens and source, thin lens and small angle approximations. θ_- and θ_+ are the two images created by microlensing, ξ is the impact parameter.

ξ is the impact parameter between the lens and the source, θ is the angle between the θ_+ image and the lens, θ_S is the angle between the source and the lens, θ_- is a secondary image created by light passing the other side of the lens, and D_L, D_S and D_{LS} are the distances between the observer and lens, observer and source and source and lens respectively. This image assumes a thin lens, which means that the thickness of the lensing plane is much smaller than D_L, D_S and D_{LS}, which is generally true when using star-sized sources and lenses at astronomical distances.

Assuming a spherically symmetric lens in space described by the Schwarzschild metric, the angle of deflection as described by general relativity is

$$\hat{\alpha} = \frac{4GM}{c^2}\frac{1}{\xi} \tag{4}$$

where ξ is the impact parameter between the lens and source (Xu et al. 2018), as illustrated in figure 19. Assuming the small angle approximation (where $\sin\theta \sim \tan\theta \sim \theta$) we can see that

$$\alpha(\theta) = (\frac{D_{LS}}{D_S})\hat{\alpha}(\theta) \tag{5}$$

$$\theta_S = \theta - \alpha(\theta) \tag{6}$$

Equation 6 is the lens equation for this system, it describes the mapping from the lens plane to the source plane

Using the Einstein ring radius where M is the mass of the lens

$$\theta_E = \sqrt{\frac{4GM}{c^2}\frac{D_{LS}}{D_L D_S}} \tag{7}$$

and substituting $\xi = \theta D_L$ we can see that

$$\theta_S = \theta - \frac{\theta_E^2}{\theta} \tag{8}$$

Solving this for theta using the quadratic formula we find two solutions

$$\theta_\pm = \frac{1}{2}(\theta_S \pm \sqrt{\theta_S^2 + 4\theta_E^2}) \tag{9}$$

This shows that two images of the source are created at θ_+ and θ_-, on opposite sides of the source.

The magnification of the images is a mapping of light rays from the source plane to the lens plane, and since the surface brightness of the source is conserved in the image, this can be written using the ratio of the two solid angles

$$\mu = \frac{\theta d\theta}{\theta_s d\theta_s} \tag{10}$$

Using the lens equation (6) and $x = \theta_S/\theta_E$ we can form an equation for the magnification of the source for each image ($\mu_\pm$)

$$\mu_\pm = \frac{1}{2}\left[\frac{x^2+2}{x\sqrt{x^2+4}} \pm 1\right] \tag{11}$$

The total magnification of the source is $\mu = \mu_+ + \mu_-$ and is always greater than one, meaning that any observer-lens-source system with impact parameter sufficiently close to, or lower than, the Einstein radius (θ_E) and with an unresolveably small θ_E will appear as an increase in the brightness of the source. In fact, the smaller the impact parameter between the lens and source, the higher the magnification will be. When the source is perfectly aligned behind the lens (i.e. the impact parameter $\xi = 0$) it reaches a divergent point in the source plane called a caustic, which causes an Einstein ring to form around the lens along the critical line in the lens plane, which is coincident with the Einstein radius. In reality the brightness of the source does not diverge as it

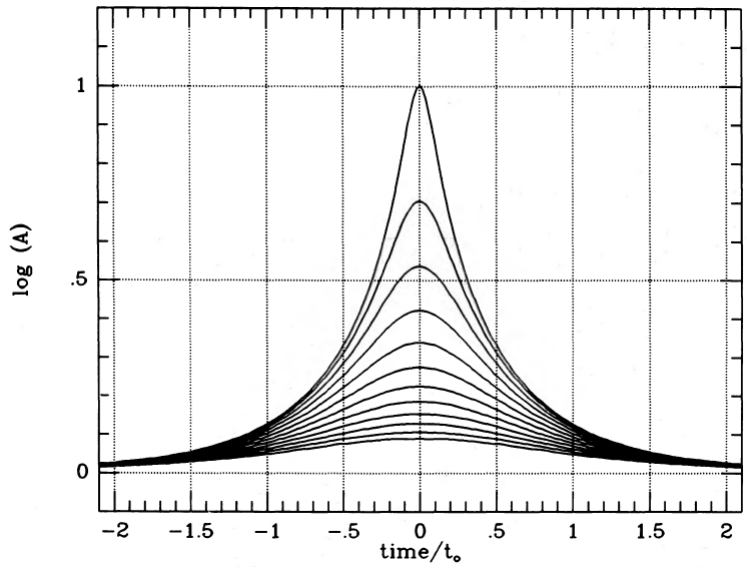

Figure 20: The shape of a typical single-lens microlensing event. A is the total amplification of light from the two images seen in a microlensing event, and the different curves correspond to $1.2 > x > 0.1$ where $x = \theta_S/\theta_E$, and the highest peak corresponds to the lowest x (Paczynski 1986).

crosses the critical point because sources and lenses are extended sources, not point-like (De-Paolis et al. 2016, Longair 2007, Meylan et al. 2006, Han et al. 1999).

Photometry of microlensing events where there is an observable change in the source-lens separation over time produce light curves of a fairly typical shape. A symmetrical peak over the course of tens or hundreds of days, which then fades back to the original brightness. This typical shape is described in Paczynski (1986), and is illustrated in figure 20 where the amplitude A of a simulated event varies with $1.2 > x > 0.1$.

In general if the distance to the source star can be obtained through other means than the microlensing event, the mass, distance and lens-source transverse motion ($\nu_\perp$) can be modelled for the lens using the time it takes the source to cross the Einstein radius (t_E) and the following equation

$$t_E = \theta_E/\nu_\perp \tag{12}$$

though degeneracy between lens mass, lens distance and the relative lens-source velocity mean that it is not necessarily possible to distinguish between them without more information about the lens, which is usually not directly observable (Tsapras 2018).

Many different survey teams have hunted for microlensing events, often looking towards the galactic plane, or towards the Large Magellanic and Small Magellanic Clouds

(LMC & SMC). Focussing on these regions gives a large number of background sources and increases the probability of a foreground star moving into the line of sight between Earth and source stars. By using source stars outside the Milky Way there is a possibility of discovering microlensing events which are due to lenses in the galactic halo, which is why searches for Massive Astrophysical Compact Halo Objects (MACHOs) concentrate observations on the LMC and SMC.

The MACHO project used the 1.27m telescope at Mount Stromlo Observatory in Australia, for 6 years beginning in July 1992. It observed the Large Magellanic Cloud (LMC) 55% of the time, and the other 45% split between the galactic centre and the Small Magellanic Cloud (SMC) looking for microlensing events with the hope of identifying massive compact halo objects (MACHOs). In a subset of 30 fields towards the LMC observed between 1992 and 1998, they reported the detection of between 13 and 17 microlensing events (Alcock et al. 2000).

Expérience pour la Recherche d'Objets Sombres (EROS) again searched for microlensing events associated with MACHOs and brown dwarfs between 1990 and 1995 (EROS-1) and between 1996 and 2003 (EROS-2) (Beaulieu et al. 1998). EROS-1 detected two candidate microlensing events in 1993 using the 1 meter Schmidt ESO telescope, though one of those was observed to vary again by EROS-2 and thus eliminated. EROS-2 observed 120 galactic bulge clump-giant microlensing events, and 27 microlensing event candidates in the galactic plane away from the galactic centre (Rahal et al. 2009).

Since 1996 the Optical Gravitational Lensing Experiment (OGLE) based in the University of Warsaw, Poland using the Las Campanas Observatory in Chile, searched for microlensing events as evidence of dark matter and exoplanets, primarily looking towards the galactic bulge and the Large Magellanic Cloud. The project is still running at the time of writing (Wyrzykowski et al. 2015). By 2005 over 2000 microlensing events had been observed between OGLE I & II, MACHOS, EROS and Microlensing Observations in Astrophysics (MOA) (Sumi et al. 2006). OGLE III observed over 31 square degrees of the galactic bulge and observed 3718 events between 2001 and 2009, with 1409 detected in real-time by the OGLE early warning system (Wyrzykowski et al. 2015). OGLE IV searched almost 3000 square degrees of the galactic plane for microlensing events between 2013 and 2019 and found 630 events (Mróz et al. 2020). Figure 21 is an example of a microlensing event light curve from OGLE.

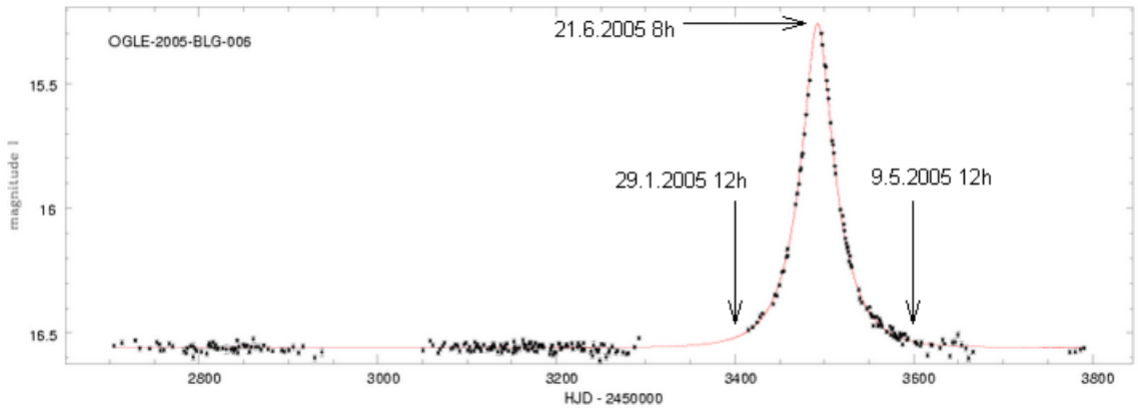

Figure 21: Light curve of OGLE-2005-BLG-006, a microlensing event observed by the OGLE team (Greenstein 2013).

3.7 Miscellaneous Variable Stars

There are a few types of photometrically variable stars which should be discussed here even though they don't neatly fit in the GCVS classification system.

Be Stars

Be stars are hot subgiant stars with a temperature between 10,000 K and 30,000 K, which have or continue to show emission lines in their spectra. The cause of the emission lines and photometric variability is believed to be due to the ejection of material due to rapid rotation 1000-2000 kms^{-1} which forms a decretion disc of hot material around the star (Labadie-Bartz et al. 2021). Radio and interferometric observations have confirmed the existence of an equatorial disc, but as of yet a model of how the disc forms is incomplete. It has been suggested that rather than the disk forming in mass-loss events of the star, the disk formation may occur due to angular-momentum transport from the core of the star outwards to the envelope and the disk.

The photometric variability of Be stars is irregular in magnitude and can occur on timescales from weeks to decades and may contain some quasi-periodic components. Figure 22 shows a V band light curve of the Be star CX Draconis (Clark et al. 2003, Baade et al. 2018).

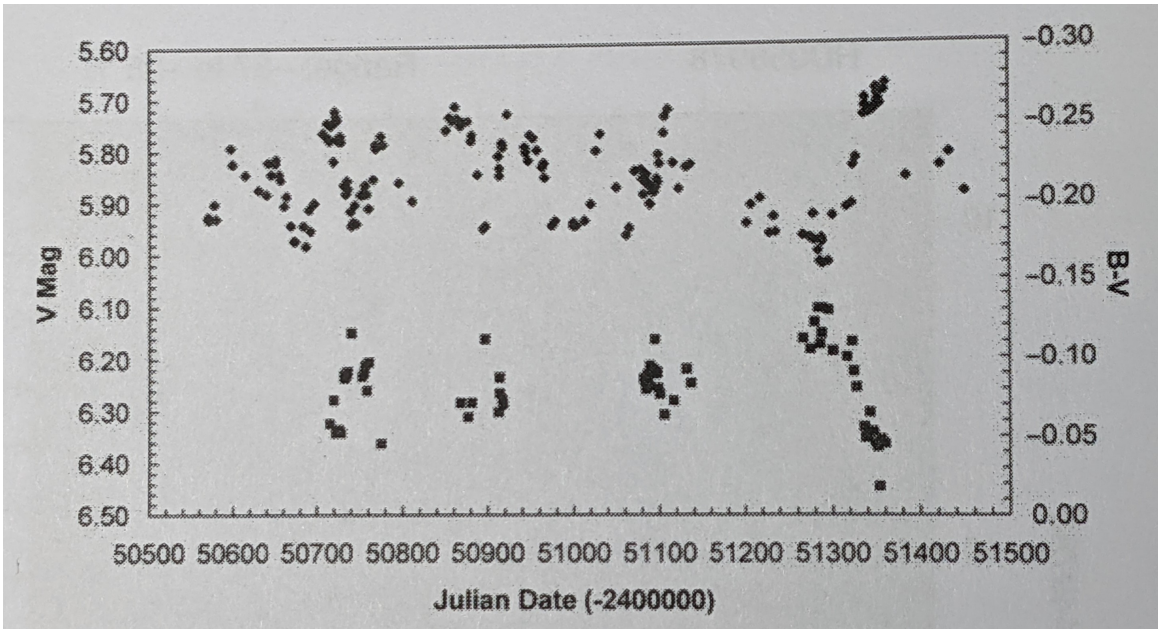

Figure 22: CX Draconis a Be star imaged in the V band (Percy 2007).

Wolf-Rayet Stars

Wolf-Rayet (WR) stars are highly luminous population I stars, reaching luminosities up to $10^6 L_\odot$. They are typically identified by their broad emission lines in carbon, nitrogen, oxygen and helium, but with weak or absent hydrogen lines. There are subclassifications: WC, WN, and WO corresponding to strong C and O emission lines, N and He emission lines and O emission lines respectively.

WR stars are helium-burning stars which are undergoing high mass loss at up to $10^{-4} M_\odot$ per year creating stellar winds up to $5000 kms^{-1}$, which have stripped off most of the outer layers of the star. Although there is variability due to the high mass loss it is not completely clear that there is no pulsation involved in the variability, though the GCVS current does list them under eruptive variables (Percy 2007, Hillier et al. 2021).

Wolf-Rayet light curves are highly complex, as seen in figure 23, WR123 as imaged by the MOST satellite.

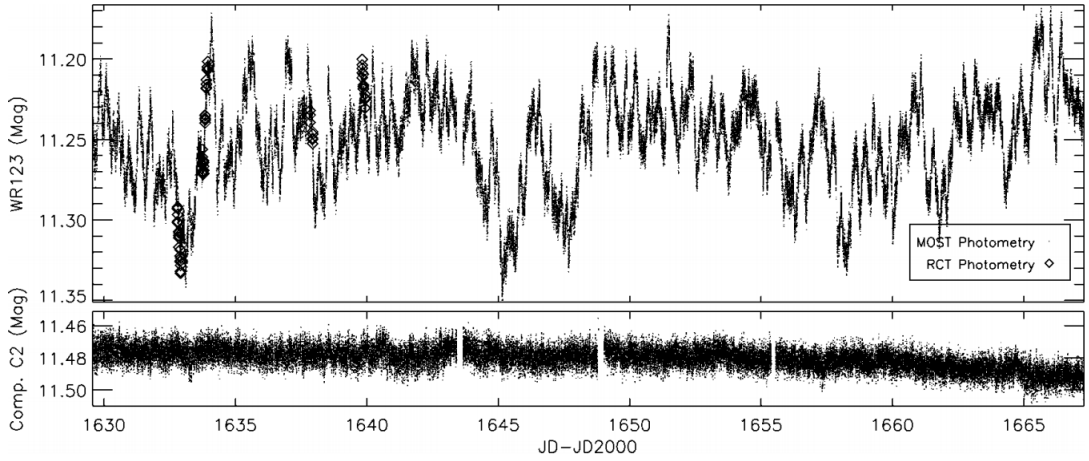

Figure 23: Light curve WR123 by the MOST satellite (Lefèvre et al. 2005).

Luminous Blue Variable Stars

Luminous Blue Variable (LBV) are massive stars which are experiencing high mass-loss of about $10^{-5} M_\odot$ per year, and are identified by a period of photometric and colour variability and a change in the stellar spectrum. These stars non-periodically change from a hot spectral type to a cool one where the rate of mass loss seems to slow down, before going back to a hot spectral type again in a process called S Doradus variability. The spectral change is larger for more luminous stars, and form an amplitude-luminosity relationship.

A second kind of more energetic giant eruptions which can increase in brightness by up to 3 magnitude, though it is not clear if LBVs can undergo both kinds of variability. The cause for these two types of variability are not currently understood, nor is it understood whether or not they are completely separate processes.

The high mass-loss of the stars means that many examples are surrounded by nebular composed mostly of stellar material, possible evidence of past eruptions (Weis et al. 2020, Figer et al. 2020).

Active Galactic Nuclei

The GCVS includes a section for variable objects which have mistakenly been identified as variable stars. One of those objects are variable quasistellar extragalactic objects, or active galactic nuclei (AGNs).

Sometimes galactic cores appear to be highly variable, varying across the whole range of the electromagnetic spectrum on the order of days to years. The unified model for an AGN has a supermassive black hole (SMBH) at the centre of a galaxy, surrounded by an accretion disc with matter falling into the black hole. The accretion disc itself is surrounded by a torus-shaped disc of material which can obscure the centre of the AGN, and two jets of material moving at a significant portion of the speed of light. The amount of energy involved means that AGN emit strongly in X-ray, ultraviolet and optical wavelengths, with bolometric luminosities up to 10^{48} erg s^{-1} (figure 24).

The current model which is used to describe the optical variability in AGN involves a bright region of the accretion disc surrounding the SMBH, interactions between matter in the accretion disc cause it to fall into the SMBH and heat up the disc itself. This disc is itself surrounded by a torus of optically thick material which can obscure the bright disc if viewed from certain angles. If the AGN is orientated in such a way that we are looking down into the torus, we can see the optically variable material, but if instead we are looking sidelong at the accretion disc such that the optically opaque torus blocks our view of the accretion disc (Padovani et al. 2017, Peterson 2001, Urry et al. 1995).

Although not actually variable stars, due to the automated processes used in this project it is not entirely unexpected that some active galactic nuclei may be observed accidentally.

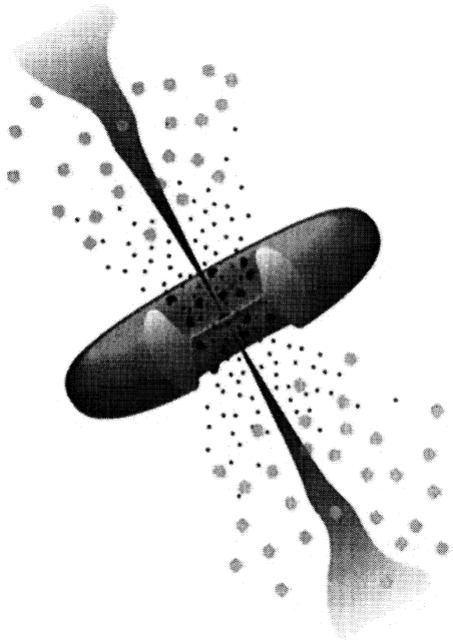

Figure 24: Unified model of an AGN, with a supermassive black hole in the centre, with matter from an accretion disc infalling to the black hole; vast amounts of energy is being released as jets from opposing poles of the black hole. The black ring around the centre represents the optically thick torus which surrounds the black hole and can obscure the optically variable region (Urry et al. 1995).

3.8 PIRATE and Variable Stars

Throughout this project I have been mostly interested in photometric observations of microlensing events, cataclysmic variables and supernova. Therefore it is important to understand what these variables are and what to look for in their light curves. But sometimes targets are observed before they have been classified, or a target which has previously been classified might later in the light curve display behaviour which warrants reclassification. In those cases it is important to understand other types of variability so that they might be identified.

In the following chapter I will discuss how I have selected targets for this project. The primary source of targets comes from the Gaia Science Alerts project, and the Gaia Science Alerts Working Group 10.

4 Gaia

In chapter 3 we looked at the different types of optical variable stars which I could expect to see over the course of my project. In this chapter we will first look at the Gaia satellite and then the Gaia alerts system, which was used to identify potential targets. Lastly we will look at the Cambridge Photometry Calibration Server (CPCS) which is a tool used to ease collaboration between users of small aperture telescopes by performing photometry on calibrated data and uploading all the user data for the target to its own website.

4.1 Gaia Satellite

Gaia is a mission proposed in 1993 as a successor to the Hipparcos mission which flew between 1989 and 1993 and was primarily interested in making measurements of the astrometry of stars.

Gaia launched from French Guiana in October 2013, reaching a Lissajous orbit around the Sun-Earth L_2 Lagrange point and began taking scientific measurements in July 2014. The nominal end of the mission took it to Summer 2019 and at the time of writing, extensions to the mission take it to 2021-2022 with possible further extensions planned which could take it to the end of 2024 $\pm$6 months, at which point it will run out of gas for attitude control [5].

The design of the payload gives the telescope 2 fields of view 106.5° apart with one focal plane consisting of 106 CCDs with various different functions as illustrated in figure 25.

The satellite rotates at approximately 1° per minute perpendicular to the direction the telescope is pointing, so the images move across the sensors from left to right once and then again around 106 minutes later as the image passes through the second telescope. The axis of rotation is set to 45°away from the Sun, and the satellite slowly precesses this axis around the Sun once every 63 days on average. Combined with the satellite's orbit around the Sun in the L2 Lagrange point the satellite follows a complicated scanning law, illustrated in figure 26. On average the telescope will visit every field of view around 70 times over the course of 5 years, with the frequency of observation dependent on position in the sky.

[5]Gaia FAQ page, accessed 02/05/2020 www.cosmos.esa.int/web/gaia/faqs

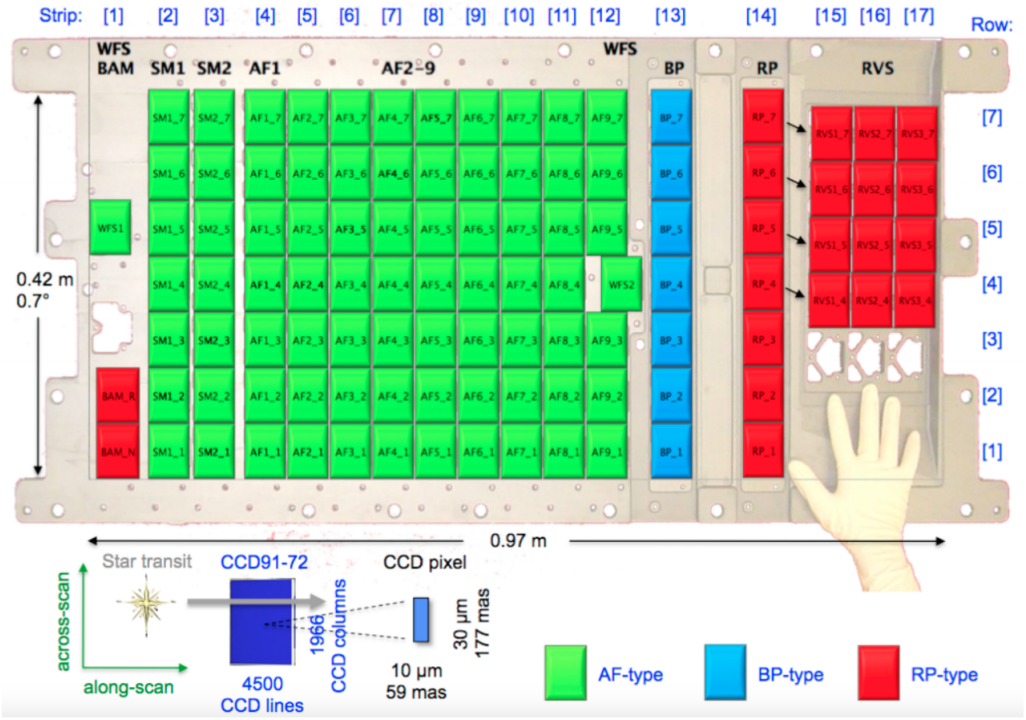

Figure 25: The focal plane of the Gaia satellite. Although all the CCDs are similar chips, the difference in colour denotes the different anti-reflection coating, surface-passivation, thickness and resistivity of the silicon wafer. The broadband sensors in green have a passband centred on 650nm, the blue sensors are centred on 360nm and the red sensors are centred on 750nm. As well as being split by the various passbands the sensors play different roles as well, there are wavefront sensors (WF), object detectors (SM), astrometric field detectors (AF), sensors for low resolution spectro-photometry (BP and RP) and radial-velocity spectrometery (RVS) (Gaia Collaboration et al. 2016).

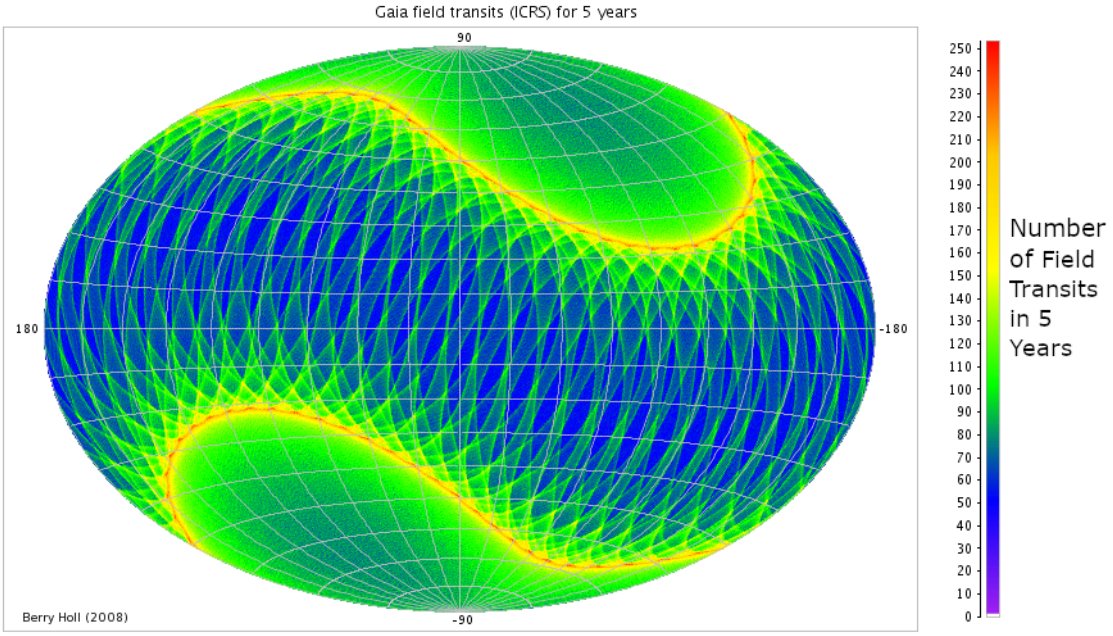

Figure 26: A model of the scanning law for Gaia after 5 years of operation, using the ICRS coordinate system (Holl 2012).

There are several different periods between observations of a particular stellar object, the first being the rotation of the satellite from the first field of view to the second 106 minutes later. 6 hours after the first observation the first field of view will come back into view, though due to the orbit and precession it will be an overlap with a slightly different field of view. This means over the course of 8 hours there are four observations of the same object, and then it can be several weeks before it comes back into view, again depending on the position on the sky.

The primary goal of Gaia is to take a census of 1 billion stars, the measurement of parallaxes and transverse kinematics, along with photometry between 3 and 20 magnitude in the Gaia G passband - the passband observed by AF-type chips in figure 25, and radial-velocity spectrometry. The goal is an overall snapshot of the structure and dynamics of the Milky Way, though only around 1% of the actual stars in the Milky Way will be measured.

The data collected by Gaia is being released in batches, with improved understanding of the data and larger data sets each time. For example, at the time of writing there are two data releases. The first (DR1), in September of 2016, contained RA, DEC and G band photometry for over 1.1 billion sources along with RA & DEC positions, parallaxes, and proper motions for all the stars which are also identified in the Tycho-2 catalogue. The second release (DR2) was in April of 2018 and contained full positions, parallaxes, and proper motions for more than 1.3 billion stars. The third data release

is due some time in 2020.

The data transmitted by the satellite is covered 24 hours a day by three 35m radio telescopes: Cebreros (Spain), Malargue (Argentina) and New Norcia (Australia), though the download period is variable between 12 and 24 hours a day depending on the regions of the sky monitored by the satellite. In addition to the big data releases, the information collected by Gaia is also monitored daily for photometric transients by the Gaia Alerts team.

4.2 Gaia Alerts

Over time, as the Gaia satellite revisits each area of the sky and records the magnitude of each object, it builds up a picture of the photometric variation for that object. With some filtering to reduce the total number of candidates these targets can be released to the astronomical community for follow up.

The Data Processing and Analysis Consortium (DPAC) handles the data acquired by Gaia. After download the data is first handled by the Initial Data Treatment (IDT) facilities in Germany and Spain, before being transferred to Cambridge (UK) where it undergoes further processing by AlertPipe, a pipeline used by the Gaia Photometric Science Alerts System (GPSAS). This system reduces the total number of candidates, and information Gaia can provide for each target (spectra, light curves, Gaia DR2 data) is passed to a member of the GPSAS team for visual inspection.

After the final manual inspection alerts are made public via the Gaia Alerts website[6] between 1-3 days after the most recent observation of the target by Gaia. Figure 27 is an example of the webpage for Gaia20cil, a target published in May of 2020, it includes all of the Gaia photometric and spectroscopic data collected so far along with basic positional information.

Gaia target naming convention has all targets begin with GaiaYY*** where YY is the year the target was published, and *** is a three letter alphabetical sequence to identify the order of targets published that year. For example, the first target published in 2020 was Gaia20aaa, the second was Gaia20aab etc. Gaia20cil is the 1598^{th} target published in 2020.

Out of 30 targets a day which are visually inspected by the GPSAS team, on average 6 targets a day are published. Given enough time it would be possible to observe every target published using PIRATE (assuming they are visible from Tenerife), but

[6]http://gsaweb.ast.cam.ac.uk/alerts/alertsindex

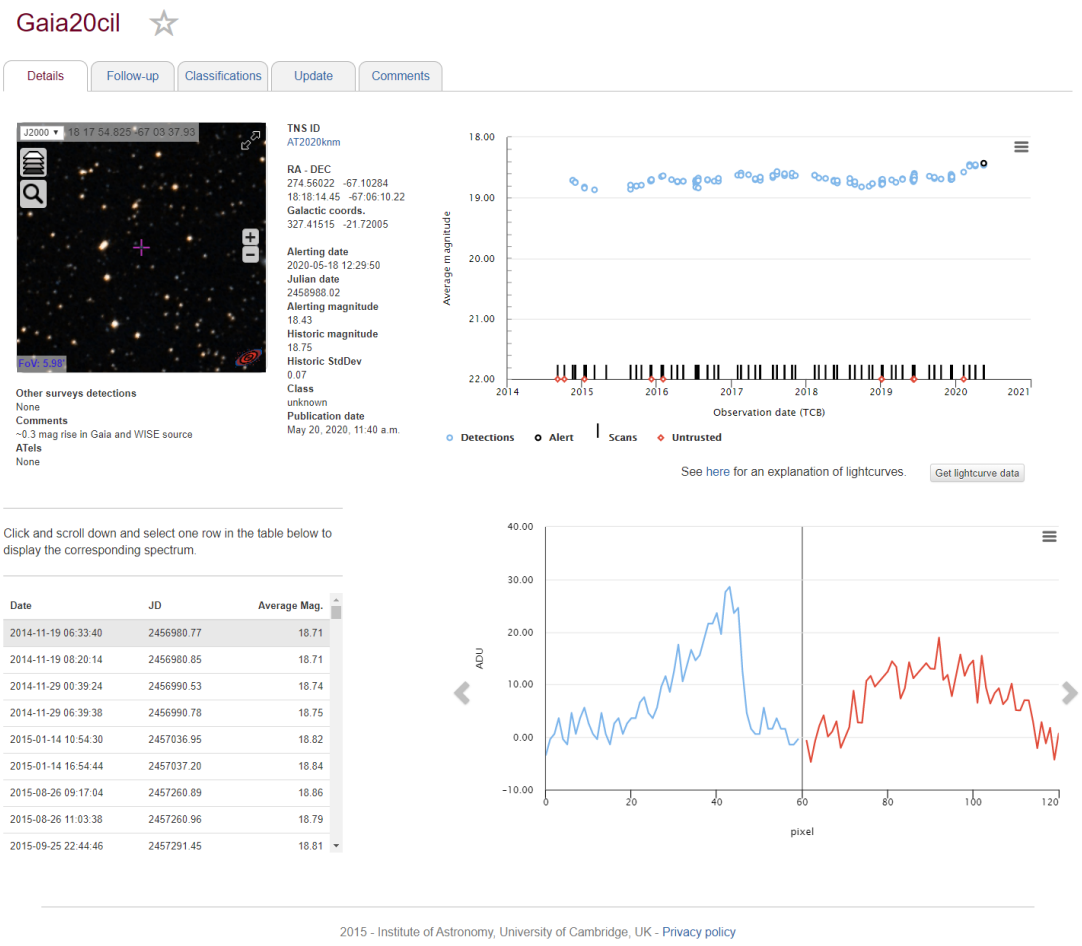

Figure 27: The Gaia20cil Gaia Alerts page, the blue data points in the top right are the Gaia light curve, the red and blue spectra in the bottom right are the low resolution spectra captured by Gaia, and the image is from DSS2 data as seen through ALADIN (GSA 2020b).

to conduct long term monitoring of these objects some discretion is necessary to pick out the more interesting candidates (Wyrzykowski et al. 2012b, Delgado et al. 2019a).

One important consideration when picking targets is to know what other astronomers are picking to follow up, as collaboration between multiple telescopes can be important. Early on in the project I joined a Gaia Science Alerts Working Group GSAWG10 which is primarily interested in photometric follow up. For most of the course of my project an e-mail would be sent out once per month by Lukasz Wyrzykowski or one of his colleagues with a list of interesting follow up targets from which I would pick the targets which I could observe and which were interesting to me.

Recently the working group e-mails have ceased in favour of using a new members-only website which is a part of the Gaia Science Alerts system called Gaia Marshall. Gaia Marshall is a page for members to point out specific targets of interest and to request photometric or spectroscopic follow up, or even classification.

As well as providing a way for collaboration between astronomers for deciding tar-

gets to follow up, the Gaia Alerts team also provide a method for processing and collecting the data from multiple sources into one place with the Cambridge Photometry Calibration Server (CPCS).

4.3 Cambridge Photometry Calibration Server

The Cambridge Photometry Calibration Server[7] was developed by Sergey Koposov and maintained by Lukasz Wyrzykowski. The main use of the tool is to take instrumental photometric results for a target from multiple users, calibrate them and store them together in an accessible way. It is primarily used for Gaia targets, but the magnitude calibration portion is not limited to only Gaia, and can be used for any target with known RA and DEC which doesn't change rapidly (such as asteroids).

To achieve this a user needs to perform normal image calibrations (bias, dark subtraction and flat fielding) and extract photometric readings for all the objects in the frame containing the target. This can be performed using a number of different tools such as Source Extractor (Bertin et al. 1996), DAOPhot (Stetson 1987) and the Astropy package for python (Astropy Collaboration et al. 2013).

The photometric readings and corresponding errors along with the Right Ascension and Declination for each object in the frame need to be recorded in an ascii file in the Source Extractor format. This file can then either be uploaded to the website manually filling in a form with other necessary details, or uploaded automatically using a bash command.

Other information is also required to upload data, first of which is an event ID which is a unique ID for each target which can be created on the CPCS website, such as ivo://Gaia16aye for the target Gaia16aye. Also required are: the modified Julian date for the middle of the exposure, the exposure length in seconds and a matching radius which the CPCS would use to search around coordinates for stars in the frame. Another feature of the CPCS is that it can automatically determine the most probable filter used for an exposure out of the filters used in the catalogues it uses for cross-matching. But there is also an option to force the program to use a filter if you know which one was used. Figure 28 shows the web form for uploading a catalogue to the CPCS.

The CPCS uses archival catalogue data from multiple sources (AAVSO Photometric sky survey, APASS, Pan-STARRS1) and cross matches the data for stars in the field.

[7] http://gsaweb.ast.cam.ac.uk/followup/

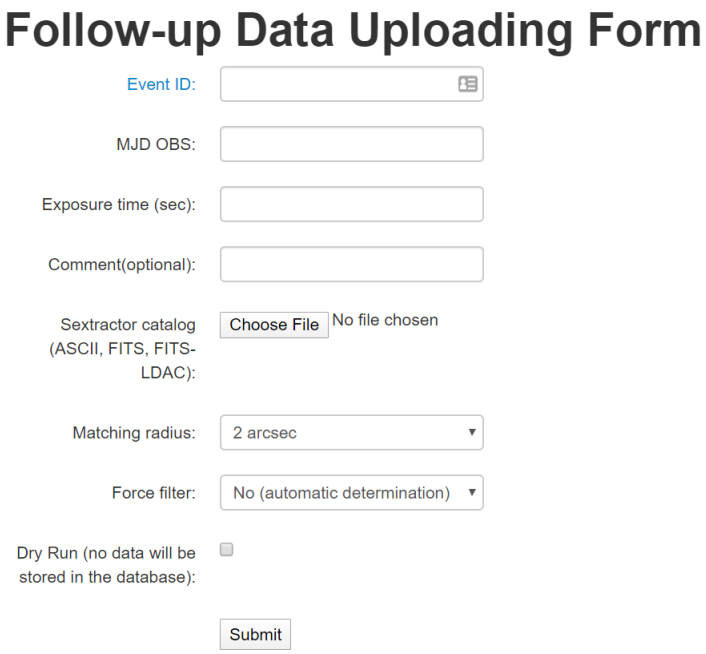

Figure 28: The Cambridge Photometry Calibration Server upload form. The form allows for performing a "dry run" which returns the result of the pipeline's matching algorithm without saving anything to the CPCS database.

For each catalogue it then calculates the zero point of the instrumental magnitudes given to it by comparing them to catalogue values for the magnitude. The percentage of outliers and the amount of scatter from the expected magnitudes is then used to determine which filter was used for the observation, along with using the calculated zero point to give the magnitude for the target. An example of the results page from a manual upload is seen in figure 29.

From the output page the system stores the observatory name, MJD, magnitude & error, scatter (as calib_err), number of datapoints, filter catalogue (such as "APASS"), the filter (such as "R"), whether the filter choice was automatic or forced, the calibration date, the whole catalogue uploaded by the user and the graphs seen at the bottom of figure 29. The information is given a unique event ID which is a cumulative value of every upload ever made the the CPCS. On the CPCS page itself it is possible to find this information in a list of all observations, or by individual observatories, and the event ID can be used to delete data points if necessary. This page is not supposed to be used for viewing the data, that happens elsewhere.

The light curve for each gaia target, made from the accumulated CPCS data, can be accessed by going to the gaia science alerts webpage for the target (such as in figure 27) and clicking "Follow-up". This takes you to a page such as in figure 30 which is the follow up page for Gaia16aye. Here the Gaia16aye data from anyone who uploaded to

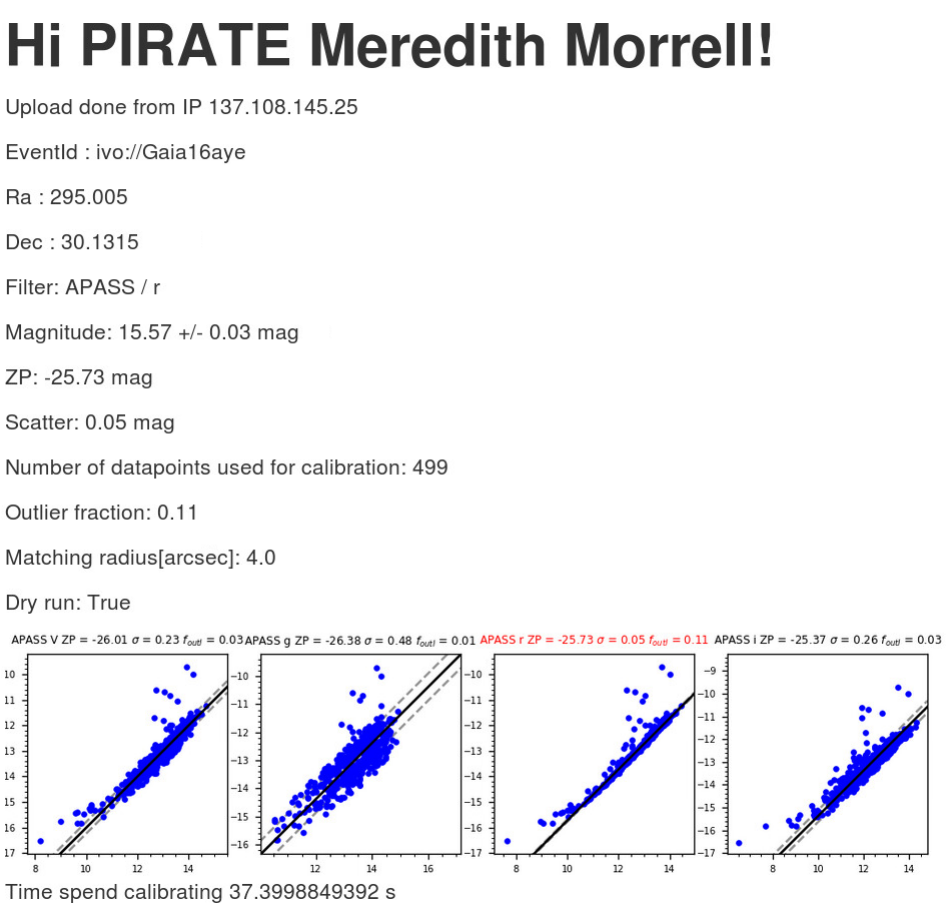

Figure 29: An example of the data returned by the Cambridge Photometry Calibration Server. Here a catalogue produced from a Johnson R image taken by PIRATE on 02/08/2018 of the target Gaia16aye has been uploaded with the necessary information and the filter not forced. The text in red shows that the CPCS has identified the image as having been taken through a filter which most closely matches the APASS/r filter out of the options available to it.

the CPCS is plotted together in the appropriate filter. Hovering over a single data point will bring up a pop-up with basic information about the datapoint and the observatory name for the uploader. Clicking on the filter legend toggles the display of data in that filter.

The web form for the CPCS data upload is very useful for understanding how to operate the system, but uploading images one at a time for anything beyond a few images is time inefficient. Since the upload can also be carried out using a HTTP POST protocol - the bash "curl" command - the entire process can be automated, uploading a new catalogue every few seconds using all the same information required by the online form.

Figure 30: The follow up page for Gaia16aye. Circular points are data points from CPCS users where the magnitude for the target has been found, upside down triangular points are where the CPCS failed to get a magnitude for the target for various reasons, and diamond points are data from the Gaia satellite observations (GSA 2020a).

4.4 PIRATE Filter Matching on CPCS

Over the course of this project PIRATE had two different filter sets: Baader RGB colour filters until 19/05/2018, and Baader UBVRI Johnson/Bessel filters after.

The CPCS has a number of different catalogues which it uses for the cross matching (PS1, APASS, VSTATLAS, OGLE, DECAPS, USNO, GAIA, SDSS, 2MASS), all of which use different filter sets. But none of the catalogues feature either of the Baader filter sets used by PIRATE, so it is necessary to find which catalogues offer the closest options.

By running PIRATE data through the CPCS, and using it's automatic filter determination, we can see which PIRATE filters match best with which catalogue filters. Table 6 shows the results for each of PIRATE's filters seen over the course of the project and a typical value for scatter, which is the major determining factor for which filter is chosen to be the best by the system.

PIRATE Filter		CPCS Automatic Filter Detection	Cross-Match Scatter
Baader Colour	**B**	APASS/g	0.08
		APASS/B	0.15
	G	APASS/V	0.07
	R	APASS/r	0.07
		Gaia/G	0.42
Baader Johnson/Bessel	**B**	APASS/B	0.08
	V	APASS/V	0.07
	R	APASS/r	0.07

Table 6: Results of using the CPCS automatic filter detection on PIRATE data.

For the Johnson/Bessel filters the connection to APASS filters seems relatively clear, the Johnson/Bessel B, V & R filters consistently correspond with the APASS B, V and r filters respectively. The filter profiles for the two sets (figure 31), though not identical, appear to span similar wavelength ranges.

While the Baader colour G filter consistently conforms to the APASS/V filter, the Baader R and B filters are not always consistent. The B filter is more frequently identified as APASS/g, with lower scatter, occasionally it is identified as APASS/B with a higher scatter. The R filter is mostly identified as APASS/r, though occasionally it is identified as Gaia/G with very high scatter.

It is not clear why these poor matches occur, and the scatter suggests that APASS/B and Gaia/G should not be used for PIRATE data. The filter profiles provide some corroboration for choosing to force the filter options with the lower scatter values.

In figure 32 the Baader colour filter profiles are displayed at the top, and the Gaia filter profiles at the bottom. It is clear that the Gaia/G profile is a sort of "full cover" profile which has a huge range between about 400 and 1000nm, which encompasses the Baader colour R filter, and both peak near 600nm. It is clear that this filter is not an appropriate substitution, so Baader colour R data cannot be automatically detected when uploading to the CPCS and must be forced to the likely best option which is APASS/r.

By comparing the Baader colour B filter at the top of figure 32 to the APASS/g and APASS/B filter profiles at the bottom of figure 31, it can be seen that although APASS/B covers a lot of the wavelength range which APASS/g covers, Baader colour

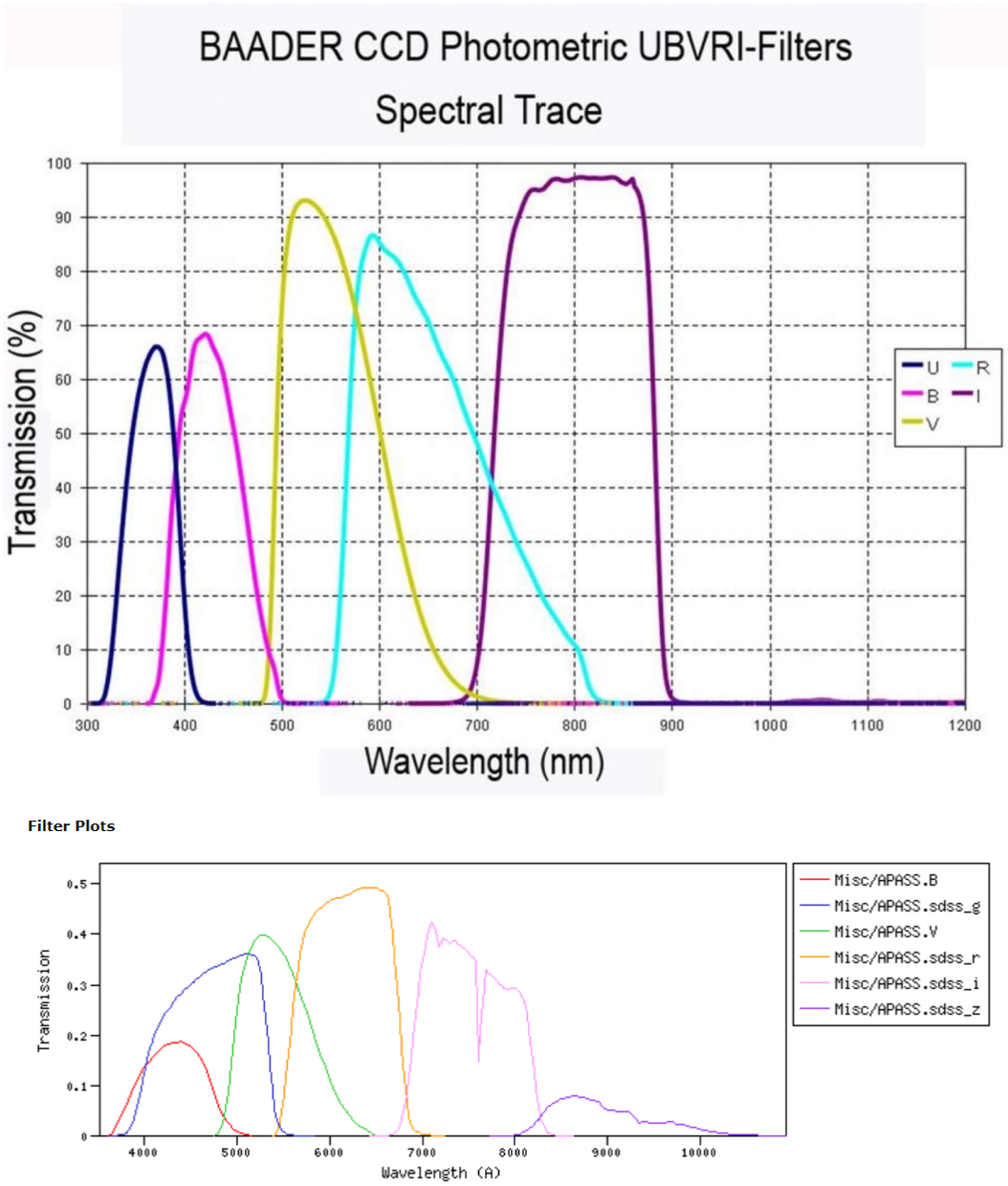

Figure 31: In the top figure are the Baader Johnson/Bessel filter [profiles (Sproats 2019), and below the APASS filter profiles (SVO 2020, Rodrigo et al. 2012, Rodrigo et al. 2013).

B more closely matches the profile of APASS/g. This backs up the scatter values in table 6 which suggest that APASS/g is a better match. To get the best results it is also necessary to force any Baader colour B data to be APASS/g when it is added to the CPCS.

4.5 PIRATE, Gaia Science Alerts & the Cambridge Photometry Calibration

The Gaia Science Alerts provides a constantly updating list of transient targets which PIRATE can observe. Although it is possible to use the GSA in an automated way

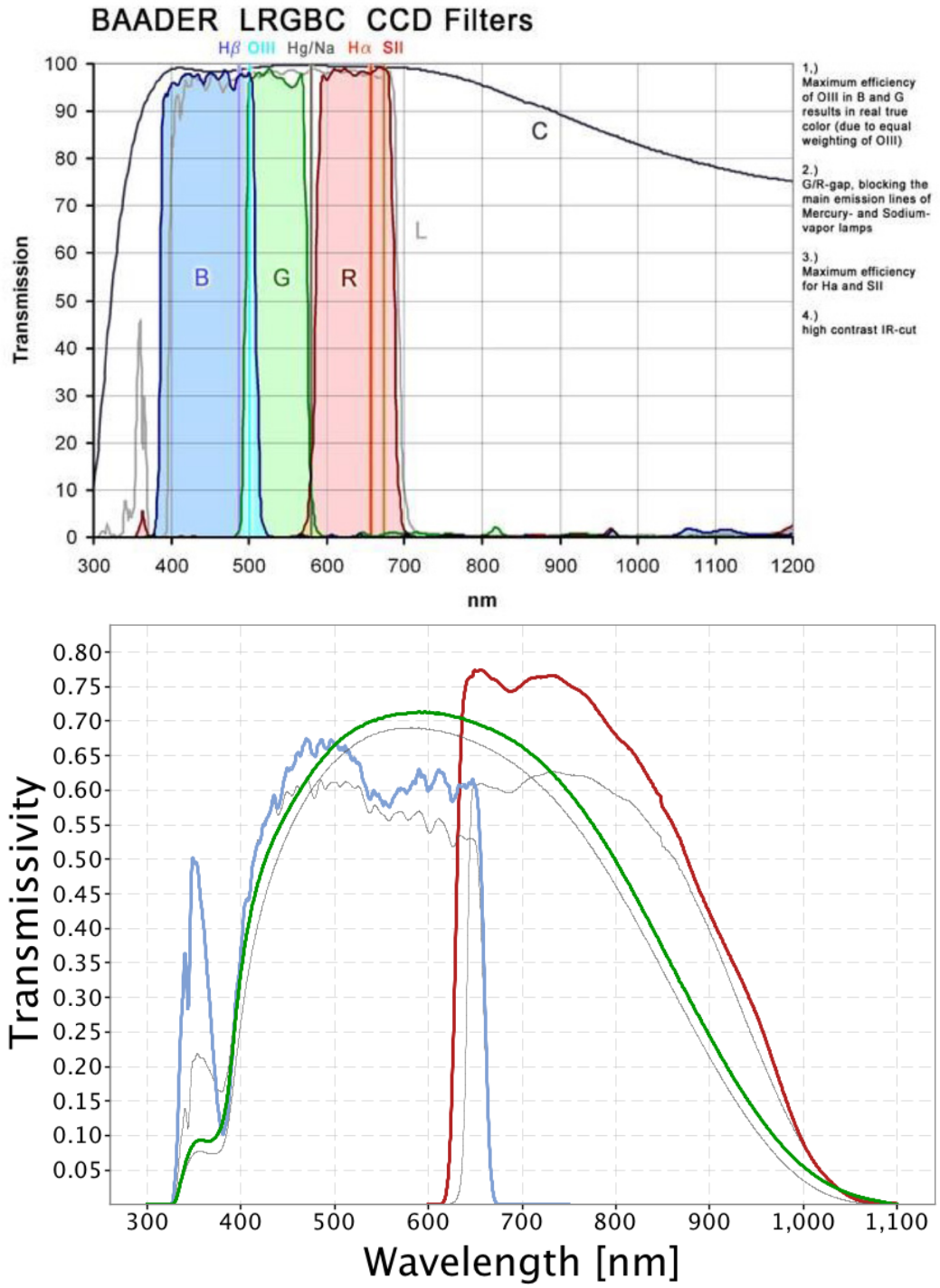

Figure 32: In the top figure are the Baader colour filter profiles (Team Baader Planetarium 2016), and below are the Gaia Satellite data release 2 (DR2) filter profiles which has Gaia/G in green, Gaia/G_{BP} in blue and Gaia/G_{RP} in red. The grey curves are pre-launch profiles (Montegriffo et al. 2018).

to select targets, the GSAWG10 e-mails originally and Gaia Marshall later on, provided a more curated list of targets which were more likely to be observed by other observatories.

After image calibration and source extraction, data collected by PIRATE can be uploaded to the Cambridge Photometry Calibration Server where it will be magnitude

calibrated and saved in a communal data repository.

As the CPCS upload can be carried out in an automated way a huge quantity of data can be uploaded very quickly, meaning it would be advantageous if all the calibration steps between PIRATE automatically taking the images and automatically uploading the data to the CPCS can also be automated. It would also be good if light curves could be generated without the CPCS, and perhaps even improving on the quality of the CPCS light curves.

The next chapter will deal with the automatic data reduction pipeline, and the light curve generation pipelines created for PIRATE as part of this project.

5 PIRATE Data Reduction

At the beginning of this project, PIRATE was only newly installed in the new facility in El Observatorio Del Teide in Tenerife, having moved from Observatori Astronómic de Mallorca only a month before (August 2016). One of the important elements to facilitate the project was to create an automated pipeline which could reliably take the raw PIRATE science and calibration frames, output calibrated frames and perform some basic data analysis where possible.

This chapter will introduce the image reduction pipeline I created for this task, and separately the data analysis pipeline which was used to create target light curves.

5.1 Image Reduction Pipeline

Images taken by PIRATE are standard FITS (Pence et al. 2010) files, consisting of a two dimensional array where each value is stored as a 16-bit unsigned integer, meaning each value is between 0 and 65535. Each position in the array represents one of the pixels of the CCD, and the value of each entry is the number of Analogue to Digital Units (ADUs) which that pixel of the CCD counted.

A standard FITS file also contains a header which contains detailed information about the image in the form of standard named cards and their values. For example DATE-OBS is the typical name for the card which has a value representing the date and time which an exposure begun. Other cards include image size in pixels, the coordinates of the requested image and the exposure length.

The pipeline needs to be run on the Open University multi user Linux server so that other science users of the telescope can access the reduced images. The Open University's Linux system uses the CentOS 6.8 Linux distribution and GNOME desktop environment at the time of writing.

Software packages exist which can be used to carry out basic astronomical image reduction of FITS files such as IRAF (Tody 1986), AstroImageJ (Collins et al. 2017) and CCDPACK (part of the Starlink package (Draper et al. 2011)). While these packages are well known and generally reliable, there are a few disadvantages to their use.

1. They are often "black boxes" which means that the user may be unaware of steps taken in the data reduction and, as such, do not fully understand the end product of the reduction.

2. They can lack customisation, meaning any extra steps which may be required for the specific set of data being used can be complicated to include.

3. Human interaction is usually required during some steps of the process, whether it be just clicking on a button to start the process, or to sit at a computer clicking through several steps for every image. This would make automating the process difficult.

For these reasons it was necessary to create a new system for the automated reduction of PIRATE images. The reduction process as a minimum needed to include:

1. Removal of the overscan

2. Creation of a master bias, master dark and a master flat for each filter.

3. Debiasing, dark subtracting and flat fielding all the science images taken each night.

4. Aperture photometry of target and comparison stars for differential photometry.

5. Ensemble photometry for making light curves.

To facilitate this Python3.0 (Rossum 1995) along with several Python packages were used. All of these can be used on a Linux based system, and with the use of the crontab system, can be scheduled to run daily.

5.1.1 Basic Reduction

The basic calibration of the data reduction are carried out using Python3.0. This was chosen primarily due to its simplicity of use, and the existence of a package of routines called Astropy (Astropy Collaboration et al. 2013). Astropy is designed specifically with astronomers and FITS files in mind and includes functions for reading and writing FITS files including headers. It is also well integrated with the Numpy (Van Der Walt et al. 2011) package, meaning that the 2D array of integers representing the image can be easily manipulated.

Before the data can be worked on, the download of the data from Tenerife to the Open University (OU) each day is carried out by an rsync command which copies over any new or edited files to the OU without coping files which already exist on the OU systems. This part of the process has to be run with suitable privileges to pass through the OU firewall restrictions.

1. The overscan is a strip of pixels which appear in each image which do not correspond to pixels on the actual CCD chip, but are read out as "virtual pixels" which can be used in some situations to determine noise generated by the camera's electronics. In the case of this reduction pipeline the overscan is not useful and can cause problems in the later steps of data reduction, so it is best to remove them first.

   PIRATE images typically have overscan on two perpendicular edges of each image, the KAF-16803 CCD has one overscan region 36 pixels wide and another 21 pixels wide (Semiconductor 1995). Initially the pipeline removed only these rows and columns of pixels from each image, but over the course of a few weeks, the images coming from PIRATE had to be rotated several times until it was in the correct orientation. To remove the need to change the orientation of the pixels which are removed as overscan, 40 pixels are now removed from all sides of all images which come from PIRATE (only 20 pixels are removed from 2x2 binning images), both science frames and calibration frames. This should not be a problem and is ample space for most scientific deployments.

2. To prevent pixels in the CCD reading out with a negative value, a bias signal is introduced by giving each pixel a non-zero number of counts. In the case of PIRATE, each pixel in a 1x1 binned frame has a bias around 1000ADU. The value is variable between pixels and over time, and must be accounted for in any photometric work.

   Bias frames are images which are taken with a zero second exposure, meaning that a bias frame contains no signal other than what the camera introduces as bias. A master bias frame is made by stacking a series of bias images and taking the median value for each pixel.

   The master bias is subtracted from every other frame used in the reduction pipeline, both science frames and the other calibration frames.

3. Dark current is noise introduced to the CCD over time when no light is reaching it. This includes thermal noise from electric current in the CCD itself, and it builds up over the length of an exposure.

   Dark frames are frames which are taken with the shutter of the camera closed so that no light can get to the CCD, but unlike a bias frame dark frames are long exposures. Ideally dark frames are taken of the same length of the science

frames which are to be dark subtracted. To reduce the number of calibration frames needed, PIRATE takes dark frames which are all 60s which can be scaled to match the exposure length of the image being dark subtracted.

Dark frames are bias subtracted and scaled down by dividing through by the exposure time to make a series of 1s dark exposures. These are then stacked and the median value is taken for each pixel. Medianing should minimise the effect of outlying pixels where an individual dark frame might have had an unusually high or low count due to cosmic rays or hot pixels. This approach is taken rather than having several master darks of different exposure lengths so that the maximum number of dark images can be used to create the master dark.

The master dark is subtracted from all flat frames and all science frames after being scaled to the correct exposure length.

4. The sensitivity of each pixel on the CCD to light is slightly variable due to the manufacturing process, and as such this also needs to be accounted for in the calibration process. This is achieved by taking flat field images, where the telescope is pointed to an area where a relatively uniform amount of light will be passed to the whole CCD, resulting in an image where all the pixels on the chip should have been exposed to roughly the same amount of light. Due to the whole telescope being involved in this process, defects or dust in the whole OTA and vignetting are also picked up and accounted for. This means that flats are needed for all filters used, as each one will have different quantities of dust on it.

   Typically flat fields can be acquired in two methods. Dome flats are taken with the telescope dome closed, and the telescope is pointed to a large screen with uniform brightness and images are taken of that. Sky flats on the other hand are acquired by pointing the telescope at the twilight sky. Finding a roughly uniform sky brightness requires pointing away from where the sun has just set, or about to rise and high above the horizon, at least 45° altitude. PIRATE currently can only take sky flats as there is no equipment set up for dome flats.

   The master flat frame for each filter is made by bias subtracting and dark subtracting each flat field frame using the master dark scaled to the exposure length of the flat field. The bias subtracted and dark subtracted flat fields are then stacked and the median value for each pixel is taken to create the master flat. The final step is to normalise the counts of the master flat by dividing each pixel

by the average value of the whole image (Norton et al. 2004).

Each debiased and dark subtracted science frame is then divided by the master flat.

Although all PIRATE FITS data is formatted with 16-bit unsigned integer arrays as representation of the CCD chip, the master flat for each filter is actually stored as an array of 32-bit floating point values to preserve the floating point values.

Some steps of the reduction process can lead to negative values in a pixel since the random nature of the noise can lead to images where the combined noise in the master bias & master dark are higher than the noise in an actual image. In this case it is important to temporarily use signed integers for the bias and dark subtraction, then to force anything negative to have a value of zero, before setting the data type back to 16-bit unsigned integer.

To compare the calibration procedure implemented in the pipeline against an established calibration package, the same calibration frames were run through the pipeline and through AstroImageJ. With a master bias, a master dark and a master flat from both the pipeline and AstroImageJ (R filter in the test case), another python script was written to look for differences between the two frames. This was achieved by stacking the AstroImageJ masters and the pipeline masters together, then subtracting one from the other.

For all of the master calibration frames, along with a few test science images, the outcome was a FITS file with value 0 in every pixel, indicating that the two methods produce the same output. AstroimageJ is capable of working with 32-bit signed values as well as 16-bit unsigned integer values, but the CCD used with PIRATE only stores data as 16-bit unsigned values.

5.1.2 Shutter Correction

The shutter of the FLI ProLine Camera which is attached to PIRATE is visible in short duration exposures; this is most easily seen in short duration flat fields. (figure 33) As the shutter of the camera opens and closes, different areas of the CCD chip are exposed at different times.

In the case of the iris shaped FLI Proline shutter, the centre of the CCD is exposed before the edges of the chip. The centre of the chip is exposed for the length of the shutter open and close action, more than the rest of the chip. Ideally the shutter would open and close in opposite order and at the same speed, meaning that the total

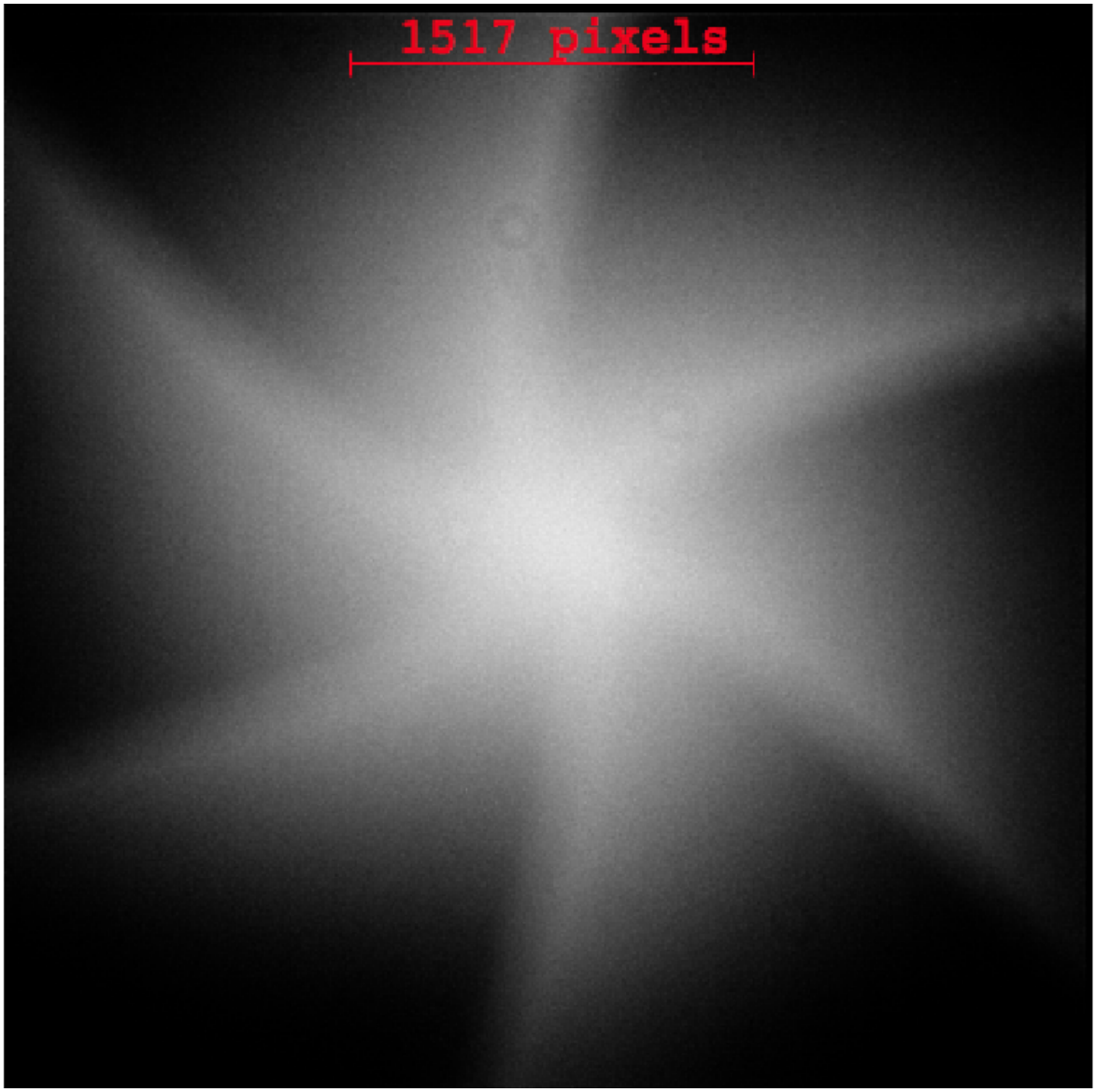

Figure 33: A very short exposure flat (∼0.5s) which illustrates the shutter pattern. The 6 leaf iris shutter is clearly visible and causes a difference in exposure time each pixel in the camera is exposed to across the image.

exposure time over the whole chip is the same, but the iris design of the FLI camera does not allow for this.

The shutter delay is of the order of 0.05s total for this camera, which means for a 1s total exposure, the centre of the chip is exposed for 5% longer than the edges, a significant difference. For longer exposure times the effect of the shutter is minimal, a 100s exposure only has a 0.05% difference across the frame.

This difference in exposure time across a single image can be important. When carrying out differential photometry, if the two stars chosen for the differential photometry have a 1% difference solely due to where they are on the CCD chip, then a typical planetary transit which is often only of the order of at most a few percent

difference in the brightness in the target can be obscured. When performing differential photometry this issue only arises when the position of the sources on the CCD change between observations, which can occur during a pier flip, or if movement of the telescope between observations causes the target to drift on the CCD.

The shutter pattern can be accounted for using a computational method for deconvolving the 2D shutter pattern using a series of twilight flats (Surma 1993).

A map of a flat field with total exposure time t, $I_{ij}(t)$, can be separated as a function of time into a shutter component (t_{sh}) which is the shutter open/close time, and a shutter free component ($t - t_{sh}$)

$$I_{ij}(t) = c\left[t_{sh} SH_{ij} FF_{ij} + (t - t_{sh}) FF_{ij}\right] \tag{13}$$

Here FF_{ij} is the intrinsic light sensitivity (flat field) of the CCD. SH_{ij} is the fraction of t_{sh} for which each pixel is exposed (the first exposed pixel has $SH_{00} = 1$, and the last has $SH_{xy} = 0$) and contains all the information about the shutter shape and kinematics. c is a constant which scales the incoming light intensity.

Normalising the flats by the count at the first exposed pixel ($I_{00}(t) = cFF_{00}t$) gives a linear equation as a function of $1/t$.

$$\frac{I_{ij}(t)}{I_{00}(t)} = \frac{FF_{ij}}{FF_{00}} - \left[\frac{FF_{ij}}{FF_{00}}(1 - SH_{ij})t_{sh}\right]\frac{1}{t} \tag{14}$$

This equation can be restated as the linear equation for the dependent variable $y_{ij}(t) = \frac{I_{ij}(t)}{I_{00}(t)}$ and the independent variable $x(t) = \frac{1}{t}$

$$y_{ij}(t) = \alpha_{ij} + \beta_{ij} x(t) \tag{15}$$

where α_{ij} is the intrinsic normalised flat field

$$\alpha_{ij} = \frac{FF_{ij}}{FF_{00}} \tag{16}$$

and β_{ij} is the shutter shading in a normalised 1s exposure

$$\beta_{ij} = -\frac{FF_{ij}}{FF_{00}}(1 - SH_{ij})t_{sh} \tag{17}$$

Using the method of determinants to calculate the linear regression, we get

$$\alpha_{ij} = \frac{1}{ac - b^2}(cD_{ij} - bE_{ij}) \qquad \beta_{ij} = \frac{1}{ac - b^2}(aE_{ij} - bD_{ij}) \tag{18}$$

which uses the following definitions, where the electron to ADU conversion factor k (e^- / ADU) has been used for weighting, and m runs from 1 to n denoting each of the series of flats.

$$a = k\sum_{m=1}^{n} I_{00}(t_m), \qquad b = k\sum_{m=1}^{n} I_{00}(t_m)\frac{1}{t_m}, \qquad c = k\sum_{m=1}^{n} I_{00}(t_m)\frac{1}{t_m^2} \tag{19}$$

$$D_{ij} = k\sum_{m=1}^{n} I_{ij}(t_m), \qquad E_{ij} = k\sum_{m=1}^{n} I_{00}(t_m)\frac{1}{t_m} \tag{20}$$

To improve the signal to noise ratio of the shutter correction term, we divide by α_{ij}, smooth the resulting map to generate something practically noise free.

Assuming the shutter response does not significantly change between exposures and over time, the map of the shutter response needs to only be created once.

The flat fields (m) should be debiased and dark-subtracted before being used in these calculations (Surma 1993).

Using this shutter function, we can remove the shutter effect from flat fields using a rearrangement of Equation 14.

$$\frac{FF_{ij}}{FF_{00}} = \frac{I_{ij}(t)/I_{00}(t)}{1 + \beta_{ij}/\alpha_{ij}t} \tag{21}$$

The numerator is the flat field (or science frame) you want to remove the shutter pattern from, β_{ij} is the shutter pattern obtained through the calculations listed above, t is the total shutter time and the FF_{ij}/FF_{00} term is the desired intrinsic flat field with the shutter pattern removed.

Once the shutter pattern has been removed from all the debiased, dark-subtracted flats and science frames, the usual process of stacking flat fields and taking the median can be carried out, and the master flat can be used for flat division (Pollacco et al. 2006).

To use this method for PIRATE all that was needed was a set of flat fields with a wide range of exposure times with approximately the same counts across the frame, and the ADU conversion factor k of the CCD used in the camera, which is $\sim$1.39. The shutter pattern β_{ij} is created once (for each binning) using equations 19 and 20 and is smoothed using the Gaussian smoothing kernel function in the SAOimage DS9 software package. The resulting shutter pattern (Figure 34) is used to correct all future flat fields using equation 21 before they are stacked and median pixel values are used to create the master flat. The same shutter correction is applied to science frames as they are calibrated between the dark subtraction and flat fielding.

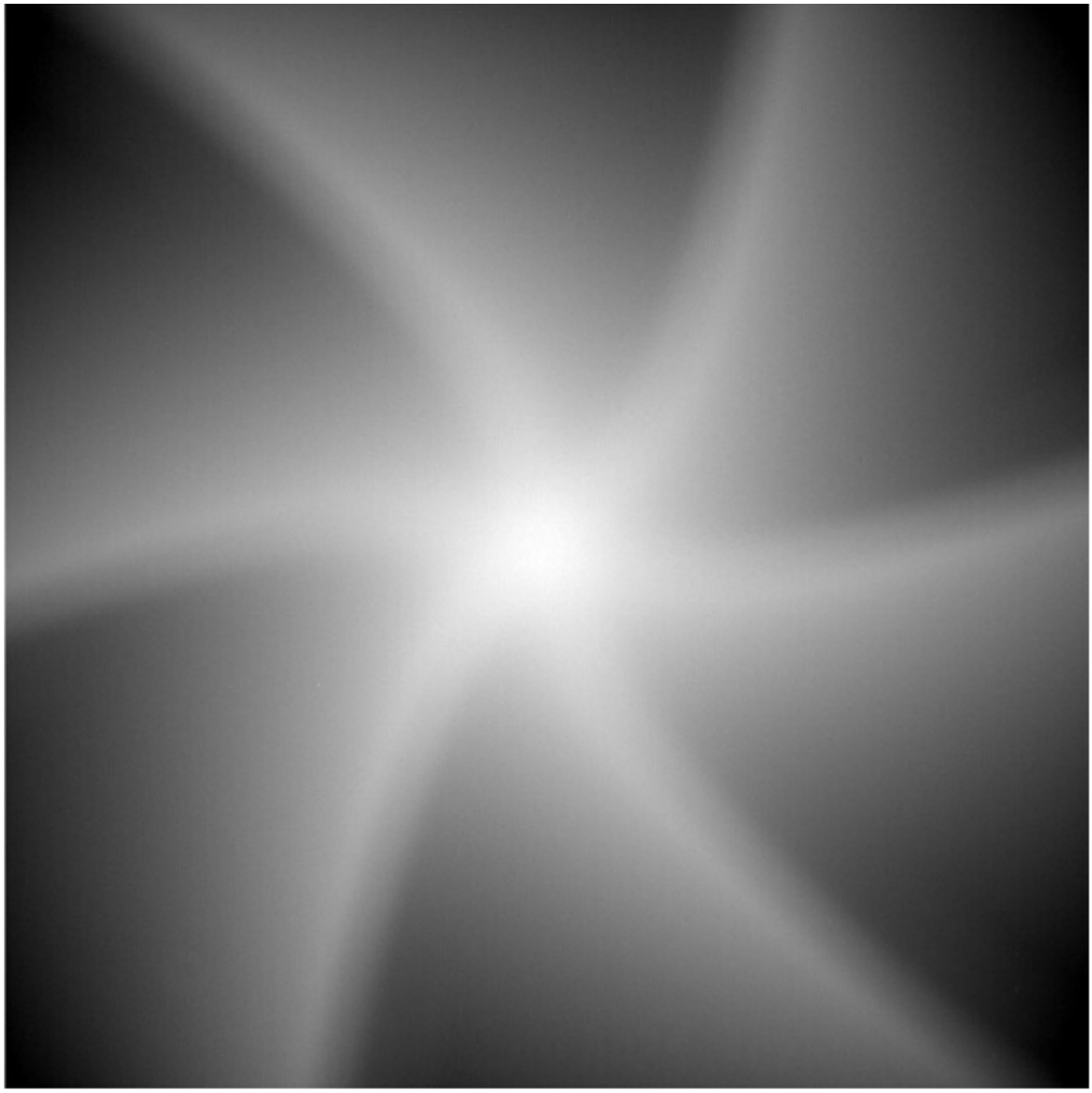

Figure 34: The 2x2 binning shutter map based on a series of 15 R filter flats. This is β_{ij} from equation 17 after it has been smoothed using the Gaussian smoothing kernel of SAOimage ds9.

This method was created as a part of the script but due to more pressing tasks was de-prioritised and hence not fully implemented for this project due to lack of time for adequate testing. Most of the targets being imaged for this project are very faint (R magnitude >16), and exposures need to be on the order of 300s. For a 300s exposure only 0.1s is added to the total exposure time at the very centre, meaning there is only a maximum difference between exposure times across the frame of 0.03%.

5.1.3 Flat Checking

ABOT routinely takes twilight flats every evening and every morning in all filters available to it. To get an acceptable average count in each flat it usually starts by taking a test exposure of 0.05s to ensure that the sky is actually dark enough to

start taking flats, and it calculates from there how long future exposures should be to reach an acceptable count rate of around 50,000. This technique means that there are often multiple flat frames each night which are inappropriate for use, taken while the telescope attempts to get a good count rate.

It is best to have flats which are all roughly the same average counts when making a master flat. At the same time, any frames which have unusual bright patches caused by the moon light reflecting through the OTA, or defects caused by equipment malfunction need to be discarded. A quick and reliable test needs to be used to identify these frames

First, a histogram of the distribution of pixel counts in the flat is created and the kurtosis of that data is calculated. Frames outside a small range of accepted kurtosis values are discarded. Kurtosis is a quick way to measure the shape of this histogram, and any histograms which have unusual spikes in them caused by a small fraction of the frame being brighter than the rest have a larger kurtosis.

The second test was to take the average count of the pixels in the images and to exclude any images outside a predetermined range.

To check the validity of these two tests two sets of flats were selected. The first was a set of 20 Baader R filter flats taken in early November which were deemed acceptable on visual inspection, and a second list of 185 Baader R filter flats taken over the course of late November and early December 2016, both acceptable and unacceptable. The first set of 20 were run through the kurtosis test to get a range of acceptable values to use on other data. The kurtosis test was also performed on the 185 test frames (Figure 35), with all but 3 good frames falling within the narrow range of kurtosis values suggested by the set of 20 frames ($\sim$-1.1 to -0.9).

Once the 85 flats which fell outside the range of kurtosis values were excluded from the list, the average counts of the remaining 100 frames were calculated and plotted, see Figure 36. By choosing to only accept average values between 35,000 and 45,000, all remaining poor quality flats were excluded. This range of average counts was chosen as at the time PIRATE was set to aim to acquire flats with peak counts at 40,000.

Overall, all poor quality flats were excluded, and only 4 out of 185 good quality flats were rejected. The rejected good frames were frames which are on the very limit of acceptability and possibly would be judged to be poor or acceptable by different people.

Originally both tests were developed and used as neither one alone seemed to suffice, but it was then discovered in early January 2017 that the shutter of the PIRATE camera

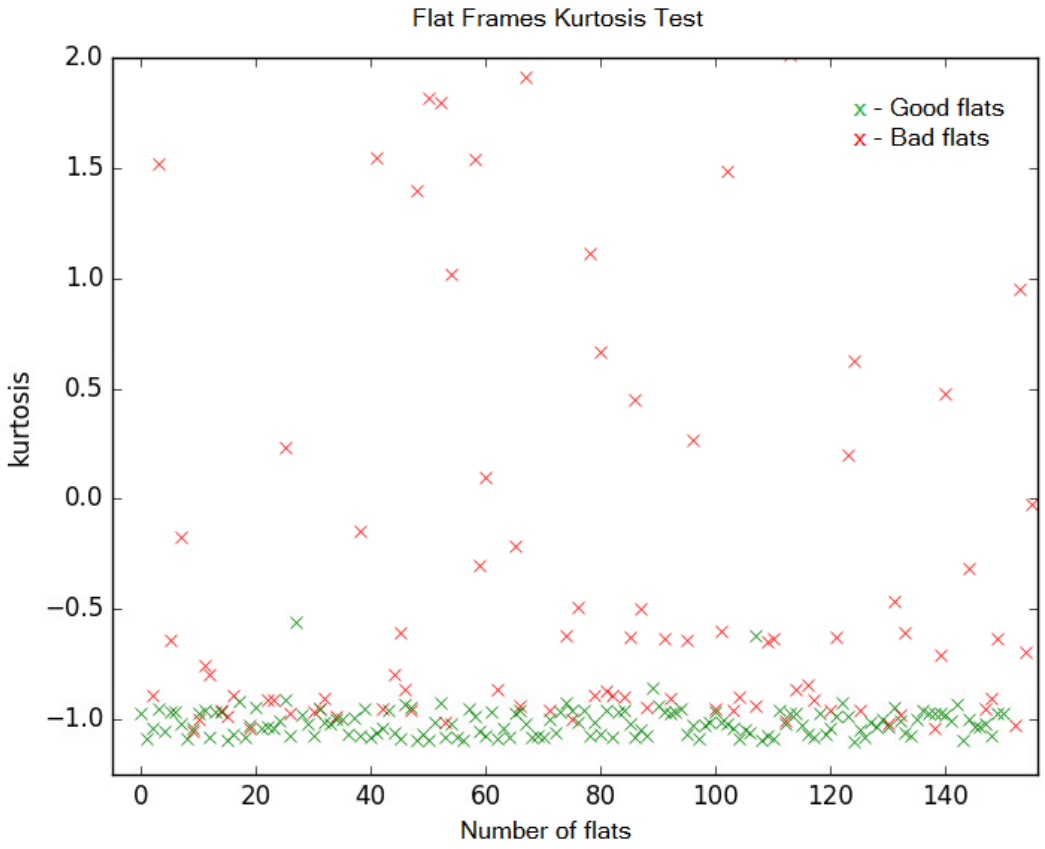

Figure 35: A test to see whether or not kurtosis could be used to exclude bad flats from the reduction pipeline. Kurtosis value for a "bad" flat (as judged by visual inspection) is indicated in red, and in green for a "good" flat. Putting limits on acceptable kurtosis values between -1.1 and -0.9 eliminates a significant fraction of the unacceptable flats.

had been sticking, causing it to not fully close. A bright spot would often appear in the centre of the image, which the kurtosis seemed to help identify. It also became apparent that the method by which ABOT was deciding whether or not a flat was reaching the desired level of 40,000 ADU was insufficient.

The method ABOT originally used to identify saturated frames was to identify if there were any pixels at or above 50,000 ADU in a flat, and then to check the closest nine pixels surrounding that to see if they were above 50,000 ADU as well. If they were, then the image was deemed to be above 50,000 throughout the whole image. This information would then be used to determine the exposure time of the next flat. Unfortunately this method proved insufficient as there were often stars in the image which would reach this level of saturation long before the rest of the frame.

At the suggestion of myself and other members of the PIRATE team, Sybilla Technologies team developed an improved method where ABOT instead uses the average number of counts in a region of the flat which is 10% of the height and width of the

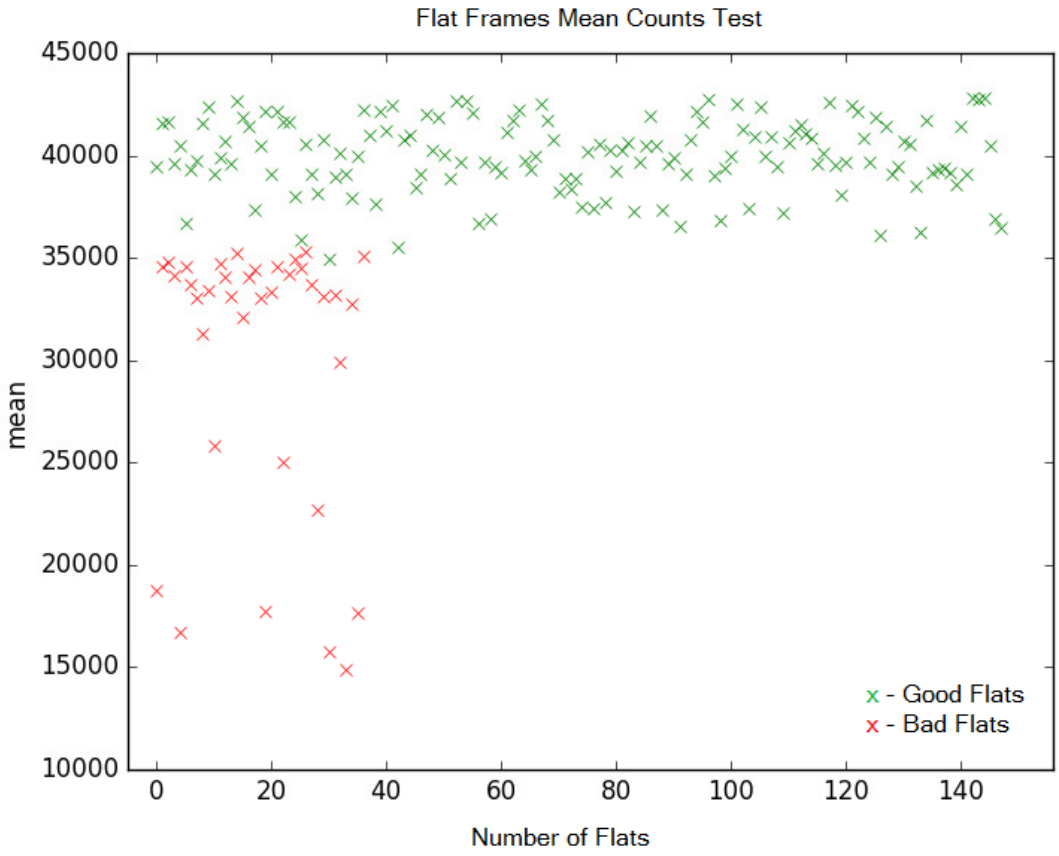

Figure 36: After the flats had been put through the kurtosis test, the remaining flats were checked for the average pixel value across the frame. Bad flats are again indicated in red, and acceptable flats are indicated in green. Limiting the acceptable values to be between 35,000 and 45,000 counts eliminates the rest of the bad flats from the set.

frame and positioned in the centre. Once this was changed, along with the fixing of the camera shutter, the kurtosis test no longer became necessary, and imitating the method used by ABOT for determining the saturation of the frame successfully picked out the best flat frames.

5.1.4 Plate Solving

By identifying patterns of stars in images, plate solving recognises the appropriate astronomical coordinates for the field in an image. The information necessary to associate a pixel in an image with an astronomical coordinate is stored in the FITS header as the world coordinate system (WCS) keywords. With associated coordinates more advanced analysis of an image can be carried out.

In the pipeline I created plate solving is performed using a locally installed version of the astrometry.net code (Lang et al. 2010), using index files provided on the astrometry.net website from the 2MASS catalogue (Skrutskie et al. 2006). Although it may

be better to use index files from an optical survey rather than the 2MASS ones, there have been no performance issues with plate solving related to the index files.

As the local version of astrometry.net can be run through the Linux command line, it can be simply run through python using a few lines of code. Though astrometry.net is capable of plate solving with no extra information, the process is made considerably fast by giving it extra information, such as: approximate centre coordinates, approximate size of the image in degrees, the plate scale, the number of stars it should use to find the solution (usually around 20) and downsampling (binning) the image to 2x2 of whatever it is to start with. Typically each frame takes less than ten seconds to plate solve successfully, though an unsuccessful plate solve can take several minutes.

When using the CPCS to magnitude calibrate frames, the RA and DEC values for targets which come from the above plate solving method are accurate enough to find objects within 2 arcseconds of the catalogue values. This is backed up by my ensemble photometry pipeline (described later in section 5.2.2), which uses a matching distance of 2 arcseconds when comparing the plate solved RA and DEC to the published RA and DEC for a target.

To minimise the total number of unsuccessful plate solves, the plate solve is run twice more on images it fails to solve the first time. The successive attempts are run using changed parameters, typically the second run allows a greater number of stars to be used in the solution (usually 120), and the third attempt makes no assumptions and runs the plate solve with none of the extra information mentioned earlier. This final attempt can take much longer to run, on the order of minutes per image but can potentially solve images which have inaccurate information in their fits header.

5.2 Data Analysis Pipeline

After the images have gone through all of the basic data reduction which is necessary for all scientific astronomical images, I implemented some basic automated data analysis. In this section I discuss how the aperture photometry, and photometric light curve generation was handled.

5.2.1 Aperture Photometry

The final goal is to create a differential light curve of flux against time for a given target star. To do this, aperture photometry needs to be carried out on both the target star which I am interested in, and on other stars in the same image as the target.

When manual basic aperture photometry is performed, it consists of choosing by eye a region in an image which appears to be a star, that is an object which is significantly brighter than areas of the image where there are no resolved objects. The aperture is chosen to be slightly bigger than the star appears to be, as the display of an image may not adequately show all the pixels which have received a significant number of photons from the star. Once an appropriate aperture is selected, the total number of counts in all pixels within the aperture are summed up to give a value which contains counts both from the star and the background. Simultaneously the sky background is calculated in a region where there are no resolved stars, and as close as possible to the star, as the background varies across an image. Those background counts are subtracted from the counts for the star, and that value represents the flux of the star (Gallaway 2015).

While it is possible to use Astropy to perform aperture photometry, there already exists a tool which is used widely in astronomy and is automatable in the same way as the astrometry.net code. Source Extractor (Bertin et al. 1996) carries out the aperture photometry for my pipeline, due to its flexibility in how the aperture shape and size is picked, the speed at which it can run (typically less than 5s per frame) and the ability to run it through the command line.

Source Extractor can select an aperture in several different ways. Of particular importance for this project are the fixed-radius aperture which was used for testing, and variable-radius aperture which picks an aperture size based on the point-spread function of the star (Holwerda 2005) which is more useful for actual application of the pipeline as stars can appear to vary in size between images, solely due to the conditions at the time the image was taken.

Source extractor also picks out stars which are saturated and flags them, and provides other useful data such as the RA and DEC of each star as long as the images are plate solved before they are run through source extractor. Figure 37 gives an example of an output text file from source extractor.

Performing aperture photometry with source extractor in crowded fields and diffuse light regions, such as in the spiral arms of a galaxy, is known to not perform as well as it does in less crowded fields. Annunziatella et al. 2013 reported that source extractor aperture photometry for magnitude 22-23 stellar sources gave magnitudes within -0.009 ± 0.059 mag for less dense fields, and magnitudes within -0.165 ± 0.287 mag in crowded fields, indicating a significant reduction in photometric accuracy. For

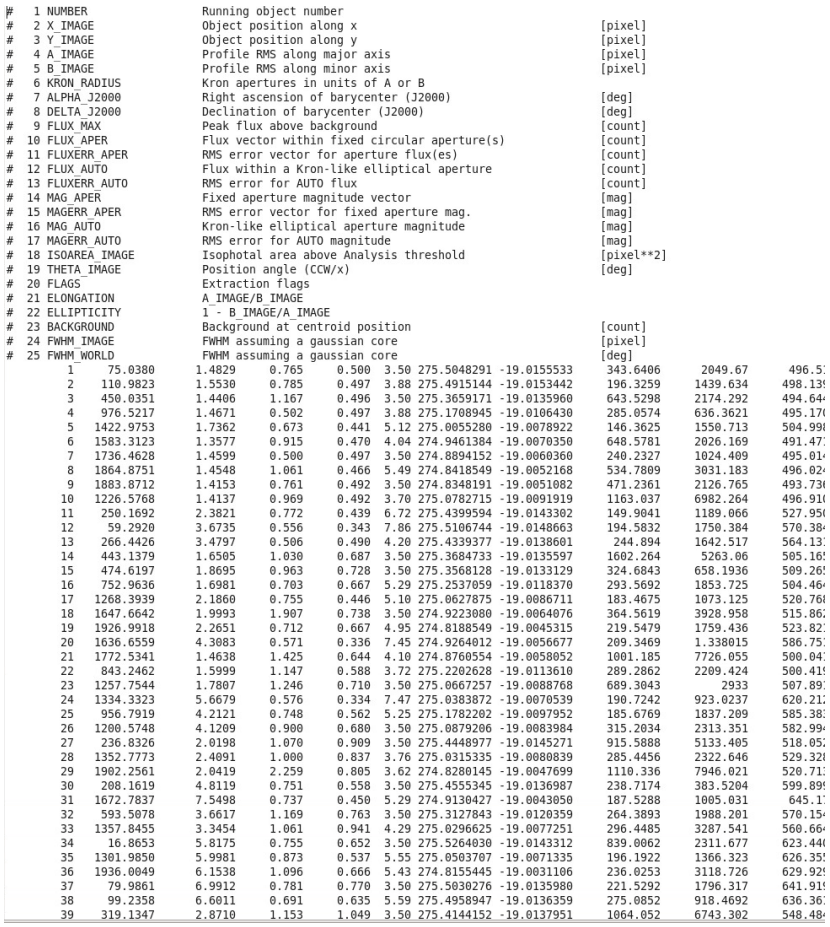

```
#   1 NUMBER                Running object number
#   2 X_IMAGE               Object position along x                                   [pixel]
#   3 Y_IMAGE               Object position along y                                   [pixel]
#   4 A_IMAGE               Profile RMS along major axis                              [pixel]
#   5 B_IMAGE               Profile RMS along minor axis                              [pixel]
#   6 KRON_RADIUS           Kron apertures in units of A or B
#   7 ALPHA_J2000           Right ascension of barycenter (J2000)                     [deg]
#   8 DELTA_J2000           Declination of barycenter (J2000)                         [deg]
#   9 FLUX_MAX              Peak flux above background                                [count]
#  10 FLUX_APER             Flux vector within fixed circular aperture(s)             [count]
#  11 FLUXERR_APER          RMS error vector for aperture flux(es)                    [count]
#  12 FLUX_AUTO             Flux within a Kron-like elliptical aperture               [count]
#  13 FLUXERR_AUTO          RMS error for AUTO flux                                   [count]
#  14 MAG_APER              Fixed aperture magnitude vector                           [mag]
#  15 MAGERR_APER           RMS error vector for fixed aperture mag.                  [mag]
#  16 MAG_AUTO              Kron-like elliptical aperture magnitude                   [mag]
#  17 MAGERR_AUTO           RMS error for AUTO magnitude                              [mag]
#  18 ISOAREA_IMAGE         Isophotal area above Analysis threshold                   [pixel**2]
#  19 THETA_IMAGE           Position angle (CCW/x)                                    [deg]
#  20 FLAGS                 Extraction flags
#  21 ELONGATION            A_IMAGE/B_IMAGE
#  22 ELLIPTICITY           1 - B_IMAGE/A_IMAGE
#  23 BACKGROUND            Background at centroid position                           [count]
#  24 FWHM_IMAGE            FWHM assuming a gaussian core                             [pixel]
#  25 FWHM_WORLD            FWHM assuming a gaussian core                             [deg]
       1     75.0380  1.4829     0.765     0.500  3.50 275.5048291 -19.0155533     343.6406      2049.67      496.5
       2    110.9823  1.5530     0.785     0.497  3.88 275.4915144 -19.0153442     196.3259     1439.634     498.13
       3    450.0351  1.4406     1.167     0.496  3.50 275.3659171 -19.0135960     643.5298     2174.292     494.64
       4    976.5217  1.4671     0.502     0.497  3.88 275.1708945 -19.0106430     285.0574     636.3621     495.17
       5   1422.9753  1.7362     0.673     0.441  5.12 275.0055280 -19.0078922     146.3625     1550.713     504.99
       6   1583.3123  1.3577     0.915     0.470  4.04 274.9461384 -19.0070350     648.5781     2026.169     491.47
       7   1736.4628  1.4599     0.500     0.497  3.50 274.8894152 -19.0060360     240.2327     1024.409     495.01
       8   1864.8751  1.4548     1.061     0.466  5.49 274.8418549 -19.0052168     534.7809     3031.183     496.02
       9   1883.8712  1.4153     0.761     0.492  3.50 274.8348191 -19.0051082     471.2361     2126.765     493.73
      10   1226.5768  1.4137     0.969     0.492  3.70 275.0782715 -19.0091919    1163.037     6982.264     496.91
      11    250.1692  2.3821     0.772     0.439  6.72 275.4399594 -19.0143302     149.9041     1189.066     527.95
      12     59.2920  3.6735     0.556     0.343  7.86 275.5106744 -19.0148663     194.5832     1750.384     570.38
      13    266.4426  3.4797     0.506     0.490  4.20 275.4339377 -19.0138601      244.894     1642.517     564.13
      14    443.1379  1.6505     1.030     0.687  3.50 275.3684733 -19.0135597     1602.264      5263.06     505.16
      15    474.6197  1.8695     0.963     0.728  3.50 275.3568128 -19.0133129     324.6843     658.1936     509.26
      16    752.9636  1.6981     0.703     0.667  5.29 275.2537059 -19.0118370     293.5692     1853.725     504.46
      17   1268.3939  2.1860     0.755     0.446  5.10 275.0627875 -19.0086711     183.4675     1073.125     520.76
      18   1647.6642  1.9993     1.907     0.738  3.50 274.9223080 -19.0064076     364.5619     3928.958     515.86
      19   1926.9918  2.2651     0.712     0.667  4.95 274.8188549 -19.0045315     219.5479     1759.436     523.82
      20   1636.6559  4.3083     0.571     0.336  7.45 274.9264012 -19.0056677     209.3469     1.338015     586.75
      21   1772.5341  1.4638     1.425     0.644  4.10 274.8760554 -19.0058052     1001.185     7726.055     500.04
      22    843.2462  1.5999     1.147     0.588  3.72 275.2202628 -19.0113610     289.2862     2209.424     500.41
      23   1257.7544  1.7807     1.246     0.710  3.50 275.0667257 -19.0088768     689.3043         2933     507.89
      24   1334.3323  5.6679     0.576     0.334  7.47 275.0383872 -19.0070539     190.7242     923.0237     620.21
      25    956.7919  4.2121     0.748     0.562  5.25 275.1782202 -19.0097952     185.6769     1837.209     585.38
      26   1200.5748  4.1209     0.900     0.680  3.50 275.0879206 -19.0083984     315.2034     2313.351     582.99
      27    236.8326  2.0198     1.070     0.909  3.50 275.4448977 -19.0145271     915.5888     5133.405     518.05
      28   1352.7773  2.4091     1.000     0.837  3.76 275.0315335 -19.0080839     285.4456     2322.646     529.32
      29   1902.2561  2.0419     2.259     0.805  3.62 274.8280145 -19.0047699     1110.336     7946.021     520.71
      30    208.1619  4.8119     0.751     0.558  3.50 275.4555345 -19.0136987     238.7174     383.5204     599.89
      31   1672.7837  7.5498     0.737     0.450  5.29 274.9130427 -19.0043050     187.5288     1005.031      645.1
      32    593.5078  3.6617     1.169     0.763  3.50 275.3127843 -19.0120359     264.3893     1988.201     570.15
      33   1357.8455  3.3454     1.061     0.941  4.29 275.0296625 -19.0077251     296.4485     3287.541     560.66
      34     16.8653  5.8175     0.755     0.652  3.50 275.5264030 -19.0143312     839.0062     2311.677     623.44
      35   1301.9850  5.9981     0.873     0.537  5.55 275.0503707 -19.0071335     196.1922     1366.323     626.35
      36   1936.0049  6.1538     1.096     0.666  5.43 274.8155445 -19.0031106     236.0253     3118.726     629.92
      37     79.9861  6.9912     0.781     0.770  3.50 275.5030276 -19.0135980     221.5292     1796.317     641.91
      38     99.2358  6.6011     0.691     0.635  5.59 275.4958947 -19.0136359     275.0852     918.4692     636.36
      39    319.1347  2.8710     1.153     1.049  3.50 275.4144152 -19.0137951     1064.052     6743.302     548.48
```

Figure 37: Part of a typical source extractor catalogue, an ascii text file. The first lines which begin with a # are given over to descriptions of the items recorded in the rest of the data. Each row of the data represents one source in the image, and each column is one of the variables listed at the top of the file in order.

source extractor PSF fitting is possible, but requires the use of an additional tool called PSFEx, and in that case source extractor and PSFEx find magnitudes within -0.003 ± 0.014 mag in the less crowded field, and -0.063 ± 0.110 mag in the crowded field. While the overall performance is improved with PSF fitting, there is still a significant decrease in performance between the non-crowded and crowded fields.

While this project has focused on using source extractor's aperture photometry, the inclusion of PSF fitting would be a good time investment for future revisions.

5.2.2 The Ensemble Photometry Pipeline

The next step in creating a light curve is to perform differential photometry. Astronomical images of the same field can be significantly different from frame to frame even when taken consecutively. Even when as much care as possible is taken to ensure that all parameters under the astronomer's control are kept the same between frames, differences in seeing and weather conditions mean that stars can occupy different numbers

of pixels in an image, overall number of counts may vary between frames, and small slewing differences can mean a star will appear in a different place on the CCD. Differential photometry takes care of this by using reference stars, which are stars known to be relatively constant brightness, and considering the relative flux of the target compared to the reference star, or ensemble of multiple reference stars. While the flux value gained is not absolute, the difference in relative flux over time can be calculated (Budding et al. 2007).

My script for generating light curves is also written in python, with the addition of the Pandas (McKinney 2010) package - particularly the use of DataFrames. Since the aperture photometry is carried out by source extractor, each image which has the potential to be used in a light curve has a catalogue with several parameters for each star.

To create a pipeline script which can perform basic aperture photometry, source extractor values for flux for each star need to be extracted from source extractor catalogues. The first step is to convert each source extractor catalogue into a DataFrame, using Pandas.

By performing plate solving before using source extractor, the source extractor output can contain the right ascension and declination for each source, along with the necessary flux values for differential photometry. Because right ascension and declination values for a given star can vary slightly between images due to small uncertainties in the plate solving processes and small changes in the seeing causing the stars to distort slightly, the distance between pairs of right ascension (α) and declination (δ) values is calculated using the equation for great circle distances (equation 22).

$$\theta = arc\cos\left(\sin(\delta_1)\sin(\delta_2) + \cos(\delta_1)\cos(\delta_2)\cos(\alpha_1 - \alpha_2)\right) \tag{22}$$

If the difference is found to be less than the matching distance (θ), the star is assumed to be the same (Birney et al. 2006). The mean seeing value reported for el Observatio del Teide is around 0.76 arcseconds Varela et al. 2002, with highs around 1.2 arcseconds. Through use of the pipeline, 2.0 arcseconds proved to be the smallest matching distance which consistently found the target object.

With the target found from each source extractor catalogue, the instrumental magnitude, x position and y position for the target in pixel coordinates, and the full width half maximum of the target in each image is plotted to provide a diagnostic for any problems which may have occured during the data taking, such as defoccussed images

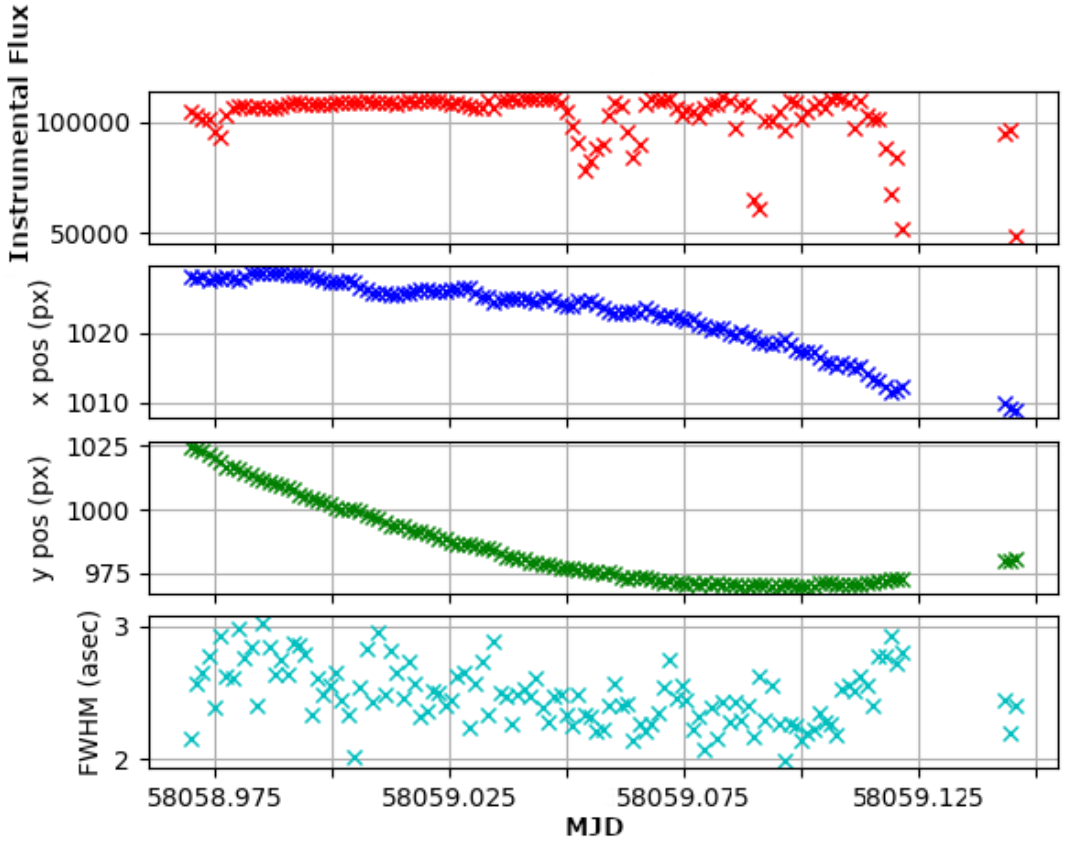

Figure 38: The raw data from the Kojima Microlens from November 2017. The graphs from top to bottom are: instrumental flux, x position on the CCD, y position on the CCD and FWHM in arcsec

which would appear as larger than normal FWHM, or drifting targets which would be visible in the pixel coordinates. An example is given in figure 38.

Generally, a single reference star is not enough to get accurate light curves, more often multiple reference stars are used and summed together before being used to scale the target flux (Budding et al. 2007). The selection of a suitable set of reference stars is the first step towards building an ensemble.

It is preferable to select reference stars which are relatively close to the target, as choosing more distant reference stars increases the likelihood that the variability across the CCD chip will have an effect on the relative flux counts. To do this, again equation 22 is used on all the stars left in the source extractor catalogue after the target has been removed. Any reference stars which have a target distance lower than the desired maximum radius are kept, while anything outside of the range is dropped. For PIRATE using a target distance of 10 arcminutes covers an area which is about 1/5 of the total chip ($\sim$ 45am$\times$45 am). For particularly crowded fields, an allowed distance of 10 arcminutes can lead to hundreds of possible reference stars. To lessen the computing time, choosing a maximum number of reference stars makes the script

choose smaller target distance for the reference stars in 1 arcminutes increments until the number of reference stars is below that limit.

In addition to the distance from the target star, other constraints are also used to select an optimum list of reference stars. A reference star must appear in every source extractor catalogue which is used for the light curve. Reference stars must also be at least 10% as bright and no more than five times as bright as the target. This is achieved by finding the average flux of the target across all catalogues, and comparing the average flux of each possible reference star to this value.

With the target data identified, and possible reference stars listed, the next step is to organise the list of reference stars in order of preference. An ideal reference star would be one which has a differential light curve which doesn't significantly vary over the course of the target observations. With this in mind, every possible reference star is paired off with every other possible reference star and differential photometry is performed for every pairing.

For every pairing, the Root Mean Square (RMS) is calculated of the differential light curves, and then the pairings are ordered from lowest RMS to highest. Since the RMS is calculated using the average flux measurement of the differential pair ($\bar{x}$), it gives a quantitative measure for how much the light curve differs from a straight, flat line, meaning a lower RMS should give the pairings which have the flattest light curves.

$$RMS = \sqrt{\frac{1}{n}\sum (x_i - \bar{x})^2} \tag{23}$$

Equation 23 for the RMS uses the individual differential flux measurements for the pair in each image (x_i), for n data points.

With the ordered list of pairings, the reference stars are then picked from best to worst by choosing the reference stars which appear most frequently in the top 20% of the pairs list to the least frequent in the list.

The next step in the pipeline is to introduce the ensemble photometry. At this point we have a list of reference stars which appear to have the flattest light curves over the covered time span, ordered from best to worst.

Based on a method by Honeycutt 1992 and building on a method used by Burke et al. 2006 for performing differential photometry on a set of data obtained over long periods, where inhomogeneity can be large, Holmes et al. 2011 worked on an ensemble photometry method for transiting exoplanets.

The ensemble E_j is a weighted average of the flux F_{ij} of the reference stars i in

the image j. So E_1 is the ensemble of the reference stars in the first image, E_2 is the ensemble of the reference stars in the second image and so on. The weighting ω_{ij} for each reference star i in each image j uses the light curve RMS (σ_{ij}) of the differential light curve obtained when using the reference star i as the only reference star for differential photometry with the target star.

$$E_j = \frac{\sum_{i=1}^{N} \omega_{ij} F_{ij}}{\sum_{i=1}^{N} \omega_{ij}} \qquad \omega_{ij} = \frac{1}{\sigma_{ij}^2} \tag{24}$$

Where N is the number of images in the light curve.

For each new ensemble the flux ratio $d_{*,j}$ of the ensemble with the target star for the image j is calculated

$$d_{*,j} = \frac{F_{*,j}}{E_j} \tag{25}$$

E_j is the reference star ensemble for image j (as above), F_* is the flux of the target star in image j.

Using this method, the target star light curve is calculated first using just the best reference star from the list made earlier, then the light curve is generated again using the best two reference stars, and so on until the list of possible reference stars is exhausted.

Holmes et al. 2011 then used the differential light curve $d_{*,j}$ which had the lowest RMS value as the indicator of the best light curve. This technique may not work for this project as the variables looked at here have significantly higher amplitude changes than the planetary transits which Holmes et al. 2011 was looking for. Instead a different technique was investigated for this project, looking at the "string length" of each light curve.

5.2.3 String Length Minimisation

The string length (SL) of each light curve is calculated simply using normalised Pythagoras' theorem (equation 26) between consecutive data points. Here ΔMJD_i is the time interval between consecutive points in the differential light curve, ΔF_i is the difference in differential flux between consecutive points and N is the number of data points.

$$SL = \frac{1}{N} \sum_{i=1}^{N} \sqrt{\Delta MJD_i^2 + \Delta F_i^2} \tag{26}$$

The idea behind the string length technique is that the differential light curve of the target star with a one star ensemble should give some arbitrary value of string length, but subsequent additions of reference stars to the ensemble should reduce the value of the string length if they are reducing the noise in the data. Reducing noise in light curve measurements should reduce the variation of the measurements around the light curve the star is following, making all those measurement closer together. If this is the case, the value of ΔF should decrease between consecutive points overall leading to a lower string length, and the light curve with the minimum string length should be the best representation.

The method is easy to calculate, doesn't require tailoring to specific targets, and should be independent of the shape a variable light curve takes, meaning it should be automatable to fit in with the rest of the pipeline.

Testing this on multiple targets yielded unexpected results. Figure 39 shows a selection of typical string length vs ensemble size graphs from targets observed over the course of this project. Note that the x-axis "ensemble size" is 1 less than the number of reference stars used in the ensemble.

Of the four examples, only Gaia17bie displays anything close to the behaviour expected before the method was implemented, reaching a minimum at ensemble size 41 (which uses 42 reference stars in the ensemble). All three of the other examples find a minimum within ensemble size of 10 or less, and in fact both Gaia17bjn and Gaia18cjk found the minimum with the first reference star. Out of 86 generated light curves, ⅔ of the targets reach a string length minimum with 10 or less reference stars used in the ensemble.

It is important to notice is that the absolute value of string length changes very little, the largest change in string length between two points in Gaia18cjk in figure 39 is about 0.015, less than 1% of its maximum string length. For example, in Gaia17bjn after adding the third star to the ensemble the string length doesn't change by more than ~ 0.002 out of a maximum 10.482. It is very unlikely that the changes to string length after adding the third star make a significant difference to the light curve generated.

The reason for the unexpected behaviour is likely due to the sorting method used to calculate the best reference stars for the target. It is likely working very effectively, the star picked as the best candidate reference star really is the best reference star in ⅔ of targets. If that is the case adding more stars may either have very little effect on the light curve, such as in Gaia17bjn after the third reference star, or even increase

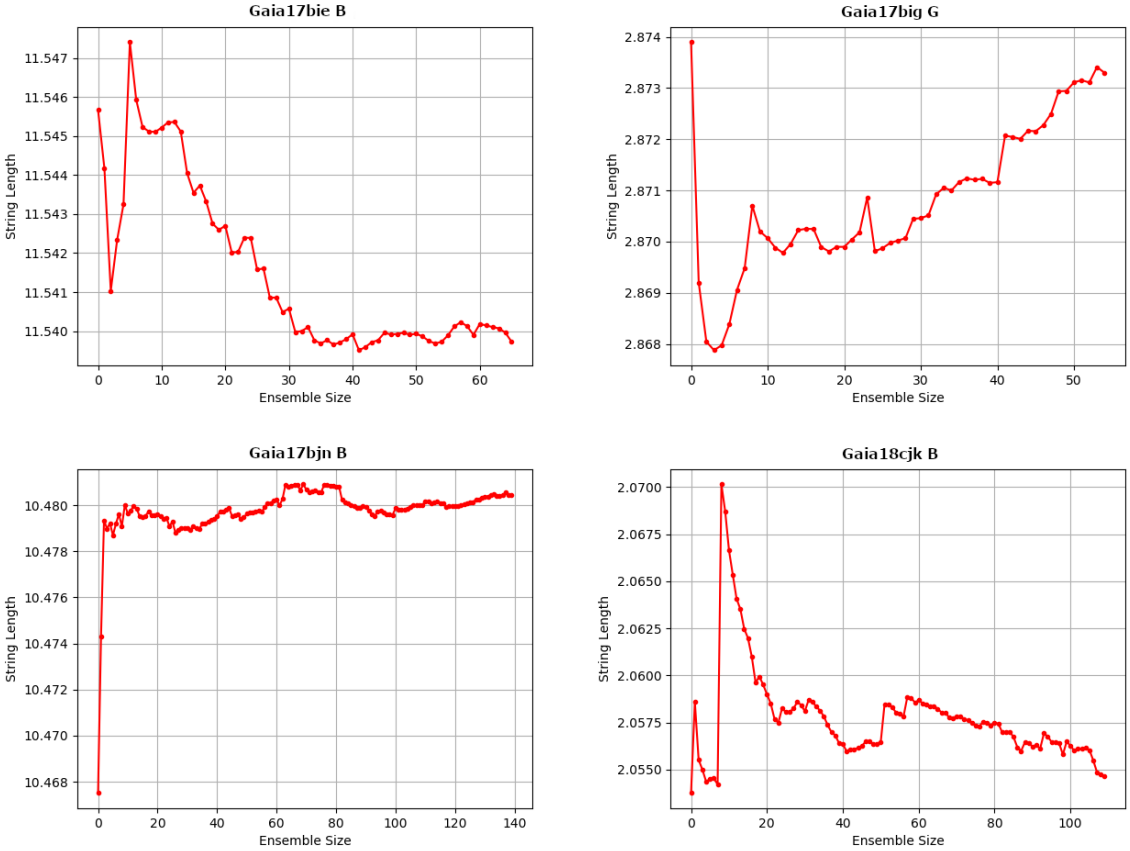

Figure 39: The string length for 4 sets of data. The ensemble size is 1 less than the number of stars used for the ensemble, so ensemble size 0 actually uses 1 star for the "ensemble". From top to bottom, left to right the data are from Gaia17bie B filter, Gaia17big G filter, Gaia17bjn B filter, Gaia18cjk B filter.

the probability of adding a reference star to the ensemble which has a negative effect on the light curve shape. The 9th star added to the Gaia18cjk ensemble (the highest point) seems to be an example of a star which had a negative effect on the overall light curve, with the 10th reference star onwards appearing to lower the string length towards the minimum which was found with the first reference star.

Inspection of light curves, and comparison of string length to root squared error for some light curves where a best fit line was calculated and used for the RSE (see figure 40), the string length minimum does appear to be useful as a tool for assessing the best light curve, despite the unexpected behaviour when compared to the ensemble size. So the minimum string length was used for the remainder of the project as a measure for the best ensemble size when generating light curves.

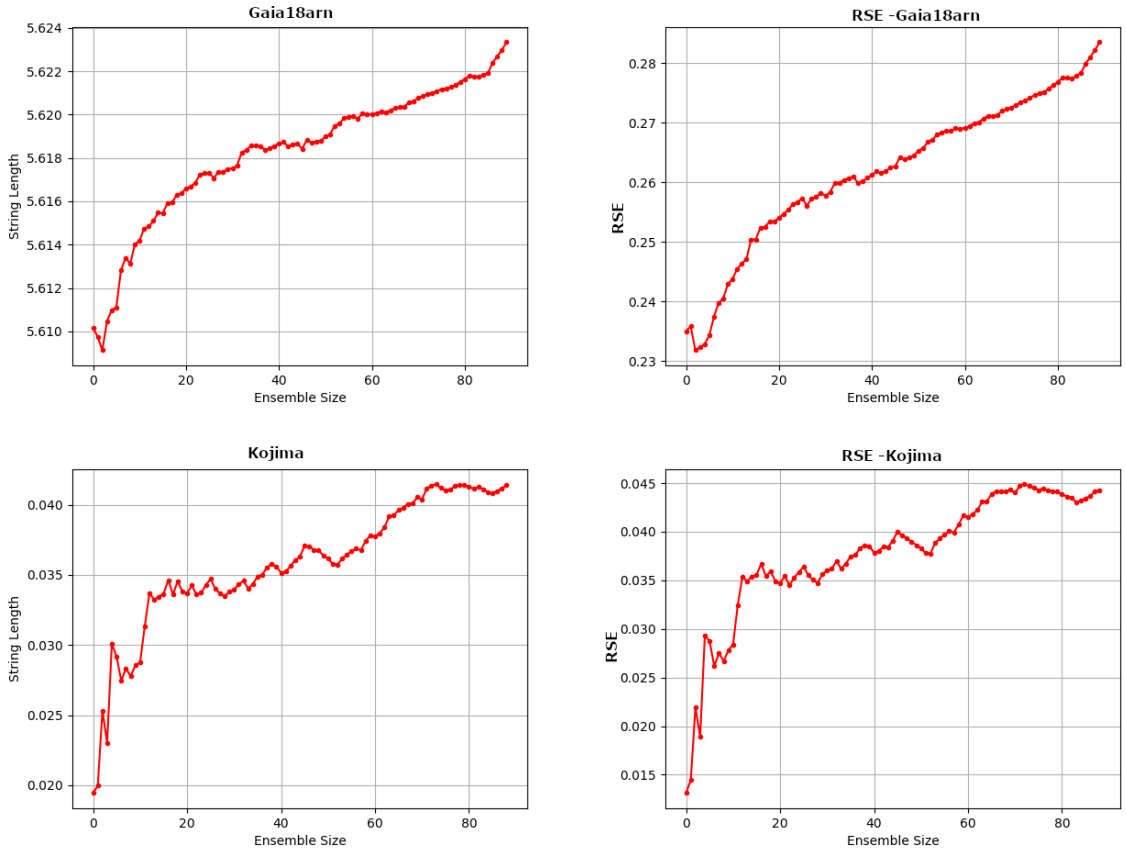

Figure 40: The string length and root square error compared to fits calculated using least-square methods for the two targets. The left is the string length, and the right the RSE. The top two are Gaia18arn in the V filter, and the bottom two are the Kojima microlensing event in the R filter. While the two methods do not give identical results, they do agree on the number of reference stars used, and have a very similar shape over all.

5.3 PIRATE Pipelines and Variable Monitoring

Through the use of Python, astrometry.net and source extractor, I have created a pipeline which can take raw PIRATE data downloaded from Tenerife: bias, dark and flat calibrate, plate solve, carry out aperture photometry and ensemble photometry without the need of human intervention. The use of string length minimisation means that even though selection of reference stars is carried out automatically, I have some indication of which ensemble size to choose when discussing the target light curve.

These tools mean that the vast quantities of data captured by PIRATE can be sorted through more quickly than through manual data reduction, something which is necessary for the 20,000+ images collected during the course of 2.5 years of data collection for this project.

6 Cambridge Photometry Calibration Server Versus Ensemble Photometry Pipeline

During this project two methods were used for creating light curves, both of which could be integrated into the automated data reduction pipeline. The first of those is the ensemble photometry pipeline (EPP) described in section 5.2 which is a Python script that uses Source Extractor catalogues and outputs a differential light curve using ensemble photometry. The second is the light curve generated by feeding Source Extractor catalogues to the Cambridge Photometry Calibration Server described in section 4.3 which outputs a magnitude-calibrated light curve using catalogue cross-matching.

The initial assumption was that the ensemble photometry method should produce light curves with less scatter around the assumed model for the data. In this section I compare the output of the two methods in Baader R, G and B filters using Gaia17bts (figure 41) and Johnson R, V and B filters using Gaia18arn (figure 42) as case studies.

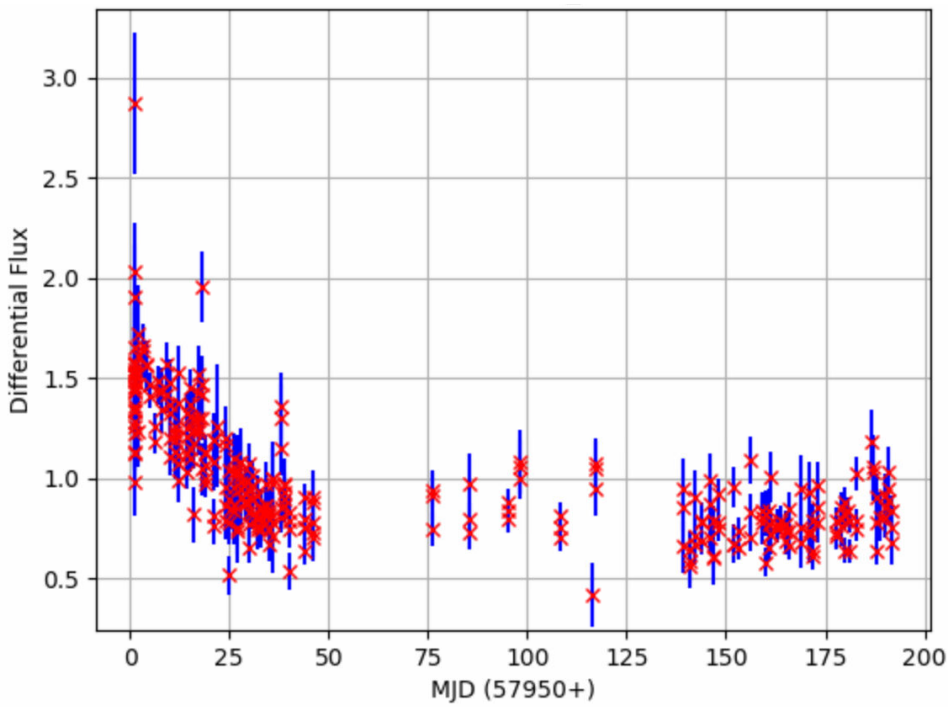

Figure 41: Gaia17bts as observed through the Baader R filter by PIRATE. The data has been plotted using the EPP and this plot is from before it has magnitude calibrated. The target was a single-lens microlensing event caught shortly after the peak.

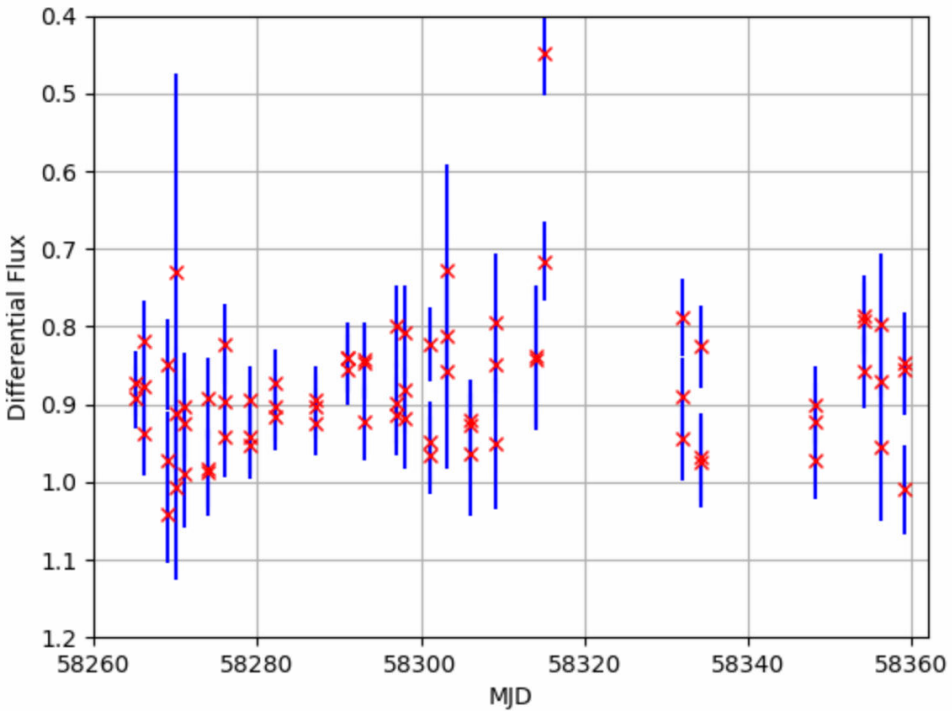

Figure 42: Gaia18arn as observed through the Johnson R filter by PIRATE. The data has been plotted using the EPP and this plot is from before it has been magnitude calibrated. Although the target had risen in brightness shortly before PIRATE began taking data, the target appears to have remained at approximately constant brightness during the time PIRATE was observing it, with scatter due to noise as opposed to intrinsic to the source.

PIRATE observed Gaia17bts over around 200 nights beginning in July 2017 and captured the declining phase of a single-lens microlensing event, along with a few weeks of data after the event when the source had returned to the baseline brightness. Gaia18arn is an unknown variable which brightened by $\approx$ 0.25 mag over about 1 month in February 2018 and since then has remained at the increased brightness. The PIRATE data for Gaia18arn covers around 100 nights of this increased brightness and at first glance appears to neither be increasing or decreasing.

The choice for targets to make this comparison was limited as they had to meet several criteria. The desired comparison involves fitting a relatively simple model to the light curve data obtained from each of the EPP and CPCS. To that end, the targets needed to have a relatively well sampled light curve, covering a relatively large time span. The CPCS and the EPP also both needed to have successfully generated a light curve of the target. In addition to those essential criteria for the comparison, it would be wise to get a comparison of how the two generators perform both for relatively flat light curves, as well as for light curves showing some large scale variation.

Gaia17bts fulfilled all of the criteria very well, and additionally it shows both large

scale variation and a long section of relative inactivity which are easily separable into two sections that can be tested independently, and it is covered in Baader R, G, B meaning that three out of the six filters used in the project can be tested. Gaia18arn appears to be a relatively flat light curve, and although the number of measurements is limited, it was at least imaged over the course of 100 days.

6.1 Calibrating the EPP Data to the Standard Photometric Magnitude System

Before the EPP and the CPCS data for each target can be compared, the EPP data needs to be calibrated to the standard magnitude system which the CPCS data already uses. The step after this is to create a model which approximates the overall trend for each light curve while averaging over short term fluctuations. This is not meant to be a model which represents what the star is undergoing physically, rather just a representation of overall trends. As long as the same method is used on both the EPP and CPCS data then it can be used to make a comparison between the two methods.

In the case of Gaia17bts it will be useful to split the data into two sections, the decline section and the flat section. There is a convenient gap in the data as seen in figure 41 to facilitate this, and the split was carried out before calibrating any of the EPP data on to the standard magnitude system.

To calculate the magnitude difference for calibrating the EPP light, the data points which appear in both the CPCS light curve and the EPP light curves were extracted. The standard deviation between the two sets of data was calculated, then the EPP data had a constant 0.01 magnitude added to it and the standard deviation was recalculated. This process was repeated over a range surrounding the CPCS apparent magnitude, with the minimum value for the standard deviation indicating the magnitude shift needed for the EPP magnitude calibration. This process was repeated for all the filters mentioned above. Figure 43 is an example of the plots generated using this method, and shows that the magnitude difference necessary for the Gaia17bts R EPP data calibration was 14.96 mag.

Figure 44 is a plot of Gaia18arn V data from the EPP plotted over the CPCS data after it has been calibrated using the above method.

Similar graphs to figure 43 were created for all filters of Gaia18arn and all filters for both sections of Gaia17bts.

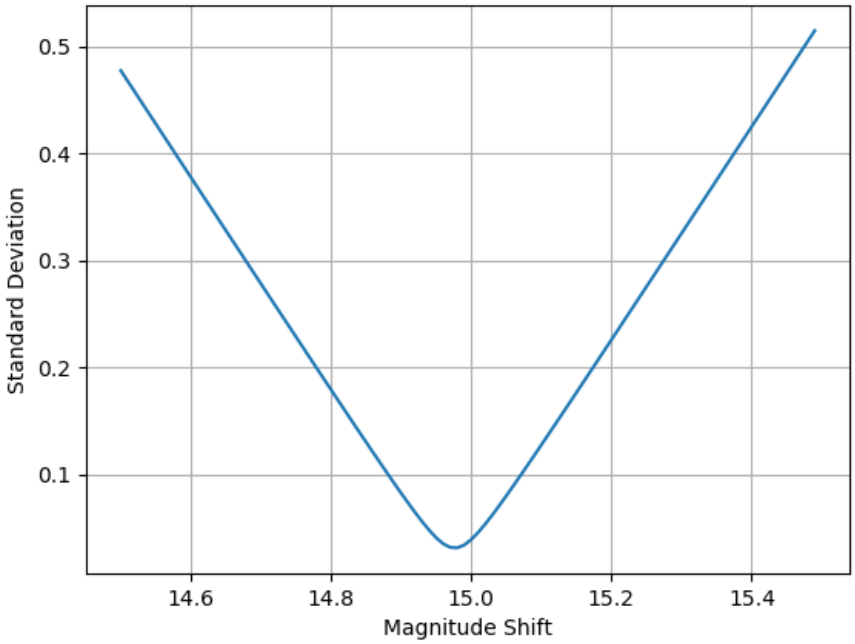

Figure 43: Standard deviation of the difference between CPRS magnitude and EPP magnitude as a function of relative magnitude shift. This example shows the difference in magnitude between the EPP differential photometry light curve and CPCS light curve for Gaia17bts through the Baader R filter is 14.96 mag.

6.2 Fitting the Data

To get a quantitative measure for the scatter in each of the light curves it is necessary to calculate the RMS of the data around some model which has been fit to the data. As mentioned earlier this process was made simpler for Gaia17bts by splitting it into two sections, the decline and the flat section.

For the Gaia17bts data I chose a second order polynomial fit for the decline, and a linear fit for when it appears to return to baseline after the microlensing event has concluded.

For all of the Gaia18arn data, given there is no clear picture for what the star is physically doing, I chose the simplest model that is consistent with the appearance of the light curve. For all filters I chose a linear fit expecting that there may be some small overall increase or decrease in brightness during the time it was observed, but for the most part the star appears to have stayed at a constant brightness.

Figure 45 shows a linear fit to the Gaia17bts data for the flat section of the light curve after being processed by the EPP (top) and the CPCS (bottom). The fit parameters were calculated using weighted linear regression, where the weighting for each

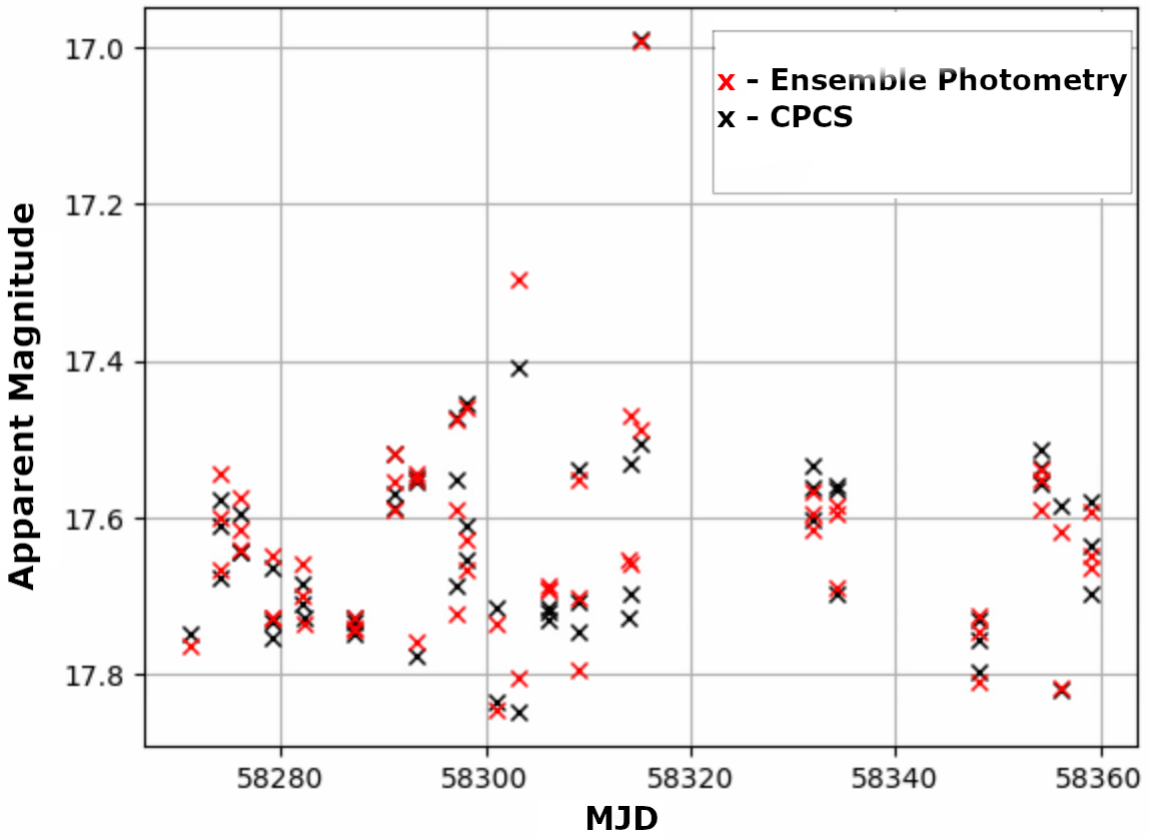

Figure 44: Gaia18arn data in the Johnson V filter. The data in red is the result of the EPP processing after it has been calibrated to match the CPCS data, which is displayed in black. Uncertainties are not displayed here for clarity.

point is given by the uncertainty for each data point. This accounts for why the lowest point in both graphs has very little influence on the fit itself, as the associated uncertainty is relatively large.

At first glance the two models appear to be very similar, with a slight decline in brightness of 0.01 mag over 110 nights.

The slope calculated by the fitting routine is very shallow, i.e. the light curve is very nearly flat, as would be expected for a source having returned to baseline after a microlensing event. The relative uncertainty for both values of the slope is very large, $(4.093 \times 10^{-4} \pm 4.990 \times 10^{-4})$ in the EPP light curve and $(5.372 \times 10^{-4} \pm 5.156 \times 10^{-4})$ for the CPCS light curve, but the slope in both cases lies within a small range around 0. The two slopes are consistent with each other within uncertainties.

To see how one model compares to the other we can plot the model from the EPP light curve along with the band indicating the $\pm 1\sigma$ uncertainty associated with the least-squares fitting technique. In figure 46 this is plotted along with the model from

the CPCS light curve, and we can see that although there is some difference between the two models, the CPCS model is within the $\pm 1\sigma$ uncertainty of the ensemble light curve fit.

The same procedure was performed for the other filters for the flat section of the Gaia17bts light curve, along with the decline section of the Gaia17bts light curve where a second order polynomial was fitted, and the Gaia18arn light curve, which was also fit with a linear model. The outcome of this shows similar results in all filters for both

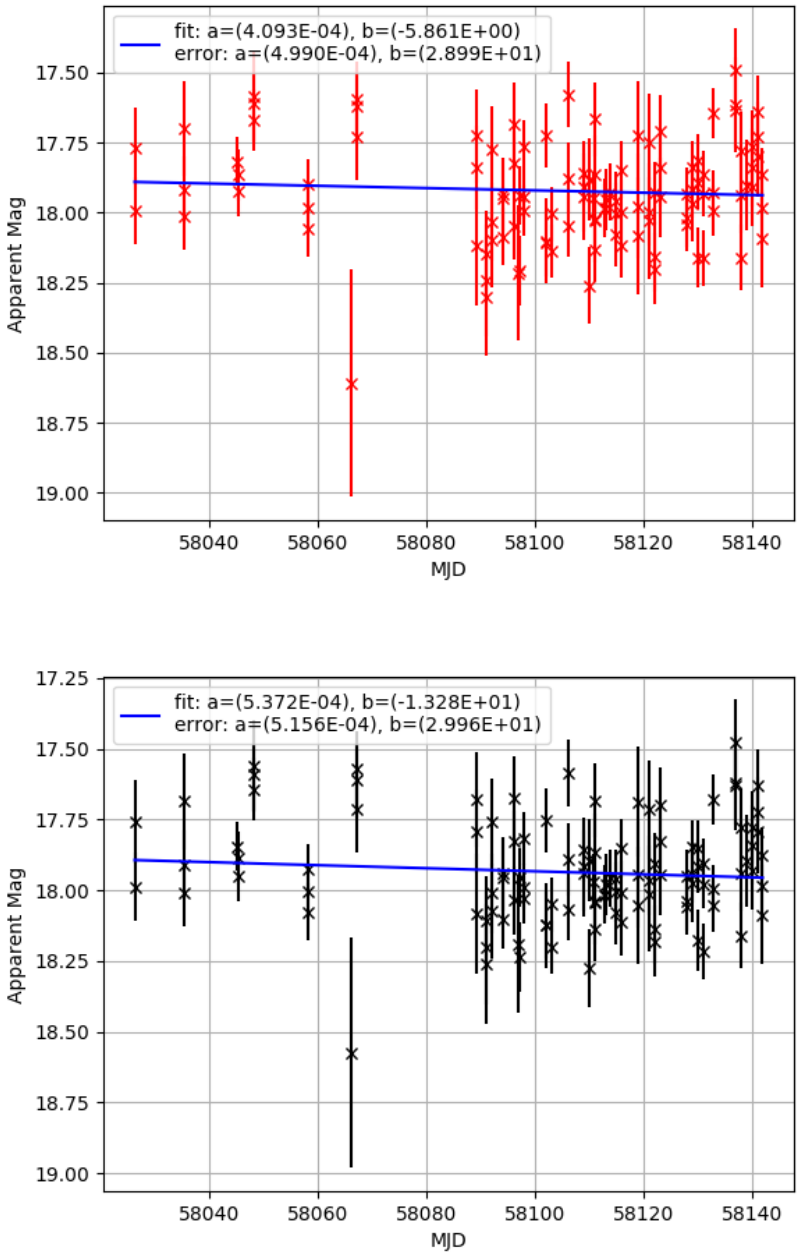

Figure 45: The EPP light curve for the flat section of Gaia17bts in the Baarder R filter in red and the CPCS light curve of the same data in black. Both have been fit with a linear function using python and sciPy.

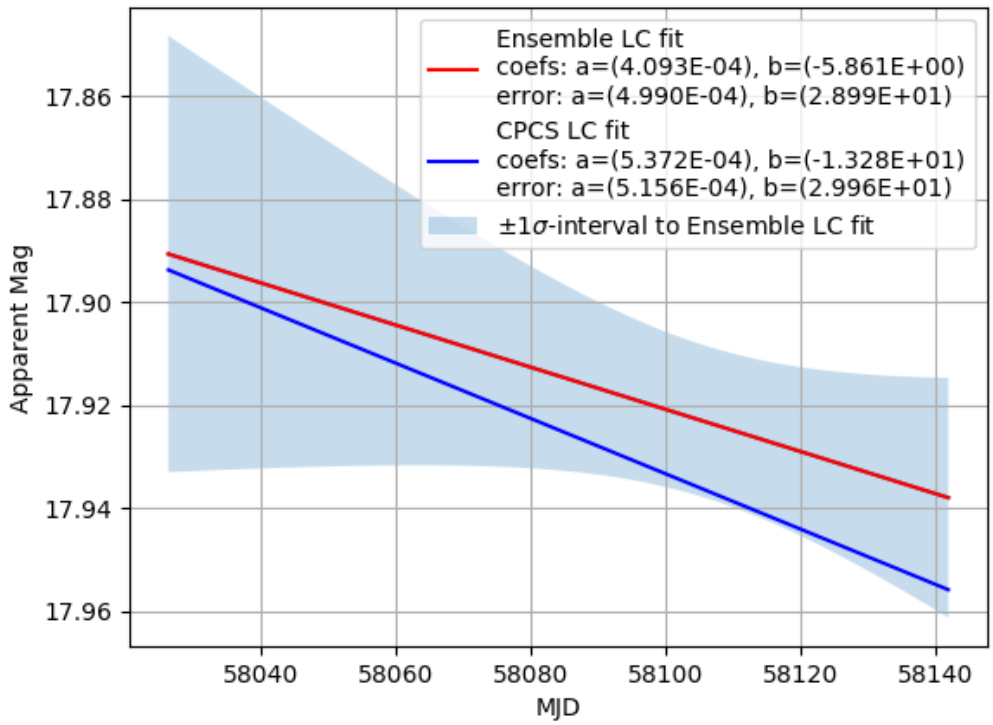

Figure 46: The Gaia17bts R filter fits and the uncertainty associated with the ensemble light curve fit

targets, where the fit to the CPCS light curve falls within the $\pm 1\sigma$ uncertainty band of the EPP light curve, apart for Gaia18arn through the Johnson B filter.

Figure 47 shows the fitting for the Gaia18arn B data. Although the two fits do both decline in brightness over the course of the observations, the CPCS fit appears to decline by 0.4 mag, whereas the ensemble fit only appears to decline by 0.08 mag. Clearly there is something different about this set of data.

By looking at the two light curves in figure 48 we can see that the two methods have given similar results except for the first few data points where the CPCS has calculated the target to be slightly brighter than the EPP. This difference in the first few data points of this target are significant enough that the two models for the Johnson B filter are also significantly different from one another.

The data shown in 48 is at about at the limit of what PIRATE is capable of measuring with much accuracy, and it is likely that the uncertainties displayed are underestimates. Without the first few discrepant data points the fits would likely have been significantly closer. Given more time it would perhaps have been beneficial to investigate those few frames more closely to attempt to uncover the reason for the difference, however given how close the data are to the noise limit such an investigation

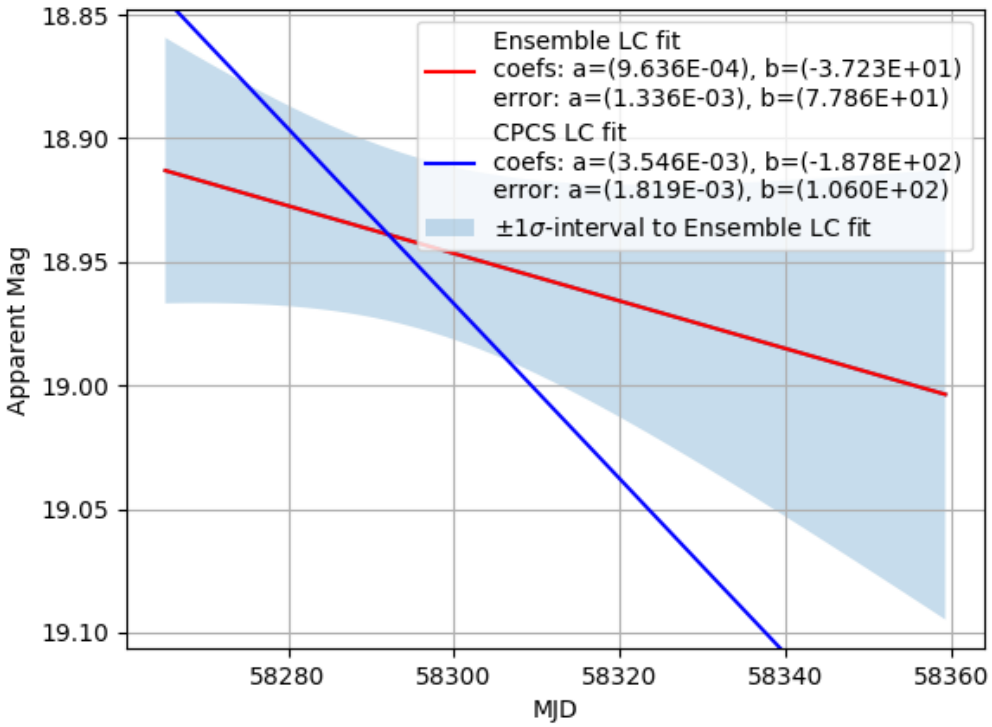

Figure 47: The Gaia18arn B filter fits and the uncertainty associated with the ensemble light curve fit.

may be questionable, and the time spent would probably be better spent elsewhere.

6.3 Assessing Light Curve Quality

Using the model fits calculated in the previous section, the RMS for the three light curves in the three filters each was calculated using

$$RMS_{fit} = \sqrt{\frac{1}{N}\sum_{i}^{N}(x_i - x_{fit})^2} \tag{27}$$

where x_i is the magnitude of the i^{th} observation, x_{fit} is the value of the model fit at the same modified Julian date as x_i, and N is the number of observations. Table 7 gives all of the RMS values calculated.

In general there is only a very small difference in the RMS of the two methods with the exception of the Gaia18arn B data.

At first glance it is tempting to say that the result of this testing would be that the EPP and CPCS are practically indistinguishable, and that both should be suitable for the monitoring of variable stars. Unfortunately the lack of suitable further samples which fit the necessary criteria for the test limits how useful the result can be, and the

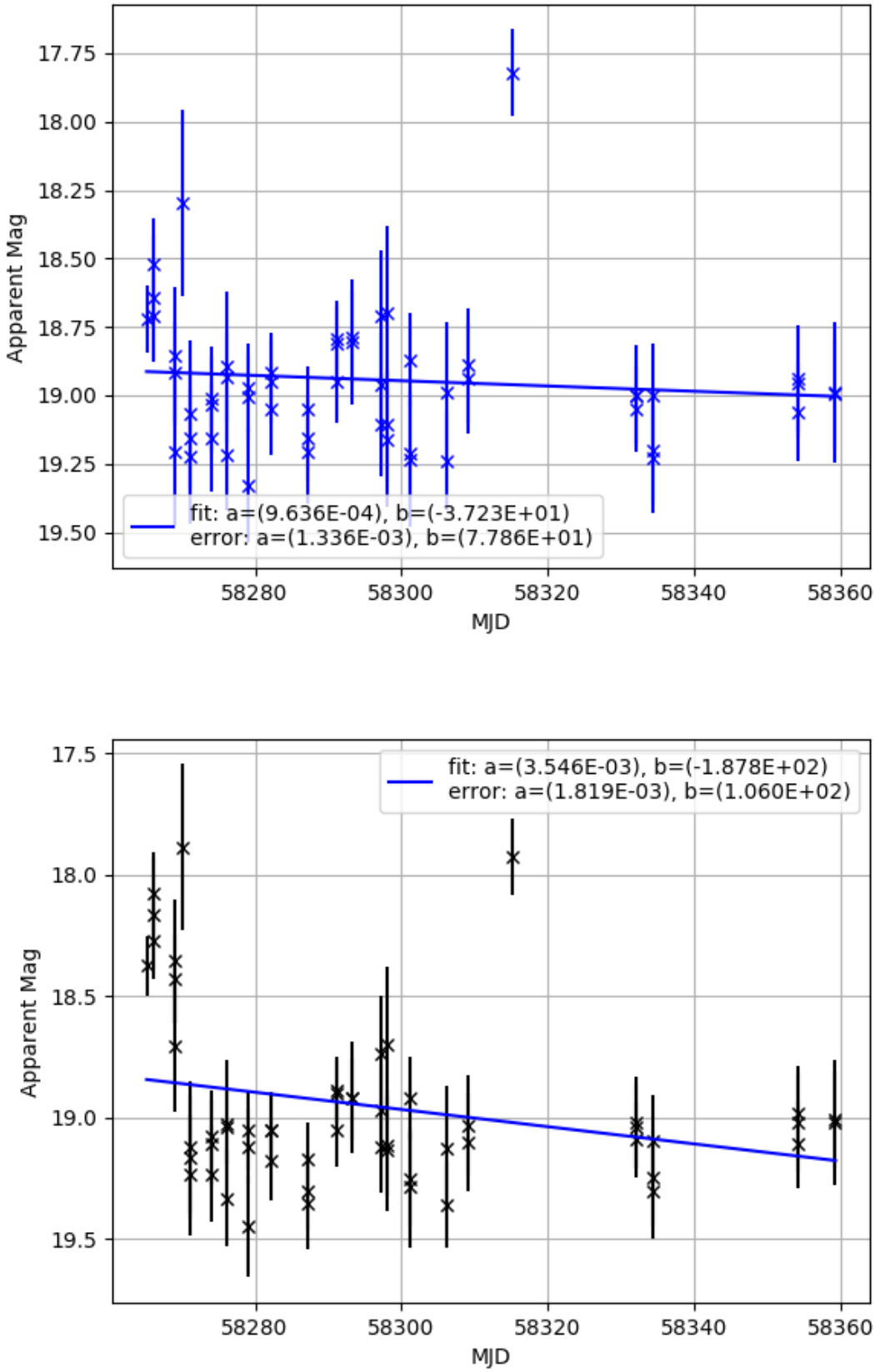

Figure 48: The top figure is the EPP light curve for Gaia18arn in the Johnson B filter and the bottom is the CPCS light curve of the same data. Both have been fit with a linear function using a least squares method.

Johnson B result implies that the findings here need to be treated as preliminary, and further tests are desirable.

Ideally the same test needs to be performed on more targets in every filter, both for flat light curves and varying light curves. In particular the Johnson B test needs to be repeated more rigorously, and the discrepancy needs to be investigated further.

Despite concerns, a decision on which method to rely on for the majority of the light curve discussion needs to be made. So I will suggest that the results at least do not highlight one method to be superior to the other, and so I must find other reasons to select a method going forward.

I have chosen to use the EPP light curves and only use CPCS light curves to magnitude calibrate the EPP light curves where available. This is primarily because the CPCS does not take into account source extractor flags, which may indicate if the target star is blended or saturated. Additionally there are more targets which failed to produce a CPCS light curve than there are targets which failed to produce an EPP light curve. There will be some circumstances where the EPP does not generate a light curve and the CPCS will. In those circumstances CPCS light curves will be considered with the understanding that the results may differ slightly from what might be seen from an EPP light curve.

Target	**Filter**	**EPP LC RMS**	**CPCS LC RMS**
Gaia17bts (Flat)	**R**	0.175	0.178
	G	0.205	0.206
	B	0.243	0.251
Gaia17bts (Decline)	**R**	0.175	0.174
	G	0.175	0.175
	B	0.218	0.218
Gaia18arn	**R**	0.0836	0.0797
	V	0.128	0.128
	B	0.247	0.344

Table 7: RMS values calculated for Gaia17bts and Gaia18arn when compared to the models fit previously.

7 Gaia16aye

Gaia16aye is the name given to a microlensing event which was recognised as variable by the Gaia alerts pipeline for the first time on 05/08/2016 when a new data point from Gaia for the target was shown to be 1.2 magnitudes brighter in the Gaia G filter than most recent previous data point captured on 20/06/2016, which was consistent with all previous data points taken by Gaia for the target. The alert for the target was first published on the Gaia alerts website on 09/08/2016 and the first ATEL (Bakis et al. 2016) was published on 15/08/2016 which described an achromatically increasing K8-M2 type star, with photometric follow-up carried out by five different telescopes and spectroscopic data collected by two. In fact it had already peaked once before the Gaia alert, and was brightening for the second time in the observations described in that first ATEL (Bakis et al. 2016. By the time of the second ATEL (Wyrzykowski et al. 2016) on Gaia16aye on 19/09/2016 the object was understood to be a binary microlensing event and was reporting on the third brightening event which peaked on the 18th of September.

PIRATE was undergoing commissioning in Tenerife in August 2016 having recently been moved from the old site in Mallorca, but began collecting data on the target as soon as it was capable in early September, which I took over when I started this project in October of 2016.

In the following I will describe binary microlensing, as an extension of section 3.6 where we discussed single-lens microlensing events. Then I will discuss the data collected on Gaia16aye by the astronomy community, and the results which were obtained through the efforts of Lukasz Wyrzykowski and his team in modelling the light curve. Then I will move on to the analysis which was carried out of the target for this project.

7.1 Binary Microlensing

Gaia16aye is a binary microlensing event, which is more complex than the microlensing events described in section 3.6. The additional complication arises from having a lens which is composed of two massive objects, either a binary system with two stars, or a planet orbiting a star, or even a dark stellar remnant such as a black hole or a neutron star orbiting another massive object.

By changing the lens to two point sources A and B, the deflection angle (equation 4) becomes dependent on the positions $\vec{y}_A$, $\vec{y}_B$ of the two masses M_A and M_B in the

lens plane (LPI). Figure 49 is a representation of a binary microlensing situation where the red dashed line represents the path of light which has been emitted by the source as it travels towards the observer.

The deflection angle $\alpha(\vec{y})$ is now linearly dependent on mass and so the deflection can be thought of as single deflection which is a superposition of each deflection caused by one of the masses (Bourassa et al. 1973).

$$\alpha(\vec{y}) = \frac{4G}{c^2}\left(\frac{M_A(\vec{y}-\vec{y}_A)}{(\vec{y}-\vec{y}_A)^2} + \frac{M_B(\vec{y}-\vec{y}_B)}{(\vec{y}-\vec{y}_B)^2}\right) \tag{28}$$

We can find the position of the vector $\vec{\eta}$, using the small angle approximation such that Ω and $\alpha(\vec{y})$ are small, and the small angle approximation $\tan\theta \approx \theta$ holds, along with the following relationships, which can be read from figure 49

$$\tan\Omega = \frac{|\vec{y}|}{D_L}, \quad \tan\Omega = \frac{|\vec{F}|}{D_S}, \quad \tan(\alpha(\vec{y})) = \frac{|\vec{K}|}{D_{LS}}, \quad \vec{\eta} = \vec{F} - \vec{K}$$

we can form a new lens equation.

$$\vec{\eta} = \vec{y}\frac{D_S}{D_L} - \alpha(\vec{y})D_{LS} \tag{29}$$

With the total mass of the lens as $M = M_A + M_B$ the analogous value to the Einstein ring radius becomes

$$\rho = \sqrt{\frac{4GM}{c^2}\frac{D_L D_{LS}}{D_S}} \tag{30}$$

This is the radius of the critical line on which the images of the source would be visible if the source was directly behind the mid point between the two lensing masses (Schneider et al. 1986).

In the case of a binary lens, there is no singular caustic point like with the single lens case. In fact there is an extended caustic closed boundary, any source positions outside the caustic boundary are effectively only lensed by one of the masses due to how small the effect of the second mass is. Any source positions within the caustic boundary are effectively being lensed by both masses creating five images of the source. Crossing the boundary has the same effect as the caustic point in singular microlensing, the source magnification formally diverges in the case of point masses. Because the caustic boundary is closed, if the source crosses the boundary once it must at some point cross out of the boundary again meaning that binary microlensing events peak in pairs.

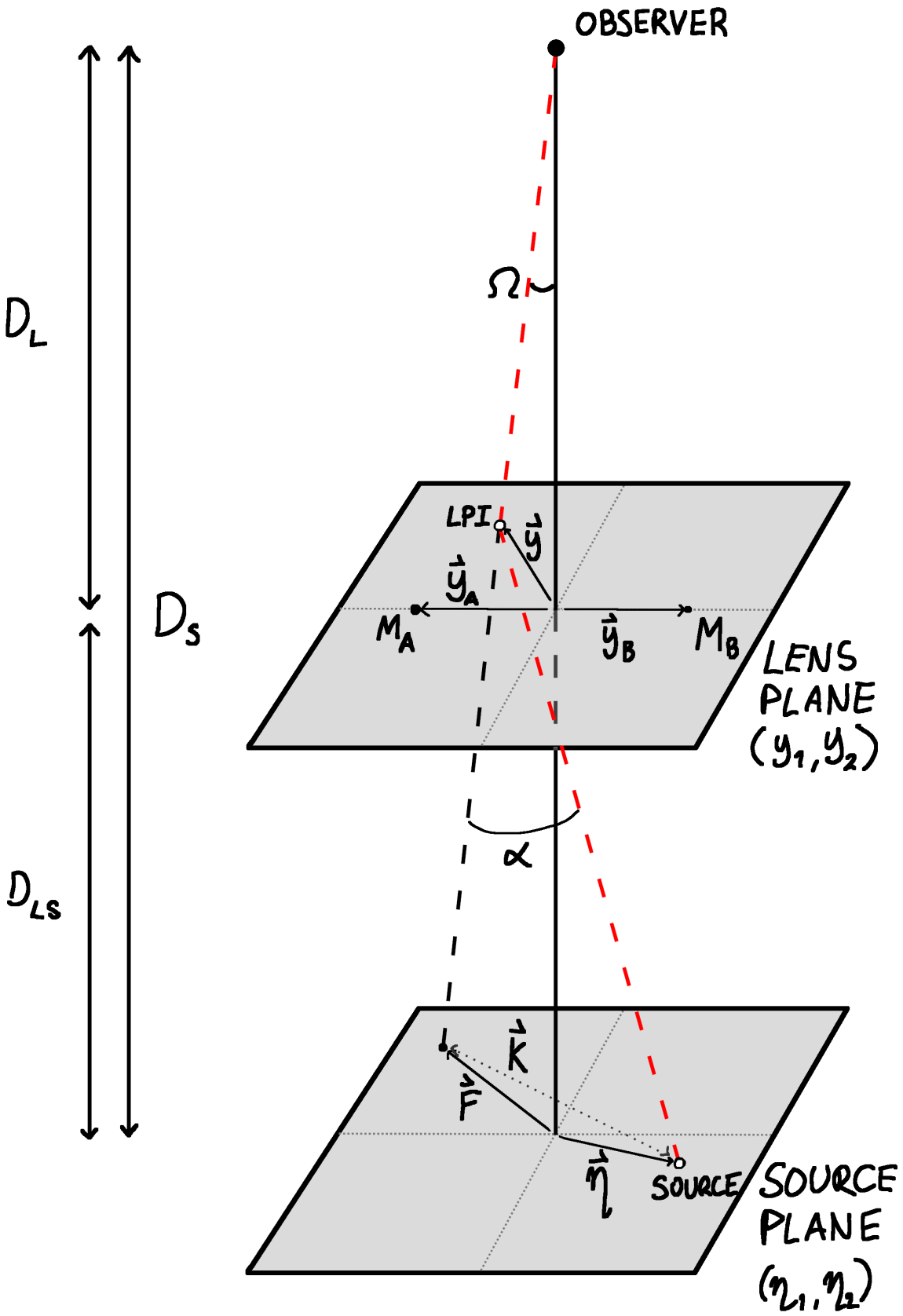

Figure 49: A representation of a binary microlensing system. The grey surfaces represent the lens and source planes, which contain the lensing masses and the source respectively. The red dashed line represents the path of light emitted by the source as it passes close to the lensing masses and is deflected towards the observer. LPI here stands for "Lens Plane Image" and is the image of the source as seen on the lensing plane.

Schneider et al. 1986 discuss in detail the caustics and critical lines of having two point mass lenses of equal mass at different separations relative to their Einstein radius (figure 50).

In figure 50a the separation is greater than the Einstein radius ($d > 1$), the caustics (top half) are very small and any source passing behind the lens will act more like it is being lensed by two separate masses if it passes close enough to both.

In figure 50b the separation is equal to the Einstein radius ($d = 1$), the previously separate caustics are now touching, forming one long caustic region.

In figure 50c the separation is smaller than Einstein radius ($d = 0.5$), the caustics form a familiar shape with 6 cusp points and a relatively large enclosed caustic boundary.

In figure 50d the separation $d = 8^{-0.5} \approx 0.35$, this is where the closeness of the binary system begins to break the caustics into smaller regions again.

In figure 50e the separation $d = 0.3$, here the closeness of the binary system has broken the caustic regions into 3 separate parts causing the binary system to act more like a single lens, as can be seen in the critical lines which are becoming more circular akin to the critical lines of a singular lens system.

The pairs of peaks created by a binary microlens are very distinct and can occur multiple times over the course of an event. The first binary microlensing event OGLE-7 was observed in 1993 by the OGLE team, a magnitude increase of 2 over the course of 60 days. Figure 51 is the OGLE-7 light curve, which serves as an example of a typical binary microlensing event with one pair of caustic crossings (Udalski et al. 1994). The first extrasolar planet detected through microlensing was also achieved by OGLE: OGLE 2003-BLG-235/ MOA 2003-BLG-53 (Bond et al. 2004).

In binary microlensing events there are additional parameters related to the binary nature which must be considered when characterising the light curves: the mass ratio of the lensing masses (q), the separation of the lensing masses relative to the Einstein radius (d), the time of caustic crossing events (t_*), the angular size of the source (ρ_S) and the angle between the line connecting the two masses and the vector the source is following (ϕ). Modelling an event can become very complicated when these are included with the free parameters from a single lensing event: the distance to the lens (D_L), the minimum impact parameter (ξ_{min}), the time of the minimum impact parameter (t_0) and the Einstein ring radius (θ_E) (Alcock et al. 2000).

For protracted events there are other geometric conditions to consider as well. The

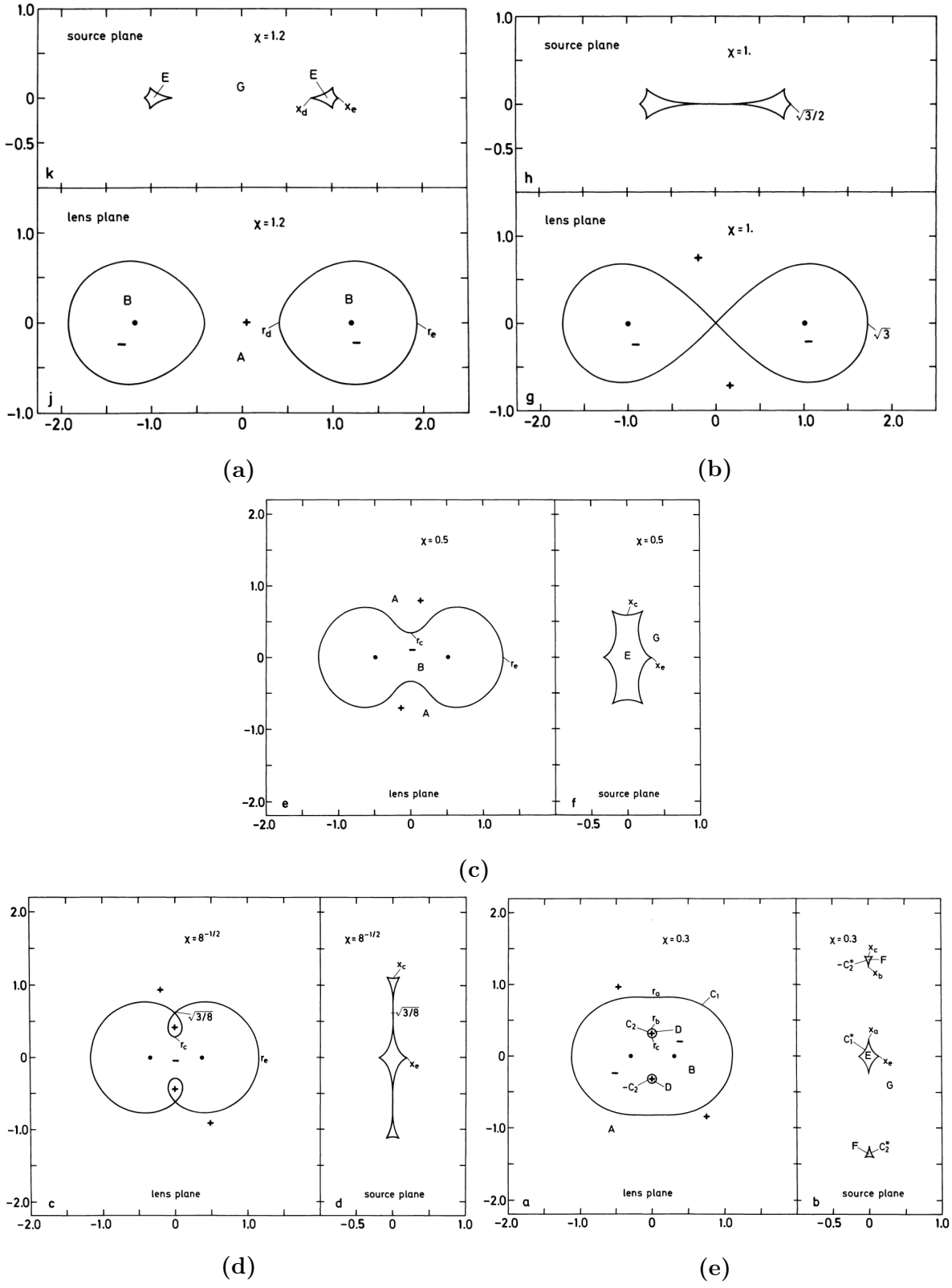

Figure 50: The effect of having two point masses acting as a lens in a binary microlens. From left-to-right and top-to-bottom the two point masses move closer together. The top-half/right-half of each figure represents the caustics and the bottom/left half illustrates the critical lines in the lens plane (Schneider et al. 1986).

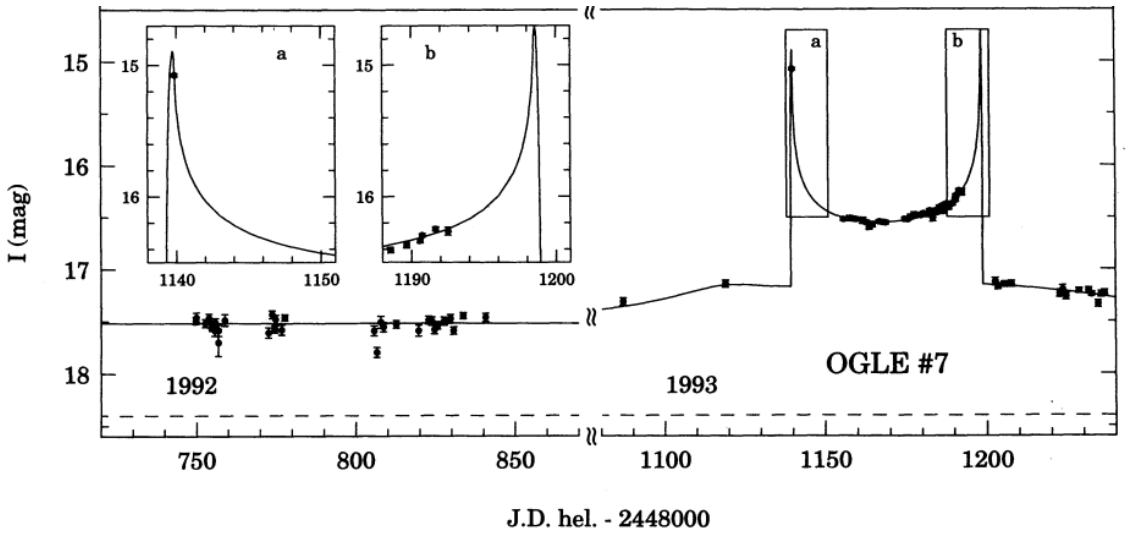

Figure 51: OGLE-7 Binary microlensing event. The solid line represents the best fit binary microlens model (Udalski et al. 1994).

change in parallax of the lens and source due to the orbit of the Earth around the Sun mean that the source and the lens transverse path can no longer be treated as a straight for events which take a significant fraction of the Earth's orbital period. If the orbit of the lensing masses is short enough relative to the total event time, the shape and orientation of the lens, and therefore the caustic boundaries, will also change over the course of the event.

As with the single lens system, the lensing mass is difficult to calculate. It is related to the event timescale t_E, a measurable quantity, but also to the relative lens-source proper motion (μ) and the lens-source parallax (π_{rel}) (Wyrzykowski et al. 2015).

$$t_E = \frac{\sqrt{\kappa M \pi_{rel}}}{\mu_{rel}} \tag{31}$$

But there are two other second order effects which are less difficult to measure in binary microlensing events than single lens events. The first of these deviations are known as finite-source effects and allow the angular Einstein radius (θ_E) to be measured.

In the single lens case, finite source effects can only be measured when the impact parameter distance becomes similar to the size of the source in the source plane, that is to say that the lens appears to cross over the surface of the star. By crossing the surface of the source the point-source approximation no longer holds, and the deviations in the light curve from the point-source model means that the source crossing time (T) can be measured. If the minimum impact parameter distance η_{min}, the event timescale (t_E) and the angular source size (θ_*) are also known then the following equations can

be used to gain the Einstein radius

$$T = 2\sqrt{\rho_*^2 - \eta_{min}^2}t_E, \quad \theta_E = \frac{\theta_*}{\rho_*} \tag{32}$$

where ρ_* is the source radius in units of θ_E.

The likelihood of a source crossing in a single lens event is low when the ratio of source radius to Einstein radius is of order 10^{-3} for main sequence stars, but for binary lens systems the region of space which the lens would need to cross for finite source effects to be measured is extended into the caustic boundary. This means that finite source effects can be measured any time the lens passes a caustic boundary in a binary microlensing event (Nemiroff et al. 1994, Hamolli et al. 2015).

Microlensing events are geometric events which rely heavily on the position of the observer, the source and the lens. During an event, observations made on Earth will be affected by the orbit of the Earth around the Sun. These effects can only occasionally be observed if they take long enough for the Earth to be in a different position in its orbit, called annual parallax, or by using space based observations using telescopes such as Spitzer which is based in a heliocentric orbit, called space-based parallax. By measuring the difference in two light curves captured by observing a lensing event simultaneously from Earth and from a heliocentric orbit we can calculate the microlens parallax (π_E) (Gould 1992, Gould 1994).

These two observables can be used to then calculate the mass of the lens (Wyrzykowski et al. 2020).

$$M = (\frac{c^2}{4G})\frac{\theta_E}{\pi_E} \tag{33}$$

Mao et al. 1991 estimated, based on the observed number of stars which appear to be binary stars, and the likelihood of the distance between the lensing binary being close to the Einstein radius for the system, that around 10% of stellar microlensing events observed towards the galactic bulge would be due to binary star lenses.

The first detection of a binary microlensing event towards the galactic bulge was observed by the Optical Gravitational Lensing Experiment (OGLE) and reported in Udalski et al. 1994. By looking towards the bulge of the galaxy as opposed to the disk, the number of potential sources and lensing objects is much greater, so it is perhaps unsurprising that the first binary microlensing event discovered in the disk of the galaxy wasn't reported on till Rahal et al. 2009 (GSA14), and even then it was too poorly sampled to analyse significantly.

7.2 Gaia16aye Observations and Modelling

This section is primarily a summary of the information in Wyrzykowski et al. 2020. During this project PIRATE collected a lot of data on Gaia16aye, which was uploaded to the CPCS and collected with other community data, and it is important to include the details from that paper here for further discussion.

The Gaia16aye source star is located in the northern part of the galactic plane, and was discovered to be varying by the Gaia satellite and the alerts team in early August 2016. After the initial identification and over the course of more than 600 nights, more than 25,000 photometric measurements in five passbands, and more than 20 spectra were obtained of the target by 63 different telescopes. All of the raw photometric data collected by the collaboration of telescopes were processed by the individual observer, then catalogues for each image were uploaded to the Cambridge Photometetric Calibration Server described in section 4.3 where the data could be collated into one light curve, see figure 52.

Figure 52 demonstrates some of the typical features of a binary microlensing light curve, at least 3 large peaks are visible which correspond to caustic crossings. Normally caustic crossings have to occur in pairs, and this event is no exception, the first crossing event was before the event was picked up by Gaia. As well as the caustic peaks, between the peaks the star stays brighter than its usual background level, also typical of binary microlensing events. There is a fifth event around 200 days after the fourth crossing; this is a near miss of the caustic boundary. The source star got close to the caustic boundary a fifth time, but didn't cross it.

Gaia is positioned at the L2 Lagrange point, placing it 0.01AU from the Earth, meaning space parallax could be observed for the target. The difference in magnification between the satellite and ground based observatories provides one component of the microlensing parallax, and the difference in timing of a peak provides the other component. Taken together the microlensing parallax can be used to account for the relative motion of the source and lens, since in an event which lasts a few months or more, the orbit of the Earth needs to be accounted for.

The orbital motion of the lens had to be given full Keplerian modelling, and a Monte Carlo Markov Chain method was used to calculate a best fit for all the necessary parameters (Figure 53). To limit the amount of computing time necessary to calculate the model, only a limited set of data was used from a few observatories. That data was also binned by the day except for at crucial points like crossing events.

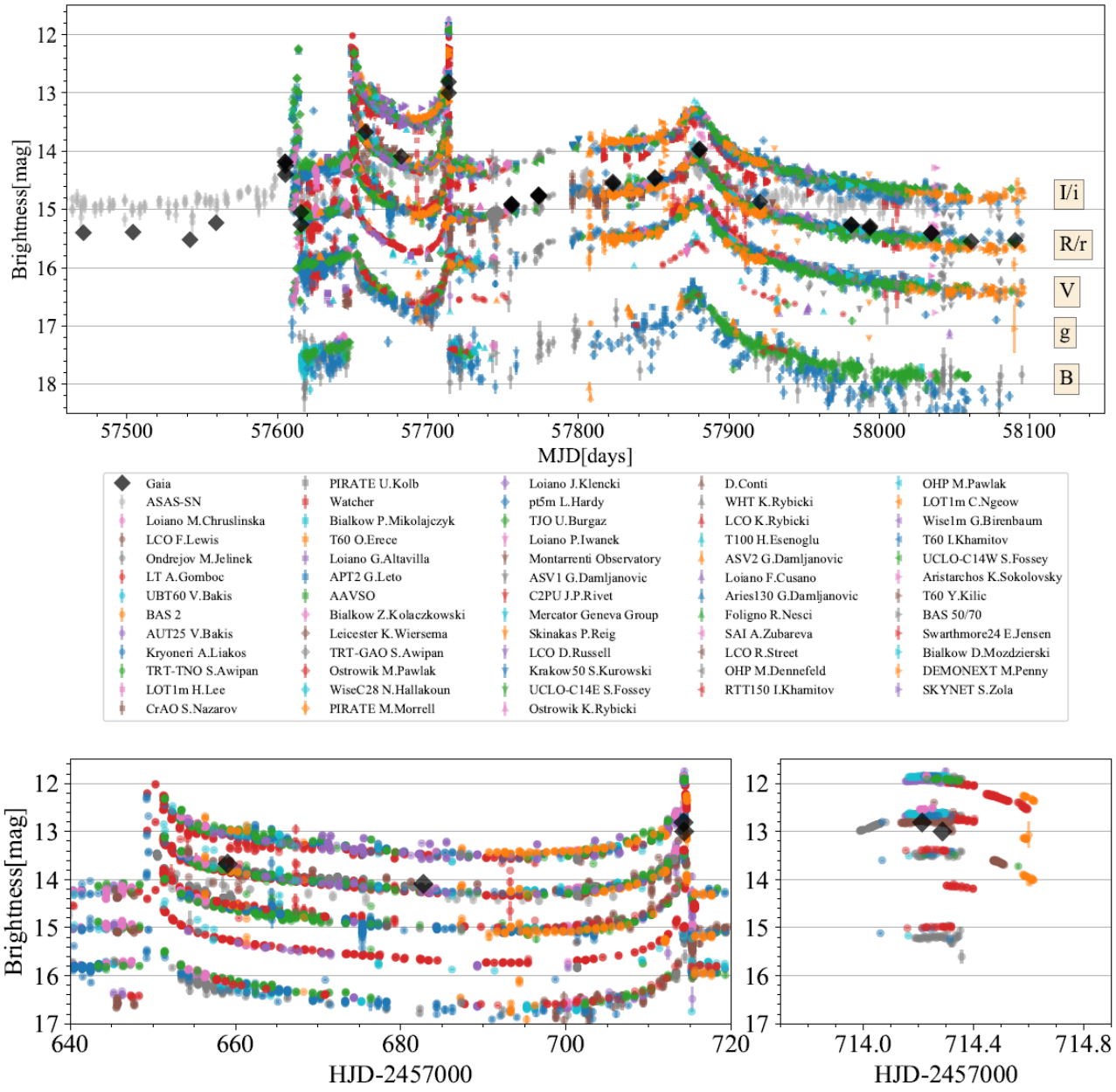

Figure 52: The collection of 25,000+ photometric data points collected by 63 observers of Gaia16aye. The top plot shows the overall light curve, the bottom left shows the third and fourth caustic crossing events, and the bottom right shows just the data collected when the fourth caustic crossing occurred. Data collected by PIRATE is labelled as "PIRATE U.Kolb" and "PIRATE M.Morrell" as I initially uploaded data to the calibration server using my supervisor's account before getting my own account (Wyrzykowski et al. 2020).

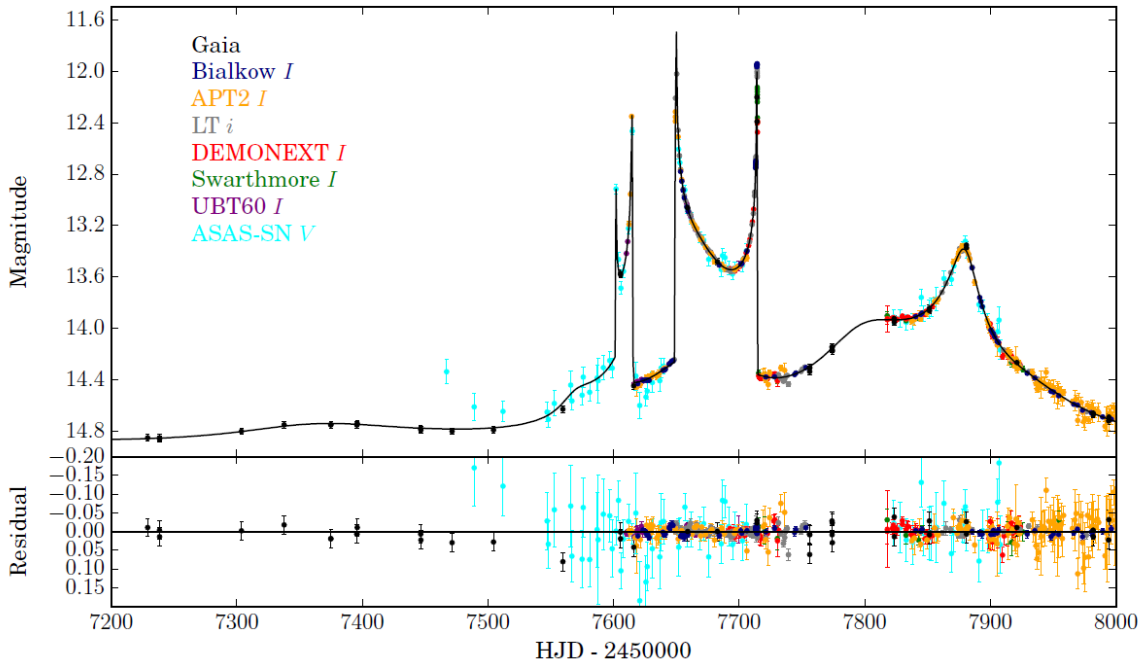

Figure 53: The final model light curve for Gaia16aye created by Wyrzykowski's team. The insert shows the trajectory of Earth and Gaia during the caustic crossing event around HJD'=7714 (Wyrzykowski et al. 2020).

Parameter	**Parameter Description**	**Value**
θ_E (mas)	Einstein ring radius	3.04 ± 0.24
μ_{rel} (mas/yr)	Relative source-lens parallax	10.1 ± 0.8
M_A ($M_\odot$)	Mass of lens component A	0.57 ± 0.05
M_B ($M_\odot$)	Mass of lens component B	0.36 ± 0.03
D_l (kpc)	Distance between observer and the lens	0.78 ± 0.06
ρ_S (μas)	Angular radius of the source	9.2 ± 0.7
D_S (kpc)	Distance between observer and the source	15.7 ± 3.0

Table 8: Gaia16aye model parameters (Wyrzykowski et al. 2020).

Spectra obtained at various points in the light curve by several different observatories maintained similar features, implying that the light being received for the spectra was primarily from the source star, with low lens contribution. They also indicated that the source is a K5-type giant or supergiant. The physical results gained from the model about the system are listed in table 8.

The final model for the source-lens motion due to microlens parallax, and caustic changes due to the orbit of the lens stars is shown in figure 54. The coloured curves represent the shape of the caustic boundary which is a consequence of the lensing pair.

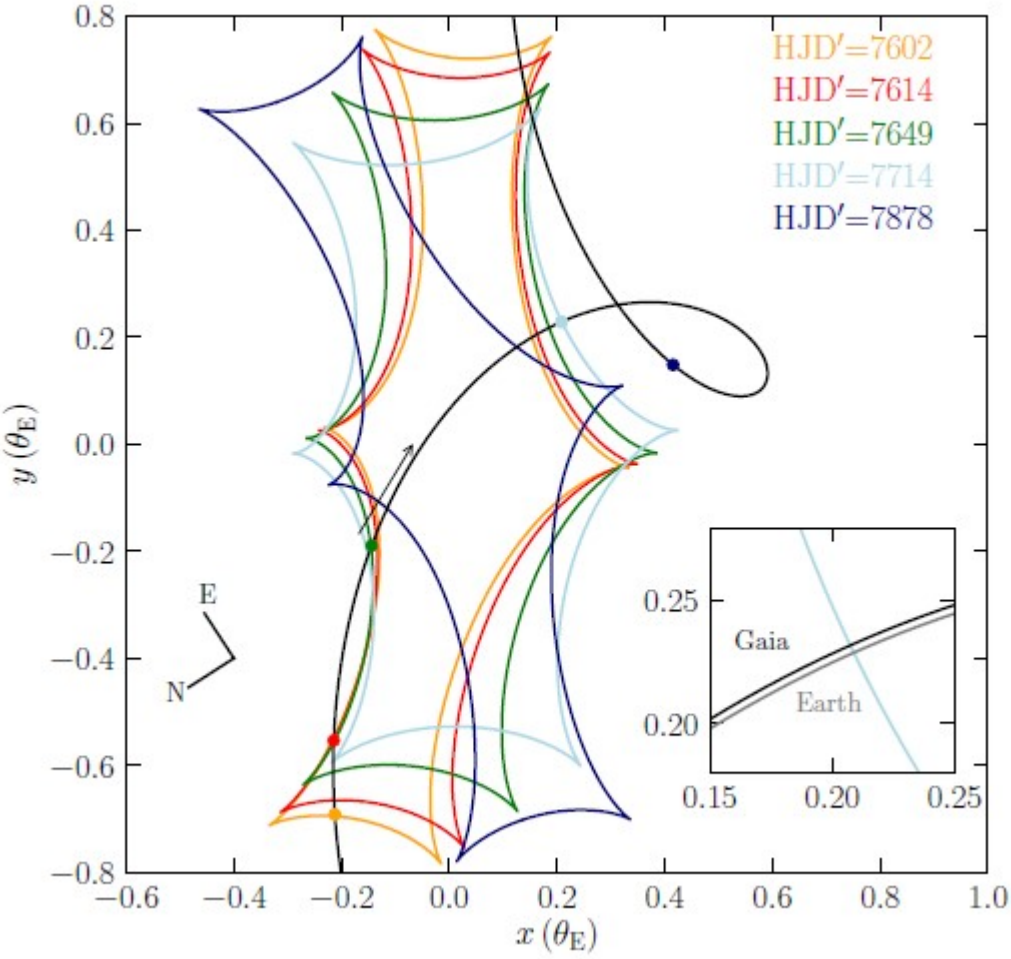

Figure 54: The final model orbital motion for Gaia16aye created by Wyrzykowski's team (Wyrzykowski et al. 2020).

The different colours represent the position of the caustic on modified Heliocentric Julian Dates ($HJD' \equiv HJD - 2450000.0$) when a caustic crossing occurred. The black line represents the path the source appears to take relative to the caustics, with the coloured points representing where a crossing event occurred, and the black point representing the near-miss event when the source approached a caustic cusp but didn't cross it.

7.3 PIRATE Gaia16aye Data

PIRATE started collecting data on Gaia16aye in early September 2016, having only been commissioned in August of that year. Presented here is the data collected between May 2017 and January 2019. Commissioning issues and a faulty camera shutter meant data collected between September 2016 and May 2017 was difficult and time consuming to reduce, or unreliable. It was deemed better to spend time elsewhere than trying to get this early data to a place where it might become useful. Over 2200 images

were collected, initially across the three Baader filters R, G and B, and then after 20/05/2018 the filters on PIRATE were changed to Johnson R, V and B. Figure 55 shows the PIRATE data which was uploaded to the CPCS for analysis displayed in colour, in context with the data collected by the other telescopes listed in figure 52, here shown in grey. The square data points are Gaia satellite data. The black vertical line indicates the change of filters and demonstrates the difference between the Baader and Johnson filters, which is clearest in the difference between Baader B and Johnson B.

The same data was also analysed using the EPP detailed in section 5.2.2. The main benefit of the CPCS over the EPP is that it effectively achieves absolute photometry, rather than the differential photometry which the EPP performs. The data from the EPP needs to be calibrated to the same magnitude as the CPCS data. This calibration was performed as described for Gaia17bts and Gaia18arn in section 6.

Figure 56 shows the two methods plotted together, with the CPCS data in black and the EPP data in colour. We can see that the overall shape of the two light curves matches well.

The R data from the CPCS seems to be more spread out, this is what was expected from the EPP, the ensemble photometry method should output light curves which have less spread around the overall shape of the light curve. With the R data it seems to have achieved this, but there doesn't appear to be an appreciable difference in the G and the B data.

Gaia16aye is in a relatively crowded field (figure 57) and in some of the Gaia16aye light curves there are data points which haven't been picked up by both methods. In particular in the R data around MJD 58100 it is clear that some of the black and red data points do not necessarily have counterparts for one another. This is mostly due to the flagging system in source extractor which points out stars which suffer from over saturation or blending if the telescope takes defocussed images and spread the target over a larger area of the chip. The EPP excludes any points which are flagged for such reasons, but CPCS uses a system which doesn't use these flags. It still identifies images which are saturated and saves the data point, represented as triangular points in the collaborative light curves.

Some of the data also appears to dip far below the overall shape of the light curve, after visual inspection of a few frames it becomes clear that these data points have signal to noise for Gaia16aye lower than the surrounding data, which means they are

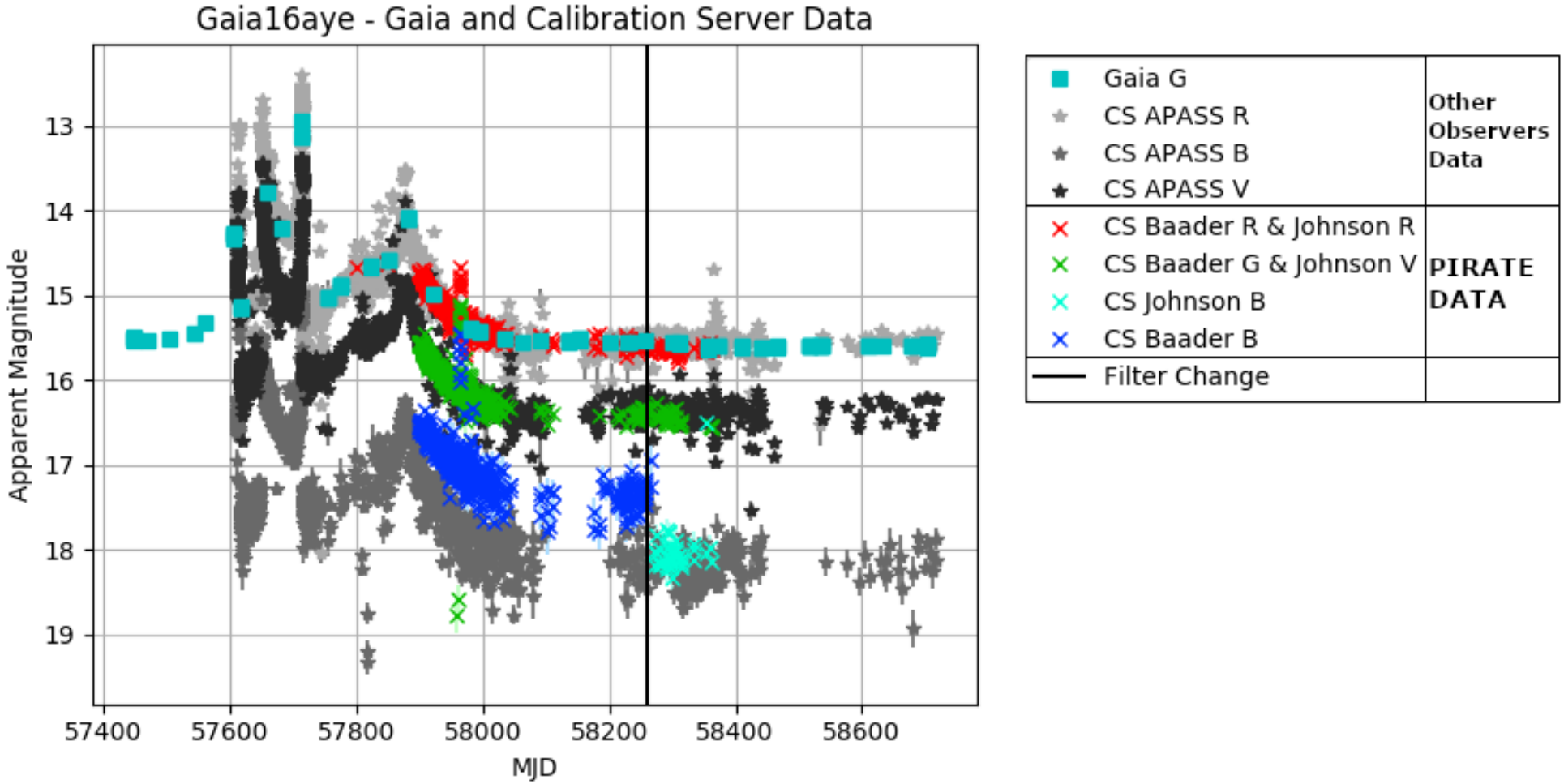

Figure 55: Gaia16aye data collected by PIRATE (red, green, blue and cyan crosses) which was uploaded to the CPCS for photometric calibration, along with the data collected by Gaia (turquoise squares) and data collected by other telescopes which was also uploaded to the CPCS (greyscale stars). The black bar indicates when the filters were changed on PIRATE.

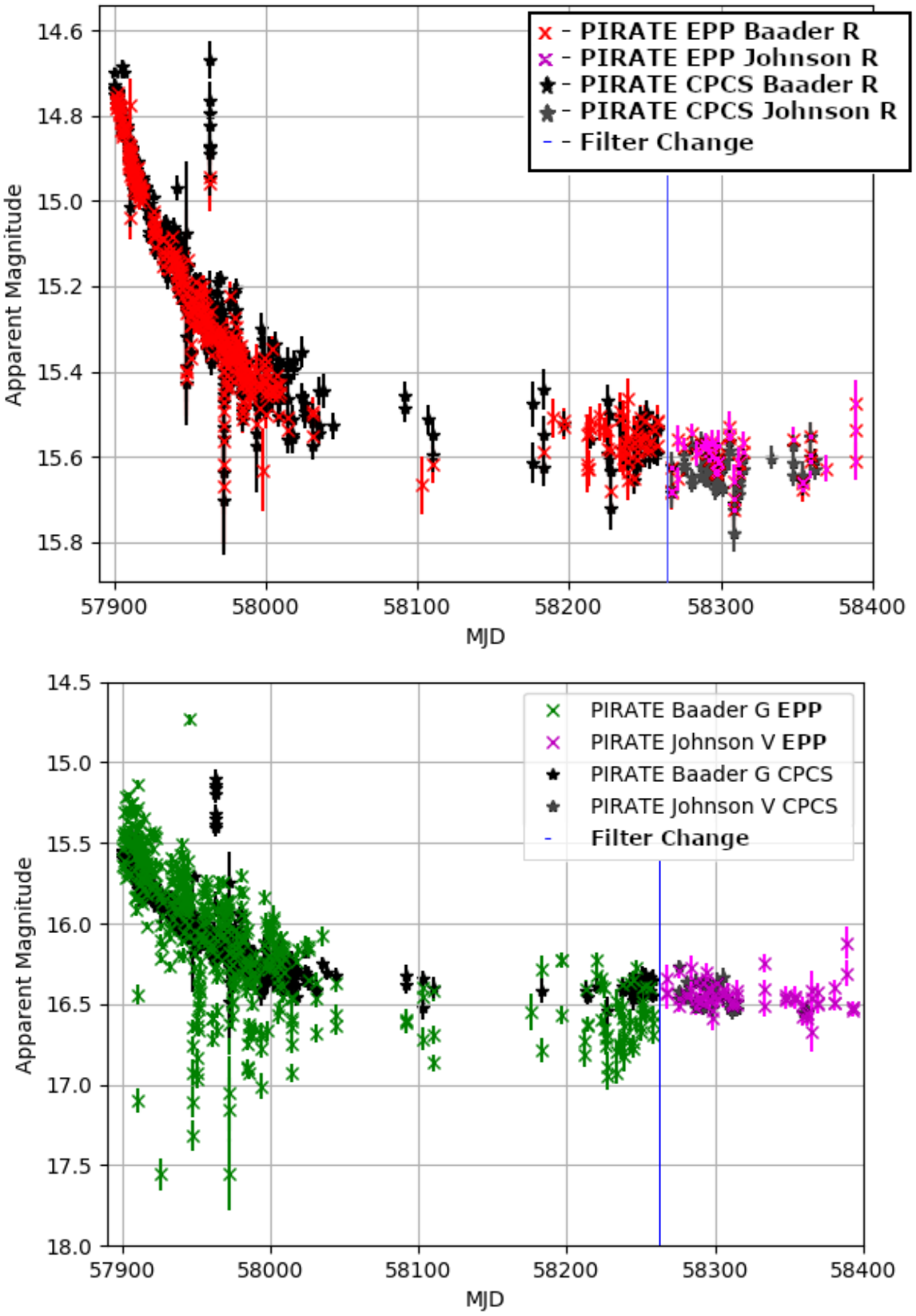

Figure 56: (Continued on the following page)

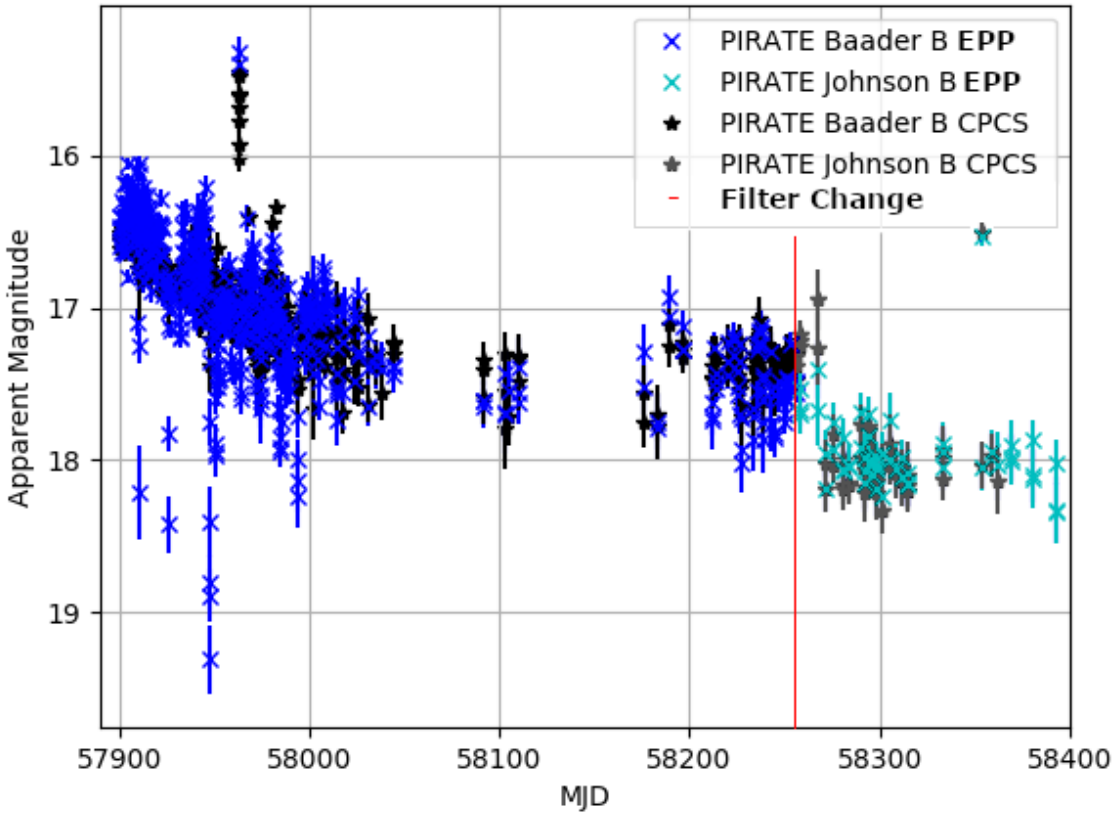

Figure 56: The three figures have the PIRATE data for Gaia16aye both from the EPP and from CPCS. The EPP data has been calibrated to the apparent magnitude scale using the method described in section 6.

only marginal detections, and leads to the larger error bars for these data points than the data which appears to be following the microlensing light curve more closely.

7.4 Gaia16aye Colour Index

The geodesic which a photon follows through spacetime does not depend on the wavelength of the photon, only its velocity, which is the speed of light. This means that gravitational lensing should affect all wavelengths of light in the same way, and that the light curve of a microlensing event should be achromatic - it should be the same at all wavelengths. To test this for Gaia16aye we can calculate the colour of the source star over the course of the event.

The colour of a star is indicated by its colour index. With the apparent magnitude (m) of a star as observed at two different wavelengths we can calculate the colour index (CI).

$$CI = m(\lambda_1) - m(\lambda_2) \tag{34}$$

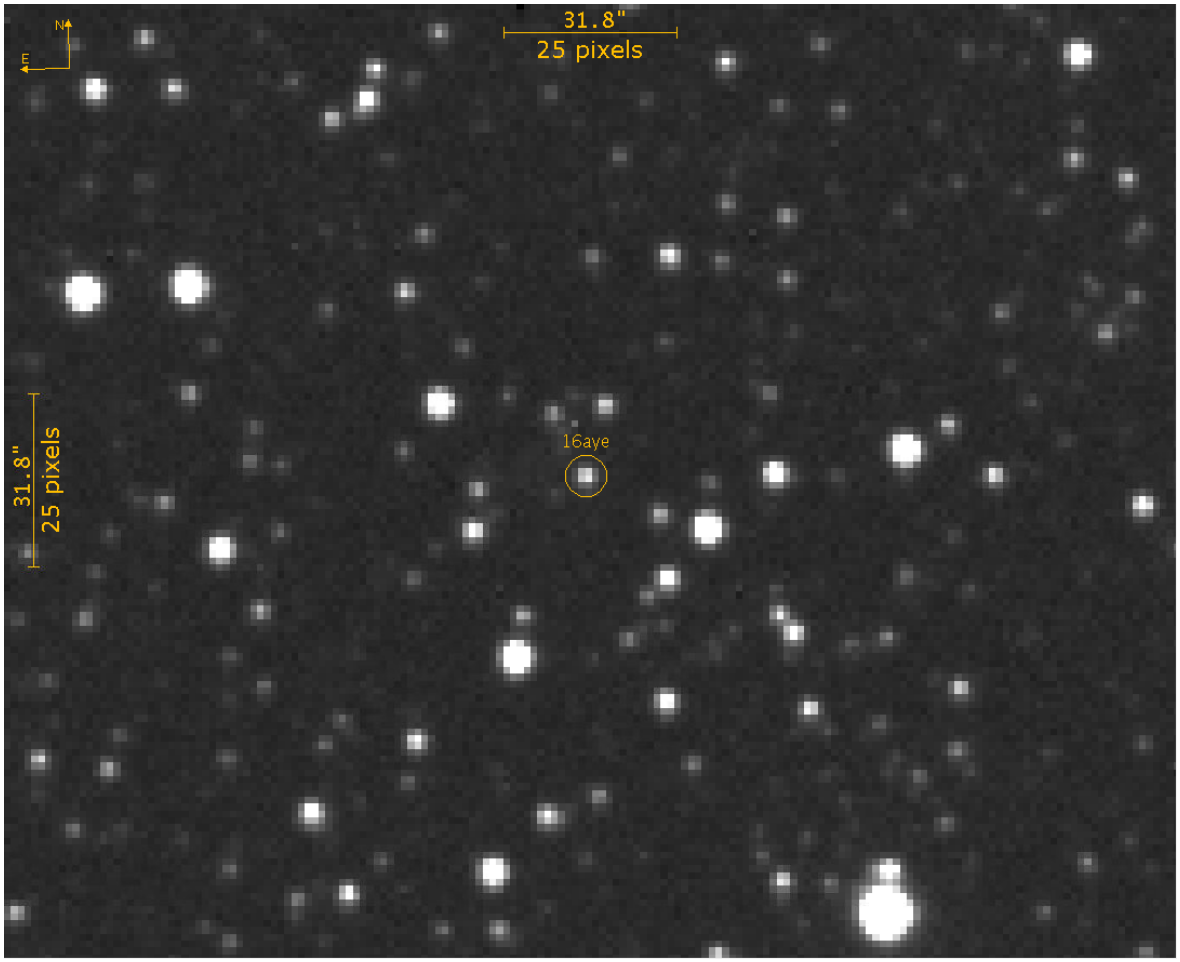

Figure 57: Gaia16aye as imaged by PIRATE through the Baader R filter on 10/08/2017.

Assuming the source star doesn't change colour over the course of the microlensing event, if both wavelengths change at the same rate then the colour index should remain constant. If any variability is seen in the data, or a trend up or down in the data, then it is possible that the source star might be variable in some way.

To check the variation of colour index over time of Gaia16aye, we need data in multiple wavelengths from a single telescope over a long period when the target was still being lensed. The PIRATE data taken between May 2017 and the date of the filter change 20/05/2018 is taken through three different filters, and the target was still being lensed, though it may have reached the end of the event in early 2018.

To calculate the colour index the values for magnitude taken from the CPCS were binned by observing night by taking the average of the magnitude for that night in each filter, with the date set to midnight of the observing night. For each night when the target was observed in a pair of filters, the colour index for those filters was calculated and the results were plotted against time. The pairings G-R, B-R and B-G are shown with the context of the light curve in figure 58, and zoomed into the part of the data where the microlensing is still occurring in figure 61.

At first it was thought that the increasing size of the uncertainty later on could be due to increasing airmass as the target was imaged lower in the sky, but due to the algorithm PIRATE uses to calculate the best time to observe a target during the night, the altitude of the target is highly variable during this period, there is certainly no trend towards lower altitude observations later on as seen in figure 59.

Taking another look at the raw data (figure 60) for this period for other clues to why the measurements become more uncertain later on, it becomes apparent that the increase is due to the decrease in brightness of the target by about 1 magnitude, which equates to a 2.5x decrease in flux.

At first glance of figure 61 it appears that the colour index might be showing some sort of periodic variability in the first half.

Upon investigation this variability appears to have a period of roughly 30 days, and may be due to the increase in sky brightness which comes with the full moon. Figure 62 shows a zoom in of the variable section of the G-R data, along with the sky background for each Baader R image taken during the same period. The same section of the other colour index pairings are also shown in the same figure, and do not appear to show the variability at all.

To investigate this further I binned the sky brightness data in the same method used to create the data for the colour-index calculations, limited the data to just between the ranges visible in figure 62 where the variation is most visible in the colour-index data. I then calculated Pearson's correlation coefficient between the two sets of data to see if they correlate with any statistical significance. A value of 0 would imply no statistical significance to the correlation, while values of +1 and -1 would imply strong statistical significance of correlation or anti-correlation respectively.

The value for Pearson's r calculated was 0.067, which implies that any correlation between the two sets of data is statistically insignificant. As a further investigation into the correlation I plotted the colour-index data vs the sky brightness to see if there is any visually identifiable trends, this is shown in figure 63, where the full data set is plotted above, and a zoom of the plot to the lowest 1000 counts of sky brightness. This does not appear to show any identifiable trends, which backs up the calculated correlation coefficient.

The lack of correlation here means that I cannot be sure what has caused the pattern in the colour-index data. A lack of correlation does not necessarily mean that the pattern is not due to the increased sky brightness when the moon is full, but I

also can not rule out that the pattern is due actual colour variation in one of the stars involved in the microlensing event. This deserves further investigation.

Figure 64 has (G-R) along the x-axis, vs the Baader G magnitude along the y-axis. The plot on the right is just to give an indication of the minimum expected uncertainty for the measurements. The minimum uncertainty for the G magnitudes comes from the noise calculations in section 2.5, and the G-R minimum expected uncertainty is the propagation of the expected errors from section 2.5, where the uncertainty has been propagated using the same equation as for the (G-R) data.

$$\sigma_{(G-R)} = \sqrt{\sigma_G^2 + \sigma_R^2}$$

In this graph we are again looking for variations in colour index, the B filter was excluded as an option for this graph as the B data are the faintest and therefore the noisiest. Over the range of G magnitudes if the colour index G-R does not change we should see a vertical line of data.

I chose to switch the axes on figure 64 and performed a simple linear fitting to see if there is any trend in the data. Figure 65 shows the fitted model $y = 0.054x - 0.33$ that does slope upwards slightly, which may indicate that the G-R colour index changes very slowly with the change in G magnitude. The value for the RMS relative to the fitted model is 0.825, which given that the G-R values only range between approximately 0.70 and 0.95, is a huge RMS value. This means that the linear fit made to the data can not be taken as evidence that the colour index changed over the course of the observations.

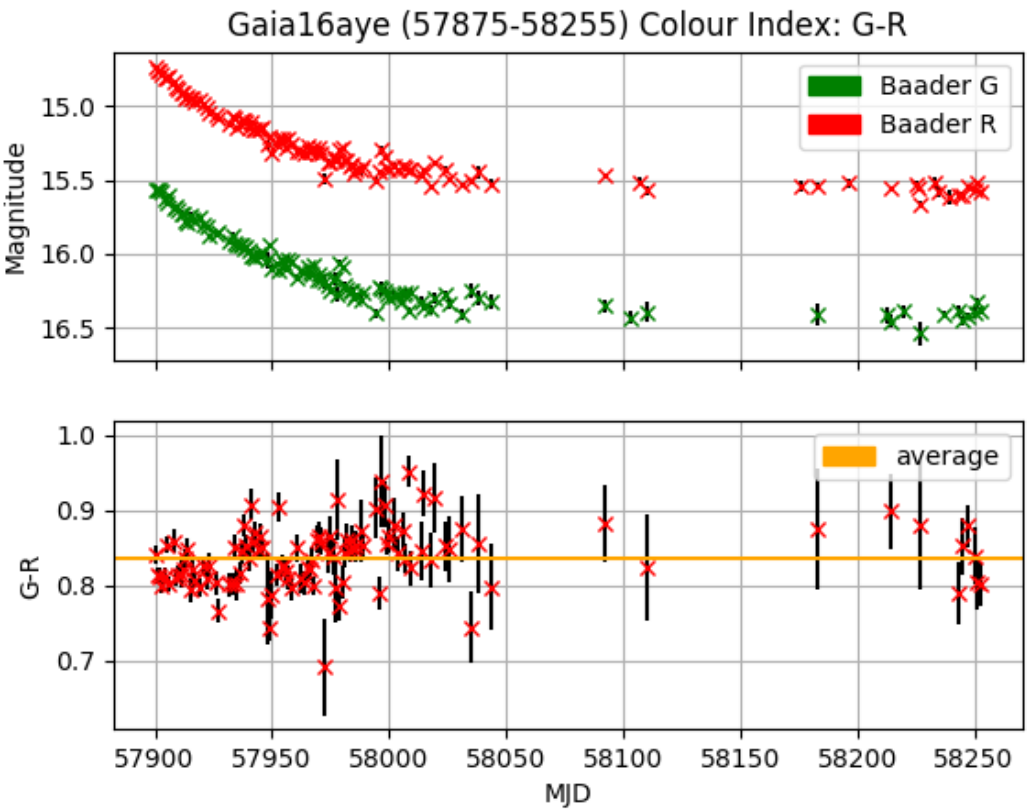

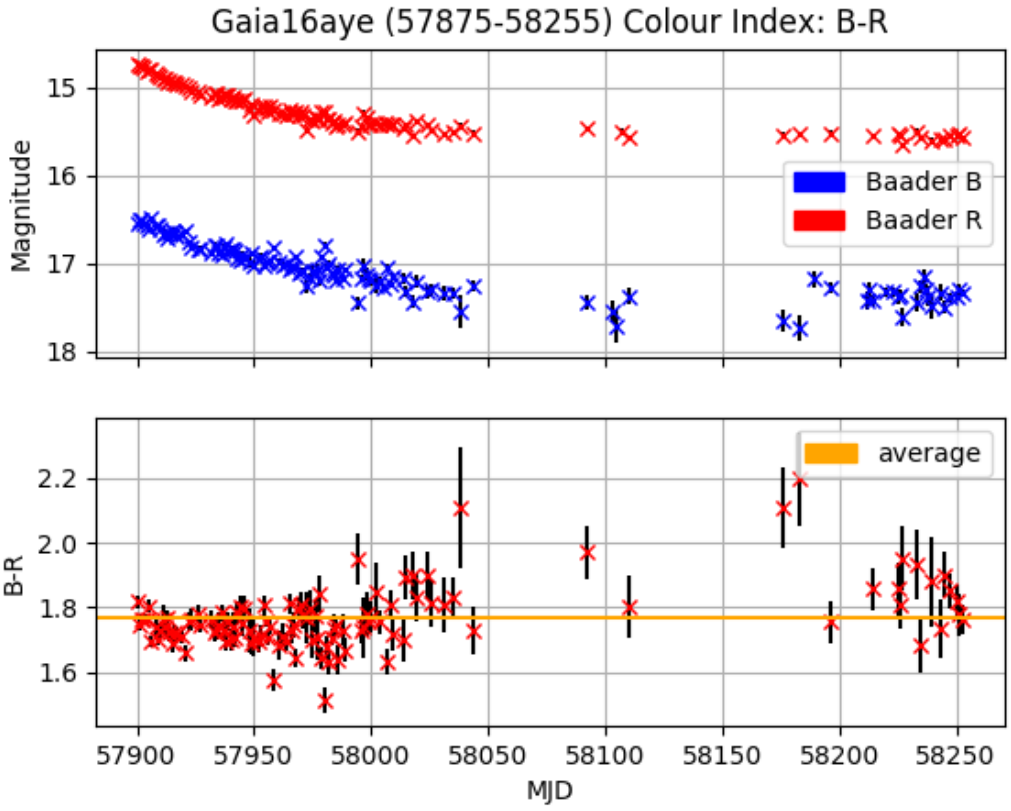

Figure 58: (Continued on the following page)

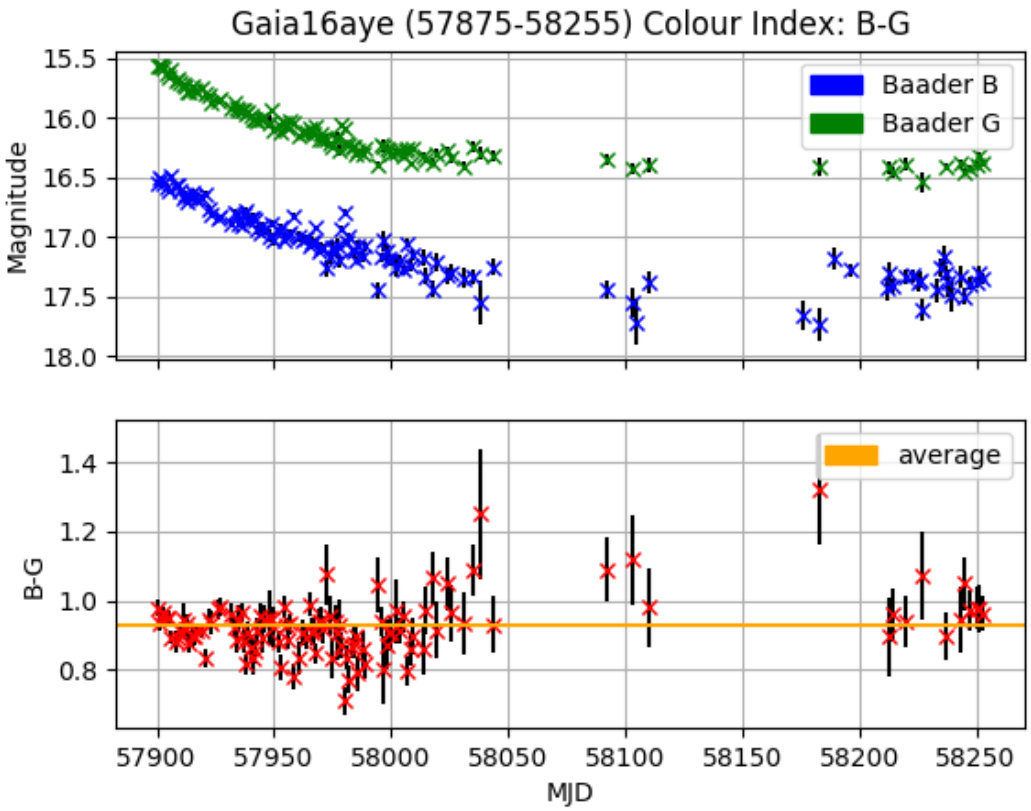

Figure 58: The Colour Index of Gaia16aye between 57875 and 58255 MJD as seen by PIRATE. The top part of each graph shows the light curves for the target over the period, and the bottom shows the CI for the two colours above, along with the average colour for that index in orange. All data was photometrically calibrated using the CPCS.

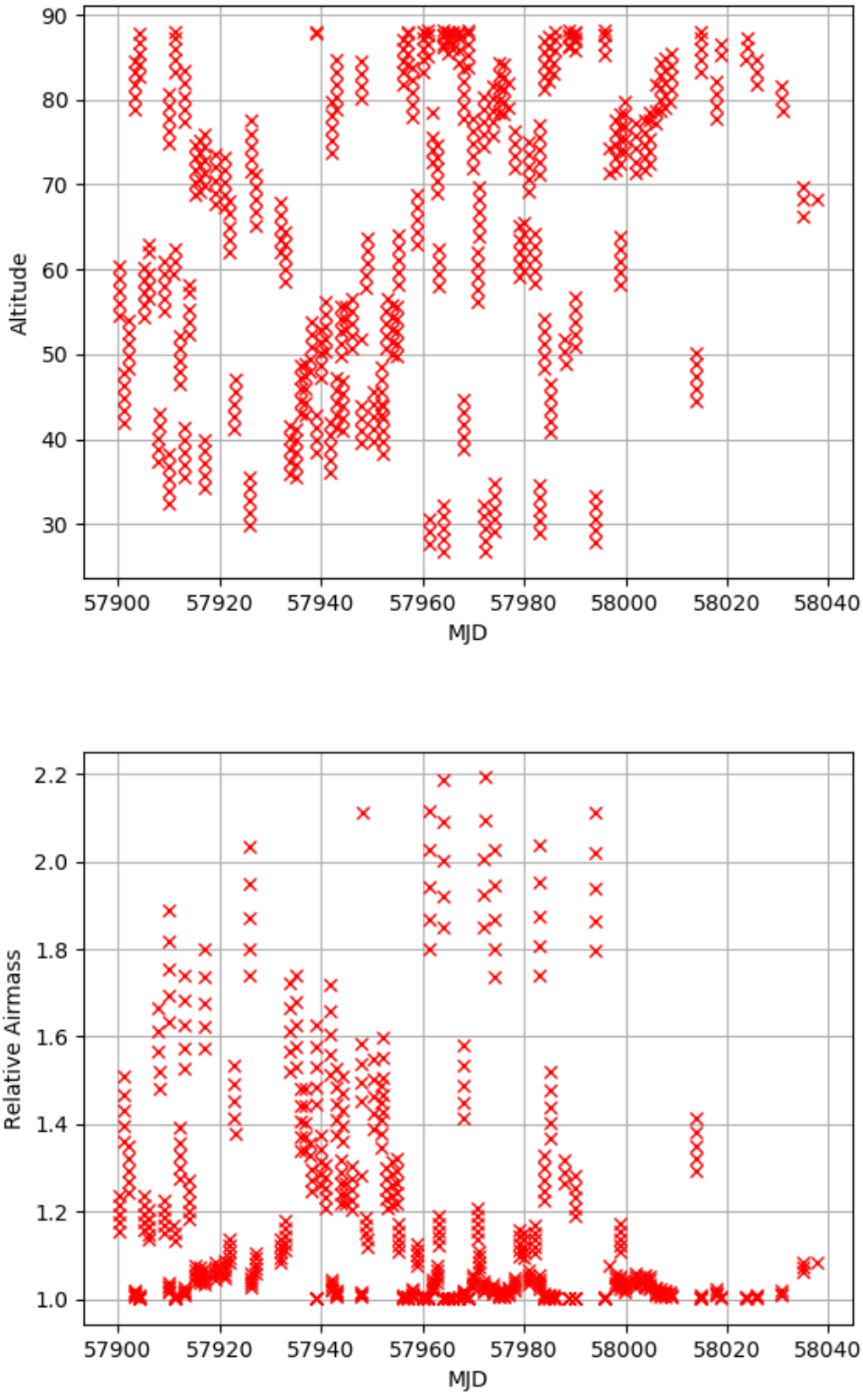

Figure 59: The altitude and airmass of the PIRATE Gaia16aye observations taken during the decline period.

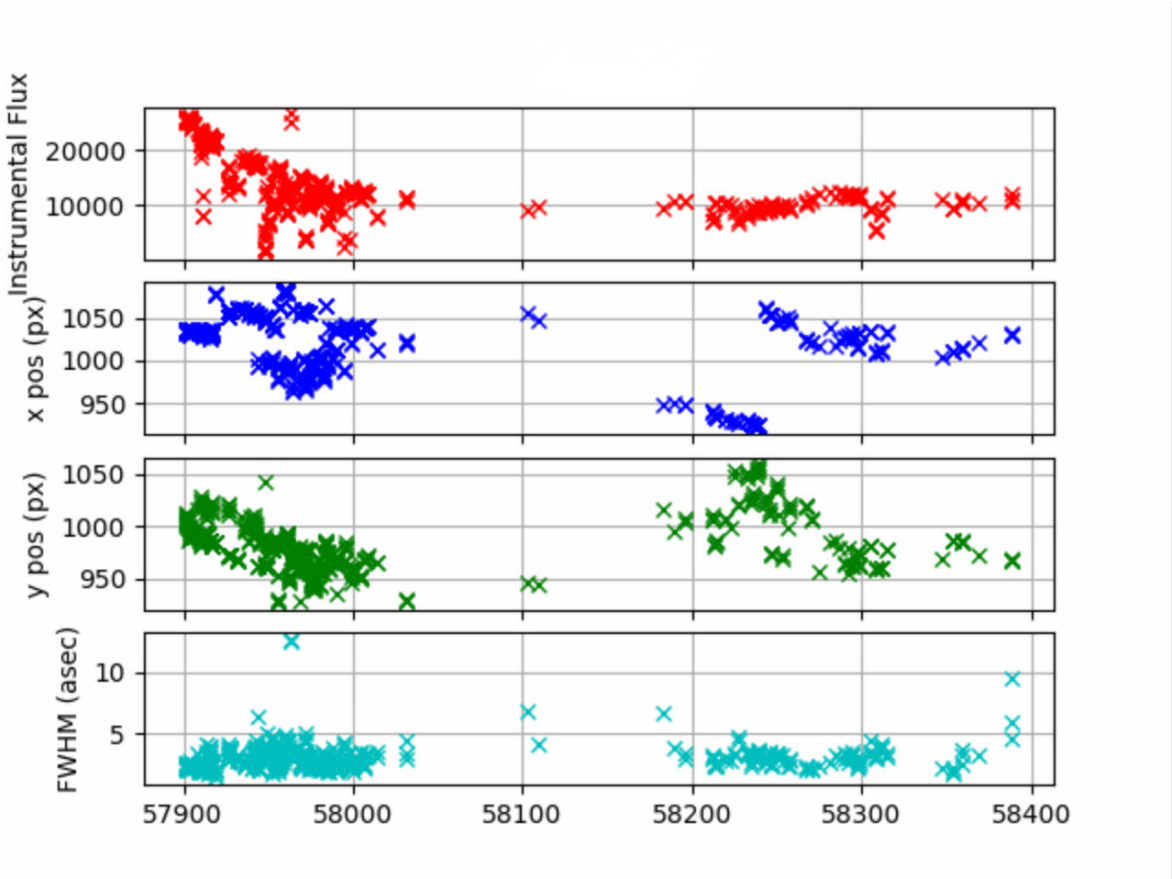

Figure 60: Raw data from the PIRATE observations of Gaia16aye, including the instrumental flux, x & y positions of the target on the CCD and the FWHM of the target. The instrumental flux between MJD 57900 and 58040 decreases from about 25,000 counts to 10,000.

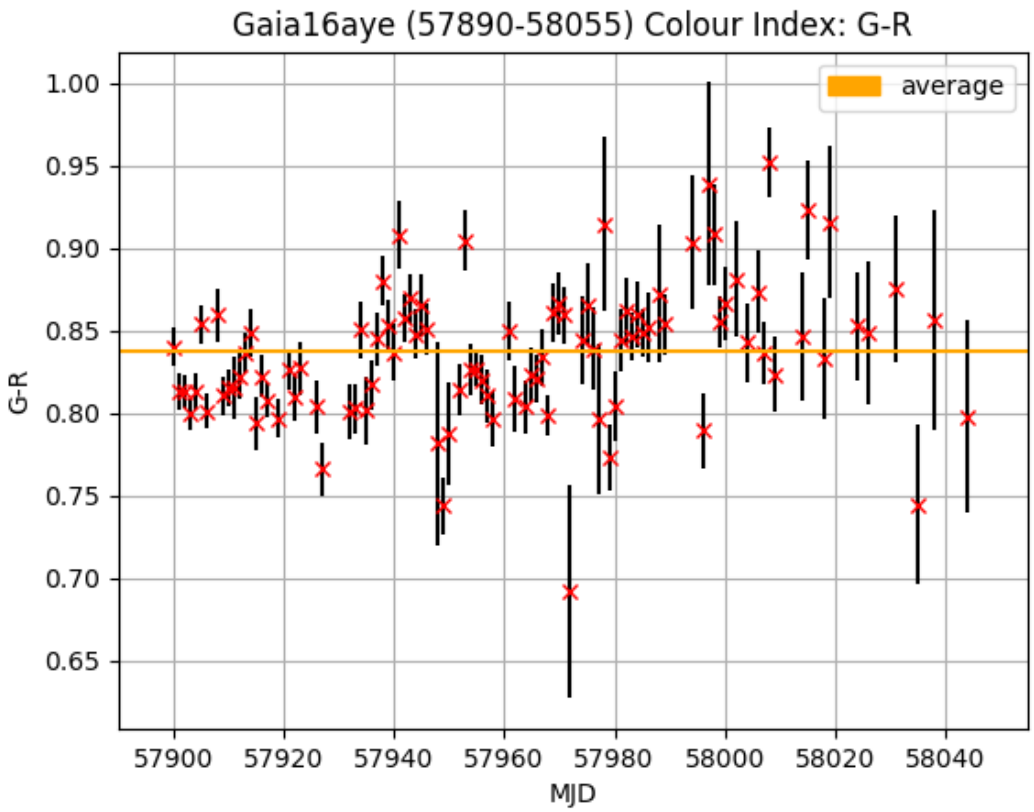

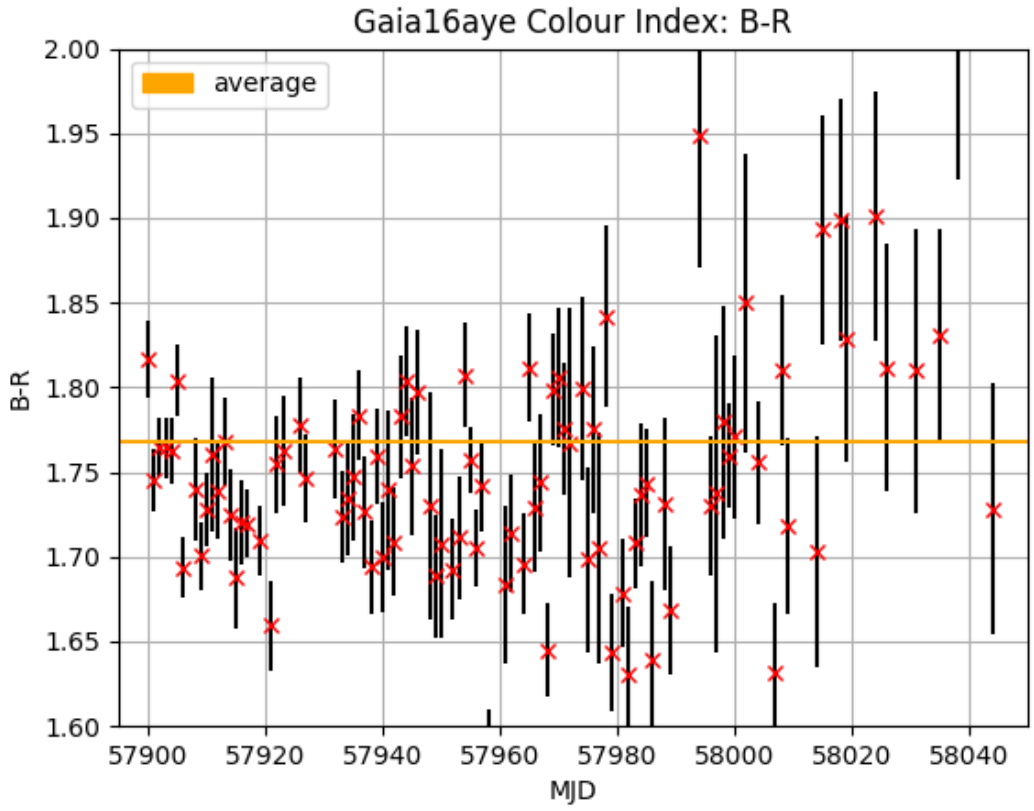

Figure 61: (Continued on the following page)

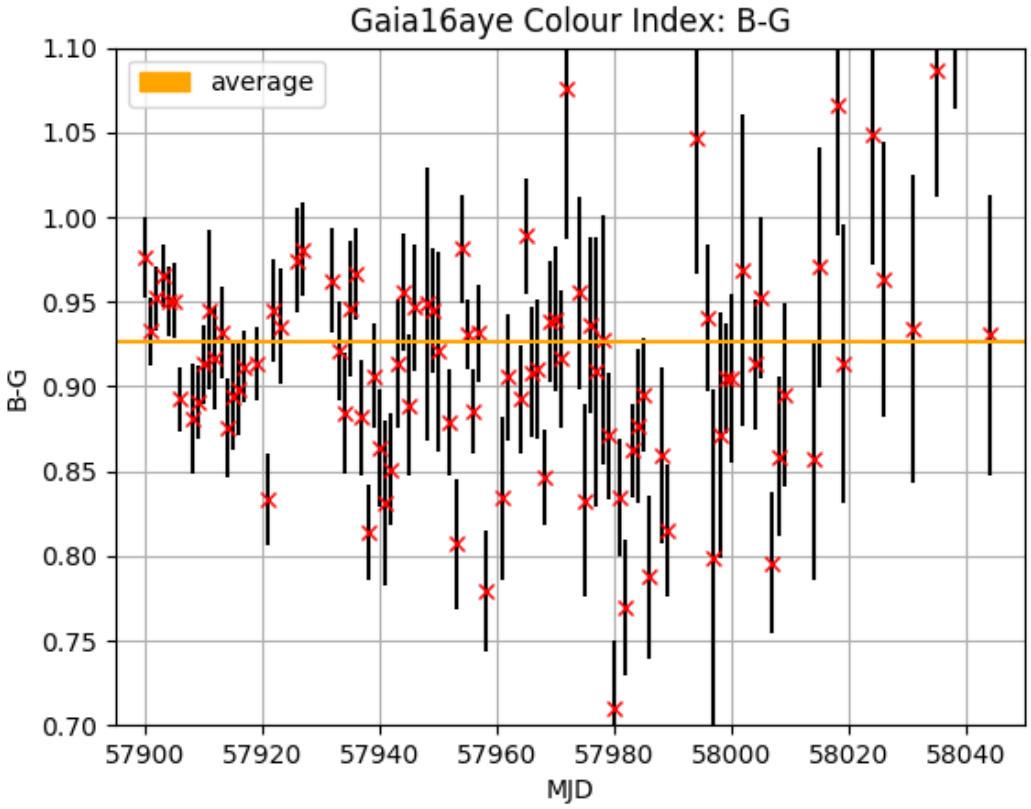

Figure 61: The Colour Index of Gaia16aye between 57890 and 58055 MJD as seen by PIRATE.

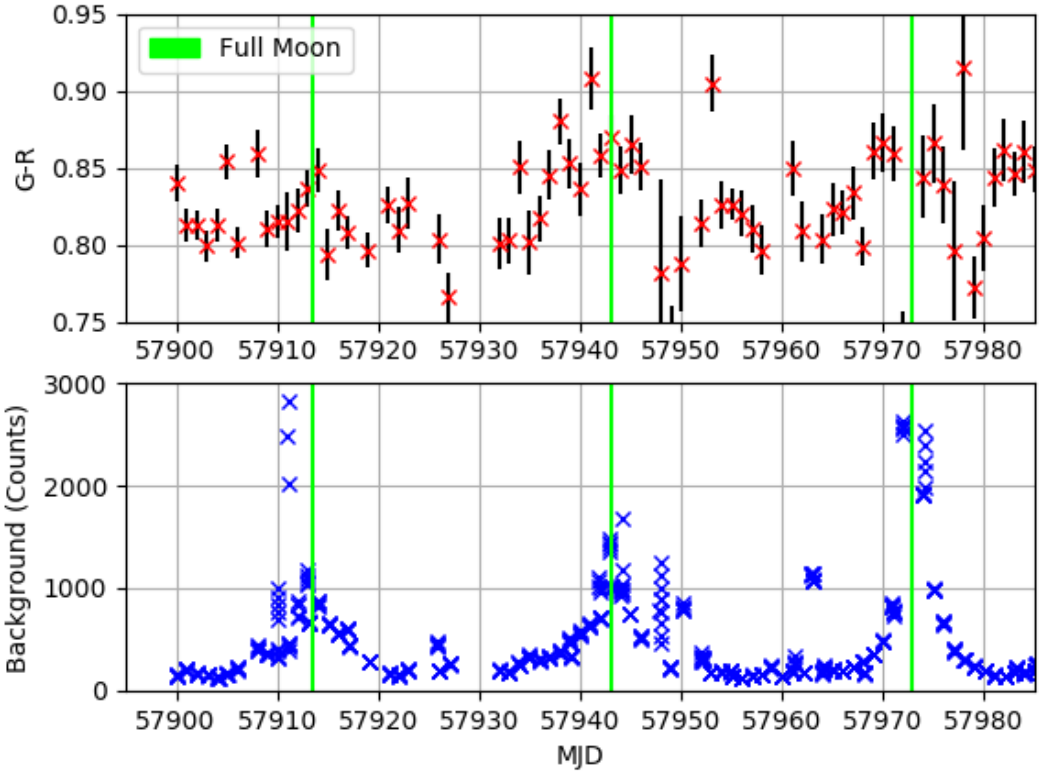

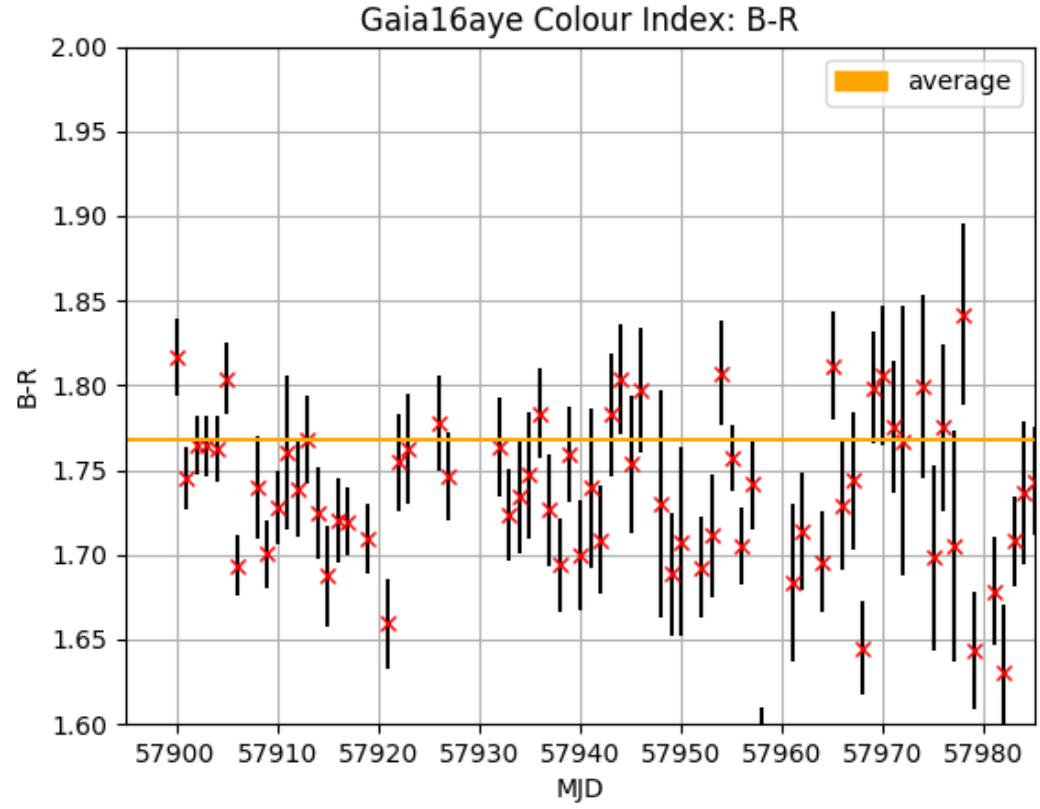

Figure 62: (Continued on the following page)

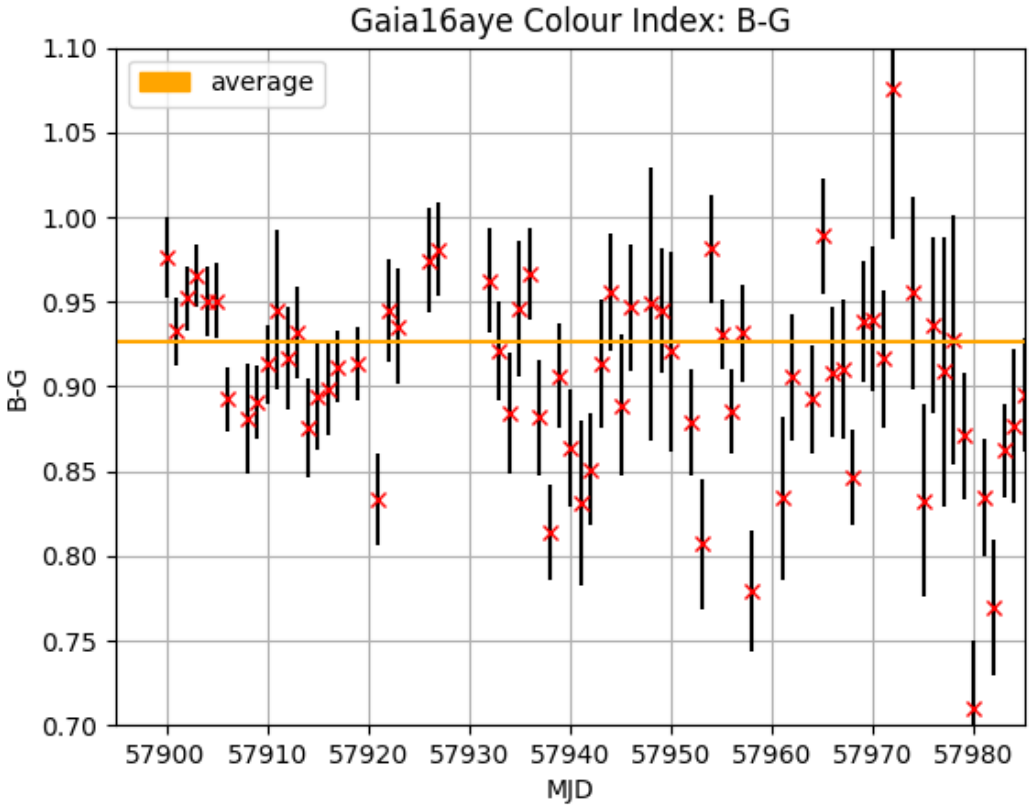

Figure 62: The Colour Index of Gaia16aye between MJD 57890 and 57990 as seen by PIRATE.

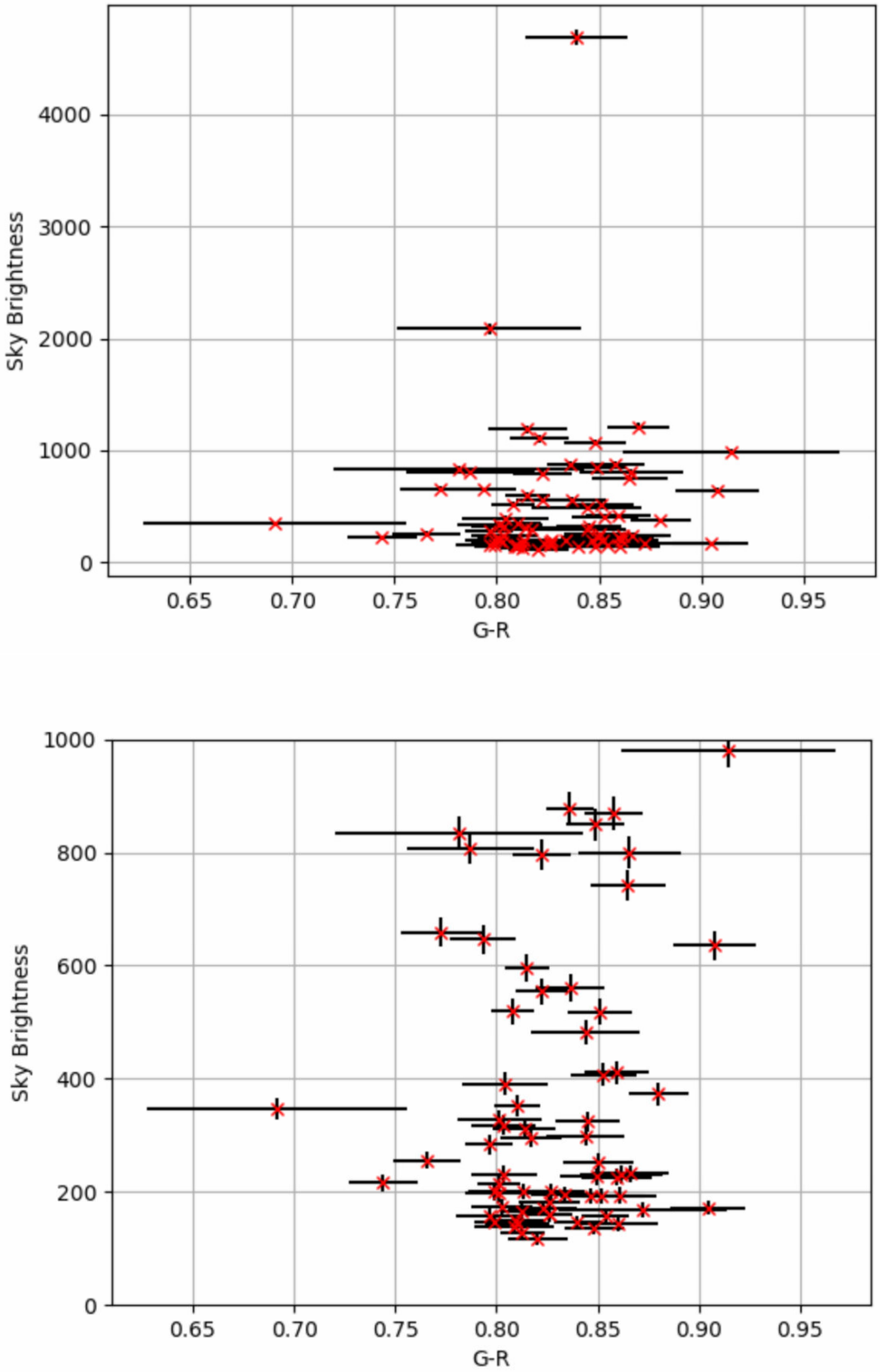

Figure 63: A correlation plot of the G-R colour index for Gaia16aye on the x-axis, vs the sky brightness on the y-axis. The top plot shows all of the data, while the lower plot shows just the data below 1000 counts in sky brightness.

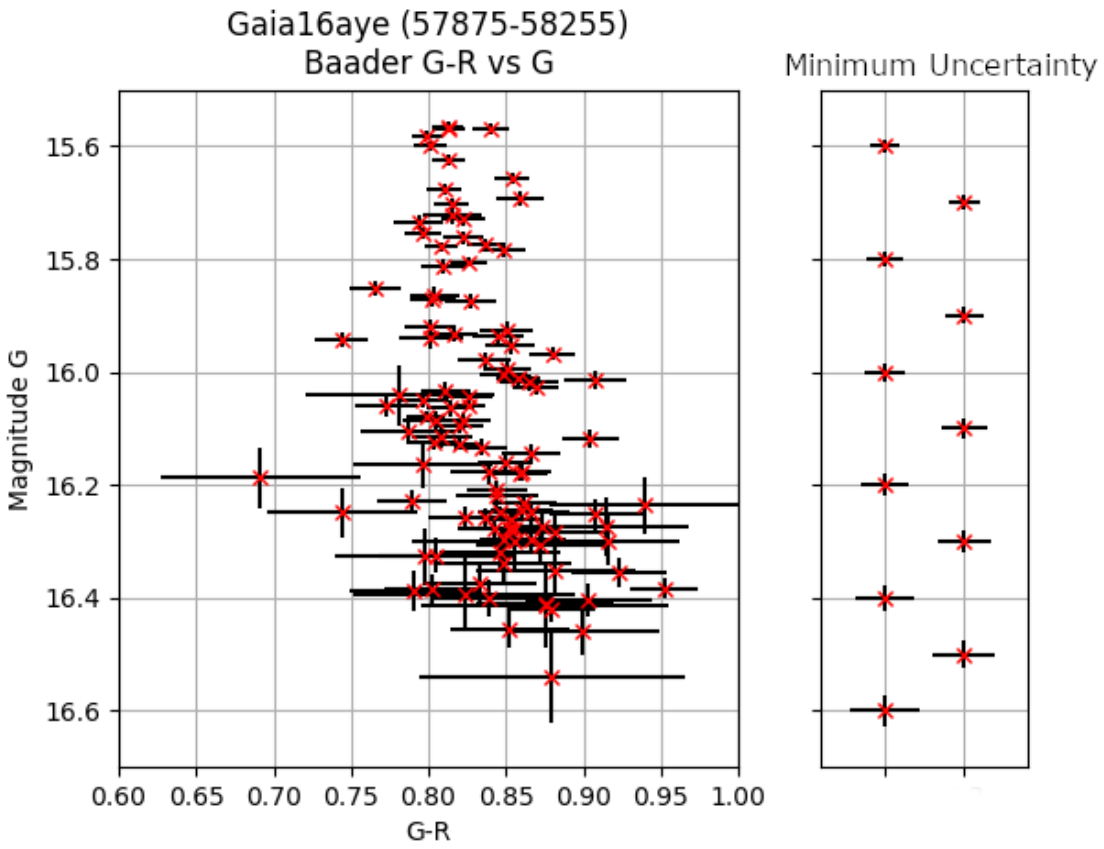

Figure 64: Gaia16aye G-R colour index vs G magnitude. The minimum uncertainties demonstrated on the right of the graph are taken from calculations of expected noise and read out noise for targets observed by PIRATE in section 2.5.

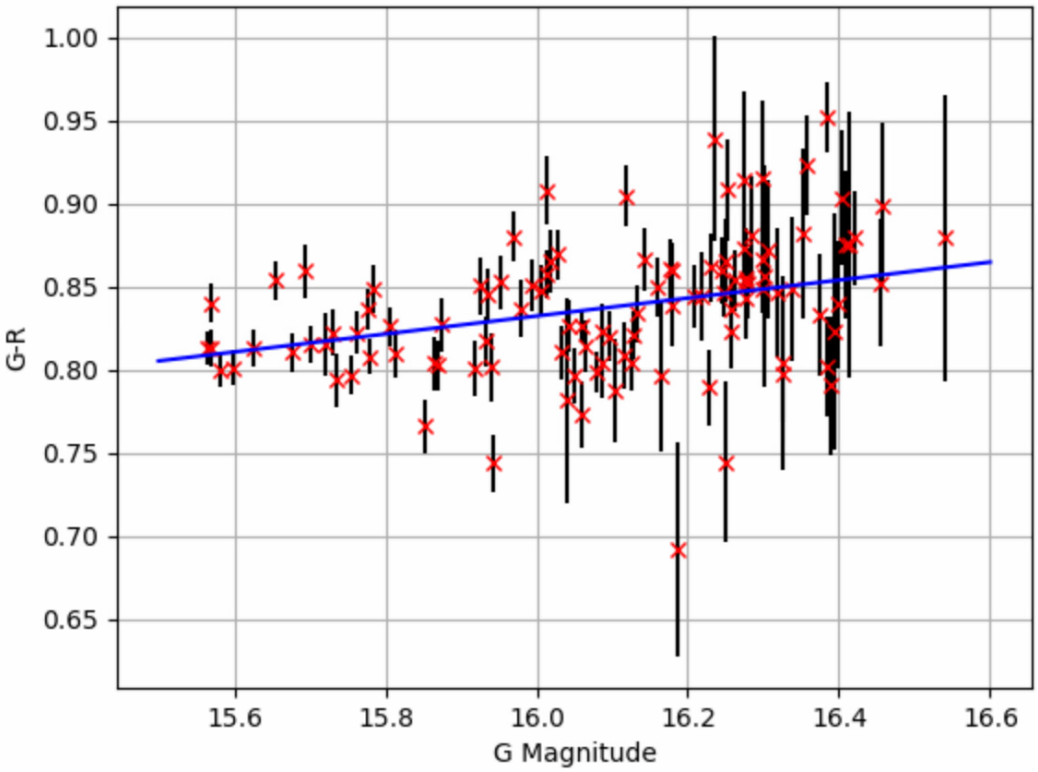

Figure 65: Weighted linear regression model fitted to the G vs G-R data, the model is the linear function y = 0.054x - 0.033 calculated using python.

8 Long Term Follow Up of Gaia Science Alerts Targets

A major part of this project has been the long term automated observation, reduction and basic analysis of variable targets. Many of the targets chosen came from the list of Gaia alerts objects which are released on a daily basis (see chapter 4). As there are too many targets in the list to observe them all for extended periods of time, the target selection came from suggestions by the Gaia Science Alerts Working group 10: Photometric Follow-Up (GSAWG10), which has been an e-mail sent out by Lukasz Wyrzykowski or one of his team each month.

In addition to the GSAWG10 targets, during a short time early on in the project an automated pipeline was tested which selected every Gaia science alert which was visible from Tenerife and sent it automatically to the telescope for observation. The test was successful, though at the time there was no way to select targets based on their suspected classification, which lead to most of the supernovae targets which were observed in early 2017.

PIRATE has imaged a wide variety of variable star types for this project, and this can potentially be used to identify what type of variability PIRATE is the most suited to observing. Most targets observed for this project were only imaged a handful of times per night, so the conclusions drawn about suitability of variable type will focus mainly on light curves generated this way. Each target will be considered individually and the suitability of each type will be discussed at the end of this chapter.

I used PIRATE to collect over 45,000 images during my project, with over 2,700 hours exposure time. The main acquisition period used for this project was between May 2017 and January 2019, which gives more than 20,000 images for 78 different targets including Gaia16aye (chapter 7) which needed to be reduced and analysed. All of these data were processed using the automated reduction pipeline described in section 5.1, and then analysed using both the data analysis pipeline described in section 5.2 and the Cambridge Photometry Server which was described in section 4.3.

Table 9 is a list of all the targets observed by PIRATE over the main acquisition period along with their "suspected classifications" from the Gaia alerts website and the number of images obtained for the target in all filters by PIRATE.

Although the Kojima microlensing event was not first discovered by the Gaia satellite, it was followed up by the Gaia alerts community and will be discussed amongst

the other Gaia alerts microlensing events. Gaia16aye is a special case of a microlensing event which involves a binary system acting as the lens called a binary microlensing event and was discussed separately in chapter 7 due to both the interesting nature of the event and the large optical follow-up the target received both by PIRATE and many other telescopes all over the world.

Targets which were picked out for observation for this project mainly fall into 5 different classes: microlensing events, supernovae, cataclysmic variables, active galactic nuclei (AGN) and unknown variables. The selection of targets came from two places: the GSAWG10 mentioned earlier, and a few targets came from random selection by an automated tool which was tested early on in the project.

When given the choice of targets to follow up, microlenses were chosen because an interest was sparked after the early start on observations of Gaia16aye which lead to the possibility of studying population statistics of microlenses and stellar multiplicity on a small scale within the Gaia Alerts. Cataclysmic variables and unknown events were selected secondarily for the possibility of finding out more about the target from photometric light curves. The AGN and some supernovae targets arose from later identification of targets which were initially unknown.

Target	RA & DEC (Degrees)	Suspected Class	Filter (& Number of Images)	Observation Period
Gaia16aye	295.00474 30.13149	BML	Baader B(784), G(777), R(784) Johnson B(84), V(83), R(84)	10/08/2016 - 01/10/2018
Gaia17bbj	267.62549 -1.80206	SN Ia	Baader B(63), G(63), R(63)	01/06/2017 - 14/07/2017
Gaia17bbt	236.38984 30.14543	SN	Baader B(30), G(31), R(30)	01/05/2017 - 05/06/2017
Gaia17bbu	222.94606 43.64471	SN II	Baader B(26), G(26), R(26)	24/04/2017 - 30/05/2017
Gaia17bdd	255.79882 61.45726	SN Ia	Baader B(18), G(18), R(18)	05/05/2017 - 31/05/2017
Gaia17bdk	265.63446 -34.10374	ML	Baader B(103), G(104), R(103)	11/05/2017 - 24/08/2017
Gaia17beb	277.19502 32.45163	CV	Baader B(50), G(50), R(50)	21/05/2017 - 04/06/2017
Gaia17bej	274.25440 -31.38352	ML	Baader B(103), G(102), R(103)	25/07/2017 - 30/08/2017
Gaia17bes	298.07823 39.66714	U	Baader B(3), G(3), R(3)	05/06/2017 - 07/06/2017
Gaia17bhq	159.20166 -9.45989	SN Ia	Baader B(6), G(4), R(6)	08/06/2017 - 10/06/2017
Gaia17bhs	153.63547 -2.27357	SN Ia	Baader B(15), G(11), R(15)	27/05/2017 - 14/06/2017
Gaia17bht	154.73788 1.65873	SN	Baader B(10), G(8), R(10)	04/06/2017 - 17/06/2017
Gaia17bic	137.14485 48.6073	SN Ia	Baader B(21), G(16), R(21)	31/05/2017 - 18/06/2017
Gaia17bie	353.12034 23.93637	SN Ia	Baader B(66), G(66), R(66)	27/05/2017 - 14/07/2017
Gaia17big	155.83067 22.39402	SN Ia	Baader B(18), G(15), R(18)	26/05/2017 - 19/06/2017
Gaia17bii	170.87824 -8.65332	SN II	Baader B(15), G(15), R(15)	26/05/2017 - 28/06/2017
Gaia17bij	163.01852 11.59496	SN Ia	Baader B(23), G(20), R(23)	26/05/2017 - 01/07/2017
Gaia17bim	2.31559 30.48592	SN II	Baader B(54), G(54), R(54)	29/05/2017 - 14/07/2017
Gaia17biq	10.57603 40.89923	Nova	Baader B(56), G(56), R(56)	27/05/2017 - 14/07/2017
Gaia17biu	154.77343 46.45391	SN	Baader B(30), G(29), R(30)	26/05/2017 - 06/07/2017
Gaia17bjj	9.33110 29.07809	SN	Baader B(63), G(63), R(63)	01/06/2017 - 14/07/2017
Gaia17bjn	13.44718 40.93015	CV	Baader B(61), G(60), R(61)	31/05/2017 - 14/07/2017
Gaia17bjo	125.39715 76.34213	Blue Transient	Baader B(19), G(15), R(19)	07/06/2017 - 22/06/2017
Gaia17bjq	190.71097 -30.41206	SN Ia	Baader B(10), G(9), R(10)	01/06/2017 - 16/06/2017
Gaia17bjv	177.77551 43.41448	SN Ia	Baader B(48), G(45), R(48)	04/06/2017 - 14/07/2017
Gaia17bjw	178.22188 44.12392	SN Ic	Baader B(75), G(72), R(75)	30/05/2017 - 11/07/2017
Gaia17bjy	185.97579 9.12454	SN Ia	Baader B(41), G(39), R(41)	06/06/2017 - 14/07/2017
Gaia17bls	210.44193 9.49926	SN II	Baader B(4), G(4), R(4)	08/06/2017 - 11/06/2017
Gaia17bnz	243.67618 16.23324	SN	Baader B(90), G(94), R(90)	23/09/2017 - 15/04/2018
Gaia17bol	301.06550 29.24992	U	Baader B(28), G(25), R(28)	05/10/2017 - 21/12/2017
Gaia17bts	17.21965 73.89625	ML	Baader B(338), G(337), R(338)	16/07/2017 - 23/01/2018
Gaia17bue	355.38622 -10.08864	U	Baader B(6), G(6), R(6)	22/07/2017 - 24/07/2017
Gaia17bxh	73.97187 46.40092	U	Baader B(191), G(190), R(191)	27/09/2017 - 15/04/2018
Gaia17byb	84.04131 43.19971	U	Baader B(44), G(42), R(44)	26/09/2017 - 31/10/2017

Target	RA & DEC (Degrees)	Suspected Class	Filter (& Number of Images)	Observation Period
Gaia17cem	257.24636 21.88561	AGN	Baader B(81), G(85), R(81)	29/09/2017 - 15/04/2018
Gaia17cff	259.98272 41.68041	AGN	Baader B(85), G(84), R(85)	27/09/2017 - 15/04/2018
Gaia17cga	328.19686 56.13867	CV	Baader B(127), G(123), R(127)	13/09/2017 - 23/01/2018
Gaia17chf	325.84088 73.68689	CV	Baader B(109), G(107), R(109)	17/09/2017 - 22/01/2018
Gaia17cmd	115.43990 16.21836	AGN	Baader B(210), G(206), R(210)	18/10/2017 - 15/04/2018
Gaia17cpa	310.19523 32.79639	U	Baader B(61), G(61), R(61)	22/10/2017 - 05/01/2018
Gaia17cpb	292.09003 56.57936	SN Ia	Johnson B(4), V(4), R(4)	30/05/2018 - 03/06/2018
Gaia17ctl	271.40021 -33.60972	ML	Baader B(15), G(15), R(15) Johnson B(114), V(116), R(117)	10/05/2018 - 11/05/2019
Gaia17cxa	96.63438 16.27301	U	Johnson B(216), V(219), R(221)	29/08/2018 - 03/05/2019
Gaia17dce	302.91748 9.31264	CV	Baader B(9), G(9), R(9) Johnson B(164), V(172), R(174)	11/05/2018 - 19/05/2019
Gaia17dcg	132.98547 -2.64016	CV	Baader B(12), G(12), R(12) Johnson B(305), V(308), R(309)	11/05/2018 - 25/05/2019
Gaia17ddi	295.10007 28.10117	ML	Baader B(95), G(95), R(95) Johnson B(130), V(131), R(133)	30/03/2018 - 01/06/2019
Gaia17ddp	293.58517 28.20143	U	Baader B(24), G(23), R(24) Johnson B(130), V(133), R(134)	05/12/2017 - 25/05/2019
Gaia18ack	202.10178 67.71773	SN Ia	Johnson B(4), V(4), R(4)	03/06/2018 - 06/06/2018
Gaia18aen	120.71694 -30.31032	U	Baader B(668), G(654), R(668) Johnson B(188), V(190), R(195)	18/01/2018 - 30/03/2019
Gaia18ajt	267.13326 -35.08802	ML	Baader B(12), G(12), R(12) Johnson B(103), V(103), R(106)	10/05/2018 - 12/05/2019
Gaia18ajz	277.56025 -8.22021	U	Baader B(9), G(9), R(9) Johnson B(157), V(157), R(159)	12/05/2018 - 16/06/2019
Gaia18akt	96.32536 12.53626	U	Johnson B(258), V(272), R(303)	28/08/2018 - 23/03/2019
Gaia18apf	54.06163 -32.88613	CV	Johnson B(235), V(237), R(249)	24/08/2018 - 09/02/2019
Gaia18aqa	9.77891 48.34285	Recurrent Nova	Baader B(6), G(6), R(6) Johnson B(255), V(259), R(264)	14/05/2018 - 15/06/2019
Gaia18arn	323.81420 50.48067	U	Baader B(31), G(30), R(31) Johnson B(173), V(178), R(185)	30/04/2018 - 16/12/2018
Gaia18atk	275.15950 -18.66146	ML	Baader B(12), G(12), R(12) Johnson B(138), V(139), R(139)	11/05/2018 - 03/03/2019
Gaia18avw	39.71863 66.43154	U	Johnson B(219), V(225), R(229)	09/06/2018 - 19/06/2019
Gaia18axf	335.16897 44.06483	CV	Baader B(12), G(12), R(12) Johnson B(230), V(233), R(238)	10/05/2018 - 31/05/2019
Gaia18axl	337.14051 54.04934	U	Baader B(39), G(39), R(39) Johnson B(243), V(245), R(250)	29/04/2018 - 25/05/2019
Gaia18azm	175.28326 24.81955	SN Ia	Baader B(9), G(9), R(9)	04/05/2018 - 14/05/2018

Target	RA & DEC (Degrees)	Suspected Class	Filter (& Number of Images)	Observation Period
Gaia18bbf	218.97354 35.28761	SN Ia	Baader B(1), G(1), R(1) Johnson B(68), V(68), R(65)	14/05/2018 - 27/07/2018
Gaia18bbt	243.75334 31.072	SN II	Baader B(1), G(1), R(1) Johnson B(33), V(32), R(32)	19/05/2018 - 11/06/2018
Gaia18bca	231.65958 28.86628	SN	Baader B(3), G(3), R(3) Johnson B(4), V(3), R(3)	14/05/2018 - 01/06/2018
Gaia18bcb	286.33528 8.60282	U	Baader B(9), G(9), R(9) Johnson B(140), V(144), R(147)	12/05/2018 - 11/05/2019
Gaia18beg	165.62621 55.59883	SN	Johnson B(429), V(431), R(441)	24/05/2018 - 31/05/2019
Gaia18bej	237.51482 42.08848	SN Ia	Johnson B(6), V(6), R(4)	03/06/2018 - 09/06/2018
Gaia18bek	251.60539 25.42146	SN Ia	Johnson B(75), V(75), R(74)	22/05/2018 - 27/07/2018
Gaia18chm	271.01587 -15.41484	U	Johnson B(30), V(30), R(30)	07/09/2018 - 18/10/2018
Gaia18chq	271.43910 -12.01455	U	Johnson B(31), V(31), R(32)	07/09/2018 - 19/02/2019
Gaia18cib	279.11483 -16.5783	U	Johnson B(30), V(30), R(30)	08/09/2018 - 18/10/2018
Gaia18cik	278.37988 -3.40325	U	Johnson B(47), V(47), R(54)	07/09/2018 - 27/04/2019
Gaia18cjk	283.78805 -6.66353	ML	Johnson B(35), V(36), R(36)	08/09/2018 - 07/11/2018
Gaia18clv	298.57743 10.70923	ML	Johnson B(49), V(50), R(50)	10/09/2018 - 05/05/2019
Gaia18cud	48.99112 49.68748	U	Johnson B(240), V(242), R(246)	27/11/2018 - 22/03/2019
Gaia18ddp	96.91086 -54.45669	SN	Johnson B(27), V(27), R(27)	27/05/2018 - 18/06/2018
Gaia18dds	311.91679 34.25163	U	Johnson B(70), V(71), R(72)	28/11/2018 - 26/05/2019
Gaia19aau	47.53781 59.39607	U	Johnson V(113), R(114)	11/01/2019 - 23/03/2019
Kojima	76.92767 24.79875	ML	Baader B(376), G(372), R(376)	01/11/2017 - 29/11/2017

Table 9: List of all the targets observed by PIRATE during the main acquisition period for this project, May 2017 to January 2019. The suspected classifications include supernovae (SN), microlensing event (ML), cataclysmic variables (CV), active galactic nuclei (AGN), unknown events (U) and otherwise named events. Images refers to the total number of images in all filters of the target. The filters used are either Baader R, G, B or Johnson R, V, B or both in the case of targets where images were taken before and after the filter swap on 20/05/2018 (MJD 58258), with the number of images taken in that filter in brackets. All coordinates are given in J2000.

8.1 Microlensing Events

Over the course of this project the GSAWG10 identified 11 Gaia Alerts events which appeared to be microlenses and which were also visible from Tenerife. Additionally one more microlensing target was identified by an amateur astronomer (Tadashi Kojima) which was also followed up by members of GSAWG10.

Figure 66 is an example of a single microlensing event, which was observed by the OGLE team in 2005. Any observed microlensing events should approximately follow this overall roughly symmetric shape; a rise in brightness from the target star's baseline, a gentle peak, and a fall back to the baseline magnitude of the star.

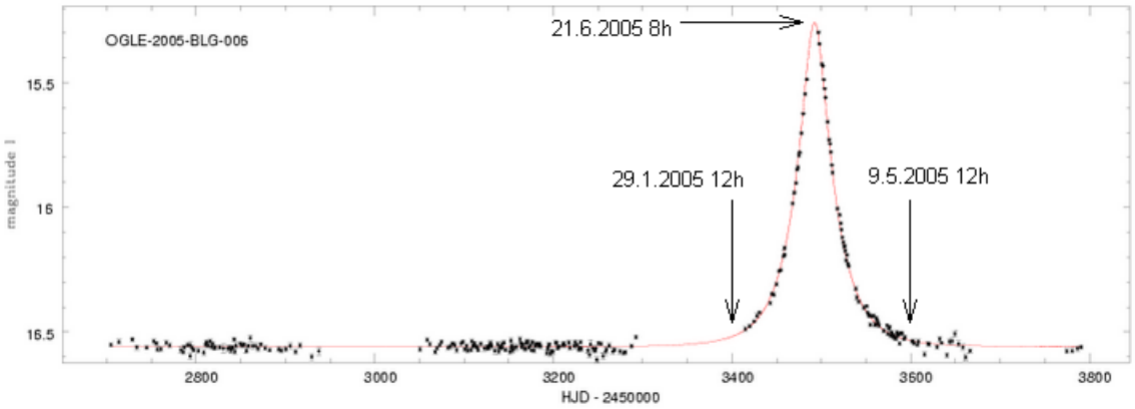

Figure 66: Light curve of OGLE-2005-BLG-006, a microlensing event observed by the OGLE team (Greenstein 2013).

One of the Gaia targets was Gaia16aye which is detailed in chapter 7, and the rest are detailed here.

Gaia17bts

Alternate Names	RA (J2000)	DEC (J2000)	Alert Date	Alert Mag (Gaia G Filter)
Gaia17bts	01:08:52.72	73:53:46.50	2017-07-14 06:03:45	17.23

Gaia17bts appears to have been a relatively short microlensing event which occurred over around 5 months in the middle of 2017. The event only got ∼0.8 magnitudes brighter than baseline, and the initial alert appears to have happened after the peak of the event. Figure 67 shows the PIRATE EPP light curve in the context of the Gaia light curve, and on its own.

Around MJD 57988 there is a small peak in the data which appears to occur in all three filters (figure 68). This target is right at the limit of PIRATE's detection threshold, so any meaningful photometry beyond just detecting the target is difficult. Through the Baader R filter at 18 mag the expected minimum standard deviation is 0.15 mag (see section 2.5), but this peak in particular appears to be around 0.5 mag. Planetary microlensing events are typically very small as the amount of magnification is dependent on the mass of the lensing body, and microlensing events are expected to affect all colours equally, so this could indicate the presence of a second lensing body. There is not enough information to conclude definitively whether or not this is a real event or an anomaly caused by the faintness of the target and the capabilities of PIRATE.

Gaia17ddi

Alternate Names	RA (J2000)	DEC (J2000)	Alert Date	Alert Mag (Gaia G Filter)
Gaia17ddi	19:40:24.02	28:06:04.21	2017-12-02 19:35:49	18.45

The Gaia data for Gaia17ddi suggests that there may be two peaking events, one at around MJD 57900 and another at around MJD 58100, so it may have been a binary microlensing event. Unfortunately Gaia Science Alerts did not pick up on the variation until after both peaks occurred, and the target is very faint with baseline of ∼19.4 mag in the Gaia data.

The EPP still seemed to pick up some of that data in the red and green filters, though the light curve shown in figure 69 is fairly noisy and does not really indicate much beyond perhaps that it slightly declined over the course of the data collection, indicating that the very tail of the event may have been captured.

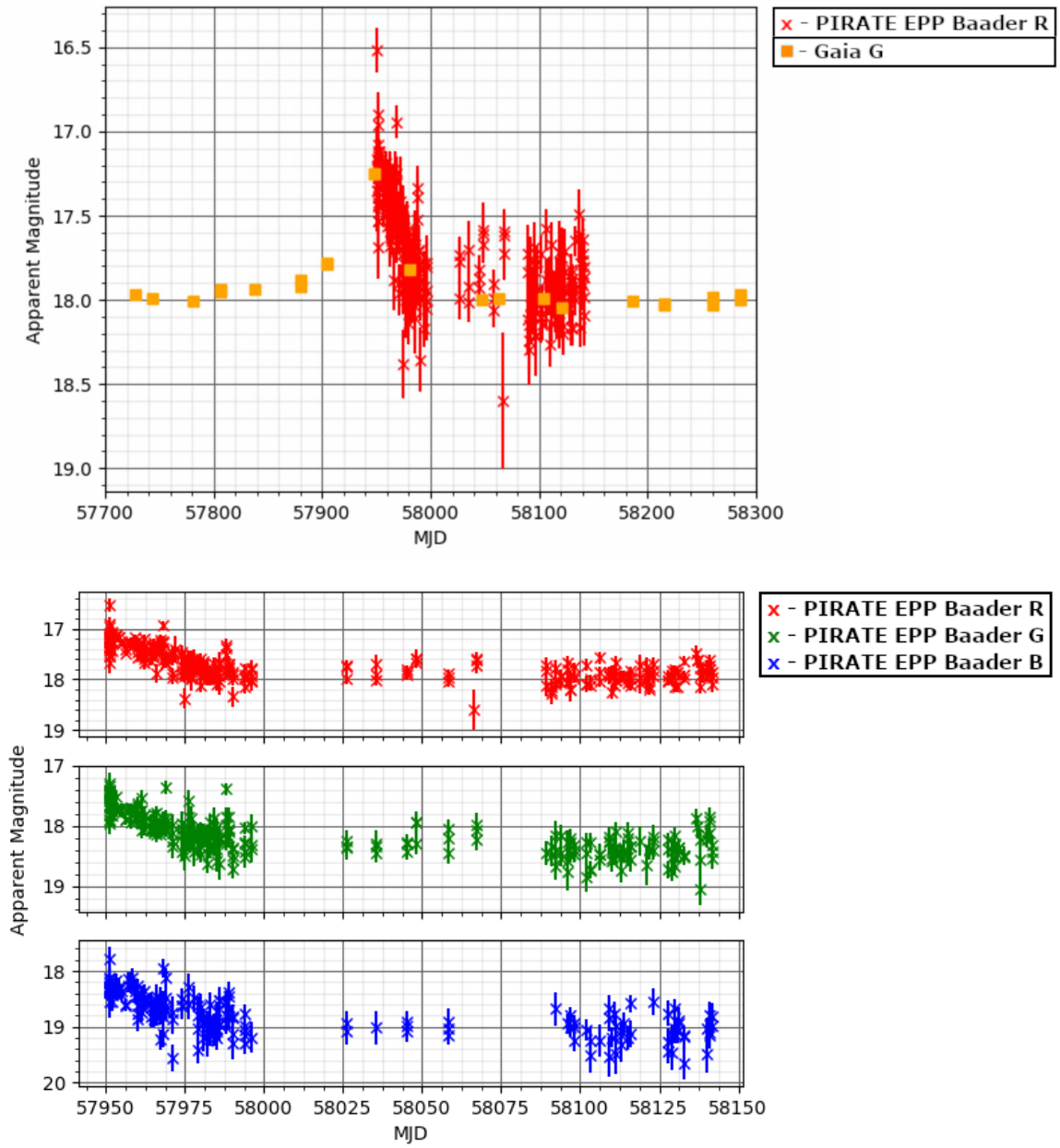

Figure 67: The top figure is the Gaia17bts PIRATE Baader R EPP light curve in the context of the Gaia G light curve. The differential light curve data from the EPP has been magnitude calibrated using the CPCS data and the method described in section 6. The bottom figure shows the PIRATE EPP data on its own.

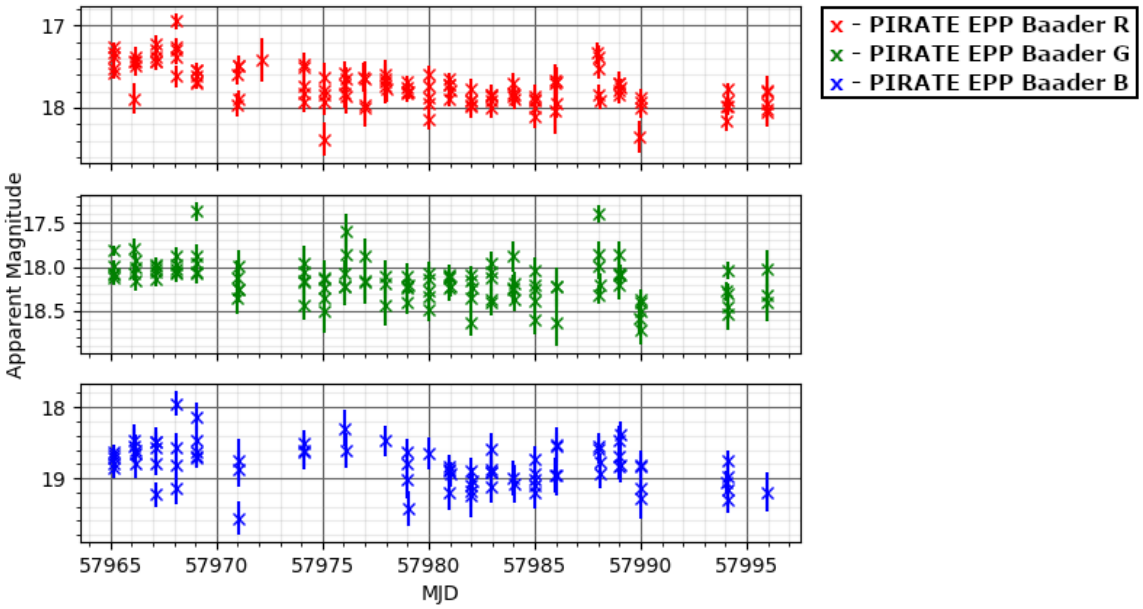

Figure 68: A enlarged portion of the PIRATE EPP Gaia17bts light curve around MJD 57988, where there is the possibility of a small secondary lensing object causing a small second rise in the light curve.

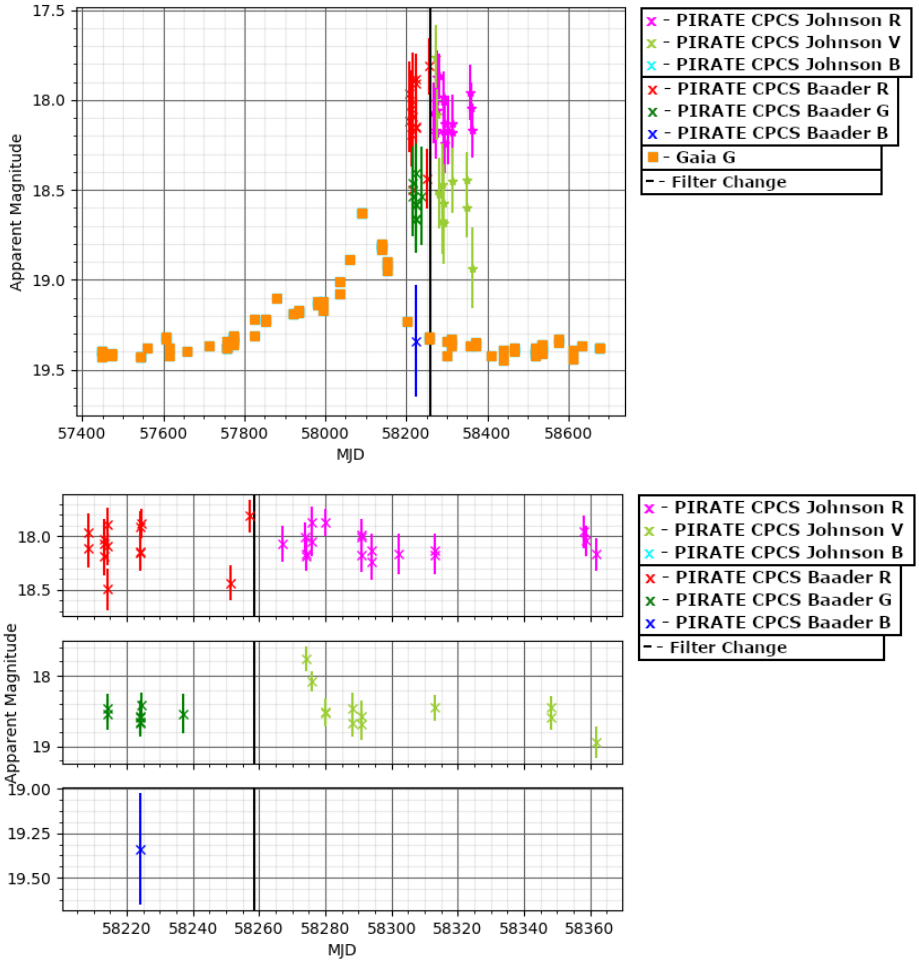

Figure 69: The top figure is the Gaia17ddi PIRATE EPP light curve in the context of the Gaia G light curve. The differential light curve data from the EPP has been magnitude calibrated using the CPCS data and the method described in section 6. The bottom figure shows the PIRATE EPP data on its own.

Gaia18ajt

Alternate Names	RA (J2000)	DEC (J2000)	Alert Date	Alert Mag (Gaia G Filter)
Gaia18ajt	17:48:31.98	-35:05:16.87	2018-02-08 08:37:53	15.59

Figure 70 is another case of a probable short microlensing event which wasn't identified until after it had already peaked. The data collected does not have any particular features which stand out, it does not even appear to be declining which means it may have been caught too late, after the event had already finished. The target was first mentioned in Kruszynska et al. 2018.

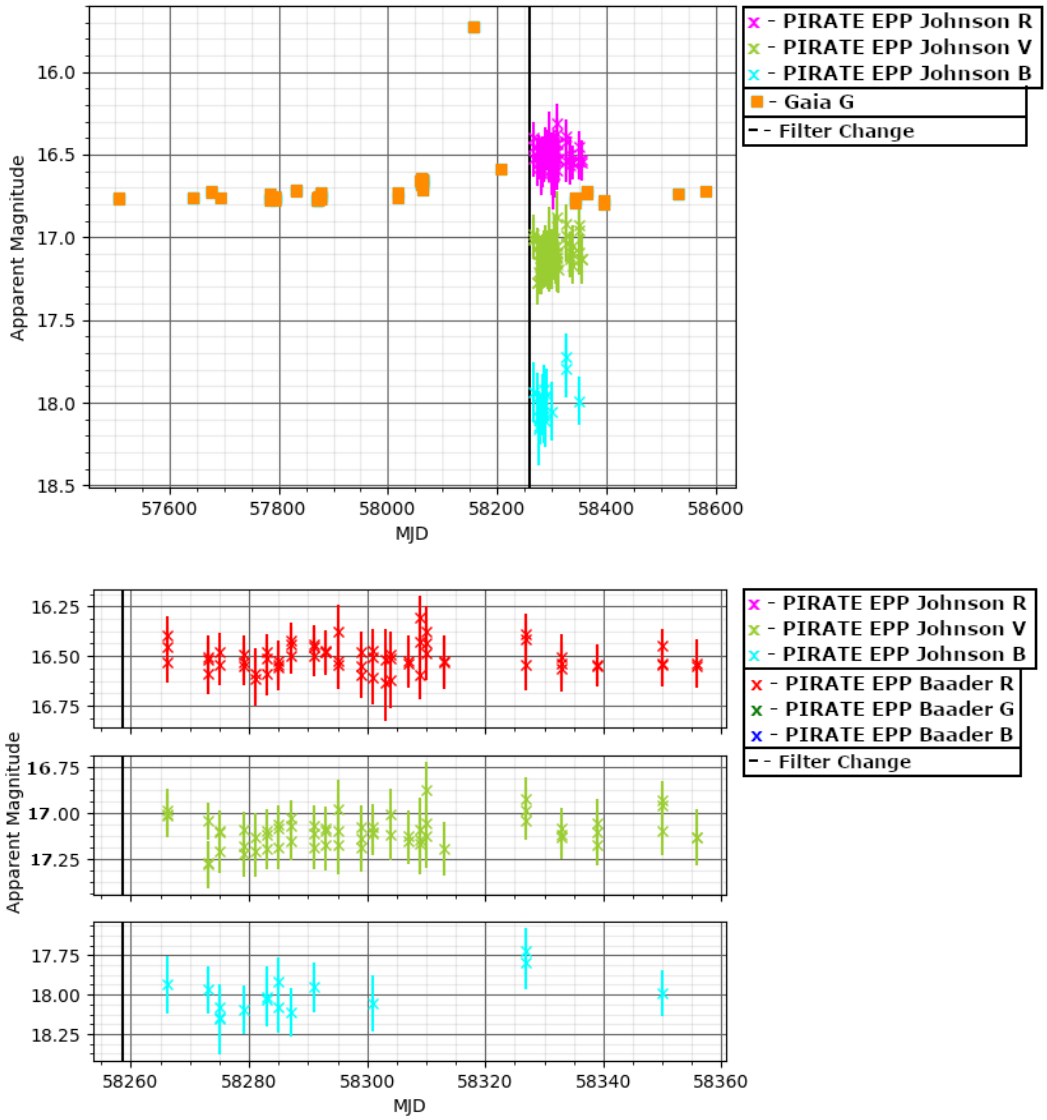

Figure 70: Light curve for Gaia18ajt, the top figure puts the EPP data in the context of the Gaia data, the bottom figure is just the EPP light curves.

Gaia18ajz

Alternate Names	RA (J2000)	DEC (J2000)	Alert Date	Alert Mag (Gaia G Filter)
Gaia18ajz, AT2018uh	18:30:14.46	-08:13:12.76	2018-02-09 14:09:47	17.91

Discovered by Gaia on 2018-02-09 (Delgado et al. 2018c). Confirmed by the OGLE team spectroscopically on 2018-05-11 to be a microlensing target (Kruszynska et al. 2018).

The Gaia data for this target shows a very clear microlensing event over the course of about 600 days. The light curve appears a little lopsided which may be explained by the length of the event. 600 days is a significantly long time because not only are the lens and source moving relative to one another - which would cause a symmetric light curve - but the earth's position also shifts by 2AU every six months.

There is not a lot of PIRATE data for this target, the only data which as come out of the CPCS is magnitude 19.0 and from the R filter. None of the PIRATE data appears to follow the Gaia light curve, the CPCS data appears to be rising when the Gaia data are declining. Overall these data are not very useful for the target in question, at 19.0 mag or fainter the expected minimum uncertainty for PIRATE is very high ~ 0.4 mag.

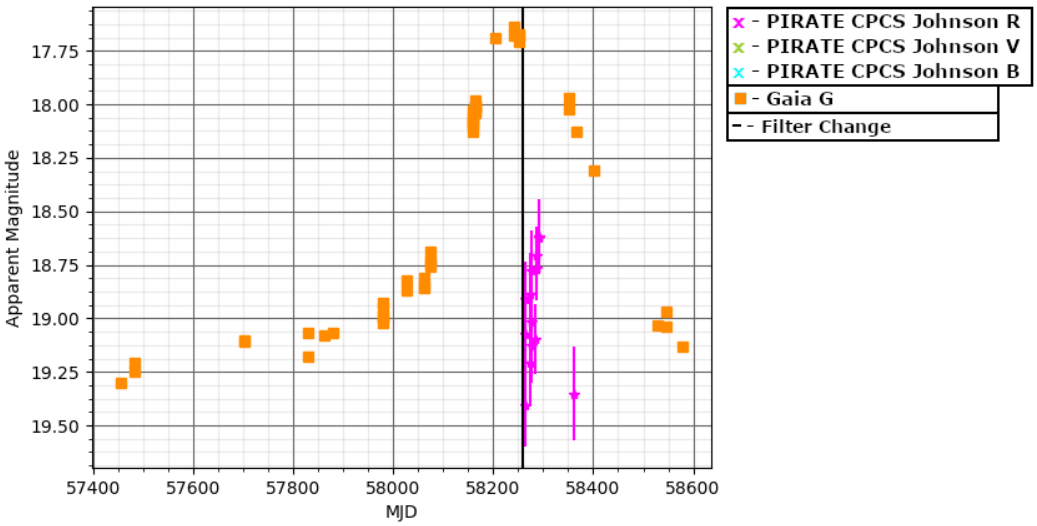

Figure 71: Gaia18ajz, the Gaia data clearly indicates that the target is a microlensing event, but the PIRATE data are very sparse due to the faintness of the object. The PIRATE R data was processed by the EPP.

Gaia18atk

Alternate Names	RA (J2000)	DEC (J2000)	Alert Date	Alert Mag (Gaia G Filter)
Gaia18atk	18:20:38.28	-18:39:41.26	2018-03-28 07:59:44	17.41

Gaia18atk is another likely microlensing target which has been picked up by Gaia shortly after it peaked, and is close to the faint end of PIRATE's capability. There is a possible feature in the light curve in the red data in figure 72 at around MJD 58300. Upon closer inspection the R data at 17 mag is expected to have standard deviation at around 0.07mag (see section 2.5), which compared to the small rise which appears to be around 0.1-0.2 mag means that the possible peak may just be due to noise.

The later data after MJD 58370 in the R filter is more spread than the rest, but this seems to be due to the target reaching closer to 17.5 which is expected to have a higher standard deviation at around 0.1 mag, something which is also reflected in the larger error bars compared to earlier data points.

Inspection of the data frames which correspond to the few data points in the R data which appear to be above the trend of the rest of the data around MJD 58300 does not reveal any inconsistencies with the rest of the data, there doesn't appear to be any focusing issues or trailling. The Johnson V filter data does not appear to show the same features around MJD 58000. There is also no data from any other observers on the CPCS follow up page so there is no corroborating, or contradicting data to help identify features either.

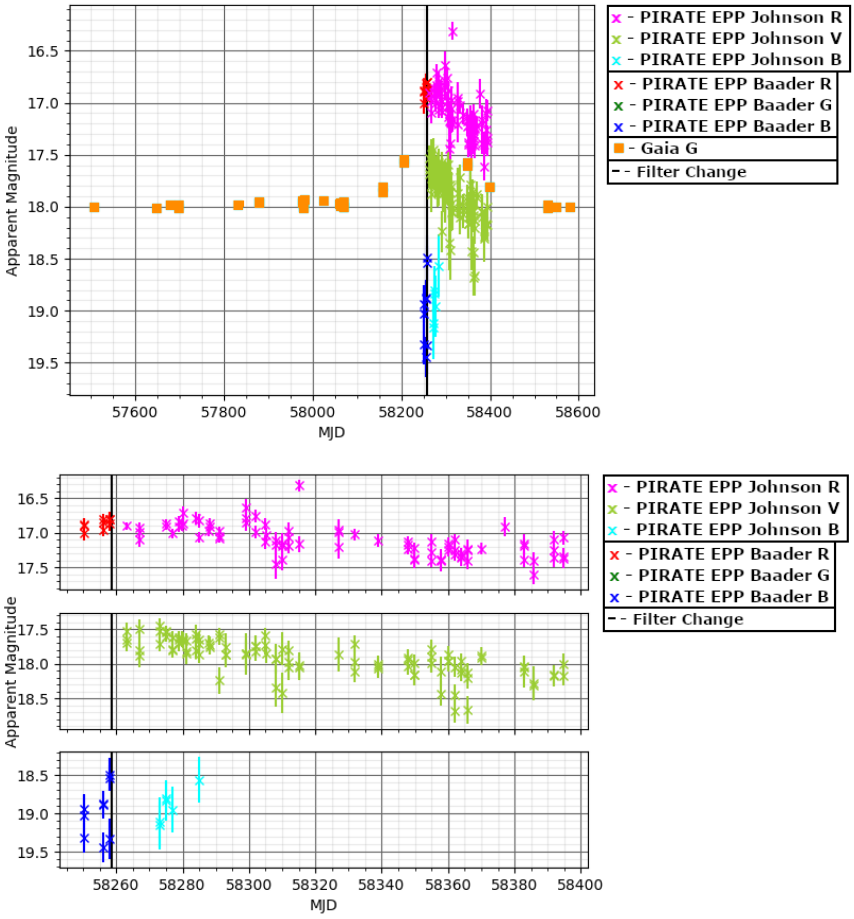

Figure 72: Gaia18atk data analysed using the CPCS given in context of the Gaia data in the top figure, and the EPP data of Gaia18atk in the middle figure. The bottom figure shows both the CPCS data and the EPP data for comparison. The EPP differential data has been calibrated to the same magnitude scale as the CPCS data.

Gaia18clv

Alternate Names	RA (J2000)	DEC (J2000)	Alert Date	Alert Mag (Gaia G Filter)
Gaia18clv	19:54:18.58	10:42:33.23	2018-08-31 03:56:07	17.63

The light curve for Gaia18clv formed by the Gaia data potentially could be a binary microlensing event, unfortunately the data collected by PIRATE starts after the first peak, and had to stop before the second peak due to both time constraints and because PIRATE was in use by others. If time had been available then Gaia18clv is still a very faint target, with the R data somewhere around 18th magnitude between peaks the data would likely be very noisy towards the beginning and tail end of the event.

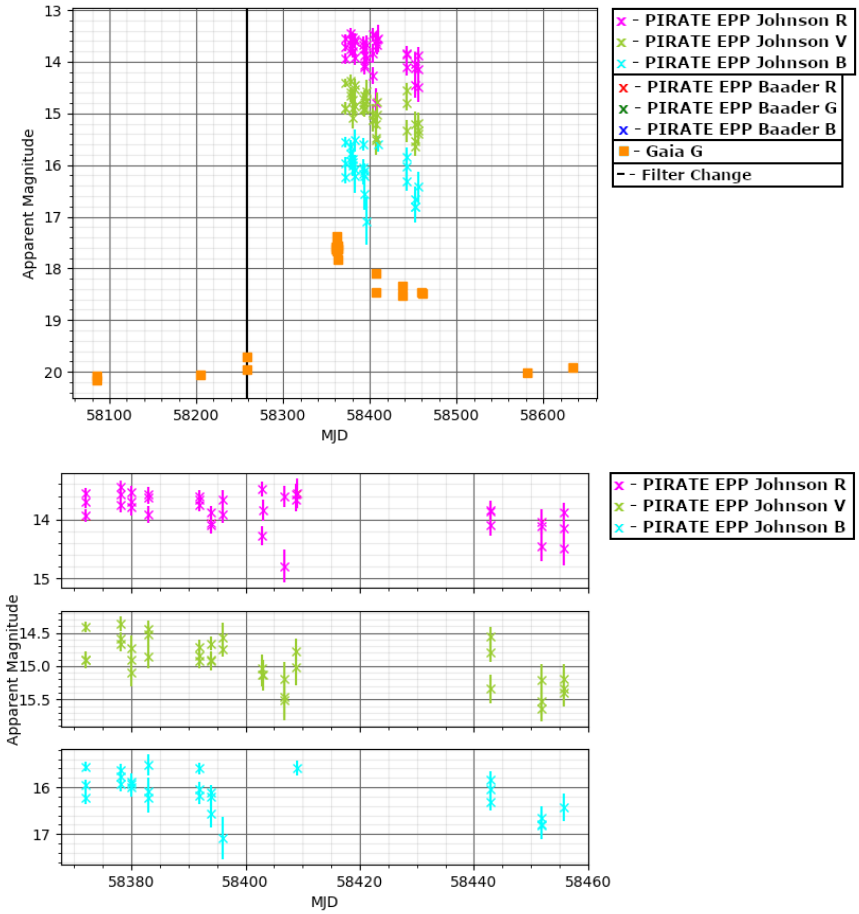

Figure 73: The top figure illustrates the EPP data for Gaia18clv in the context of the Gaia data and the lower figure is zoomed into just the section containing the light curve data. The differential light curve data in both figures has been put on a log scale and calibrated to a position where all 4 sets of data are visible as there was no CPCS data to use to calibrate the data to near the correct magnitudes.

Kojima

Alternate Names	RA (J2000)	DEC (J2000)	Alert Date	Alert Mag (Gaia G Filter)
Kojima TCP J05074264+2447555	05:07:42.64	24:47:55.50	2017-10-31	10.8

The Kojima microlensing event in late 2017 was not initially identified by Gaia, but instead it was picked up by an amateur astronomer Tadashi Kojima (Maehara 2017). PIRATE successfully captured data on three separate nights, the first one on the night beginning 2017-11-01.

Figure 74 shows both the Gaia data in R, G and B Baader filters, and the second graph shows the same data in the context of APASS R data collected by other contributors to the CPCS follow up page. As the target wasn't initially identified by Gaia there is no readily available Gaia data for the target, so the contributions from others here is used just to show context.

The target is a single microlensing event caught near maximum. Interestingly for the PIRATE data, there is a chance that the first night of data collected coincided with the maximum. Figure 75 shows the data collected on the night beginning 2017-11-01. The individual plots for each filter appear relatively flat overall, meaning that the peak may possibly have been caught. To test whether or not there is really a peak, a simple quadratic fitting was made to the nights to data and the maximum for that was calculated to give a date for the microlens peak.

Using the simple fitting model, we obtain the dates for the microlens peak in all three filters in table 10. Given the naive fitting method which leads to relatively large uncertainties, and that we don't know for certain whether or not the PIRATE data observed the actual peak the three filters do at least appear to agree that it occurred around MJD 58059.00.

For comparison Zang et al. 2019 also investigated the target and obtained a more substantial light curve including data from Spitzer (figure 76). The results from that investigation found that the t_0 for the event on HJD' 8058.76, which means that PIRATE did not catch the maximum as it likely occurred almost a full day before.

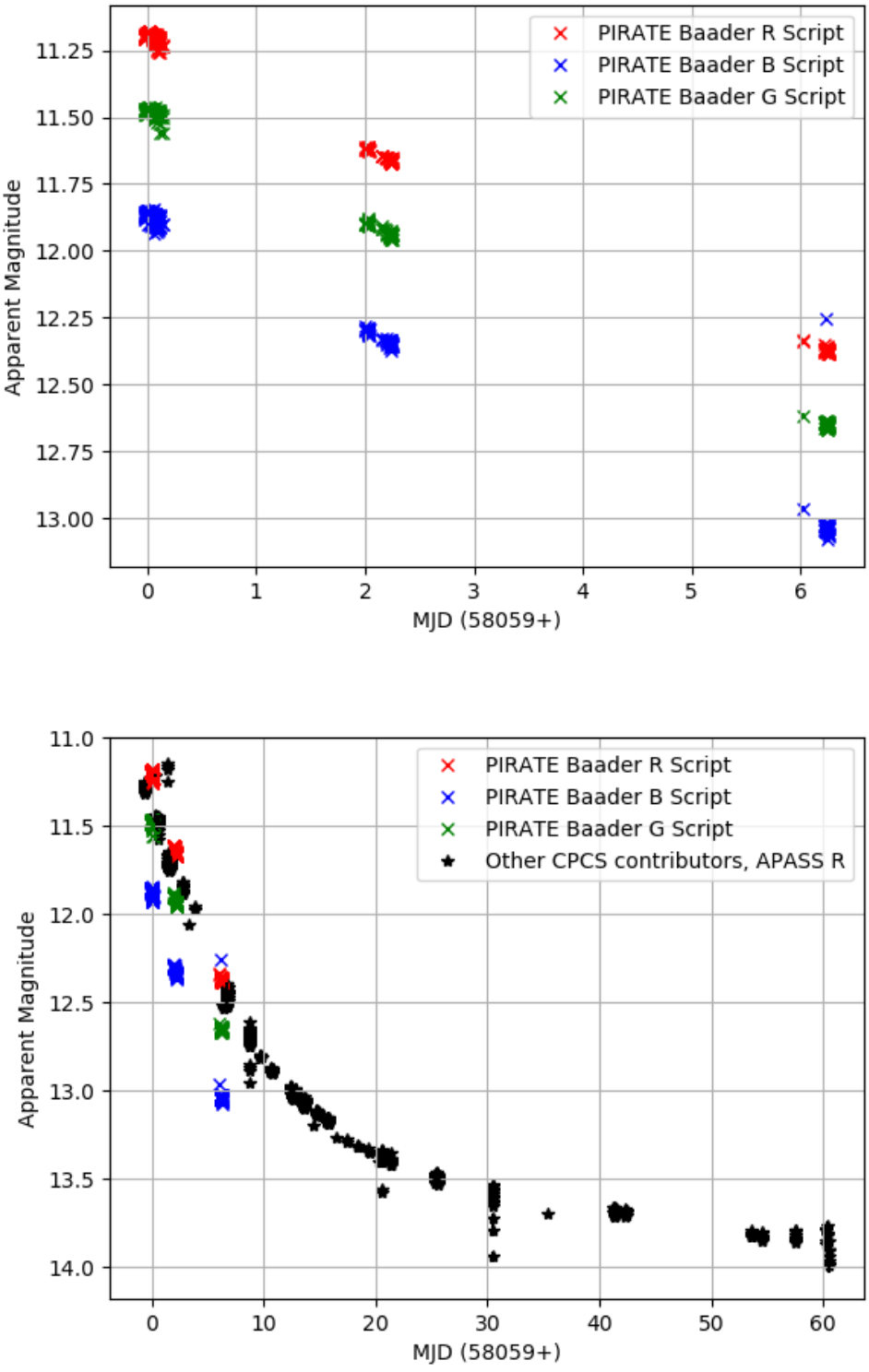

Figure 74: Kojima microlensing event, the top figure contains all of the PIRATE data from the EPP, to give the data context the lower figure also contains the APASS R data from other contributors to the CPCS data for the target.

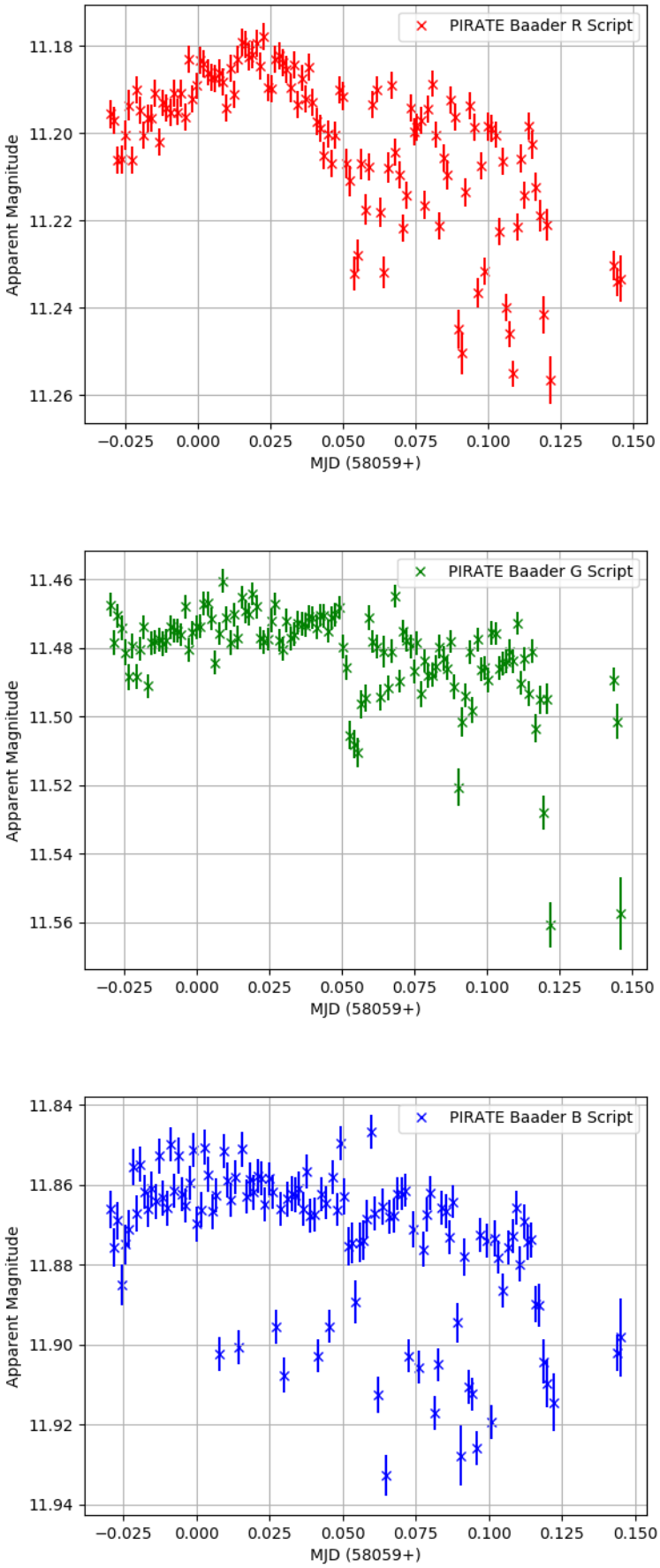

Figure 75: The first night of observations from PIRATE for the Kojima microlensing event, using the EPP.

Filter (Baader)	t_0 (MJD)	t_0 (HJD')
R	58059.0059 ± 0.1893	8059.51037
G	58058.9547 ± 0.4434	8059.45917
B	58059.0065 ± 0.2561	8059.51098

Table 10: t_0 for the Kojima microlensing equation calculated using PIRATE data from 2017-11-01. For comparison Zang et al. 2019 found t_0 to be HJD' 8058.76, which means that the PIRATE data missed t_0 by a day.

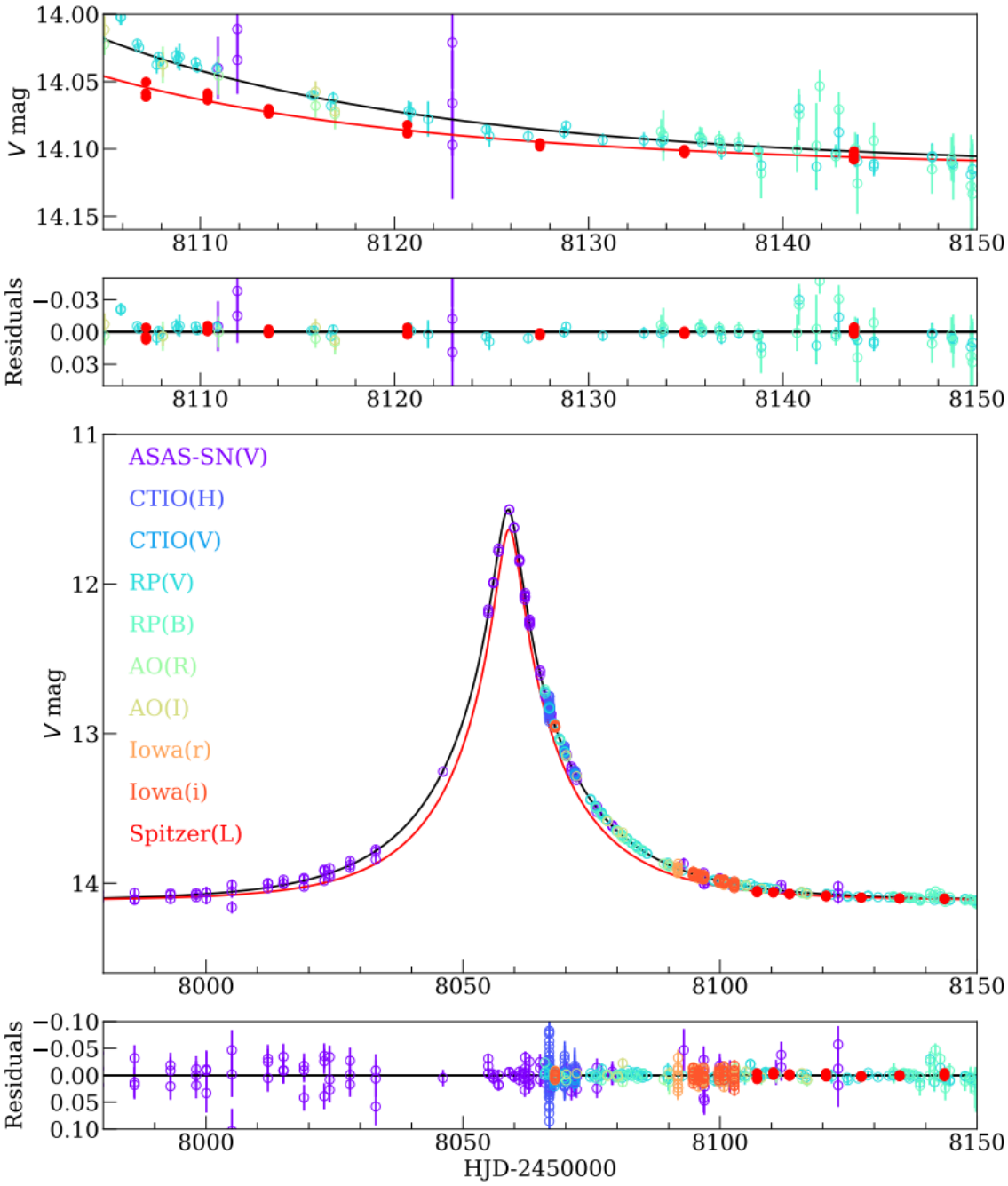

Figure 76: Kojima light curve from the paper (Zang et al. 2019).

Other Observed Microlensing Events

Alternate Names	Baseline Mag (Gaia G filter)
Gaia17bdk	18.5
Gaia17bej	17.6
Gaia17ctl	19.6
Gaia18cjk	17.0

There are a few suspected microlensing targets which were observed with PIRATE, but with data which could not be extracted either by the CPCS or by the EPP. I include them here with a brief explanation for why the data was unusable.

Gaia17bdk, Gaia17bej and Gaia17ctl all appear to be skirting the limit where PIRATE photometric uncertainty increase markedly. The Gaia G filter overlaps most with the Baader R and Johnson R filters which PIRATE uses, and at 18 mag for both filters the standard deviation for data is around 0.15 mag. While there are some targets which do still present results either from the EPP, or from the CPCS at those magnitudes, the failing targets are also in significantly crowded fields. Both of these in combination mean that source extractor, which is necessary for both analysis methods, is going to have trouble picking out the target star.

Gaia18cjk is a little brighter in the Gaia G filter, so could still at least be detectable. According to the source extractor flags, Gaia18cjk appears to be blended with another star which would account for why it was not accepted by the EPP.

PIRATE and Microlensing events

PIRATE certainly is capable of capturing the level of variation which is visible in microlensing events, a lot of the events found by Gaia peak well inside the useful PIRATE observing magnitude range, but the baseline magnitude sometimes is too faint for accurate photometry. It should be possible to identify the peak time and magnitude of single microlensing events, as was attempted with the Kojima microlensing event, but unfortunately none of the observed events were identified in time for me to schedule them in PIRATE before the peak.

8.2 Supernovae

There are a disproportionately high number of supernovae amongst the targets which were followed up. This is because early on there was an attempt to have targets chosen automatically from the Gaia alerts page according to their visibility to PIRATE, but this did not have access to information about what their suspected classification was in an automated way. Because a large proportion of the Gaia alerts appear to be supernovae the automated process picked up a lot of them. Once target selection became more specific, some targets which were initially unknown would later be identified as supernovae.

The targets which have been previously identified as supernovae can be split into two groups, ones which also have a suspected classification for supernova type, and those which do not.

Many of the type identifications on the Gaia Alerts website come from the use of GS-TEC transient events classifier (Blagorodnova et al. 2014), a tool which uses the low resolution spectrophotometry and photometry obtained by the Gaia satellite. The spectra are modelled using a Bayesian method in conjunction with a specifically constructed reference library and literature-driven priors. The classification success rate, which is dependent on supernova type, for model data is around 75% for targets brighter than 19 mag in the Gaia G filter, dropping below 60% for fainter targets.

We will attempt to either corroborate or contradict these identifications, or give them an identification with the PIRATE data where possible by attempting our own classification. The main classification of supernovae splits them by the presence or lack of hydrogen in their spectra into type I or type II respectively, but they also have relatively distinct light curve shapes. Figure 17 as discussed in chapter 3.5 of the main sub-types of supernovae light curves as observed by the Lick observatory for the Lick Observatory Supernova Search (LOSS). The key features to pick out are identified in the same chapter.

Classified

Gaia17bhs

Alternate Names	Classification	RA (J2000)	DEC (J2000)	Alert Date	Alert Mag (Gaia G Filter)
Gaia17bhs, PS17dal	Ia	10:14:32.51	-02:16:24.85	2017-05-18 14:55:19	17.52

Discovered by Pan-STARRS1 on 2017-05-11 (Chambers et al. 2017) and picked up by Gaia on 2017-05-18. No classification has yet been made for the supernova type except by GS-TEC which lists it as a probable type Ia.

The PIRATE data collected only has a handful of points before the target became too faint to observe. In figure 77 we can see that the light curve produced by the EPP appears to decline at a similar rate to the Gaia G data. By fitting a linear curve using the least squares method to the Gaia, CPCS and EPP data, we get the data in table 11. The EPP and CPCS data appear to be similar, though the Gaia data decline rate is outside the range of the other two values, even when taking into account the errors.

Filter	Decline Rate (mag/day)
Gaia G	0.048 ± 0.004
Baader R (CPCS)	0.031 ± 0.004
Baader R (EPP)	0.032 ± 0.005

Table 11: Gaia17bhs decline rates. These rates were calculated using a linear weighted least squares fit to the PIRATE data and Gaia data.

The discrepancy appears to be due to the later data points in the PIRATE data, which are above the linear decline suggested by the Gaia data. The uncertainties for those data points are quite large, at around 0.25 magnitude, which is as large as the apparent deviation from the linear decline.

For comparison, table 1 of Folatelli et al. 2010 lists the Δm_{15} decline rates of 34 type Ia supernova. Δm_{15} is the change in magnitude 15 days after the supernova has peaked, and is therefore not directly comparable in this case, as we don't have the peak of the light curve to measure from. Δm_{15} is only useful if the decline rate is constant, but about 25-30 days after maximum the decline rate of Ia supernovae slows (Phillips et al. 2017). At best we can say that 15 days at the decline rates calculated is a little

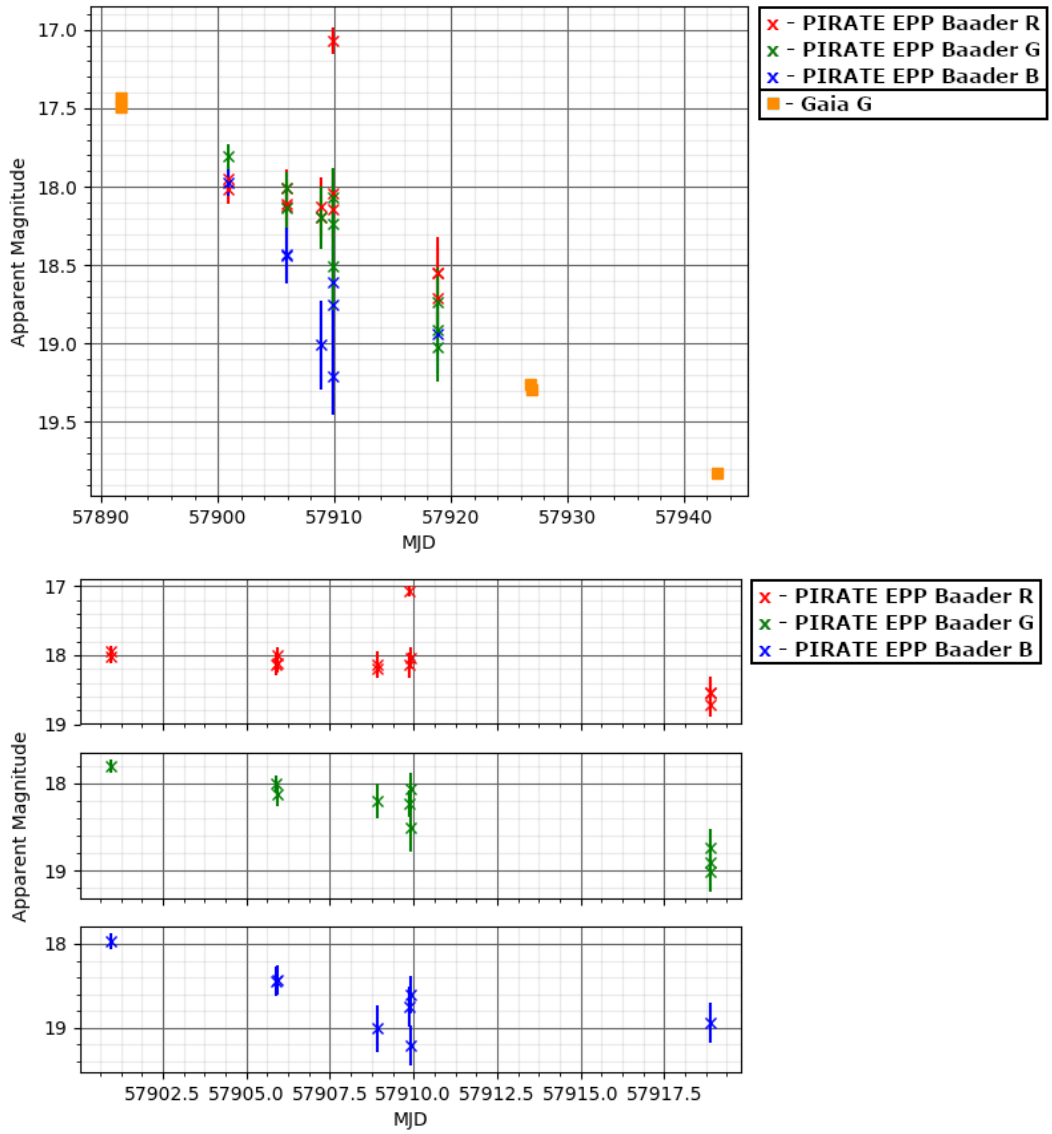

Figure 77: In the top figure, the Gaia17bhs PIRATE EPP light curve in context with the Gaia data calibrated to the apparent apparent magnitude using the method described in section 6. The bottom figure is a close up of the PIRATE EPP light curves

low compared to the Δm_{15} reference rates, which would be expected for decline rates calculated some time after peak brightness in a type Ia.

Gaia17bij

Alternate Names	Classification	RA (J2000)	DEC (J2000)	Alert Date	Alert Mag (Gaia G Filter)
Gaia17bij, ATLAS17fnt	Ia	10:52:04.44	11:35:41.86	2017-05-22 03:07:47	17.18

Gaia17bij was discovered by ATLAS on 2017-05-19 (Tonry et al. 2017c) and picked up by Gaia on 2017-05-22. Spectroscopic classification given by the Lick Shane telescope suggests it is a type Ia (Coulter et al. 2017).

CPCS picked up enough data points in all filters that the EPP data could be calibrated to apparent magnitude. There are only three data points from Gaia for this target all clustered together right at the beginning of the light curve (figure 78), which means most of the interpretation is down to the data collected by PIRATE.

There appears to be a plateau feature in all three passbands beginning at 57914 MJD, which would typically be indicative of a type II supernova as opposed type Ia.

If we assume that all of the PIRATE data occurs after peak brightness, and use only the data before MJD 57914, we can calculate the decline rates shown in table 12 after using a least squares best fit.

filter	decline (mag/day)
Baader R	0.014 ± 0.002
Baader G	0.019 ± 0.012
Baader B	0.036 ± 0.004

Table 12: Gaia17bij decline rates as calculated using PIRATE data and a linear least squares best fit.

They are very different for each passband, probably due to the small amount of data for the target. Despite the differences the decline rates are again more indicative of a type II supernova, closer to 0.01 mag per day than the expected 0.1 mag per day for a type Ia.

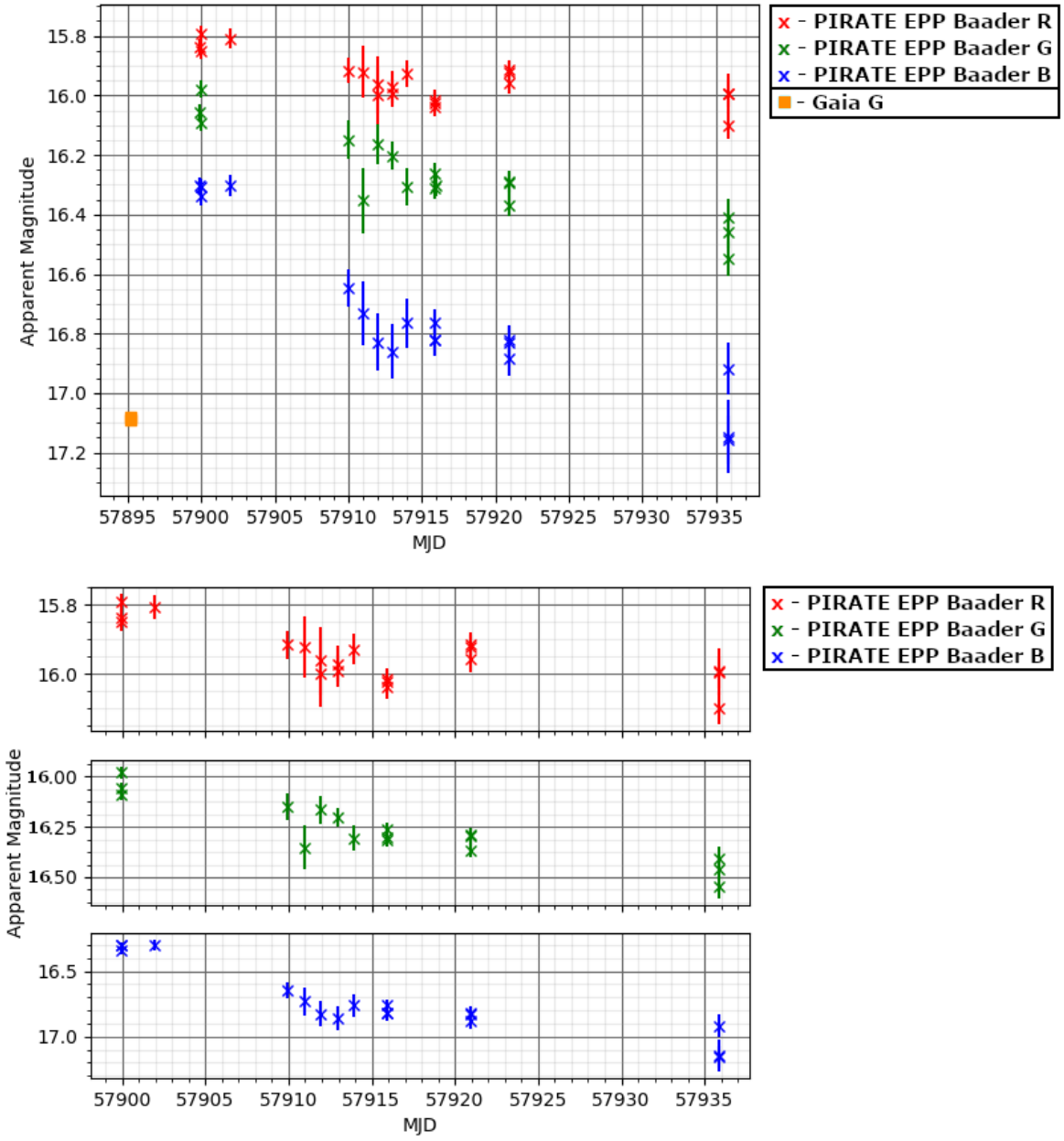

Figure 78: The top figure shows the Gaia17bij PIRATE EPP light curve with the context of the Gaia light curve. The Gaia data only appears as three points overlapping in the bottom left corner of the figure. The lower figure is the PIRATE EPP data calibrated using the CPCS data as in section 6.

Gaia17bim

Alternate Names	Classification	RA (J2000)	DEC (J2000)	Alert Date	Alert Mag (Gaia G Filter)
Gaia17bim, AT2017efy	II	00:09:15.74	30:29:09.31	2017-05-22 19:02:29	17.76

Discovered by Gaia on 2017-05-22 (Delgado et al. 2017d). Classification only by GS-TEC so far, which predicts type II.

This target started off very faint at 17.76 alerting magnitude, but PIRATE still did a good job collecting recognisable data until the target got to ∼18.2 in the Gaia G filter.

The decline rates (table 13) have assumed that the PIRATE data doesn't include the peak of the supernova as visual inspection suggests only a steady decline period for the supernova has been caught. Bumps or dips in the light curve are accounted for by the noise in the data. There is a lot of variation in type II supernova decline rates, but a type II typically declines at around 0.01 ± 0.002 mag per day. Since Gaia17bim is declining at a rate very close to this it is safe to assume that it was a type II supernova.

filter	decline (mag/day)
Gaia G	0.013 ± 0.0003
Baader R	0.012 ± 0.002
Baader G	0.012 ± 0.002
Baader B	0.012 ± 0.002

Table 13: Gaia17bim decline rates as calculated using PIRATE data.

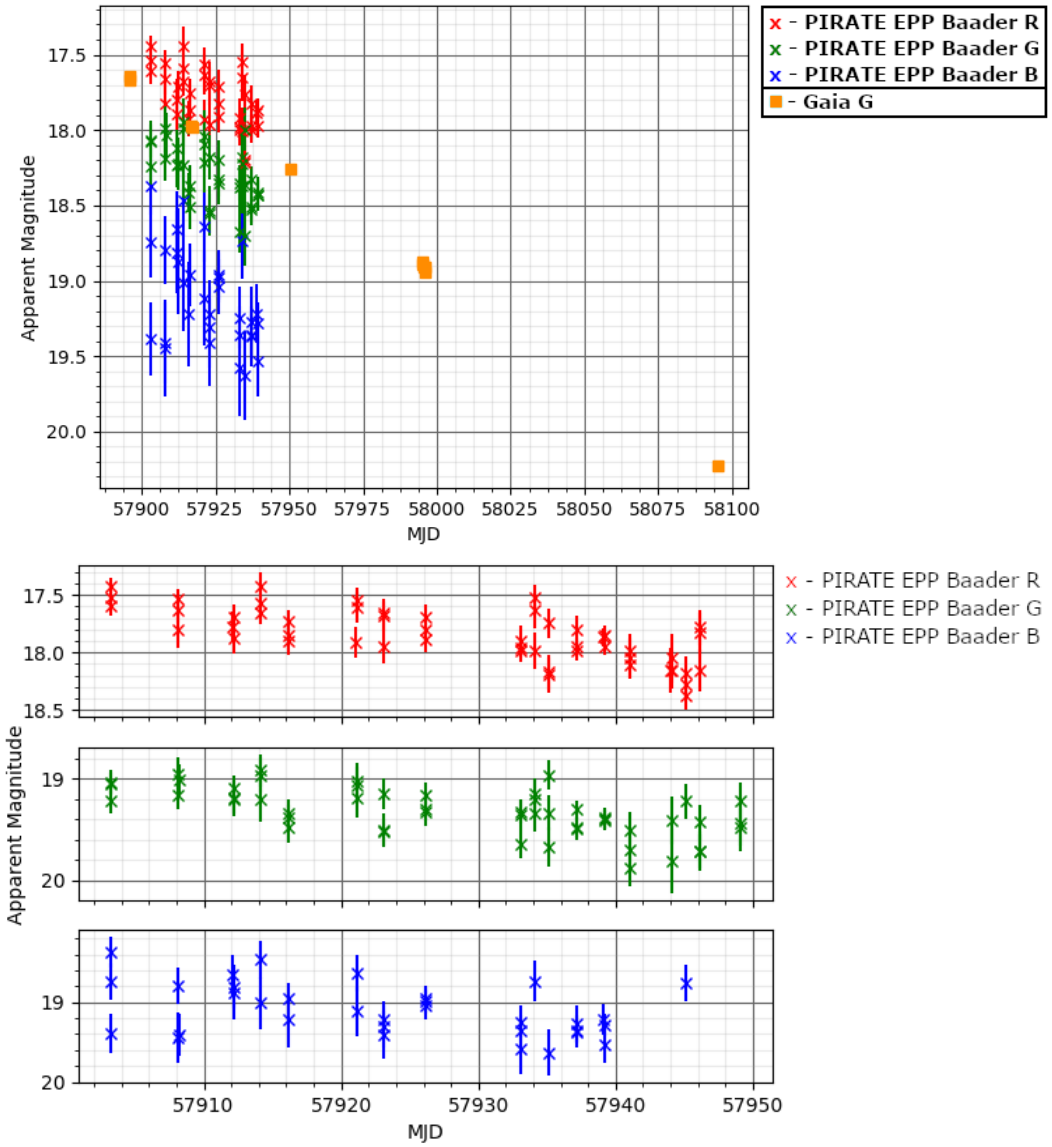

Figure 79: The top figure has the Gaia17bim Gaia and PIRATE EPP data which have been calibrated using the CPCS data as in the method explained in section 6, and the lower figure displays the EPP data for each filter individually.

Gaia17bjv

Alternate Names	Classification	RA (J2000)	DEC (J2000)	Alert Date	Alert Mag (Gaia G Filter)
Gaia17bjv, AT2017efs	Ia	11:51:06.12	43:24:52.13	2017-05-27 15:38:14	17.87

Discovered by ATLAS on 2017-05-23 (Tonry et al. 2017d) and picked up by Gaia on 2017-05-27. Classification only by GS-TEC so far, which predicts type Ia.

The light curves (figure 80) from CPCS and the EPP are a little noisy, as observations of the target didn't begin until after it was below 18.0 mag, which is very faint for PIRATE.

Decline rates (table 14) do appear to match the Gaia G data. The rates are lower than would be expected if the supernova had been caught immediately after the peak, where it should be declining at about 0.1 mag per day if it is a type Ia, but as it isn't unusual for type Ia to slow down to around 0.01 mag per day after 20-30 days; this could have been caught some time around 20 days after the peak. The only discrepancy is the B decline rate which is closer to 0.1 mag per day, but the B data are very faint at ~ 19.0 mag, and towards the end of the light curve the uncertainties are more than 0.25 mag.

filter	decline (mag/day)
Gaia G	0.052 ± 0.003
Baader R	0.051 ± 0.002
Baader G	0.051 ± 0.003
Baader B	0.104 ± 0.019

Table 14: Gaia17bjv decline rates as calculated using PIRATE data.

There may be a bump in the data in the R and G data around 57935 MJD, but the data are very noisy and there's a gap in the data of around 8-10 days just before then, which may make it appear as a feature which isn't really there. But at 18.5 mag the R filter data reaches around 0.25 mag standard deviation, which is very large and not reliable enough to make any statement about that being a true feature.

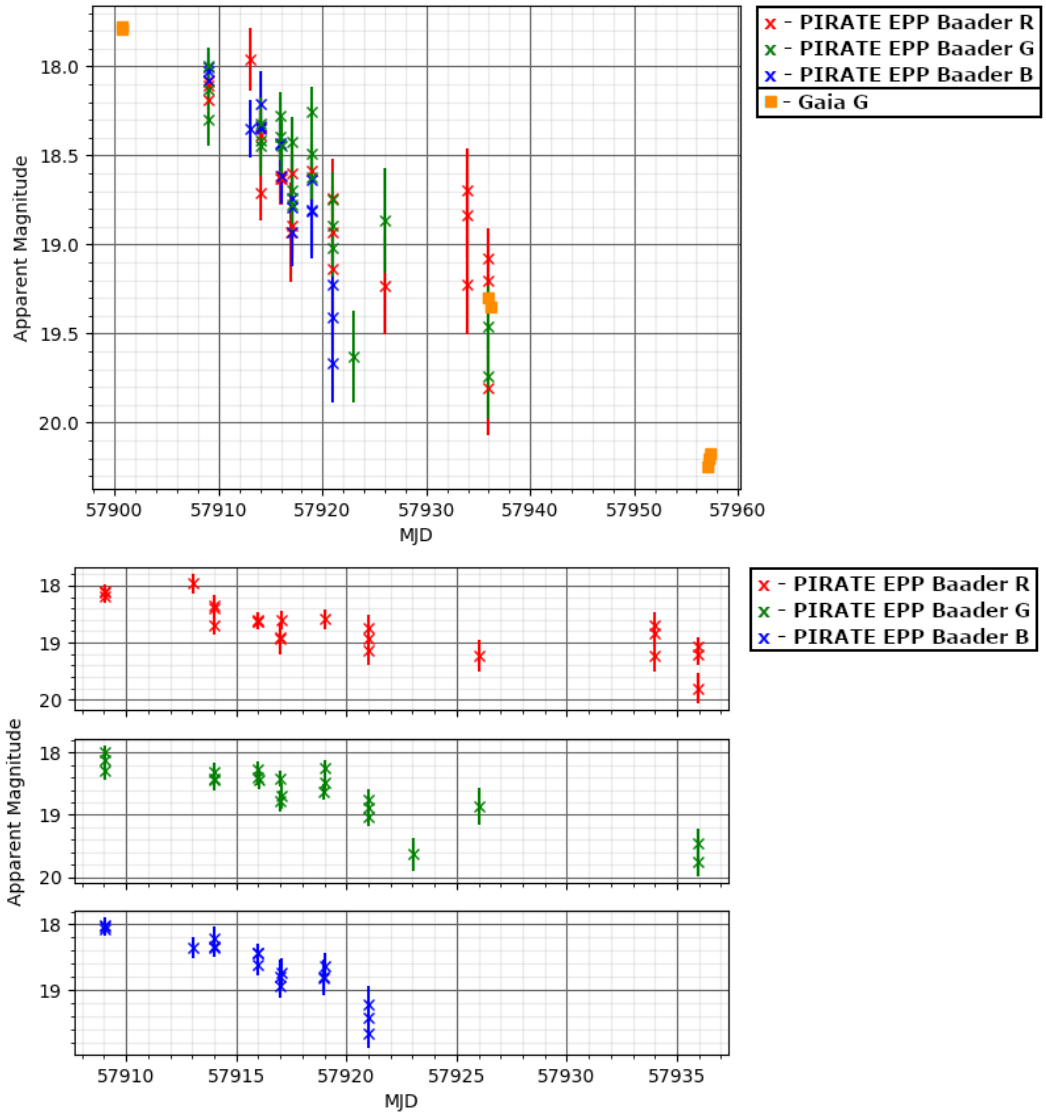

Figure 80: The top figure has the Gaia17bjv PIRATE EPP data in the context of the Gaia data, the lower figure has the EPP data displayed individually.

Gaia17bjw

Alternate Names	Classification	RA (J2000)	DEC (J2000)	Alert Date	Alert Mag (Gaia G Filter)
Gaia17bjw, SN2017ein	Ic	11:52:53.25	44:07:26.11	2017-05-27 15:38:50	16.90

Discovered by Ron Arbour on 2017-05-25 (Arbour 2017) and picked up by Gaia on 2017-05-27. Classified by Xinglong Station of National Astronomical Observatories of China (NAOC) on 2017-05-28 as a peculiar broad-line type Ic (Xiang et al. 2017a).

On 2017-06-10 a group working as part of the Intensive Monitoring Survey of Nearby Galaxies (IMSNG) program reported that photometric follow-up indicated that the target was first detected fairly soon after first going supernova (Im et al. 2017), and on 2017-06-13 a group presented data indicating that the progenitor for the supernovae had been found in archival Hubble Space Telescope (HST) (Van Dyk et al. 2017) data from the Wide Field Planetary Camera 2 (WFPC2) from December 2007. The initial brightness was 24.81 ± 0.11 mag in the F555W filter which, although not identical to the Baader filter, is very similar to the Baader G filter. Van Dyk et al. 2018 reported the target as possibly the first type Ic supernova with progenitor data, along with calculations for some of the light curve characteristics.

Type Ic are core collapse supernova which tend to have spectra which have no hydrogen lines, and little to no helium or silicon. For a star to lose such a large quantity of hydrogen and helium it must lose mass effectively, leading to the ideas that type Ic progenitors may be high mass-loss Wolf-Rayet stars (Georgy et al. 2009), or another possibility is that they are lower mass stars which have undergone envelope stripping in a binary system (Dessart et al. 2012).

The EPP failed to produce a light curve for this target (figure 81), which is likely because of where the supernova was situated, in the disc of NGC3938, a spiral galaxy approximately 20Mpc distant. The blending of the target with the galaxy means that the EPP did not produce a light curve, but CPCS did produce a light curve.

Figure 81 shows a very clear supernova peak, indicating that the target was found around 10-15 days before maximum. The same figure also appears to show that the peak occurred earlier in the blue filter (the shorter the wavelength). Since data around the peak is available for this target I have attempted to make some estimates for the maximum peak time and brightness, along with the Δm_{15}.

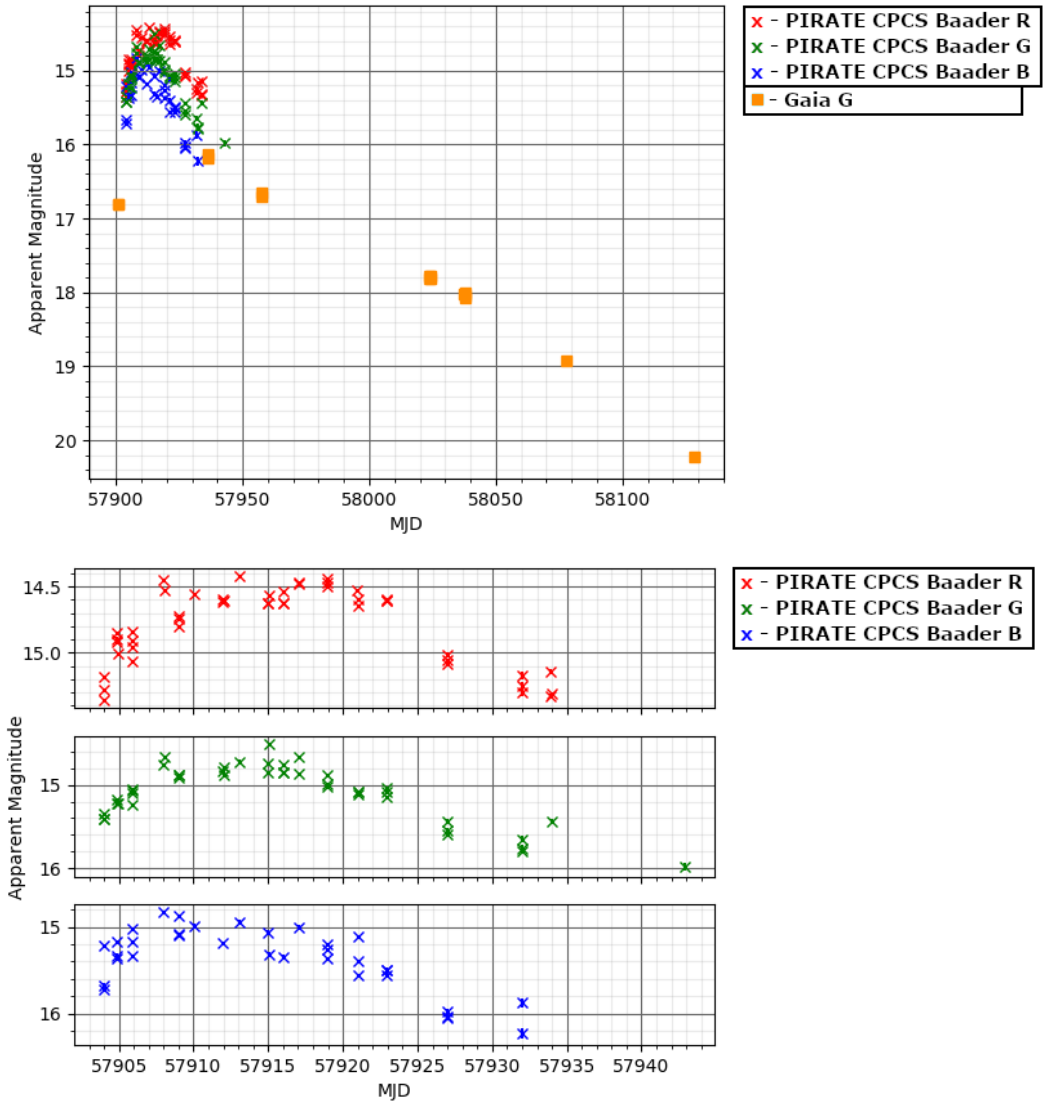

Figure 81: In the top figure the Gaia17bjw PIRATE CPCS data in the context of the Gaia data. The other three graphs show the PIRATE CPCS data individually.

To calculate the approximate maximum, a quadratic was fitted to the different filter light curves, and then the maximum of the quadratic was calculated. This only provides a rough estimation, and a full treatment would require a better model to fit to the data. The date of maximum for each filter along with the maximum brightness was used as a starting point for the Δm_{15} value which was calculated using a linear fit model. The values calculated are plotted in table 15.

For comparison, Van Dyk et al. 2018 gave V band maximum at around MJD 57912.6, and R band maximum approximately at MJD 57915.5. The V and R band filters used for these observations are Johnson-Cousins filters, but approximately correspond to Baader G and R respectively. Although the dates calculated here do overlap with the dates given by Van Dyk et al. 2018, there is a large uncertainty in the PIRATE values. While I used a simple quadratic for the fitting, Van Dyk et al 2018 used a H-free

SNe analytic model to more accurately model the light curve. The two data sets do agree that there was ~ 3 days difference between the peaks in the two passbands. This lag happens due to the progressive cooling of the expanding photosphere of the star, the effect this has on the blackbody radiation of the photosphere is to the reduce the total energy output, affecting blue wavelengths more than red, shifting the colour of the supernova from blue to red with time.

filter	**Date of Maximum (MJD)**	**Brightness at Maximum (mag)**	**Decline Rate (mag/day)**	Δm_{15} **(mag)**
Baader R	57917 ± 10	14.52 ± 3.24	0.055 ± 0.007	0.825 ± 0.105
Baader G	57915 ± 14	14.85 ± 6.10	0.062 ± 0.007	0.930 ± 0.105
Baader B	57912 ± 19	15.05 ± 8.70	0.080 ± 0.013	1.20 ± 0.195

Table 15: Gaia17bjw decline rates and information on the maximum, calculated using PIRATE data and a quadratic least-squares fit.

The $\Delta m_{15}(R)$ given by Van Dyk et al. 2018 is 0.87 mag, which was calculated using a combined light curve made from the data collected by the Katzman Automatic Imaging Telescope (KAIT) and the Nickel telescope at Lick Observatory (figure 82). A $\Delta m_{15}(R) = 0.87$ is within uncertainty of the $\Delta m_{15} = 0.825 \pm 0.105$ calculated using the PIRATE data.

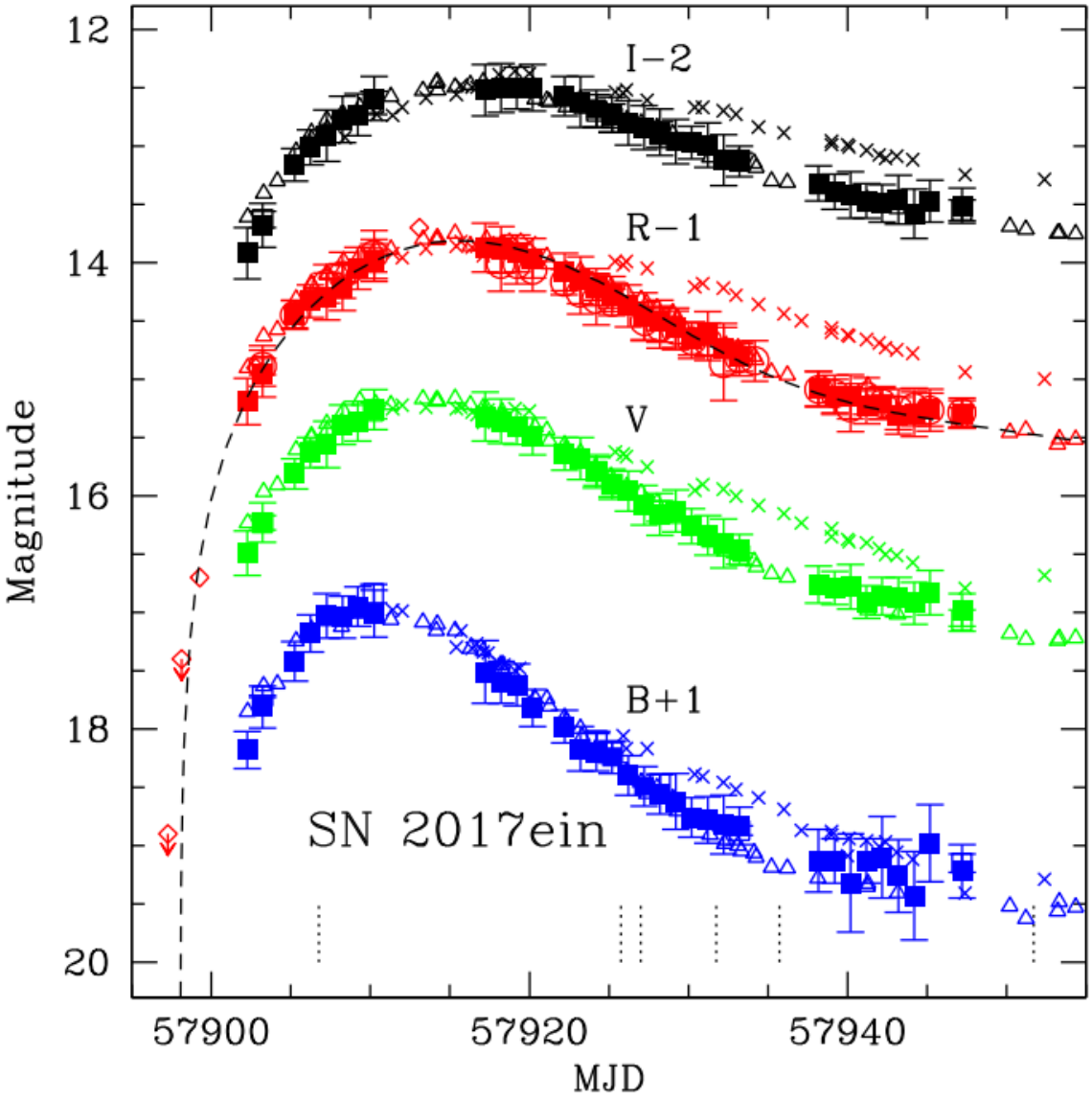

Figure 82: Gaia17bjw light curves using KAIT and Nickel data (Van Dyk et al. 2018).

Gaia17bjy

Alternate Names	Classification	RA (J2000)	DEC (J2000)	Alert Date	Alert Mag (Gaia G Filter)
Gaia17bjy, AT2017eea	Ia	12:23:54.19	09:07:28.34	2017-05-27 15:06:37	18.00

Discovered by ATLAS on 2017-05-19 (Tonry et al. 2017c) and picked up by Gaia on 2017-05-27. Classification only by GS-TEC so far, which predicts type Ia.

Another very faint target alerting at 18th magnitude, the different passbands of data are difficult to separate from one another. There appears to be something unusual going on with the R and G measurements in the last three nights the target was observed (figure 83), but there is no B data that late in the light curve. The target would be expected to be fainter than 19th magnitude if the data could be extrapolated from their decline rates, which were calculated using all but the last three nights of data (table 16).

filter	decline (mag/day)
Baader R	0.029 ± 0.007
Baader G	0.060 ± 0.010
Baader B	0.087 ± 0.014

Table 16: Gaia17bjy decline rates, the value for Baader R is taken ignoring the last 5 data points (over the same range as the B and G data

The behaviour of the data in the last three nights of observations is suspicious, as a single measurement out of three R taken at approximately the same time to be almost a magnitude brighter than the others would be a very clear indication of some activity. Upon inspection of the image frames it is clear that the target did not have a sudden brightening, in fact for all three nights the target in the R filter is only a handful of counts above background with a signal to noise less than 0.1. The measurements in these last three nights are on the edge of reasonable limits for even a sensible detection threshold, let alone carrying out accurate photometric measurements. Given this, the last three nights of data collected can be reasonably discarded as unreliable and should not be used to draw any meaningful conclusions.

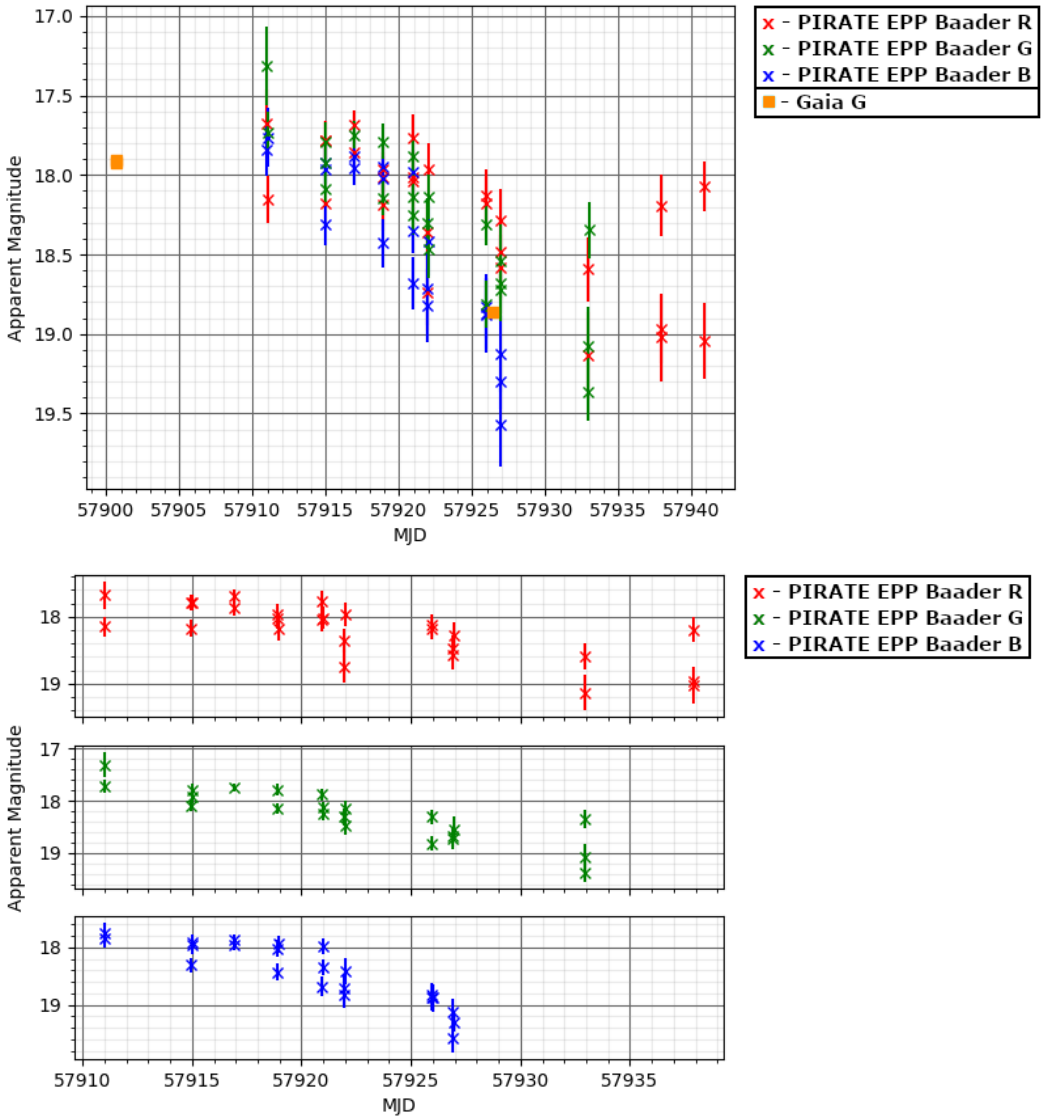

Figure 83: The top figure shows the Gaia17bjy PIRATE EPP data in the context of the Gaia data, the lower figure has the PIRATE EPP data individually.

Gaia18beg

Alternate Names	Classification	RA (J2000)	DEC (J2000)	Alert Date	Alert Mag (Gaia G Filter)
Gaia18beg, SN2018bgv	SLSN-I	11:02:30.29	55:35:55.79	2018-05-06 17:20:49	18.26

Discovered by Gaia on 2018-05-06 (Delgado et al. 2018m). Classified as a type I superluminous supernova by The Nordic Optical Telescope (NOT) Unbiased Transient Survey (NUTS) spectroscopically (Delgado et al. 2018m).

The light curves from PIRATE show a declining object which has a definite bump feature at about 58285 MJD. The feature appears in all passbands, maybe starting around 5 days earlier in the Johnson B passband. Bumps in the declining part of light curves are sometimes visible in superluminous SNe I (called undulations in Inserra et al. 2017 and bumps in Moriya et al. 2018), and there are several models which are proposed for explaining these undulations such as the infall of material onto a newly formed black hole after the initial supernova event (Dexter et al. 2013), or the supernova ejecta interacting with dense circumstellar material and creating shocks which turn kinetic energy into radiation (Chevalier et al. 2003).

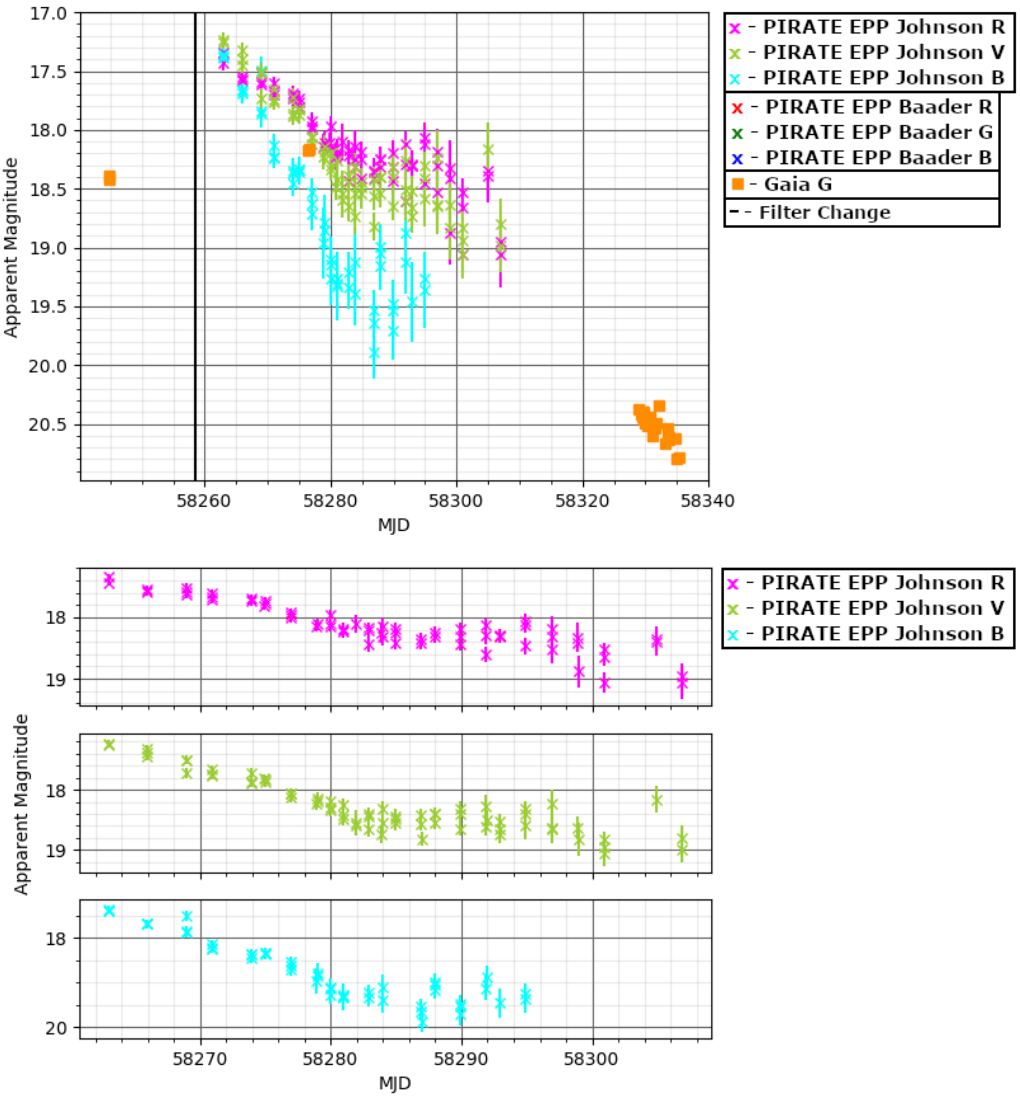

Figure 84: The top figure shows the Gaia18beg PIRATE EPP and Gaia data, and the bottom figure puts has just the PIRATE EPP data.

Gaia18bbf

Alternate Names	Classification	RA (J2000)	DEC (J2000)	Alert Date	Alert Mag (Gaia G Filter)
Gaia18bbf, SN2018aqe	Ia	14:35:53.65	35:17:15.40	2018-04-24 11:55:21	17.85

Discovered by ASAS-SN on 2018-04-05 (Stanek 2018b) and spotted by Gaia on 2018-04-24. Classification by ASAS-SN on 2018-04-12 as a type Ia (Bose et al. 2018b).

This target appears to have been mislabelled with the wrong RA and DEC somewhere along the way, likely on the Gaia alerts page. Despite there being a clear indication of a decline in the Gaia data (figure 85), the data from both CPCS and the EPP agree that the target appears to be a featureless, flat light curve.

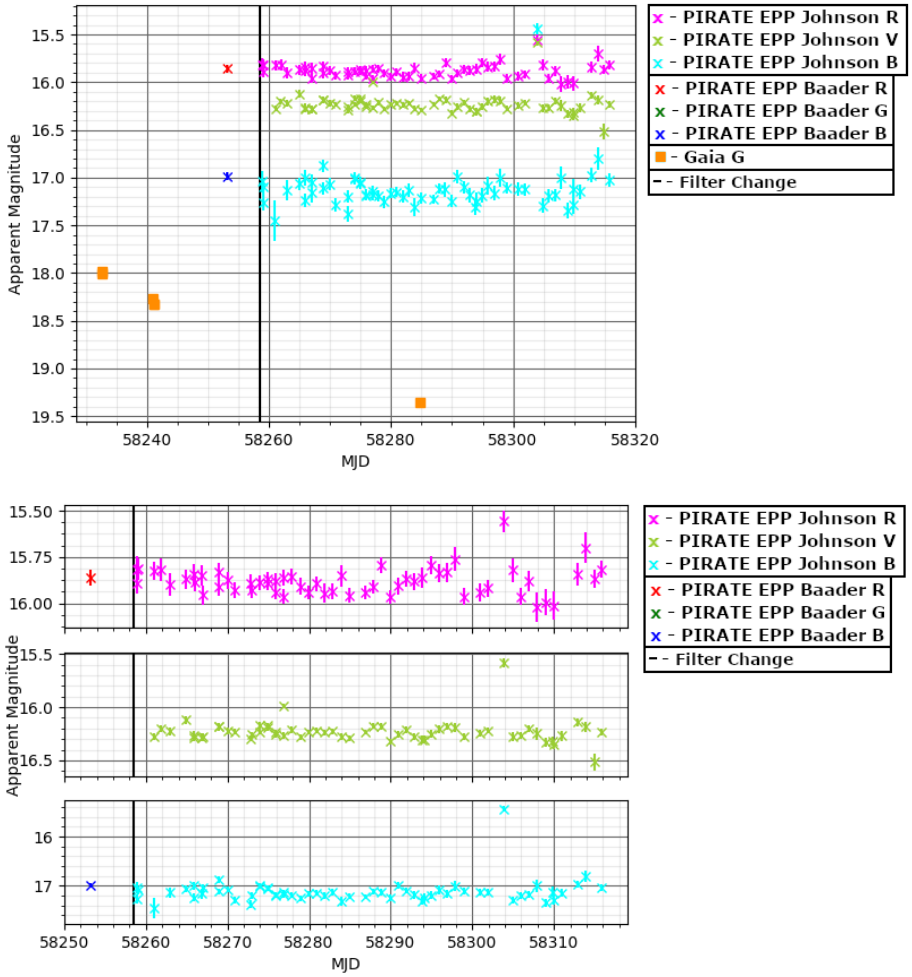

Figure 85: The top figure has the Gaia18bbf PIRATE EPP light curve and Gaia data which is not is presenting the same behaviour as the PIRATE data at all, the bottom figure has just the PIRATE EPP data.

Gaia18bek

Alternate Names	Classification	RA (J2000)	DEC (J2000)	Alert Date	Alert Mag (Gaia G Filter)
Gaia18bek, SN2018bhc	Ia	16:46:25.29	25:25:17.26	2018-05-07 18:33:43	17.80

Discovered by Gaia on 2018-05-07 (Delgado et al. 2018n). Classified by the extended Public ESO Spectroscopic Survey for Transient Objects (ePESSTO) spectroscopically as a type Ia (McBrien et al. 2018).

This target is clearly not actually a supernovae at all, in fact from the Gaia data alone this target appears to perhaps be a microlensing event. It could be some kind of outburst from the star, but what is available of the light curve appears to be a symmetrical peak which would be suggestive of a microlensing event.

The data from the EPP does appear to decrease in brightness, by about 0.5 mag over the course of the observations which cover ~ 80 days.

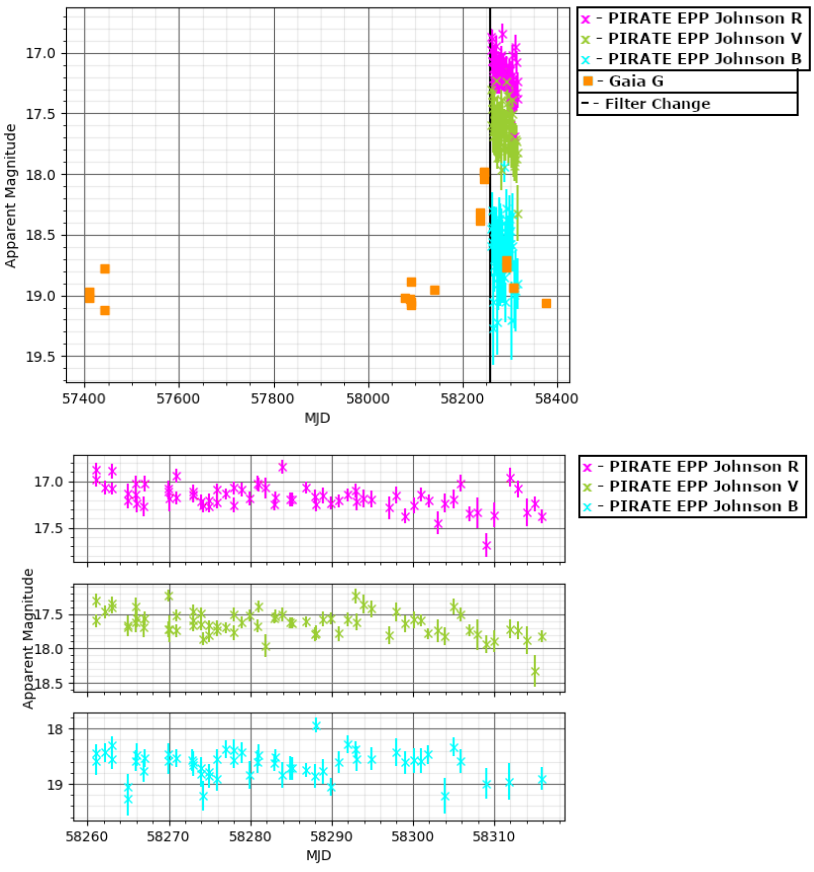

Figure 86: The Gaia18bek Gaia data appears to be a microlensing event, the PIRATE EPP data agrees and seems to have caught the declining part of the light curve.

Other Observed Classified Supernovae

There are images for some supernova targets which did not produce a photometric measurement. In most cases this is due to the target being relatively faint to begin with. If there is no target data brighter than $\sim$ 18.0 mag then it's unlikely to have been picked up by source extractor due to the low signal to noise. Some targets also happen to be in crowded fields, or blended with other objects such as Gaia17bbu which is located in NGC 9567.

Alternate Names	**Alert Mag (Gaia G Filter)**	**Discovery**	**Classification**
Gaia17bbj, AT 2017bkc	18.55	ASAS-SN (Brimacombe et al. 2017a)	Ia, ASAS-SN (Prieto et al. 2017)
Gaia17bbt, SN2017dgs	17.59	Gaia (Delgado et al. 2017a)	II, NUTS (Kankare 2017)
Gaia17bbu, SN2017czd	16.22	Koichi Itagaki (Itagaki 2017a)	II, Las Cumbres Observatory (Hosseinzadeh et al. 2017)
Gaia17bdd, AT2017cts	16.60	ASAS-SN (Stone et al. 2017b)	Ia, Liverpool Telescope (Bersier 2017)
Gaia17bhq, AT2017eem	17.88	Gaia	Ia, GS-TEC only
Gaia17bic, SN2017dae	17.42	ATLAS (Tonry et al. 2017b)	Ia, Shane telescope (Siebert et al. 2017)
Gaia17bie, SN2017dzs	16.99	Koichi Itagaki (Itagaki 2017b)	Ia, Ms Miho Kawabata (Kawabata 2017)
Gaia17big, SN2017eex	17.58	ASAS-SN (Stone et al. 2017a)	Ia, ASAS-SN (Falco et al. 2017)
Gaia17bii, SN2017byz	16.92	ASAS-SN (Tonry et al. 2017a)	II, ESO Spectroscopic Survey (Taddia et al. 2017)
Gaia17biu, SN2017egm	16.72	Gaia (Delgado et al. 2017e)	SLSN-I, NUTS (Dong et al. 2017)
Gaia17bjq, SN2017cjr	17.41	ASAS-SN (Brimacombe et al. 2017b)	Ia, PESSTO (Fraser et al. 2017)
Gaia17bls, SN2017dka	18.61	Jaroslaw Grzegorzek (Grzegorzek 2017)	II, PESSTO (Cartier et al. 2017)

Alternate Names	Alert Mag (Gaia G Filter)	Discovery	Classification
Gaia17cpb, SN2017gqr	16.81	POSS (Gagliano et al. 2017)	Ia, Mr Verilhac Daniel (Daniel 2017)
Gaia18ack, SN2017jzp	18.74	Gaia (Delgado et al. 2018a)	Ia, NUTS (Kuncarayakti et al. 2018)
Gaia18azm, SN2018ast	17.02	Yuji Tanaka (Tanaka 2018)	Ia, ASAS-SN (Bose et al. 2018a)
Gaia18bbt, SN2018anh	18.08	ATLAS (Tonry et al. 2018)	II, Palomar 60-inch (Blagorodnova et al. 2018)
Gaia18bca, SN2018bdo	18.56	Gaia (Delgado et al. 2018k)	Ia, NUTS (Fraser et al. 2018)
Gaia18bej, SN2018apn	18.14	ASAS-SN (Stanek 2018a)	Ia, ASAS-SN (Bose et al. 2018b)
Gaia18ddp, AT2018hnq	18.66	Gaia (Delgado et al. 2018t)	Ia, Lee Sang Gak (Shin et al. 2018)

Unclassified

One target which was observed by PIRATE was given the classification "Supernova" by GS-TEC, but no type.

Gaia17bjj

Alternate Names	RA (J2000)	DEC (J2000)	Alert Date	Alert Mag (Gaia G Filter)
Gaia17bjj, AT2017eis	00:37:19.46	29:04:41.12	2017-05-25 19:04:10	17.59

Discovered by Gaia on 2017-05-25 (Delgado et al. 2017g). No type classification given yet, but the Gaia alerts page does list it as a supernova.

There is no CPCS data for this target, likely because it is quite faint with alerting magnitude 17.59. The differential EPP photometric magnitudes for figure 87 have been shifted to a position where the shape of the light curve can at least be compared to the Gaia data.

There is a plateau-like feature happening in the data beginning at 57932 MJD, which may be indicative of a type II supernova, or a slowing down of a type Ia supernovae decline. The Gaia data is sparse and so does not clarify the situation, but does indicate that the target is reaching 19 mag in the Gaia G filter when the feature appears in the PIRATE data, which is where PIRATE may begin to struggle to acquire a conclusive signal to noise ratio.

We can still measure the decline rates for the different passbands as in table 18. All rates are calculated only for the data between MJD 57900 and 57930.

filter	decline (mag/day)
Gaia G	0.035 ± 0.0007
Baader B	0.026 ± 0.004
Baader G	0.042 ± 0.002
Baader R	0.036 ± 0.002

Table 18: Gaia17bjj decline rates calculated using PIRATE and Gaia data.

These decline rates higher than might be expected for a typical type II supernovae,

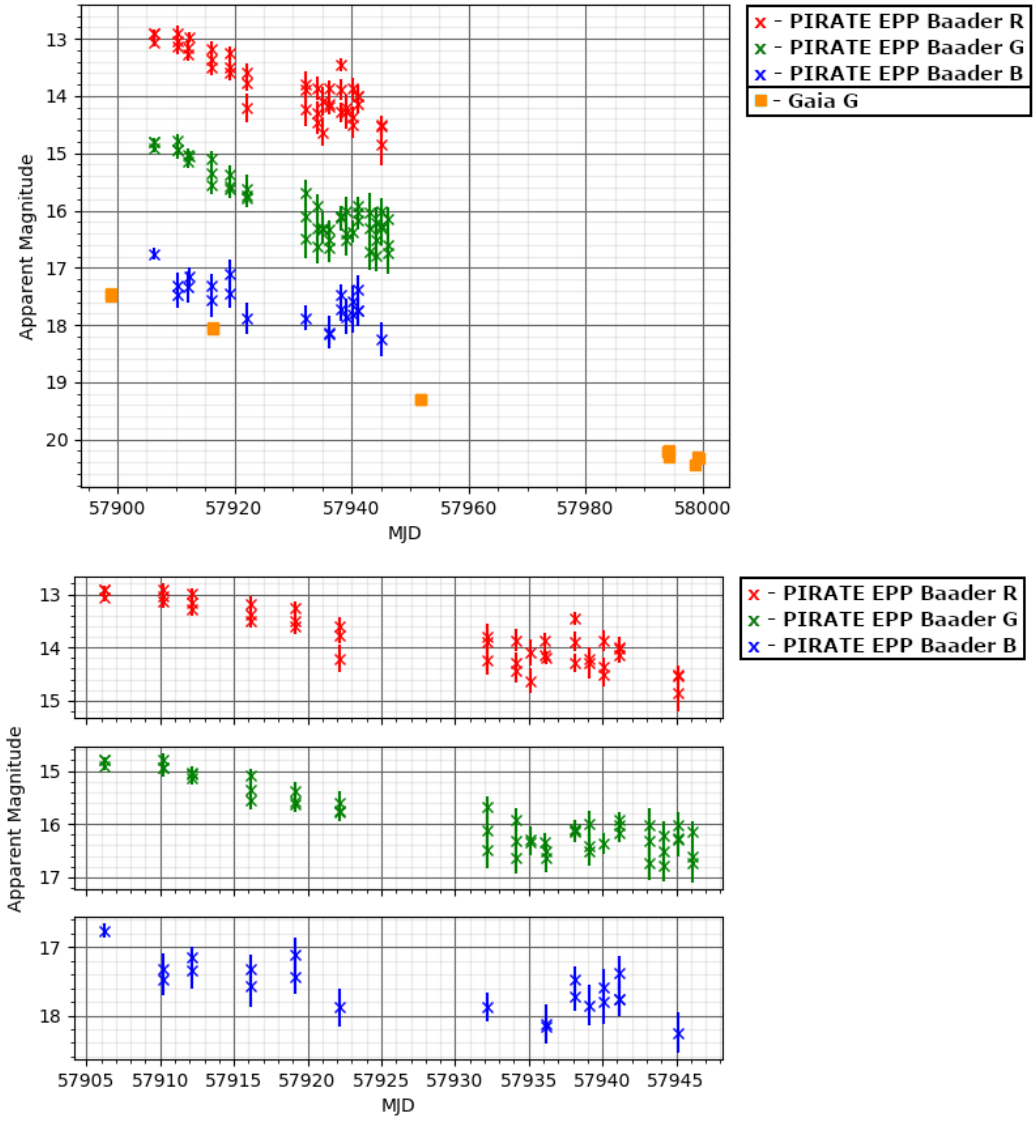

Figure 87: The top figure has the Gaia17bjj PIRATE EPP data in the context of the Gaia data, the lower figure is just the PIRATE EPP data. The magnitudes have been arbitrarily shifted to accommodate comparison with the Gaia data.

but lower than expected for pre-slow down on a type Ia. This means that supernovae type for Gaia17bjj is still not clear.

Other Observed Unclassified Supernovae

Only two targets which were classified by GS-TEC as supernova, but without a type, were observed by PIRATE, but were too faint for either EPP or CPCS to generate a usable light curve.

Alternate Names	**Alert Mag (Gaia G Filter)**	**Discovery**
Gaia17bht, AT 2017dzc	17.83	Pan-STARRS1 (Chambers et al. 2017)
Gaia17bnz, AT 2017eru	18.49	ATLAS (Tonry et al. 2017e)

PIRATE and Supernovae

Many of the supernovae observed for this project suffered from being too faint, or quickly became to faint for PIRATE to observe. The targets for which there are sufficient observations prove that PIRATE can be used to gain useful knowledge of some supernovae. Calculated decline rates are consistent for the suggested classifications in most cases, and agree with calculated Gaia decline rates.

Observations of Gaia17bjw were probably the most successful for PIRATE, being the only supernova which was observed before the maximum brightness. Simple data fittings give decline rates, and dates of maximum peak brightness which are close to published values. The difference in decline rate and maximum observed between filters is also clearly visible in the data.

Gaia18beg and Gaia17bjj show that PIRATE is sensitive enough to pick up plateau features which occur in some supernovae as they decline, important for type classification.

8.3 Cataclysmic Variables

The type of cataclysmic variable is not always easy to identify from their light curves from a short stretch of a measurements, though over longer periods many types of CV do become visually distinct. The period and intensity of brightening events can be irregular in timescale and amplitude due to the various effects which cause outbursts. Figure 88 contains two examples of CV light curves: a nova-like cataclysmic variable V794 Aql, as observed between 1990 and 2012, and an SU UMa type of dwarf novae. Although these example light curves are significantly longer than any object which will be observed during this project, it exemplifies how cataclysmic variables can be aperiodic and irregular in brightness, and that different types of CV can have significantly different light curves.

In this section we will see three targets observed by PIRATE which were initially suggested by the GSA team to be cataclysmic variables.

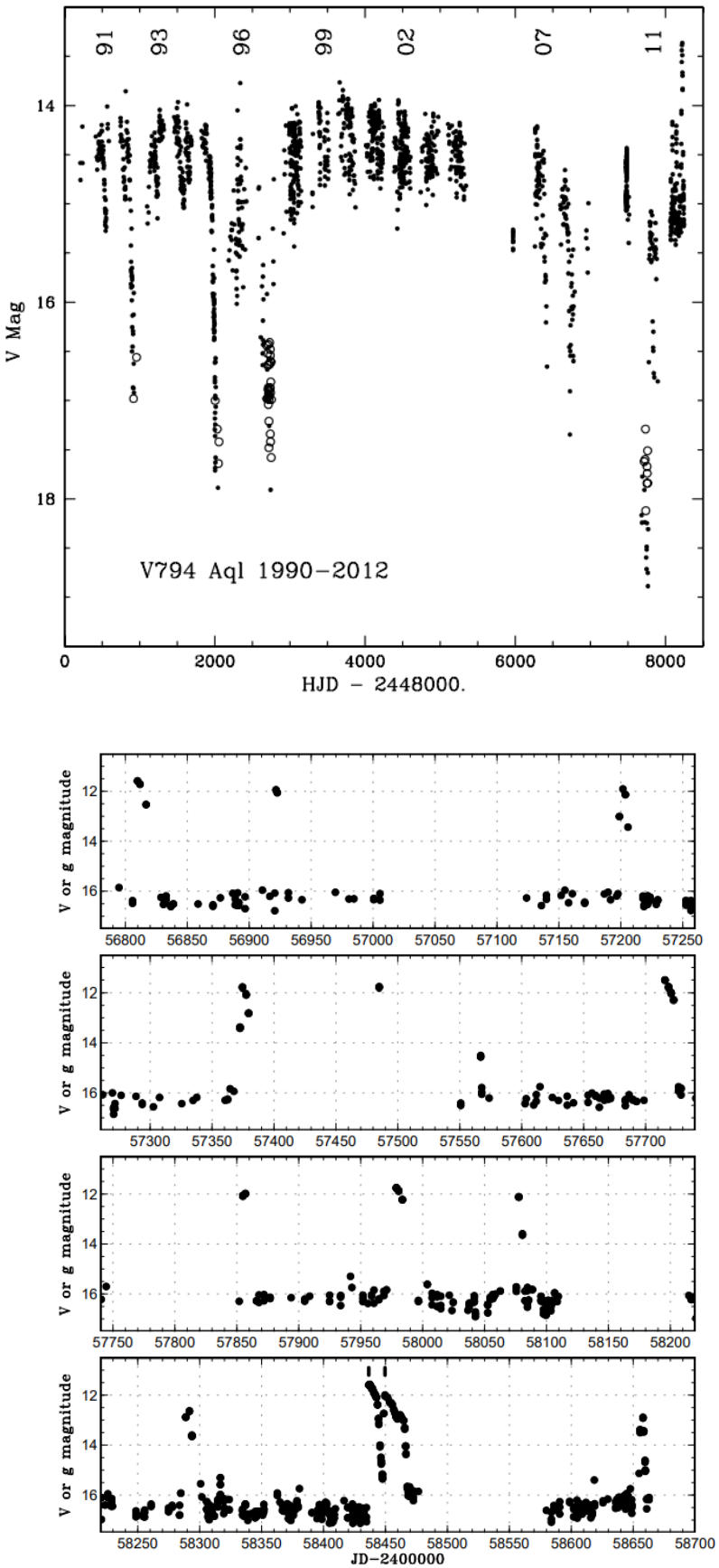

Fig. 2. Light curve of CS Ind based on the ASAS-SN data. The vertical ticks in the bottom panels represents the precursor outburst and superoutburst.

Figure 88: The top figure is V794 Aql, a nova-like light curve observed between 1990 and 2012 (Honeycutt et al. 2014). The bottom figure is CS Indi, an example of an SU UMa subtype of dwarf novae as imaged by ASAS-SN (Kato et al. 2019).

Gaia17beb

Alternate Names	RA (J2000)	DEC (J2000)	Alert Date	Alert Mag (Gaia G Filter)
Gaia17beb, AT2017dwu	18:28:46.80	32:27:05.87	2017-05-03 17:34:22	16.04

Discovered by Gaia on 2017-05-03 (Delgado et al. 2017b). Classified as a Cataclysmic Variable by TNTS by spectroscopy (Xiang et al. 2017b).

The whole light curve is very noisy, with large uncertainty due to it all being 19th magnitude or fainter, which is well below the limit at which PIRATE can carry out useful photometry beyond simple target identification.

Looking at the Gaia data (figure 89) the cataclysmic variable classification could be accurate, as the light curve appears to be some kind of classical or recurrent nova, but there is not enough data to rule out it being the latter half of a microlensing event. The target drops by 4 mag in ∼40 days, and then drops a further 1 mag over the course of the next year. Given the relatively low amount of PIRATE data, there is not a lot of useful information which can be gained beyond speculation.

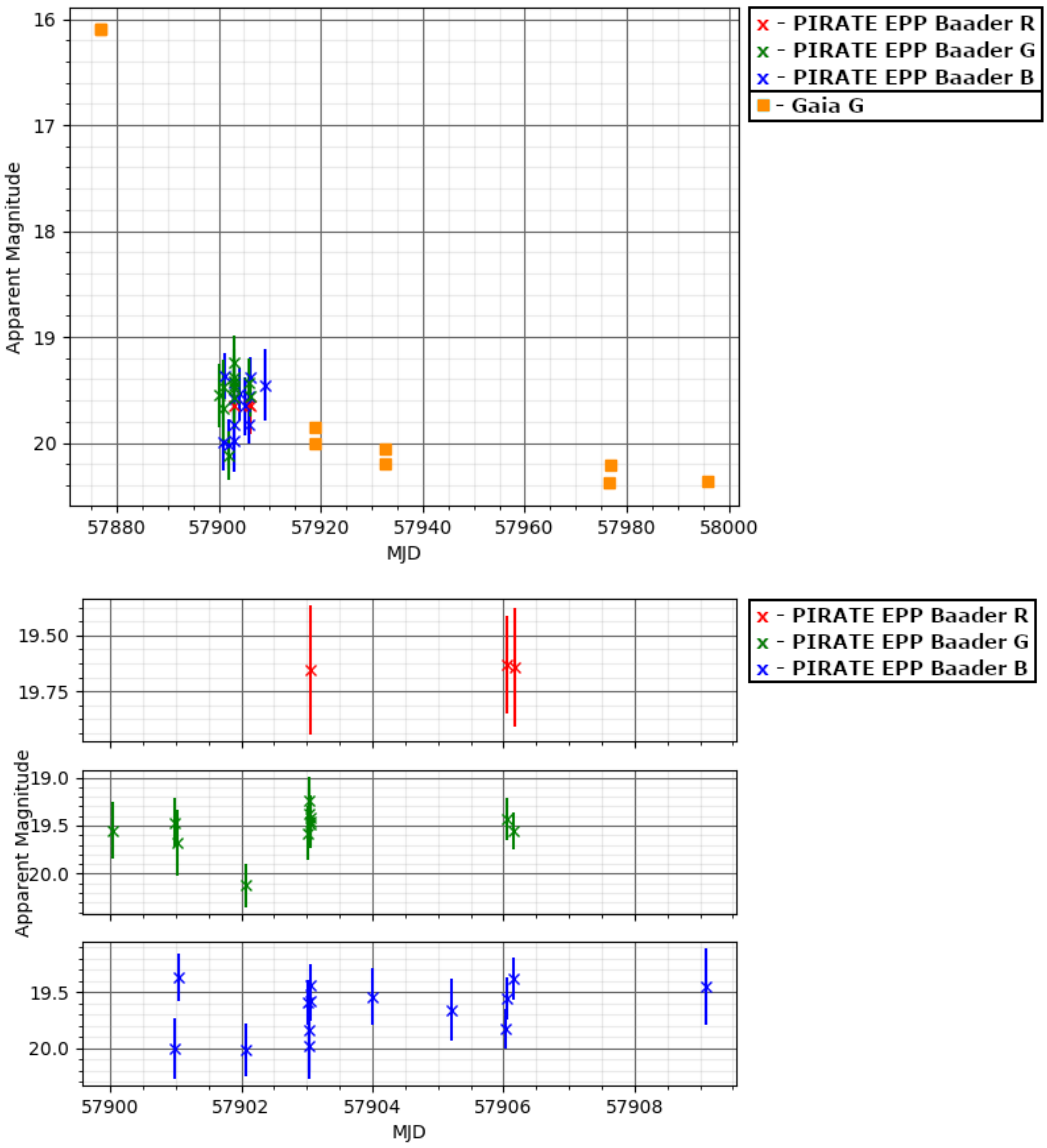

Figure 89: The top figure positions the Gaia17beb data in the context of the Gaia data, the lower figure is an expanded view of EPP data.

Gaia17bjn

Alternate Names	RA (J2000)	DEC (J2000)	Alert Date	Alert Mag (Gaia G Filter)
Gaia17bjn, AT2017eiw	00:53:47.32	40:55:48.54	2017-05-25 06:51:03	17.45

Observed to be a transient by Gaia on 2017-05-25 (Delgado et al. 2017h). The target had previously been observed by the Catalina Real-Time Transient Survey (CRTS) on 2013-10-13 as likely a cataclysmic variable (Drake et al. 2009).

PIRATE begun observing the target as it was declining from some kind of outburst with amplitude ∼1 magnitude (figure 90), and then monitored the target for a short time once it returned to baseline. The PIRATE data are quite scattered, but the EPP and CPCS light curves overlap well. The baseline activity is nearly too faint to perform quality photometry on at around 18.5-19.0 magnitudes in Gaia G, but from the look of the Gaia data there is a spread of ∼0.5 magnitudes even at baseline. This is consistent with flickering which is observed in CVs, which is caused by fluctuations in the accretion rate of the accretion disk in CV binary systems (Scaringi 2014). There are also individual data points from Gaia which seem to indicate that the target underwent outbursts on three other occasions, the first on around MJD 57575, the second about 500 days later, and the third around 200 days after the second. PIRATE only observed during the second of those events, catching a few data points on the first night which are about as bright as the Gaia data point which alerted to the target at 17.45 mag.

The outbursts look to last at most 100 days, typically less, seem to be aperiodic and inconsistent in amplitude change. There are a few types of variable which behave like this, most of them are eruptive events as opposed to CVs. Recurrent novae exist, but they are separated by tens of years unlike these which appear to be separated by only a few hundred days. It could be a dwarf nova, the example MU Centauri shows the same flickering and occasionally has outbursts on the order of 2 mag, though they do appear to be less irregular than Gaia17bjn, with smaller variation in the time between the larger outbursts (Bruch 2016). Though there are also dwarf novae like SU UMa which undergo superoutbursts in addition to normal ones, which this star could be undergoing.

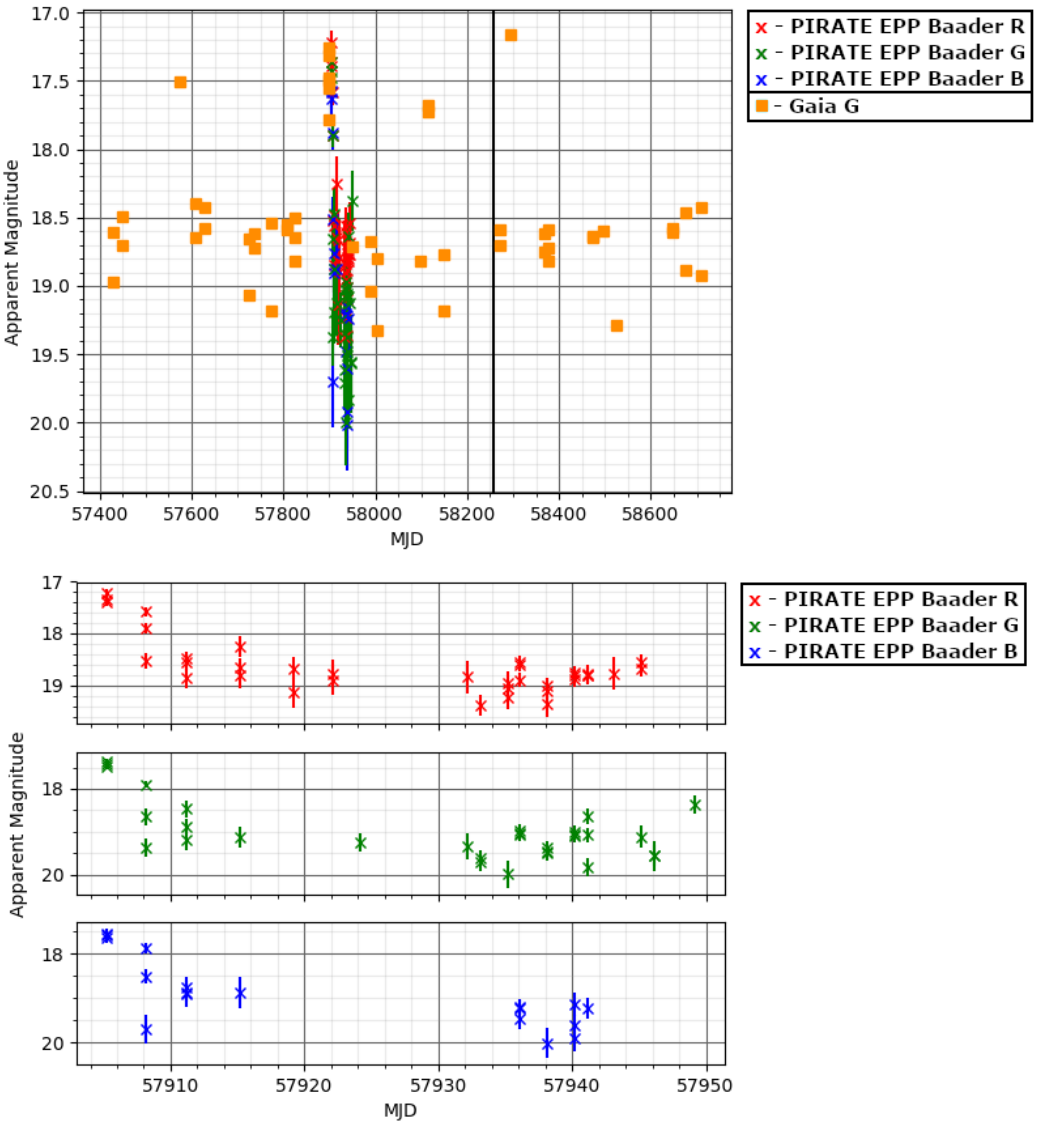

Figure 90: The top figure has the Gaia17bjn PIRATE EPP data in the context of the Gaia data, the lower figure has just the PIRATE EPP data.

Gaia18axf

Alternate Names	RA (J2000)	DEC (J2000)	Alert Date	Alert Mag (Gaia G Filter)
Gaia18axf, AT2018atg	22:20:40.55	44:03:53.39	2018-04-09 12:39:03	14.84

Discovered by Gaia on 2018-04-09 (Delgado et al. 2018i), and described as a "candidate CV".

Although the target was at 14.84 mag at the time of the alert, by the time PIRATE was trained on the target about a month later it had already declined to 18-19th magnitude. The target is very similar to Gaia17beb, it could either be a microlensing event or a nova event. The target declined by 6 magnitudes over the course of about 150 days.

The PIRATE B data possibly shows a peaking event at around 58280 MJD, with amplitude around 2.5 magnitudes. The data are very noisy around the bottom of this peak as it's at about 19th magnitude. The peak consists of 1 data point. Visual inspection of the frames on that night it is clear that the target is barely distinguishable from the background noise, and has a signal to noise ratio less than 1, the frames in R and V are the same and the target was not picked up by the EPP in those filters at all.

Without a clear identification of the first peak it is not possible to classify this as a microlensing event or a nova.

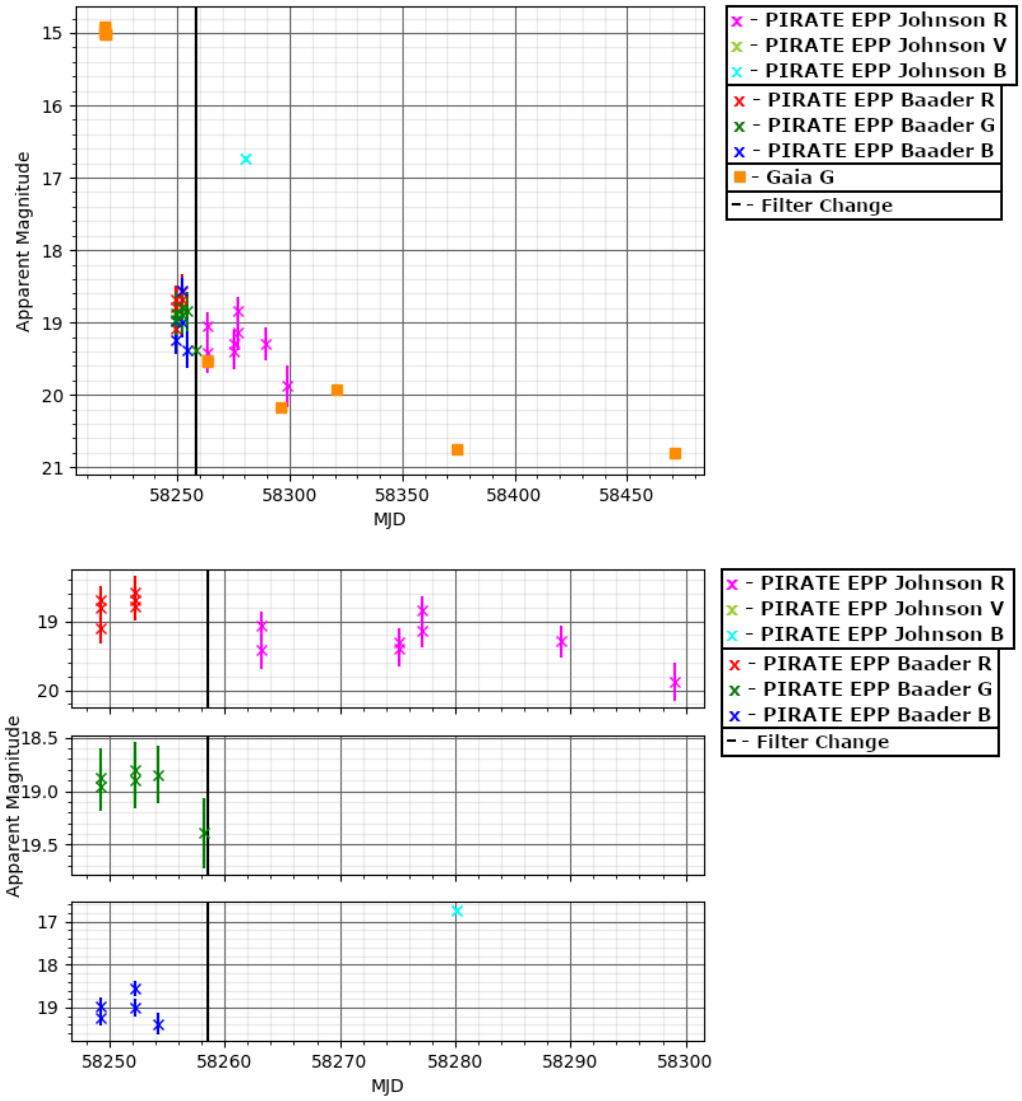

Figure 91: The top figure is Gaia18axf PIRATE EPP data in the context of the Gaia data. The lower figure is just the PIRATE EPP data. The unusually high data point around MJD 58280 is a false signal as the target is barely distinguishable from background in the image.

Other Observed Cataclysmic Variables

Most of these targets were too faint to be detected by the time the alert came through the Gaia Science Alerts page, with the exception of Gaia18apf. There is no clear reason why the target wasn't picked up by source extractor in this case.

Alternate Names	Alert Mag (Gaia G Filter)	Discovery	Classification
Gaia17biq, AT 2017egi	17.95	Gaia (Delgado et al. 2017f)	Nova, Liverpool Telescope (Williams et al. 2017)
Gaia17cga, AT 2017gpx	18.40	Gaia (Delgado et al. 2017o)	CV, GS-TEC
Gaia17chf, AT 2017gre	17.19	Gaia (Delgado et al. 2017p)	CV, GS-TEC
Gaia17dce, AT 2017iqn	16.67	Gaia (Delgado et al. 2017t)	CV, GS-TEC
Gaia17dcg, AT 2017iqo	17.34	Gaia (Delgado et al. 2017u)	CV, GS-TEC
Gaia18apf, AT 2018afn	14.51	Gaia (Delgado et al. 2018e)	CV, GS-TEC
Gaia18aqa, AT 2018ags	17.79	Gaia (Delgado et al. 2018f)	CV, GS-TEC

PIRATE and Cataclysmic Variables

The cataclysmic variable targets with PIRATE data from this project are very faint, but PIRATE did successfully collect data for three targets. PIRATE does appear to show a decline similar to the Gaia data for Gaia18axf before it becomes too faint to observe, and the PIRATE data for Gaia17bjn has caught one of the flaring events which Gaia also caught.

8.4 AGN

Variability of Active Galactic Nuclei is aperiodic and can vary in amplitude in all wavelengths. The light curves often display erratic variation around the baseline, which may itself be increasing or decreasing more slowly overall. The variation typically ranges between a 0.1-0.5 mag over the course of a day or so, but can also dip or peak by 1-3 magnitude over longer timescales. Figure 92 is an example of an AGN light curve in multiple passbands.

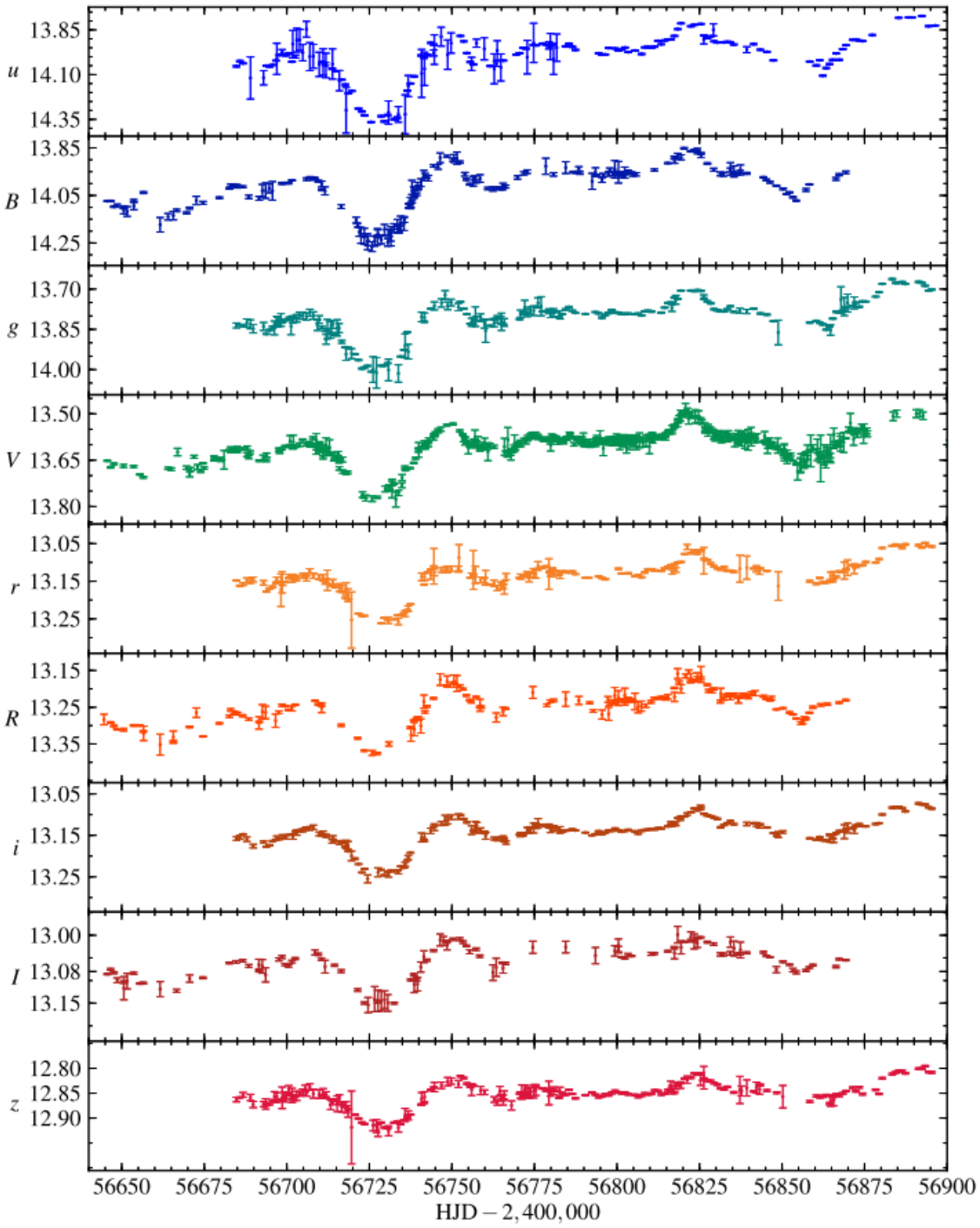

Figure 92: Light curves of NGC 5548 in multiple passbands (Fausnaugh et al. 2016).

Gaia17cmd

Alternate Names	RA (J2000)	DEC (J2000)	Alert Date	Alert Mag (Gaia G Filter)
Gaia17cmd, AT2017har	07:41:45.58	16:13:06.10	2017-09-30 10:24:01	18.38

Discovered by Gaia on 2017-09-30 (Delgado et al. 2017q) and spectroscopically classified by Dr. Nadejda Blagorodnova on 2017-10-03 as an active galactic nuclei (AGN) at z=0.11 (Blagorodnova 2017), and X-ray detection confirmed on 2017-10-27 by Swift/XRT (Sokolovsky et al. 2017).

For this target the PIRATE light curve appears mostly constant with small variations around the baseline of about 0.3 mag (figure 93), but in addition there are a few dates: MJD 58050, 58090 and 58210, where the target appears to dip for a few days by about 0.5 mag for the first one, and about 1 mag for the second and third. With the context of the Gaia data, it appears that the target rose by $\sim$ 1 mag in the 600 days prior to the Gaia alert.

This erratic behaviour could be characteristic of an AGN.

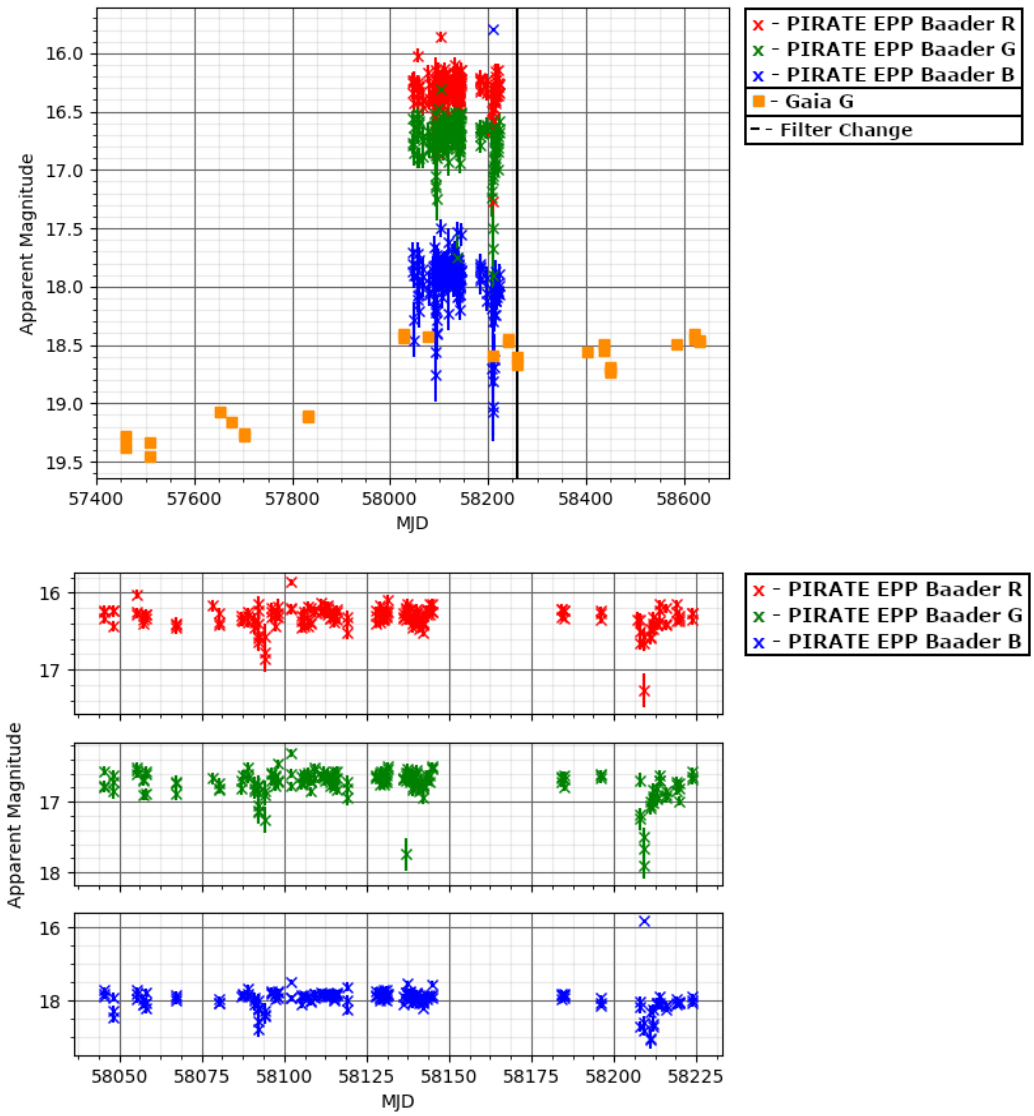

Figure 93: The top figure has the Gaia17cmd PIRATE EPP and Gaia data, the lower figure has the PIRATE EPP data.

Gaia17cem

Alternate Names	RA (J2000)	DEC (J2000)	Alert Date	Alert Mag (Gaia G Filter)
Gaia17cem, AT2017gkx	17:08:59.13	21:53:08.20	2017-08-30 20:42:23	17.81

Discovered by Gaia on 2017-08-30 (Delgado et al. 2017n), suspected to be an AGN.

This object was picked up by the Gaia alerts pipeline as it was undergoing a 1.5 mag dip from baseline (figure 94). PIRATE caught the end of the rise back to baseline for the target, though it began to dip again about 175 days after the first data was collected, shortly after a large spike in the blue data. This sort of erratic behaviour is not a definite indication that the target is an AGN, but the light curve is reminiscent of other AGN.

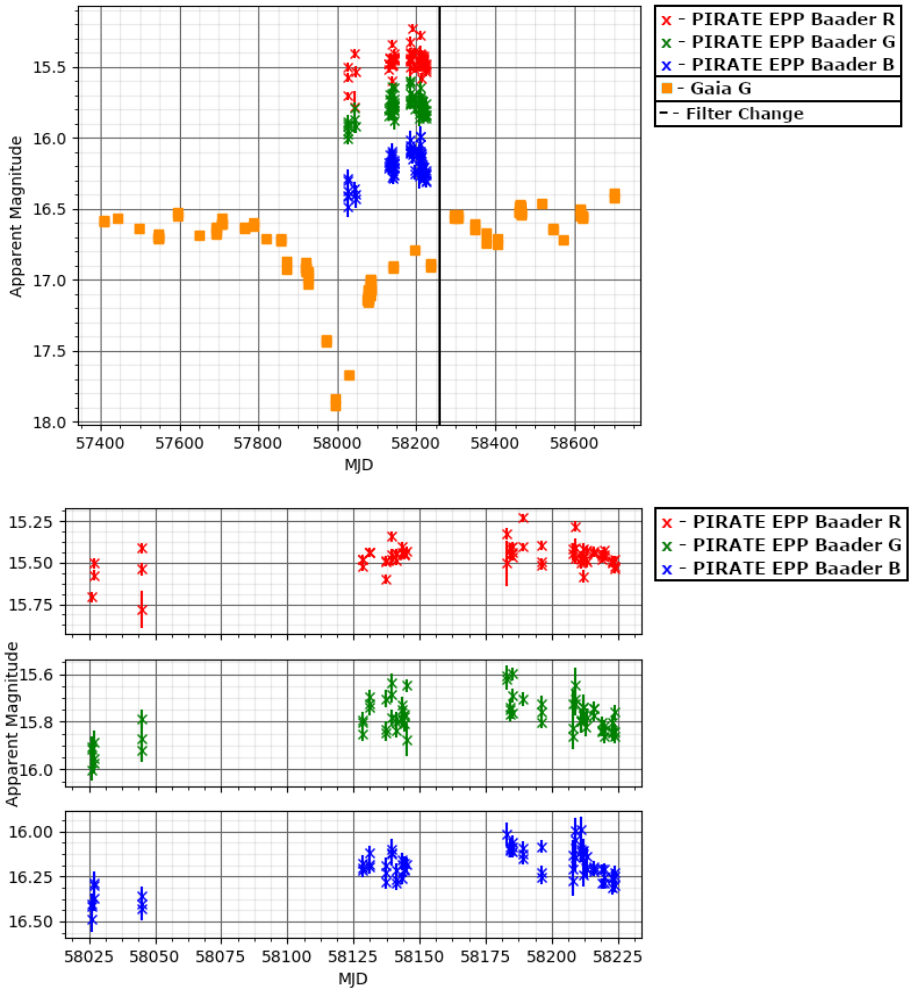

Figure 94: The top figure has the Gaia17cem PIRATE EPP data and the Gaia data, the lower figure has just the PIRATE EPP data.

Gaia17cff

Alternate Names	RA (J2000)	DEC (J2000)	Alert Date	Alert Mag (Gaia G Filter)
Gaia17cff, AT2017fro	17:19:55.85	41:40:49.48	2017-09-03 14:58:28	16.68

Discovered by ASAS-SN on 2017-07-27 (Stanek 2017). Initially classified as a type II supernova spectroscopically by the Shane telescope on 2017-08-05 (Xhakaj et al. 2017), it was later reclassified spectroscopically as an AGN on 2017-08-24 by the Las Cumbres Observatory (Arcavi et al. 2017).

The Gaia data appears to rise 2.5 mag over the course of around 150-200 days, then it fades back towards the baseline over the next 700 days, though it doesn't quite make it back to baseline in that time only fading 2.0 mag.

The spectroscopic classification for this target included a redshift calculation placing it at $z = 0.164$, with an implied absolute magnitude of -22.6 mag.

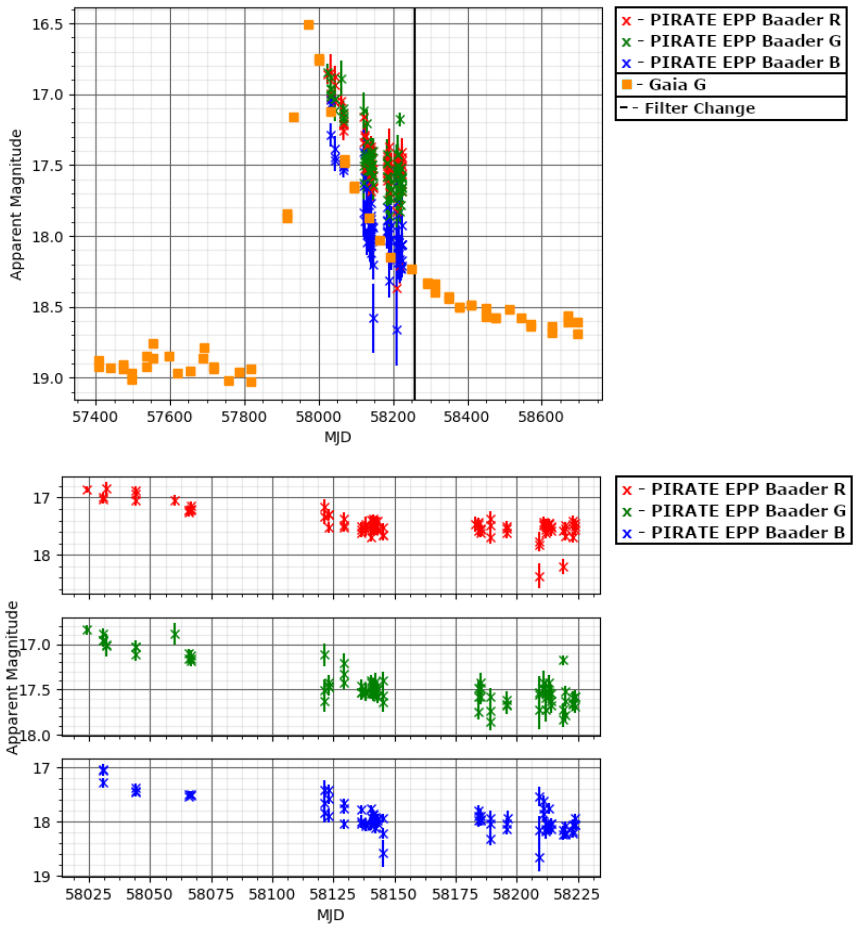

Figure 95: The top figure is the Gaia17cff PIRATE EPP data with the Gaia data for context, the lower figure has just the PIRATE EPP data.

8.5 Unknown Events

These events have no known, or even suspected classification so in this section where possible I will make suggestions based on the light curve as to what they might be.

Gaia17cxa

Alternate Names	RA (J2000)	DEC (J2000)	Alert Date	Alert Mag (Gaia G Filter)
Gaia17cxa, AT2017iei	06:26:32.25	16:16:22.84	2017-11-13 16:17:10	17.41

Discovered by Gaia on 2017-11-13 (Delgado et al. 2017s).

The Gaia data for this target appears to show a very slight decline over the course of about 500 days (figure 96). Of those, about 175 were covered by PIRATE, but the PIRATE data does not show any significant decline over the course of the data.

On MJD 58479 there is a single night where all of the data points in all filters appear brighter than the surrounding data. Inspection of the data frames from this night show that the target does have a larger signal to noise than the data in the surrounding observations, which are 16 nights before and 13 nights after. An increase in brightness of ~ 1.5 mag which occurs within a 29 day gap is a very short, very bright outburst event. Unfortunately with only one night's worth of data for the outburst, it is difficult to identify what kind of variable it may be.

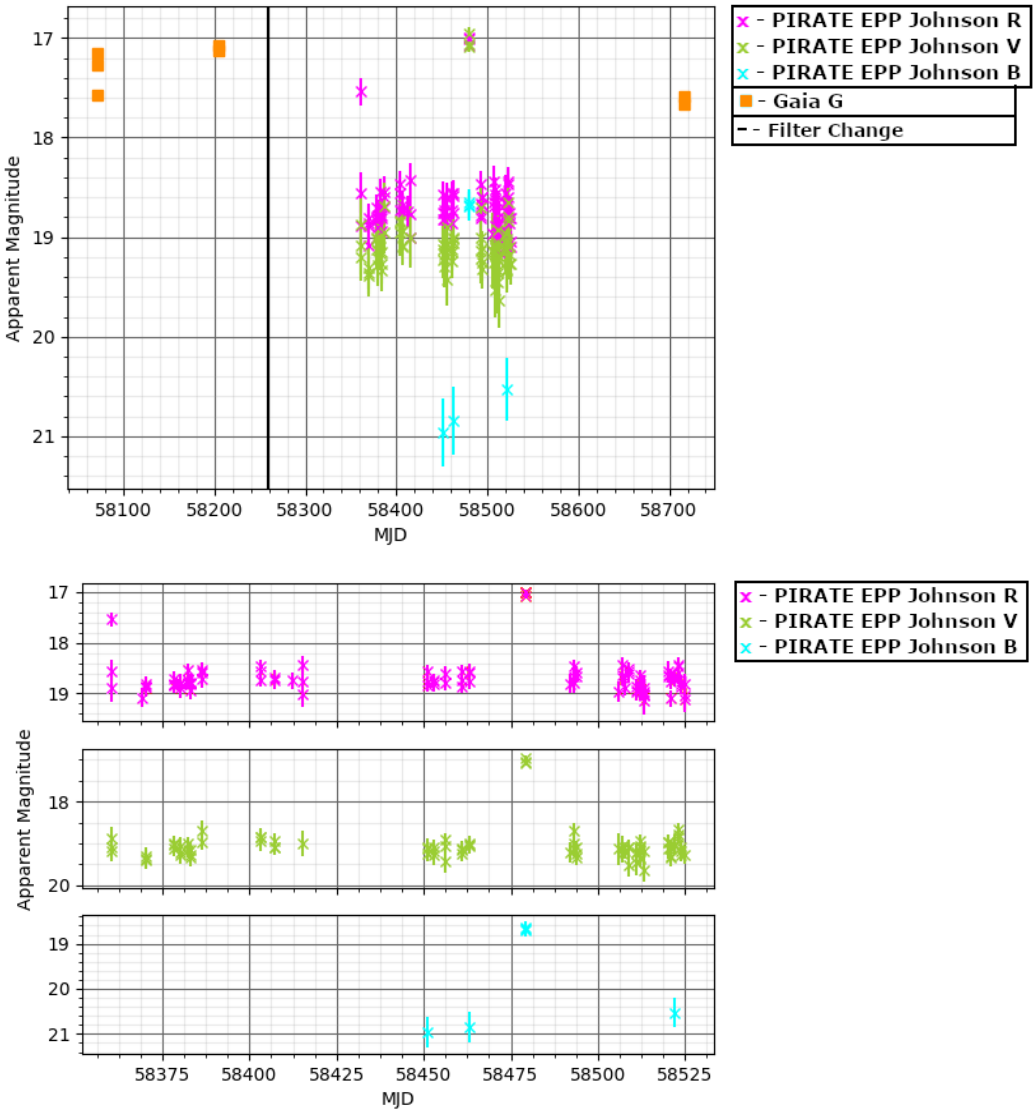

Figure 96: The top figure is the Gaia17cxa PIRATE EPP data in the context of the Gaia data, the lower figure has just the PIRATE data. Due to how faint the target is, it was not found at all in the B filter and CPCS had difficulty identifying the target. Although there were enough data points from CPCS to calibrate the EPP data using the method in section 6, there only appears to be a handful of CPCS data points in total.

Gaia18aen

Alternate Names	RA (J2000)	DEC (J2000)	Alert Date	Alert Mag (Gaia G Filter)
Gaia18aen, AT2018id	08:02:52.07	-30:18:37.15	2018-01-17 04:16:28	11.33

Discovered by Gaia on 2018-01-17 (Delgado et al. 2018b). Spectroscopic follow up of the target by OGLE suggested on 2018-05-11 that the target may be a nova, though the results were not firm, and the PIRATE data doesn't appear to support that (figure 97).

The data collected by PIRATE initially shows a decline of ∼1.5 mag over the course of about 6 months, and then some baseline reading about 200 days later. There is definitely a peak of ∼ 0.5 mag amplitude in the data at around MJD 58510, and possibly another at around MJD 58480. Without those secondary small events it could be argued that Gaia18aen is a microlensing event caught after it had peaked, but the secondary events indicate that this may be something which has irregularly spaced outbursts with irregular brightness. The Gaia data caught in the gap between the two periods of PIRATE observations also supports this as it appears the target peaked twice in that time by ∼ 1 mag.

A paper on this target is due to be published in Astronomy and Astrophysics, which indicates the target is a symbiotic star which in fact outburst on 5 occasions over the course of the observations made with PIRATE. The first two peaks occurred before and after the first cluster of PIRATE data on MJD 58089 and 58255 respectively. The third occurred on MJD 58357, which is between the two sets of PIRATE observations. The fourth and fifth peaks were caught by PIRATE at around MJD 58470 and 58518 (Merc et al. 2020). Figure 98 is the light curve taken from Merc et al. 2020 and includes data from multiple sources.

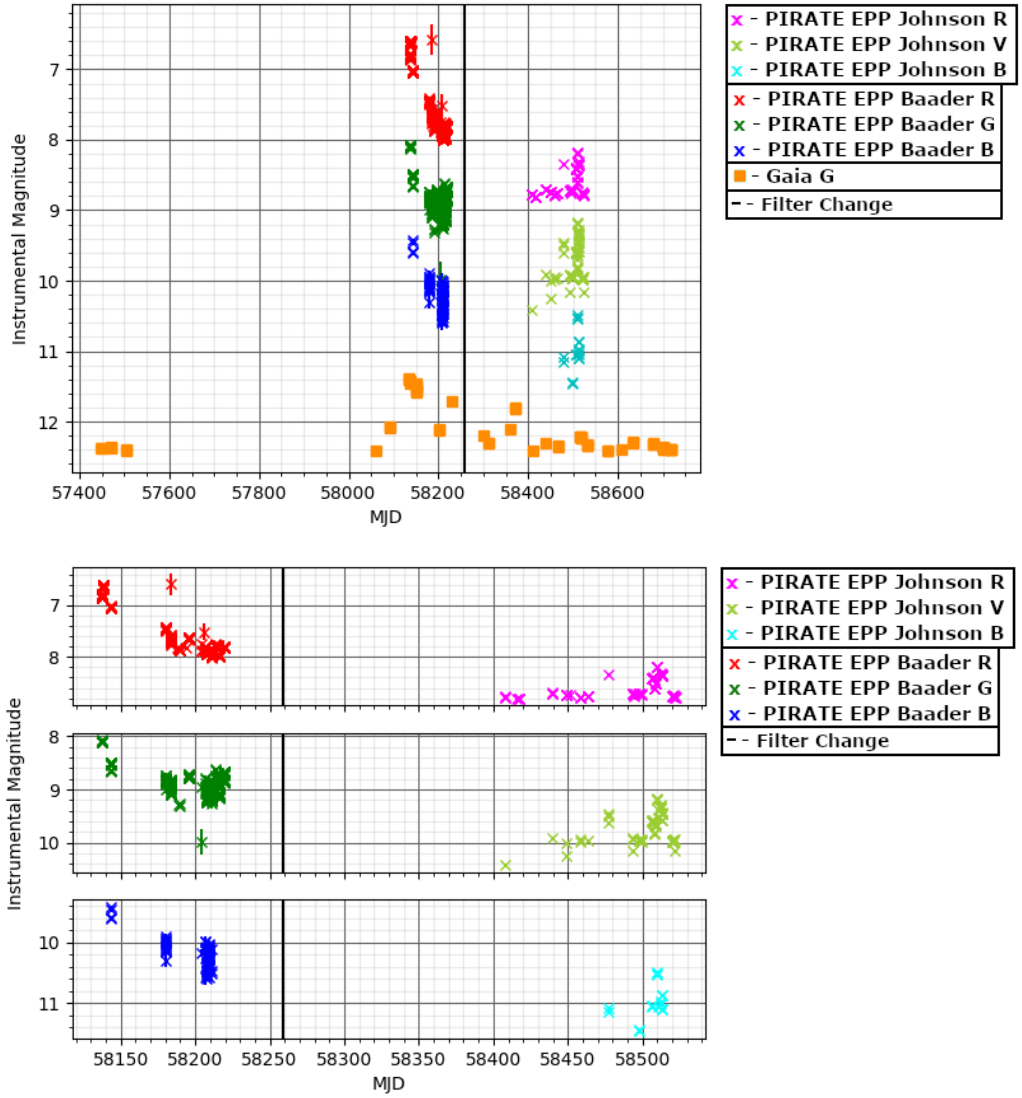

Figure 97: The top figure has the Gaia18aen PIRATE EPP data in the context of the Gaia data, the lower figure has just the PIRATE EPP data.

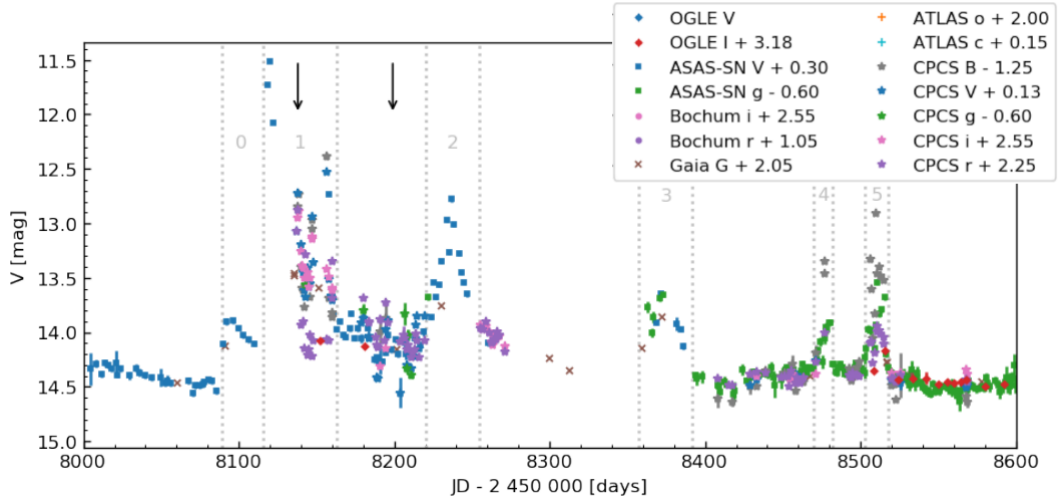

Figure 98: Gaia18aen light curve from Merc et al. 2020. The regions labelled 1-5 indicate the peaks identified in the paper.

Gaia18akt

Alternate Names	RA (J2000)	DEC (J2000)	Alert Date	Alert Mag (Gaia G Filter)
Gaia18akt, AT2018uh	06:25:18.09	12:32:10.54	2018-02-09 05:25:45	13.56

Discovered by Gaia on 2018-02-09 (Delgado et al. 2018d). Classified on 2018-05-11 by the OGLE team as a Be star (Kruszynska et al. 2018).

The Gaia light curve (figure 99) indicates that the star increased in brightness by ∼0.4 mag. Unfortunately after that it plateaued out, and wasn't alerted until after it had finished rising. Although the light curve appears to be relatively flat overall, there are some fluctuations worth mentioning. For example at around MJD 58460 there is a definite peak of around 0.1 mag in the R and V filters, though it is less clear in B. On around MJD 58385 there appears to be a dip of 0.15-0.20 mag in both the V and B filters, though the V only has one data point, and there does not appear to be an observation on that date in the R filter.

The rise in magnitude followed by some low level variation of reminiscent of Gaia17cmd which is a suspected AGN, but the OGLE team reported the star to be a Be star - a type of eruptive variable - by spectroscopic observations.

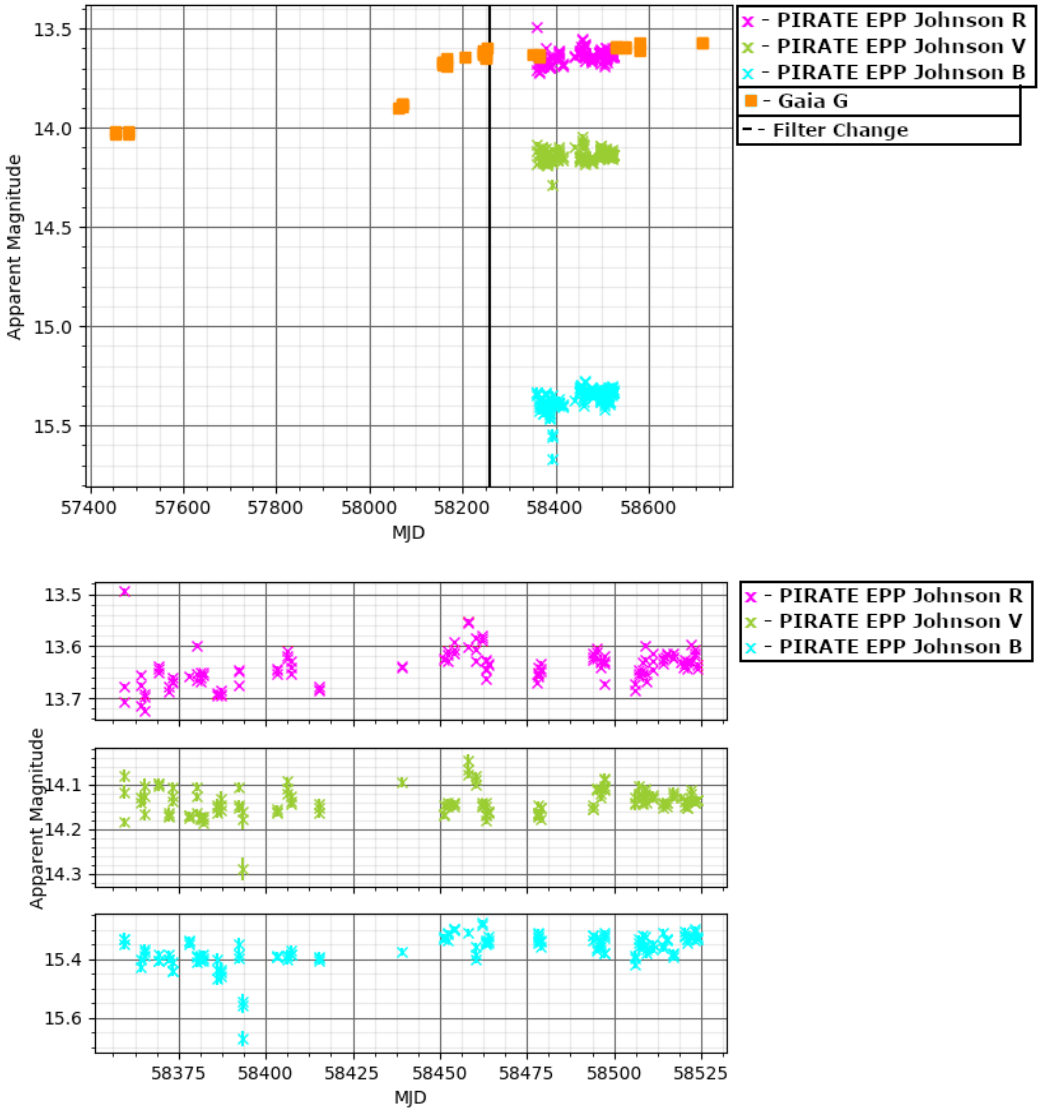

Figure 99: The top figure has the Gaia18akt PIRATE EPP data in the context of the Gaia data, the lower graph has just the PIRATE EPP data.

Gaia18arn

Alternate Names	RA (J2000)	DEC (J2000)	Alert Date	Alert Mag (Gaia G Filter)
Gaia18arn, AT2018ake	21:35:15.41	50:28:50.41	2018-03-19 12:30:35	16.88

Discovered by Gaia on 2018-03-19 (Delgado et al. 2018g).

Similar to Gaia18akt, the Gaia light curve shows this target increases in brightness once by ∼0.4 mag and then plateau. Again the Gaia alert was not published until after the increase had finished, so the final light curve collected by PIRATE is of a relatively constant brightness target, though with two possible outburst events (figure 100).

The target does appear to have increased in brightness by ∼ 1 mag on MJD 58315, but unfortunately after that there is a gap in the data for around 15 nights. This could have been a small flare event, but without more information there is not enough to say for certain. Additionally, the B data seems to have outburst just as observations began, though there is no V data for that period, and the R data does not show the event at all.

Classification is again difficult, though similarities to Gaia17cmd, which was a suspected AGN, and Gaia18akt, a spectrocopically classified Be star should not to be dismissed.

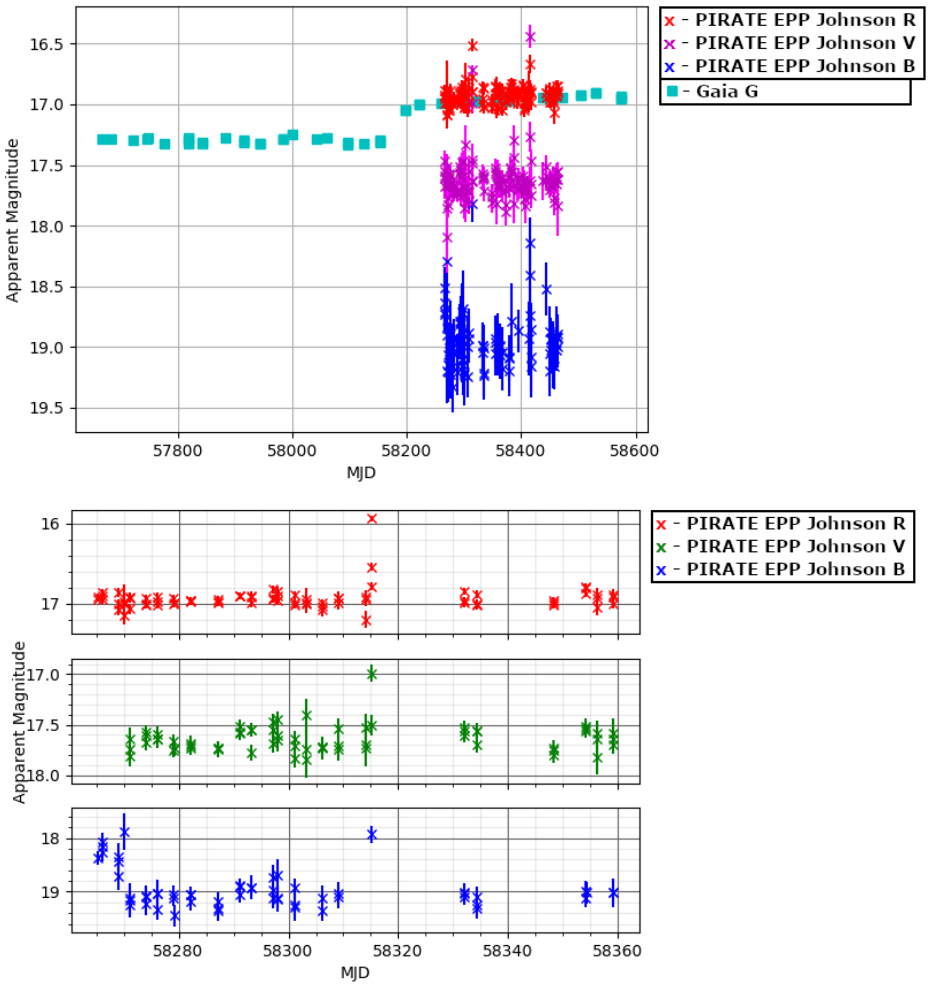

Figure 100: The top figure is the Gaia18arn PIRATE EPP data in the context of the Gaia data, the lower graph has just the PIRATE EPP data.

Gaia18avw

Alternate Names	RA (J2000)	DEC (J2000)	Alert Date	Alert Mag (Gaia G Filter)
Gaia18avw, AT2018art	02:38:52.47	66:25:53.54	2018-04-03 23:56:14	18.02

Discovered by Gaia on 2018-04-03 (Delgado et al. 2018h).

A faint target which peaked briefly over about 2 months and then returned to baseline. Unfortunately PIRATE didn't start collecting data until after the target had returned to baseline, and the baseline is around 19th mag which is fainter than PIRATE's observing range (figure 101).

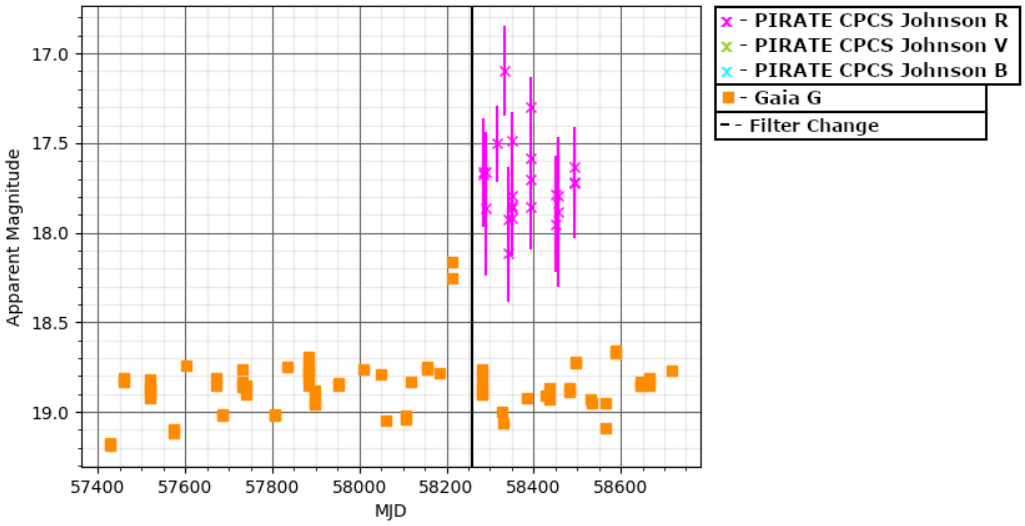

Figure 101: The Gaia and PIRATE EPP data for Gaia18avw.

Gaia18axl

Alternate Names	RA (J2000)	DEC (J2000)	Alert Date	Alert Mag (Gaia G Filter)
Gaia18axl, AT2018atm	22:28:33.72	54:02:57.62	2018-04-09 12:29:33	13.85

Discovered by Gaia on 2018-04-09 (Delgado et al. 2018j).

A ∼0.2 mag increase of a target triggered an alert, though the source faded away again very quickly in the Gaia data (figure 102), before PIRATE could image it it was already back to baseline, leaving another relatively flat light curve.

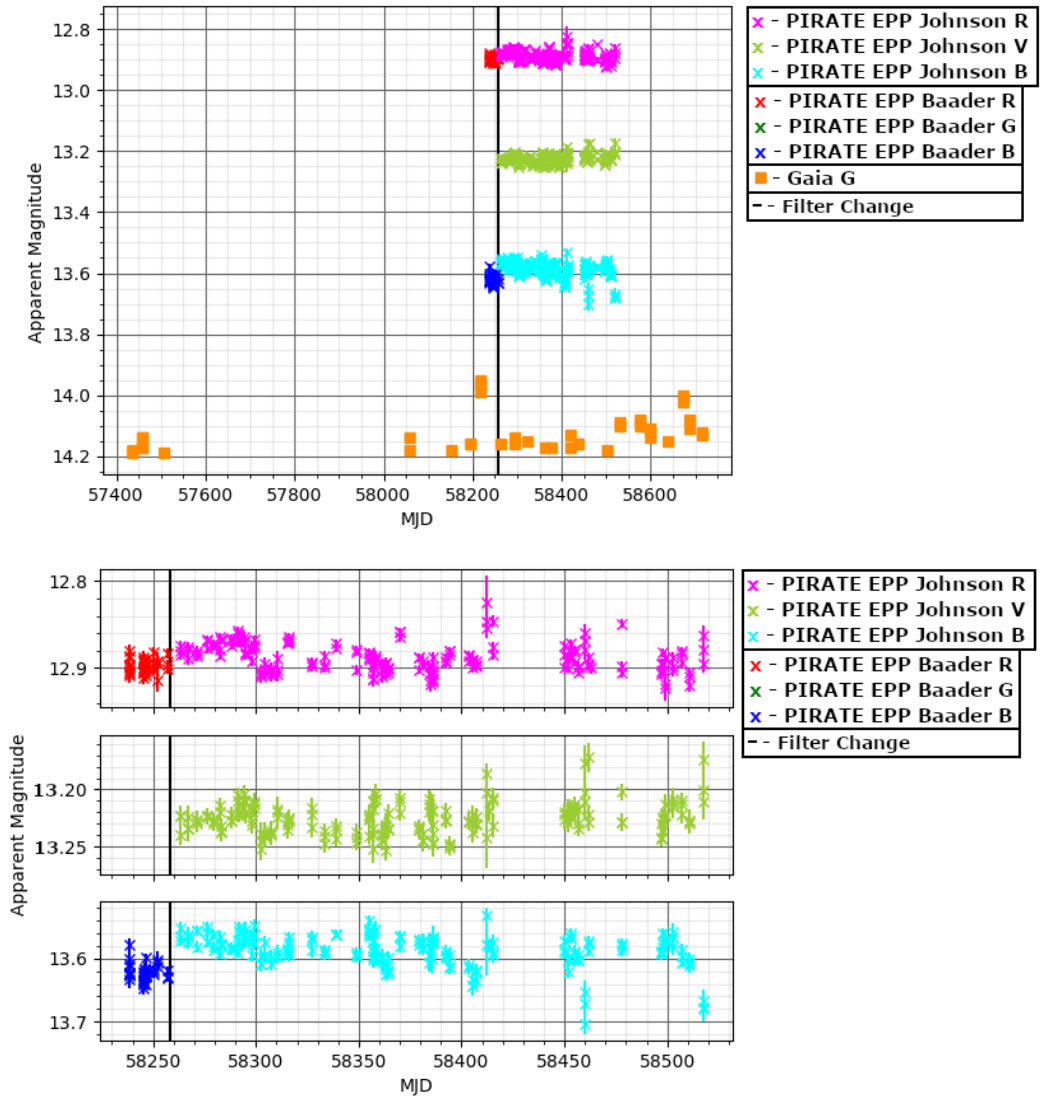

Figure 102: The top figure is the Gaia18axl PIRATE EPP data in the context of the Gaia data, the lower graph has just the PIRATE EPP data. There is an arbitrary shift in magnitude of the differential EPP data to facilitate comparison.

Gaia18cud

Alternate Names	RA (J2000)	DEC (J2000)	Alert Date	Alert Mag (Gaia G Filter)
Gaia18cud, AT2018gvg	03:15:57.87	49:41:14.93	2018-09-25 13:15:48	17.26

Discovered by Gaia on 2018-09-25 (Delgado et al. 2018s).

The source as measured by Gaia increased in brightness by ∼0.5 mag and quickly fades to baseline again (figure 103). The PIRATE data caught the end of the decline and a little of the baseline data.

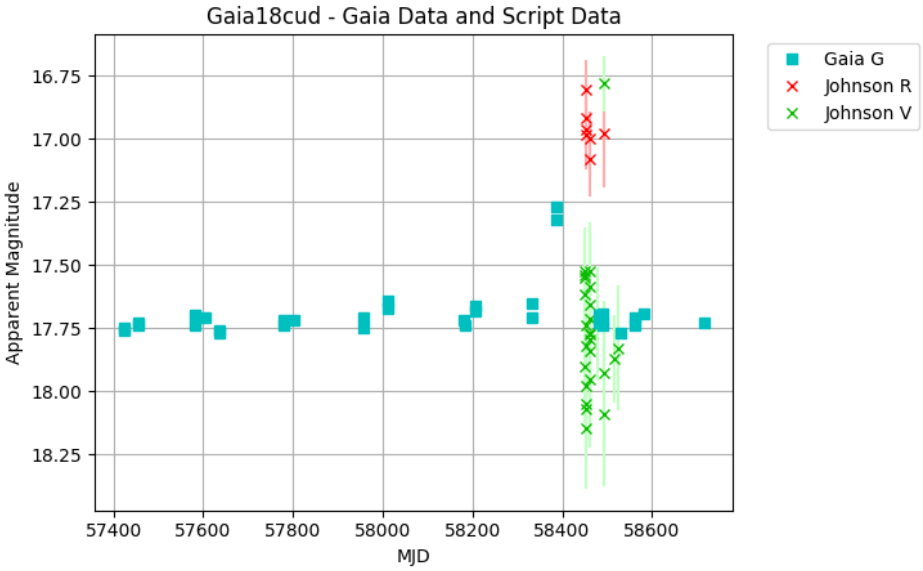

Figure 103: The Gaia18cud PIRATE EPP data in the context of the Gaia data.

Other Observed Unknown Events

Some of the targets with no suspected classification failed to produce a light curve with either the EPP or the CPCS and are listed here.

Alternate Names	Alert Mag (Gaia G Filter)	Discovery
Gaia17bes, AT2017eaj	18.82	Gaia (Delgado et al. 2017c)
Gaia17bjo, AT2017eix	17.29	Gaia (Delgado et al. 2017i)
Gaia17bol, AT2017euq	18.79	Gaia (Delgado et al. 2017j)
Gaia17bue, AT2017foq	17.95	Gaia (Delgado et al. 2017k)
Gaia17bxh, AT2017fuz	18.49	Gaia (Delgado et al. 2017l)
Gaia17byb, AT2017fvy	17.55	Gaia (Delgado et al. 2017m)
Gaia17cpa, AT2017hik	17.81	Gaia (Delgado et al. 2017r)
Gaia18bcb, AT2018bdp	17.28	Gaia (Delgado et al. 2018l)
Gaia18chm, AT2018fia	18.98	Gaia (Delgado et al. 2018o)
Gaia18chq, AT2018fie	18.24	Gaia (Delgado et al. 2018p)
Gaia18cib, AT2018flo	18.66	Gaia (Delgado et al. 2018q)
Gaia18cik, AT2018flv	18.69	Gaia (Delgado et al. 2018r)
Gaia18dds, AT2018hnt	19.61	Gaia (Delgado et al. 2018u)
Gaia19aau, AT2018lhm	15.75	Gaia (Delgado et al. 2019b)

8.6 PIRATE and Long Term Follow Up of Gaia Transients

Overall 78 targets were observed over the course of this project, 29 of which were discussed in this chapter and Gaia16aye was discussed separately. 77 of those targets were sourced from the Gaia alerts stream and the GSAWG10, and the Kojima microlensing event was sourced by word of mouth from a member of staff within the Open University.

Besides Gaia16aye, supernova Gaia17bjw was the most successful in terms of corroborating evidence found by other astronomers. Gaia18aen is also worth mentioning as data collected by PIRATE was included by the team which identified the target as a symbiotic star.

Targets which were brighter than about 16 or 17 mag have relatively clear light curves, but there are quite a few targets which are fainter than this, or are so faint that no useful information could be gained about the targets. Something which could minimise telescope time spent on these targets would be to produce light curves daily, rather than at the end of observing runs, so that the observer can monitor data quality in real time and update observing programs accordingly. This could even be achieved automatically, including the assessment of light curve quality, with time investment into the light curve generation script.

The mismatch between the observing magnitude ranges of PIRATE and Gaia means that they are not the best tools to work together. The PIRATE facility with its current equipment would be better suited to a wider-ranging set of alert streams, in particular the ASAS-SN transient stream would be a better match to the observing magnitude capabilities of PIRATE.

From my use of PIRATE and the photometric analysis I have been able to carry out I can give some recommendations for anyone who may wish to use PIRATE in a similar manner.

Most of the targets which I have imaged are at the fainter end of what PIRATE is suitable for imaging. According to the signal to noise calculations I carried out in section 2.5, light curves generated from Baader R PIRATE data at about 17.5 magnitude should have minimum standard deviation on the order of about 0.1 magnitude. I observed several targets at around this magnitude and distinguishing intrinsic variation from random noise is unlikely if the variation is below about 0.3 magnitude.

The majority of my targets were not suitable to demonstrate the capabilities of PIRATE for much brighter targets. One of the brighter targets I imaged was Gaia18akt, which has Johnson R data at around 13.6-13.7 magnitude. The signal to noise calcula-

tions suggest a standard deviation in light curves at this brightness on the order of 0.01 magnitude. This light curve demonstrates that for brighter targets PIRATE is much more capable, able to distinguish far smaller variation on the scale of 0.05 magnitude. For targets as bright as 13 magnitude, other users of PIRATE have observed exoplanet transits with 1% dips in brightness (Salisbury et al. 2021).

PIRATE can be used to image a single target to pick out variation over the course of a few hours, but for this project I was focused on targets which experience variation over time scales of a few days or longer.

PIRATE is very suitable for observing microlensing events, single or binary lens systems. I collected a large quantity of data for microlensing events, and while I was unlucky to not catch the peak of any events, this is due to the limitations of the procedure used for selecting microlensing targets rather than a limitation of PIRATE, which did pick up on the decline in the brighter targets.

The same can be said for PIRATE and supernovae events, as large variations which occur over multiple days, supernovae are prime candidates for observation with PIRATE. For the supernova which I was able to catch the peaking event, Gaia17bjw, the published values of peak time and Δm_{15} were within the uncertainty of calculations performed with only PIRATE data.

Cataclysmic variables and AGN are more difficult to recommend due to the faintness of the objects observed in this project, but as the variations for both can be relatively large at a few magnitudes, I suspect PIRATE is capable of extracting meaningful data for both as long as some time is spent selecting the brighter candidates, and selecting candidates which are are likely undergoing variations on the larger end of the spectrum. The suspected cataclysmic variable Gaia17bjn was observed at 17.5 magnitude and below, but PIRATE did pick up on a decline by around 2 magnitude. Similarly the suspected AGN Gaia17cmd was around 16-18 magnitude for most of the observations depending on filter, but PIRATE does appear to have potentially picked up some dips of around 1 magnitude.

9 Conclusions

This project has been about the demonstration of small aperture telescopes as a tool for the long term follow up of variable targets, the role automation can play in a large quantity of data acquisition and analysis, PIRATE as an example of this type of system, and the Gaia Science Alerts as a source of variable targets for follow up. In this section I will discuss both the successes in the project, as well as the areas where improvements could be made in the future.

9.1 PIRATE, a Small Aperture Autonomous Telescope

Small aperture autonomous telescopes have the potential to cheaply follow up variable and transient stars, in particular brighter targets over most time scales, and fainter targets over long time scales. Over the course of this project I have tested the Open University telescope PIRATE as an example of such a system, which is similar to other currently operational autonomous telescopes, such as: TRAPPIST, PROMPT and pt5m.

During my time using the telescope regular maintenance trips were only required once per year, for 2 nights for 2 people. Some of the more involved upgrade tasks have required an additional trip, time or personnel. The first trip involved the replacement of a faulty camera shutter shortly after the telescope had been installed. Beyond that first fix, most of the time spent on these maintenance trips was dedicated to upgrading or improving existing systems as opposed to fixing faults. For example: the installation of a GPS timing clock, installing a larger filter wheel and the replacement of the Baader filters with the more commonly used Johnson filters, installing an improved pointing model creation program. There were other tasks which required time working with PIRATE remotely, such as figuring out how to properly allocate twilight hours for flat frames taken with each each PIRATE filter, and adjusting automated focusing parameters to better suit PIRATE's needs.

The signal to noise capabilities of PIRATE were tested by comparing light curves of all the stars in a series of images of a single field, and comparing the standard deviation of those light curves to the uncertainty expected from the CCD equation. Targets observed down to 16 mag have the lowest levels of noise below 0.02 mag, but at 17.5 mag the uncertainty increases to 0.1 mag.

PIRATE is a success in terms of data vs time investment, which is one part of what

this project wanted to understand for small aperture, automated telescopes. Time would have to be spent on maintenance and upgrades on any working scientific telescope, and the time spent by me to add and remove targets from the telescope target list was negligible, at only a few minutes per target. Considering the 45,000 exposures taken, with over 2,700 hours of exposure time, the data return compared to time investment is huge, and I am only one of many users. The target which was observed longest was Gaia16aye, which PIRATE observed around 3 times in each of 3 filters every night PIRATE was available between 10/08/2016 and 01/01/2019, which led to 2,500 frames being contributed to the collaborative follow up, with no additional input required by me after adding the target to the schedule.

There are some improvements which could be made to PIRATE in future, the biggest of which would be to replace the PIRATE OTA with something with a larger diameter mirror. In particular the PIRATE telescope is already housed in a dome, and on a mount which can accommodate telescopes with a mirror up to 1m in diameter. There is an argument to be made for maximising the mirror size to fit the current capacity of the facility. For example a 24" telescope would double the light collection area, meaning currently observable magnitudes would be better quality for the same exposure time, and an increase in photometric precision down another magnitude, increasing the number of possible targets. This would also decrease the size of the visible field in each image, but for single target follow up, this would not be a problem.

For Gaia transient follow up this upgrade would be advantageous, as the regime which most of the variables come from are just fainter than the optimum of PIRATE with respect to uncertainty. But PIRATE as it is now is very capable and with different and more varied alert streams the upgrade may not be necessary, especially given that the telescope is one of the more expensive components of a typical observatory set up.

Another improvement which could be made would be to find a way to centre the target more accurately on the CCD for every exposure, and keep it there throughout the exposure. If the target is always imaged with the same few pixels, then uncertainty introduced by pixel response can be reduced. There are occasions when it might be beneficial to observe a target for most of a night, during a microlensing event peak for example, but currently the target shifts by a few pixels per hour. This could potentially be resolved with additional hardware, such as an autoguiding device, or could possibly be resolved through software solutions which find the position of the target on the chip between exposures, though more technological investigation would be necessary to see

what would be involved to update the mount's pointing model on the fly.

These sort of off-the-shelf, commercial systems like PIRATE have the potential to cheaply and easily provide a way to acquire a huge volume of data without taking up valuable time on much more expensive, larger telescopes, or the time of the observer.

9.2 Gaia Science Alerts

The use of the Gaia Science Alerts (GSA) was tested during this project, as an alerts stream for a small aperture, automated telescope. The GSA uses data acquired by the Gaia satellite to search for transient stars, which it then publishes in an alert stream. These alerts can be followed up by anyone, and data acquired can be accumulated from various observatories using the Cambridge Photometry Calibration Server (CPCS).

The GSA publishes too many alerts every day for any telescope to follow up all of them for an extended period, so it is necessary to pick and choose the most appropriate targets. The Gaia Science Alerts Working Group 10 provided that by giving lots of observers the same curated list, enabling better collaboration between observatories.

The Gaia Marshall system, which replaced the regular GSAWG10 e-mails seemed like a good place for observatories to collaborate between themselves, but unfortunately the system seems to be mostly unused at this point, the most recent post by anyone was in May 2019. This system would be very useful if it were widely used, and would encourage people to do so.

With no regular e-mails, and a lack of use of the Gaia Marshall system, the best method for using the Gaia alerts system in future would probably be to go back to checking the full list of alerts every day and using the suspected class, and comments left by the Gaia alerts team to pick targets. This process is even easily automatable using the CSV published every day, as I tried in early 2017 though back then the "suspected class" was not included in the CSV making choosing more difficult.

Although Gaia does pick up some brighter targets, most of the targets published have alerting magnitudes at 16 magnitude or fainter, which means the majority of the targets are close to as faint as PIRATE should be observing for accurate photometry. This is due to the capabilities of Gaia, which can observe down to 20 mag, meaning that it is not a perfect match for PIRATE that can only really perform accurate photometry to around 17 mag. In addition, the majority of the microlensing events and supernovae observed were published too late to catch the peak, which limits what can be learnt about those targets. Gaia was designed to create a large catalogue of stars, and not to

be a transient detector. It cannot send data back to Earth quickly, and that data is not suitable for quick processing when it arrives.

An improvement to this project would be to branch out and begin using other alerting networks in addition to the GSA. One example would be the ASAS-SN alerts stream, which publishes a few transients a day and observes a more suitable regime for PIRATE between 9 and 18 mag. Alternatively the ZWICKY Transient Facility which publishes between 0.6 and 1.2 million transients per day, through an events broker such as Lasair. In the future it would also be good to be involved with the LSST transient alerts, which will be similar to the ZTF but even larger in scale.

9.3 Pipelines and Data Processing

The creation of the data reduction pipeline was essential to keep up with the rate of data acquisition PIRATE achieved during this project. Without it a lot of time would have had to been spent on manual data reduction every day, and likely a lot less data would have been analysed as a result. To this end I wrote both a data reduction pipeline using Python and some other commonly used astronomy programs, source extractor and astromotry.net and a data analysis pipeline, also in Python, to generate light curves of the targets I observed.

I am confident in the performance of the data reduction pipeline, having spent a significant amount of time comparing results to those of other astronomical data reduction tools, such as AstroImageJ. The pipeline continues the daily reduction of all PIRATE data, having been passed on to other PIRATE users for future management.

The pipeline currently performs bias, dark and flat calibration, plate solving, source extraction, and the ability to upload data to the CPCS. It is written in such a way that it should be easily expandable for any python user.

The Ensemble Photometry Pipeline (EPP) was also successfully run on targets during this project. It produced all of the light curves in Chapter 8 except for three: Gaia17bjw, Gaia18avw and Gaia18ajz, which were all produced by the CPCS.

In the case of Gaia18avw and Gaia18ajz, both targets are extremely faint for PIRATE at 18 mag for 18avw and 19 mag for 18ajz both in Johnson R. In both cases the CPCS light curves are not really informative, and the EPP failed because the target is so faint.

Gaia17bjw on the other hand is quite bright, comfortably bright enough to give relatively small uncertainty. The failure seems to be due to the target being within

the spiral arms of NGC 3938. Photometry in the galaxies is generally more involved than photometry of isolated stars due to the background which comes from the galaxy, though it is likely that the EPP could be modified to work in these situations. Since the CPCS produced a good quality light curve and it is the only target in the project with this issue, it was deemed sensible to focus my efforts elsewhere.

One aspect of the EPP was the use of string length minimisation to choose the best ensemble size, which involved calculating the total distance between consecutive points in a light curve. The initial idea supposed that as the ensemble size increased, the string length would get shorter down to a level where addition stars would no longer improve the light curve. The string length minimisation method produced more complex results than was expected initially, but this is due to the success of the EPP in selecting good reference stars and is not a failing in the string length minimisation method. The method was used to select the best EPP ensemble size for all the light curves in the project.

The EPP is not in use by users of PIRATE, because it is a more complex pipeline which would not be simple to modify for another user. It is also quite slow, it can take several hours for a target in a crowded field with lots of images, such as Gaia16aye. For it to be useful to PIRATE users now it would be better to rewrite some of the code to put it in a more easily modifiable state, perhaps using a faster programming language, such as C, for the sections of code which take longer to run.

The CPCS quickly calculates the data necessary to generate light curves of similar quality to the EPP, including magnitude calibration. The reduction pipeline is already capable of automatically uploading data to the CPCS, and would be a much simpler option for future PIRATE users.

An obvious, if difficult to implement, improvement would be to calculate apparent magnitudes as a part of the script, making the pipeline independent from the CPCS. This would involve using a catalogue which uses Johnson filters such as APASS to perform cross matching on known stars in each image field and convert from instrumental magnitudes.

Another improvement which would be vital to telescope time efficiency would be to implement the light curve generation on a daily basis, which would more quickly indicate how exposure time should be allocated between targets.

Another example of an improvement which could be made is to attempt to extract useful information from saturated exposures. The following section describes an

attempt which was made to perform this towards the end of the project.

9.3.1 Salvaging Saturated Data

During this project a target called Hind's star was observed for around 100 nights, and during the course of data analysis it was discovered that the target contained 1-3 saturated pixels in over half of the images taken. In an attempt to salvage the images with saturated data, a method was devised for approximating the missing counts. Although the method showed promise, it is left unfinished due to time constraints and so I will describe it here.

The technique involves using a circularly symmetric Gaussian to approximate the point spread function of the star across several pixels in an image. The Gaussian used is of the form:

$$f(x,y) = A\exp\left[\frac{-[(x-x_c)^2+(y-y_c)^2]}{2\sigma^2}\right] \tag{35}$$

where x_c and y_c are the centre of the Gaussian, A is the amplitude, and σ is found using the Full Width Half Maximum (FWHM) of the star

$$\sigma = \frac{\text{FWHM}}{2\sqrt{2\ln 2}} \tag{36}$$

As there is no peak to the saturated star, directly calculating the FWHM for a saturated star isn't possible. But for a single image, there should be a relatively narrow range which the FWHM lies in. In fact, using the source extractor catalogues, by plotting the FWHM of every star in an example image, verses the total flux for that star we get the result in figure 104.

As a saturated star is not going to have a total number of counts below 2,000, we can lose data points below that limit, and calculate the mean of a normal distribution fitted to the remaining points. That value is plotted in figure 105. Although this value is not likely to be the exact FWHM for the saturated star, it gives an initial value to probe around.

With an initial value for the FWHM, the Gaussian can be calculated for a range of A and σ. Then the Gaussian can be compared to the unsaturated pixel counts for the saturated star by calculating the standard deviation between the two, and the lowest standard deviation will be the closest Gaussian to the star's point spread function.

This method was used to see if the total flux can be approximated for an unsaturated star with the pixel with peak counts removed. The results at this point were not quite

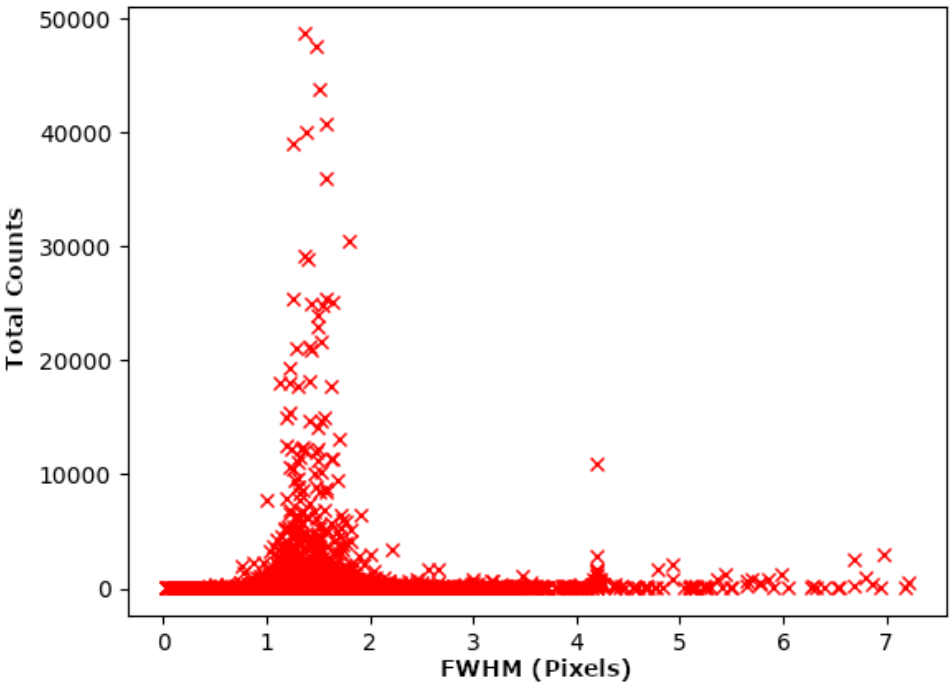

Figure 104: FWHM of all the stars in a frame as calculated by source extractor.

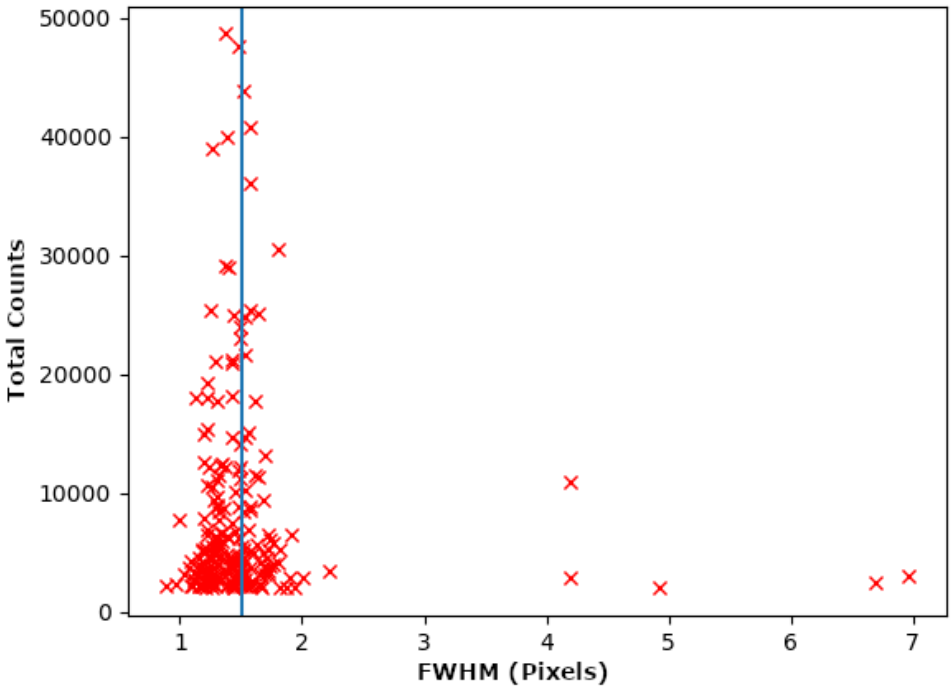

Figure 105: After dropping all the stars from figure 104 which have total count below 2,000, it becomes possible to fit a normal distribution and calculate the mean, which is plotted here as a solid line.

good enough to spend more time attempting the method on the unsaturated target. Figure 106 shows the number of counts calculated in the Gaussian, as a percentage of the known true counts of the unsaturated test star as calculated in 150 images.

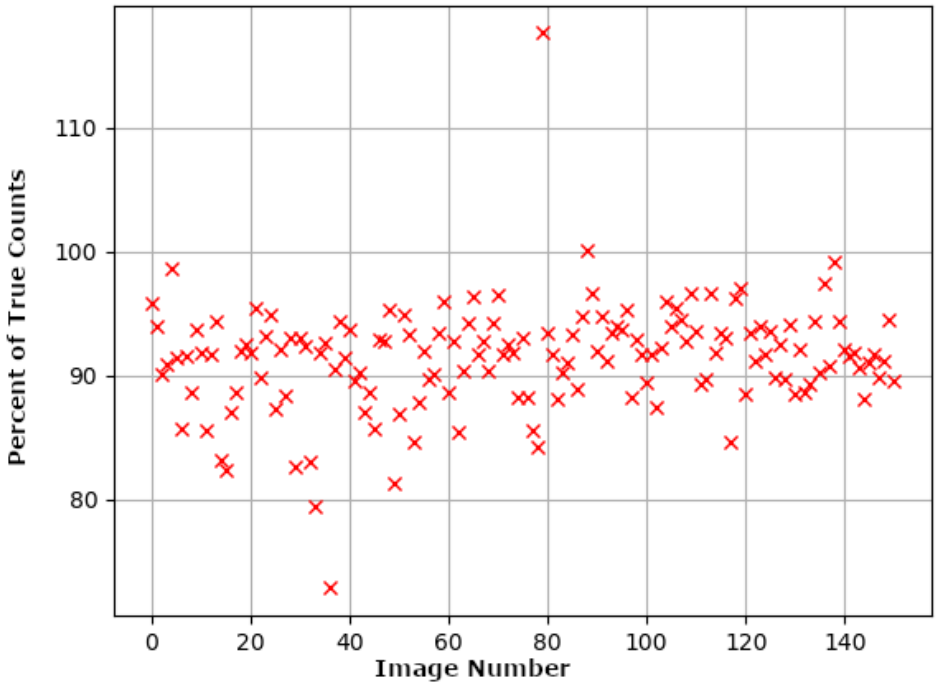

Figure 106: The total counts of an unsaturated star calculated using a fitted Gaussian, as a percentage of the true value.

Currently it is only achieving something like 90% of the true counts on average, and even then the spread of counts is very large at about 5-10%. If the spread had been closer to 1%, even not calculating the full 100% of counts, the method may have been useful. For now the method is incomplete, but I believe shows promise as a method which would be easy to implement in an automated pipeline.

9.4 Gaia16aye

Gaia16aye is the target which was observed for the longest during this project, a binary microlensing event which began in July 2016 and returned to baseline measurements in January 2018. I contributed over 2,500 observations to the collaborative effort made by the astronomical community. The long duration of the follow up for this target was both due to the event spanning several hundred days, and the rarity of binary microlensing events.

The data I contributed mostly covered the fifth peaking event, and the following

decline. Although there was more data collected by PIRATE from before the third peak onwards, the data is not in a state to make it easily workable and I decided to focus my time on the cleaner data.

With more time it would have been beneficial to work out the issues with this data and to cover more of the light curve. The work done by Wyrzykowski et al. 2020 to model the light curve took months of work for several people to achieve. I would have liked to have duplicated this work using only PIRATE data but time constraints prevented this. Rather than trying to find fault in the Wyrzykowski et al. results, it would be an attempt to demonstrate the limitations of a single instrument, while also demonstrating the usefulness of having a set of data through the same set of filters and of the same quality throughout.

The PIRATE data was more suited to a check of the colour index of the target, as I have a long run of data in several filters. Although the colour index (G-R) first appeared to show some kind of periodic variation, this was explained by an increase of background at the Tenerife site which coincides with the rise of the full moon. Aside from that false periodic variation the data does appear to show that the microlensing event was achromatic.

9.5 Other Observed Targets

I produced 30 light curves suitable for discussion including Gaia16aye. Table 20 gives the count for each type.

Type	**Number of Light Curves**
Microlensing Event	9
Supernovae	8
Cataclysmic Variable	3
Active Galactic Nuclei	3
Unknown	7

Table 20: How the light curves produced are split between types

Five targets have enough data from PIRATE to say they are likely a microlensing event when viewed with the Gaia data. Gaia16aye was picked up prior to the third and fourth peaking events, and rest were observed during the decline period. The Kojima microlensing event appeared to show the peak, but after data fitting and comparing

PIRATE dates to published dates, the peak occured one day earlier.

One event, Gaia17ddi, may even have been a binary microlens judging by the Gaia data, and another event Gaia18clv may also have been a binary. The data collected by PIRATE fell between two potential peaks. Gaia18bek was initially classified as a supernova, however the Gaia data shows it is far more likely to actually be a microlensing event, in which case PIRATE shows a section of the decline.

Ten supernovae produced light curves, seven of those were post-peak and I could therefore calculate the decline rates. Two events appeared to decline at rates expected for the suspected type, two clearly disagree with the suspected type and three were uncertain.

Two proved not to be supernovae at all, Gaia18bff displayed a relatively flat light curve and the target was mislabelled, and Gaia18bek was almost certainly a microlensing event as mentioned previously.

The last of the supernovae was Gaia17bjw which was caught around 14 days before the peak and I could therefore calculate the date of maximum and Δm_{15}. The target was more thoroughly modelled in Van Dyk et al. 2017 and the values they calculated for the date of maximum and Δm_{15} fall within the margin of error for the PIRATE values, which indicates that PIRATE is well capable of contributing to supernovae followup of this nature.

Three cataclysmic variables that I observed produced light curves. Gaia17bjn does appear to be undergoing some kind of flaring event at the beginning of the observations. The other two targets, Gaia18axf and Gaia17beb both show a decline which could be representative of a fast novae, or the decline of a microlensing event. More observations would been beneficial, but the targets grew too faint to continue observations.

Two of the AGN observed show erratic behaviour which could be associated with AGN, the third event Gaia17cff is almost certainly a nova, and the PIRATE data captures a long section of the decline, but not the peak.

Gaia18aen of the unknown variables has been identified as a symbiotic star in a paper which has been accepted for publication by Astronomy and Astrophysics. PIRATE observed the target during three of five flaring events identified in the paper. Substantial PIRATE data of the other unknown events appear to show flat light curves and some minor flaring events such as in Gaia18arn.

9.6 Concluding Remarks

Transient and variable follow up has two important parameters which require consideration, the timescale and the depth of the variables which are to be observed. Not all facilities are ideally suited to the entire range of both parameters. Small, autonomous telescope systems in general have the potential to greatly expand the follow up capabilities of humankind, and are best suited to brighter targets, and can be useful at all timescales.

With millions of potential follow up targets already available for observation, small, autonomous telescopes are an opportunity to contribute to astronomical research efficiently, and more cost effectively than if large expensive telescopes were to be used in this way.

Given the quantity of data acquired by automated telescopes, the automation of data reduction and analysis is the only effective solution. Pipelines like those created during this project will be essential for astronomical facilities in the near future.

Astronomy is heading towards an era when humankind is observing the whole sky, all the time and in all frequencies. Time domain follow up in particular is going to dominate astronomy in the near future due to the need for observations of gravitational wave counterparts, and surveys like the LSST coming online. This is going to require a lot of automation for all aspects of follow up, from target selection and data acquisition, to data analysis and light curve generation. Tools like the pipelines created for this project are going to be essential for observatories with telescopes of all sizes.

Overall, PIRATE has demonstrated that it is an efficient follow up tool for understanding variable events, and is a prime example of an easily duplicatable system.

Appendices

A PIRATE Data Standard Deviations

Collection of figures which illustrate the performance of PIRATE through the various filters used for imaging in this project. The explanation for this data can be found in section 2.5.

Gaia17bjj Baader Filters

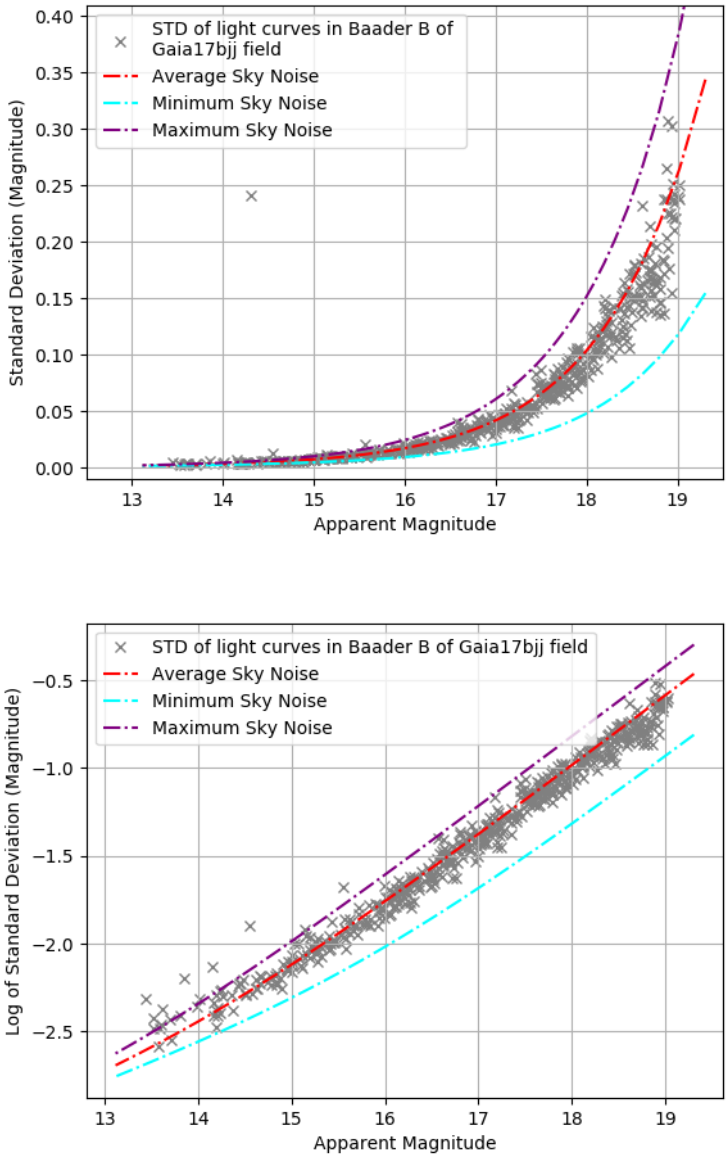

Figure A.1: Gaia17bjj data through Baader B filter, 300s exposures.

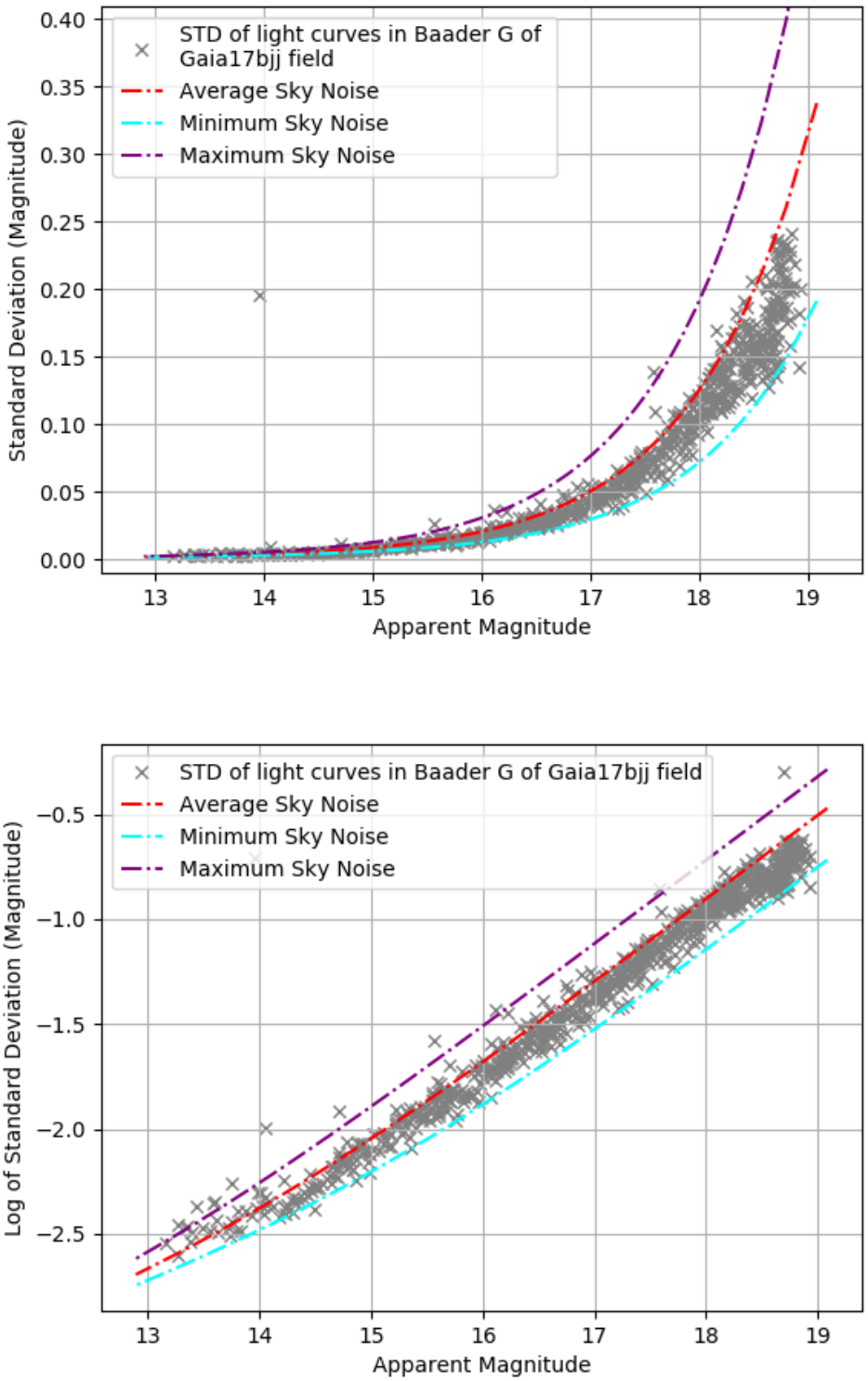

Figure A.2: Gaia17bjj data through Baader G filter, 300s exposures.

Gaia18cud Johnson Filters

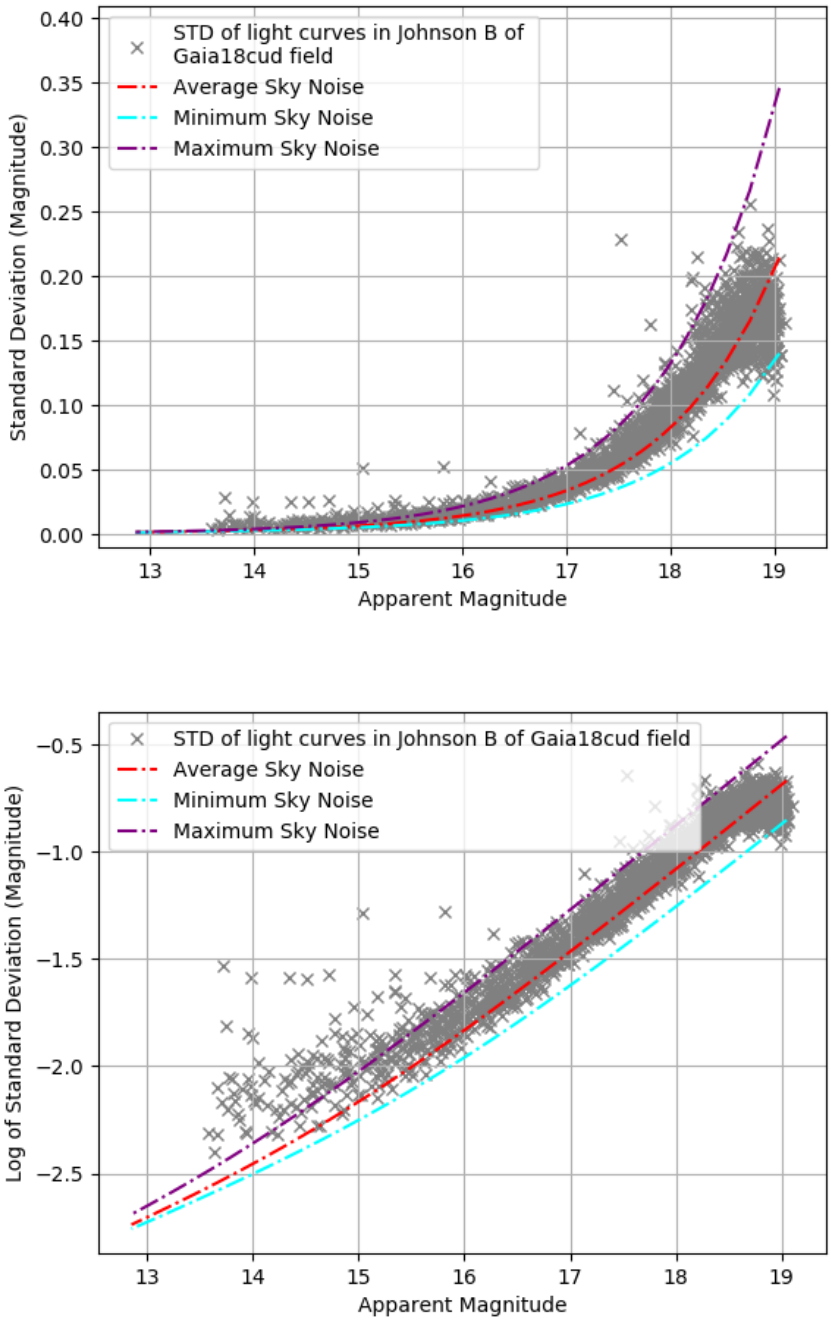

Figure A.3: Gaia18cud data through Johnson B filter, 300s exposures.

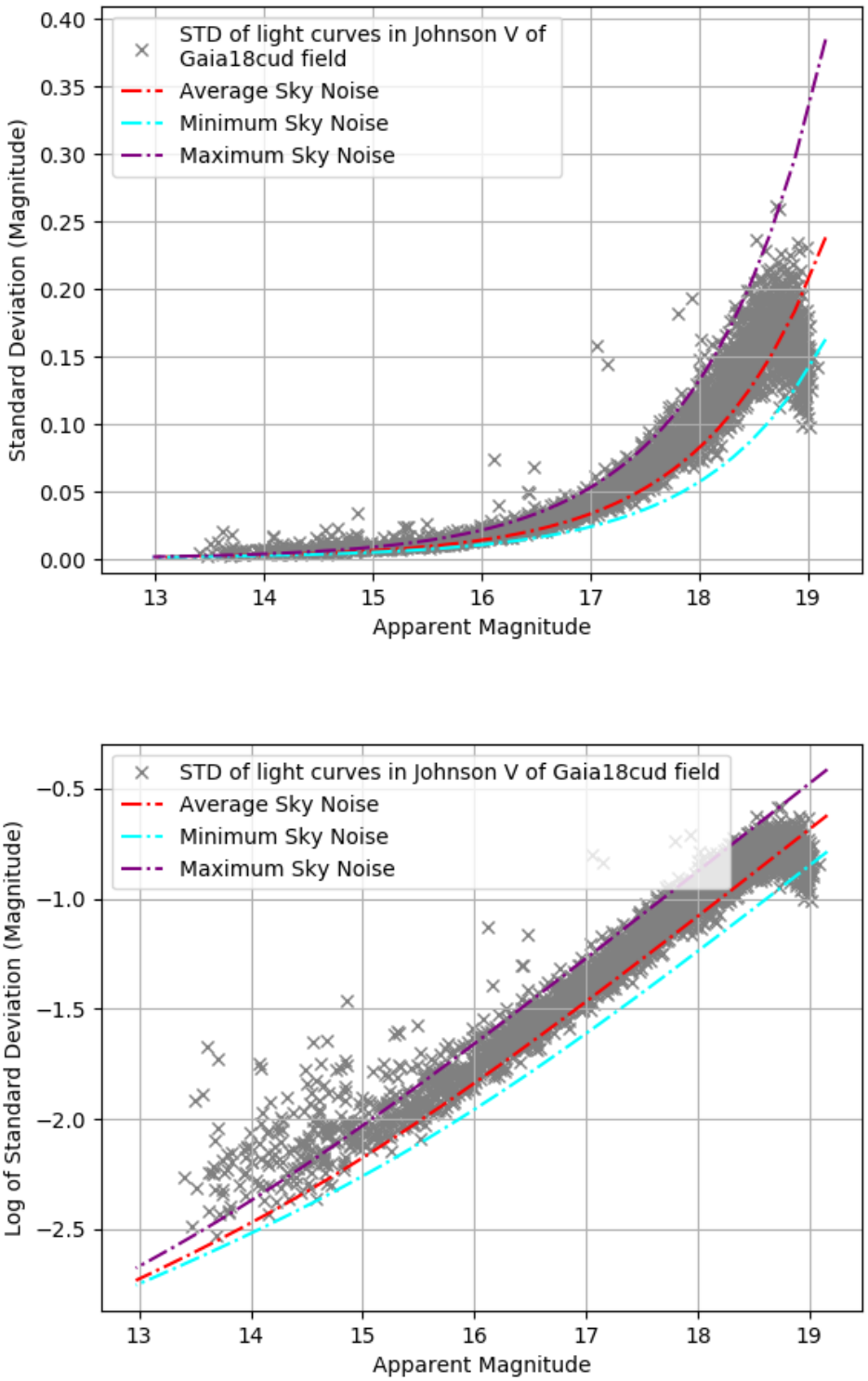

Figure A.4: Gaia18cud data through Johnson V filter, 300s exposures.

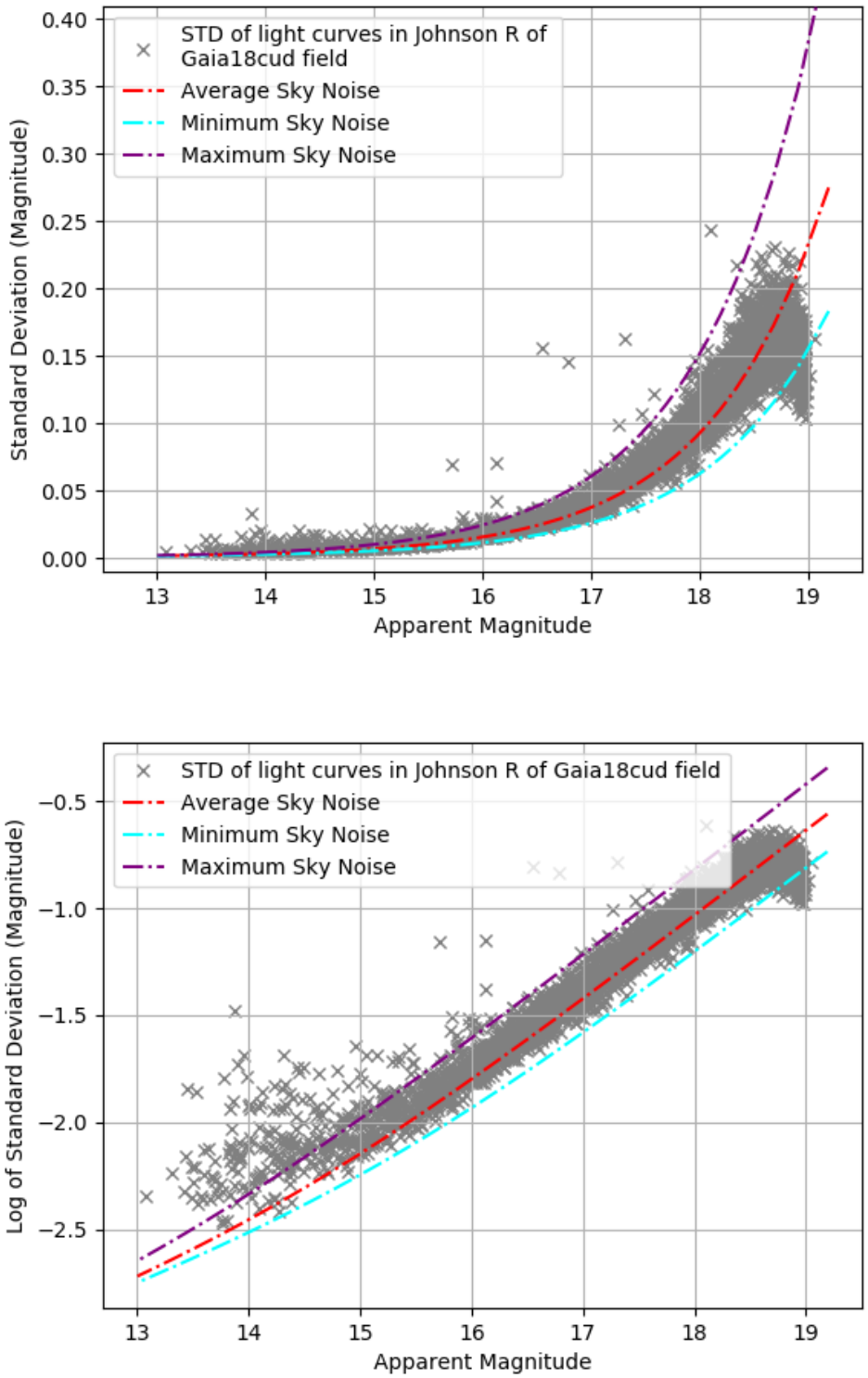

Figure A.5: Gaia18cud data through Johnson R filter, 300s exposures.

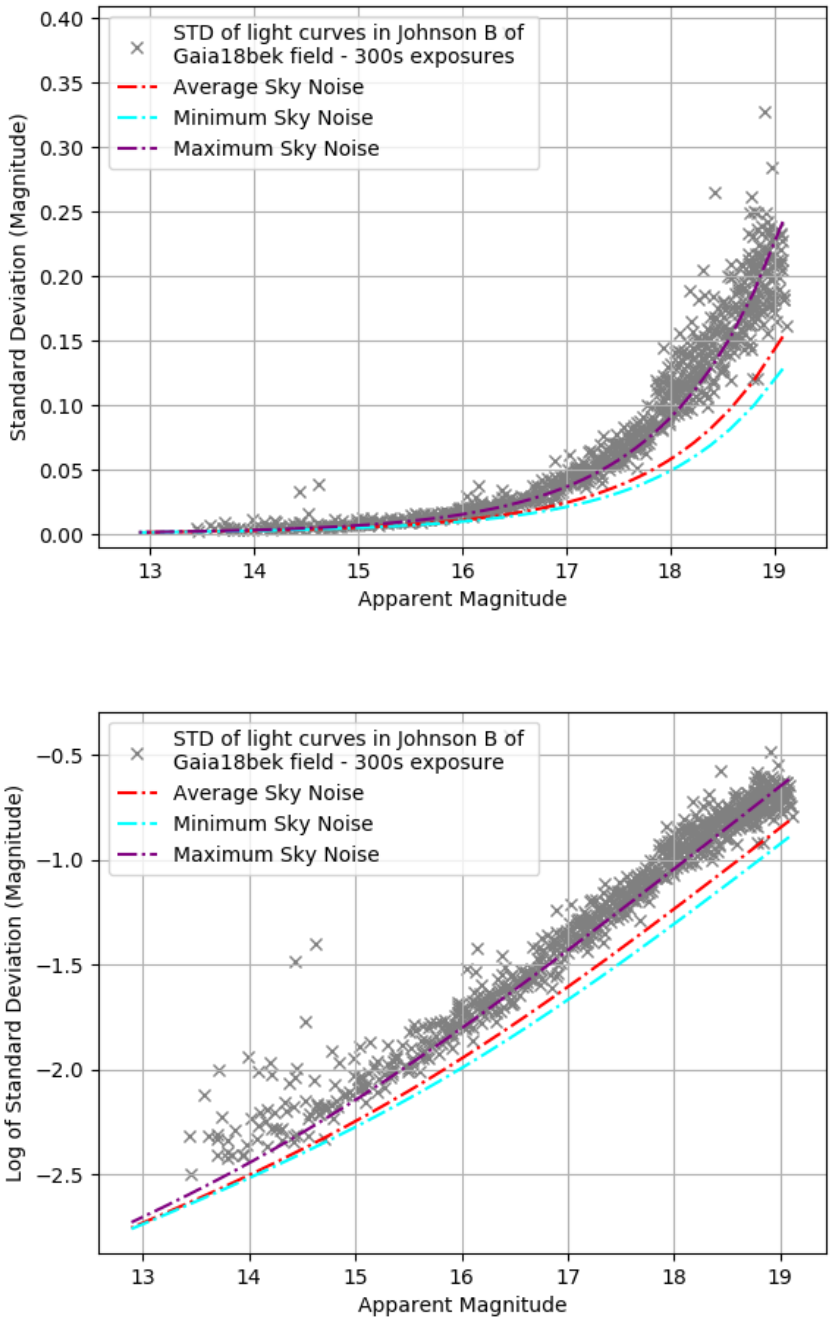

Figure A.6: Gaia18bek data through Johnson B filter, 300s exposures.

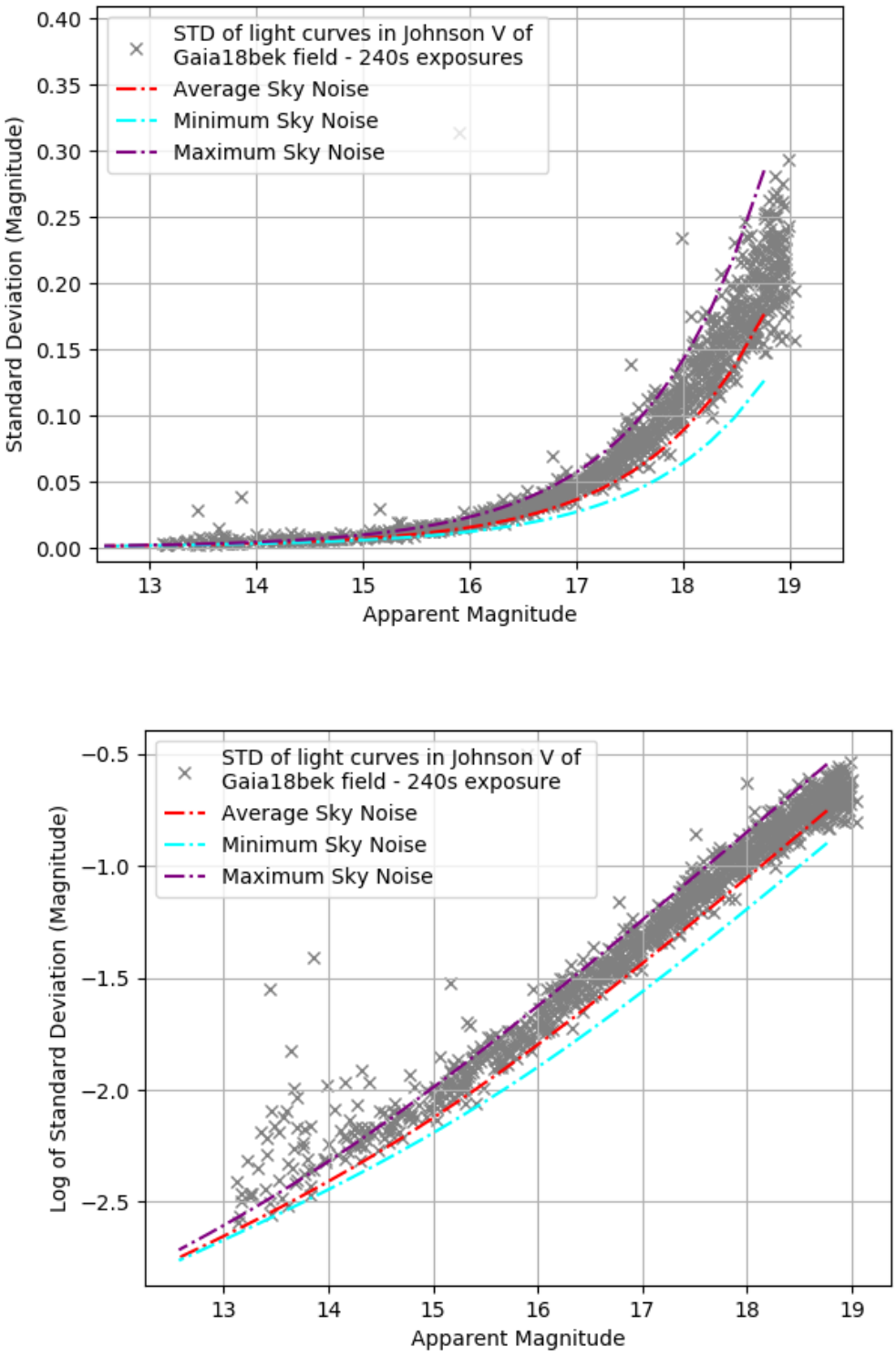

Figure A.7: Gaia18bek data through Johnson V filter, 240s exposures.

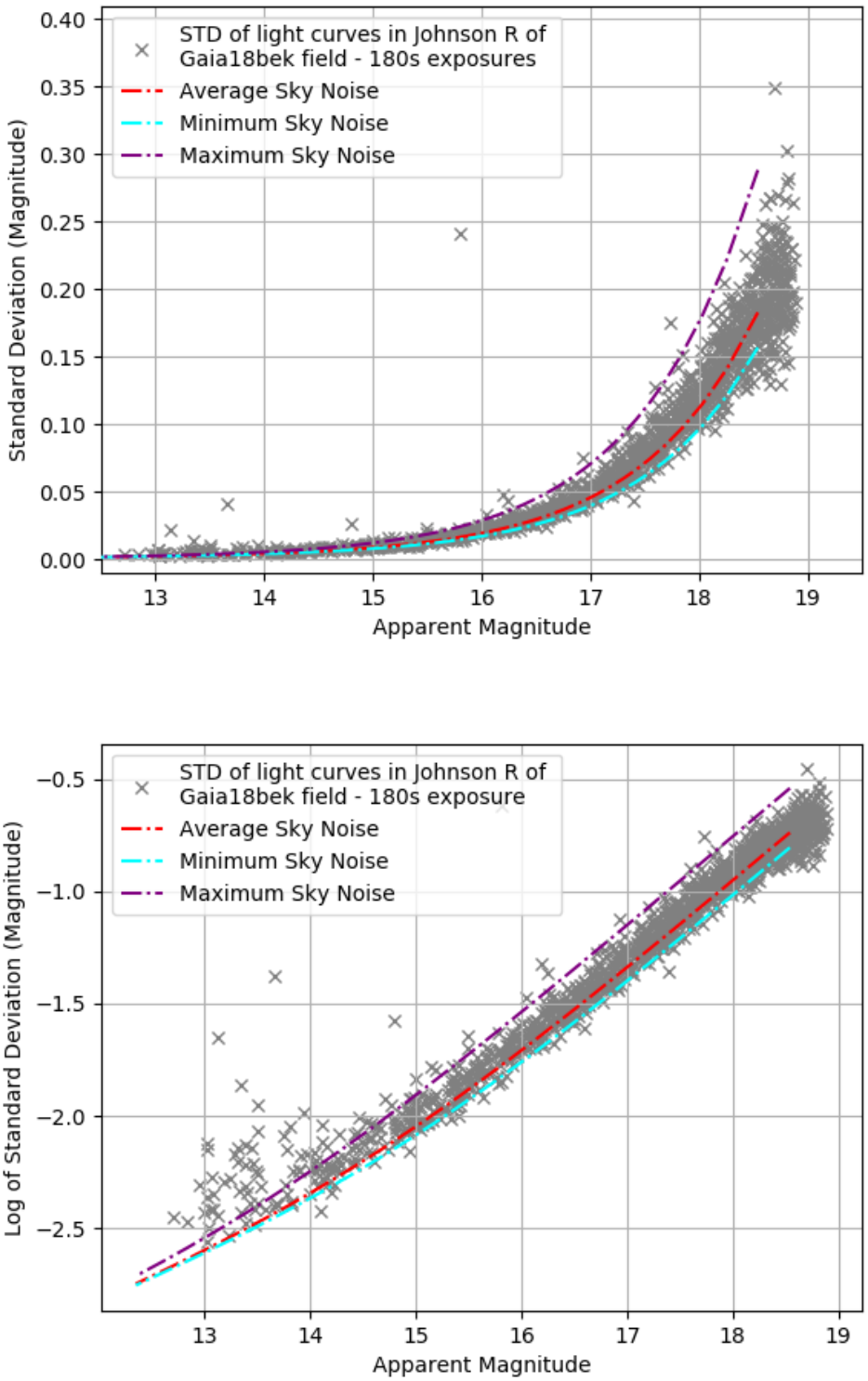

Figure A.8: Gaia18bek data through Johnson R filter, 180s exposures.

B Light Curve Fitting

The following graphs are the result of weighted least squares fitting to both the ensemble script light curves and the CPCS light curves for Gaia18arn, an unknown transient event, and Gaia17bts, a microlensing event which has been split into a declining section and a baseline section after the event, along with the comparison of the fits for the two sets of light curves.

Gaia17bts - baseline section

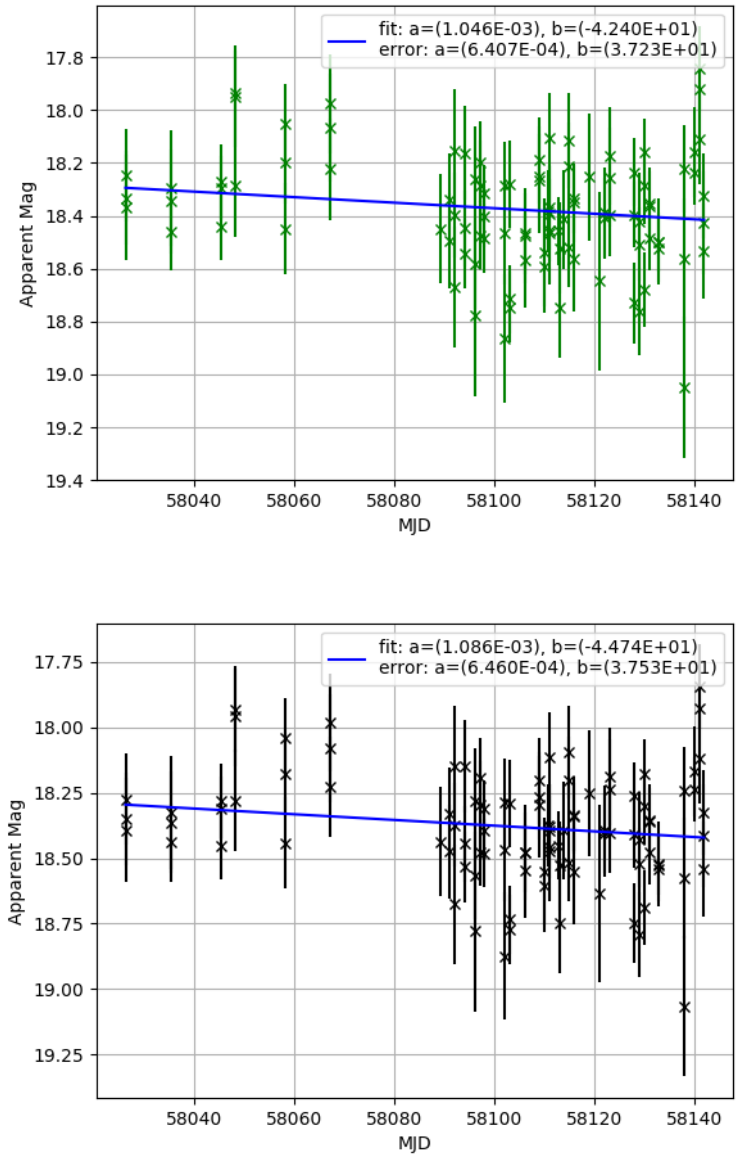

Figure B.1: (Continued on the following page)

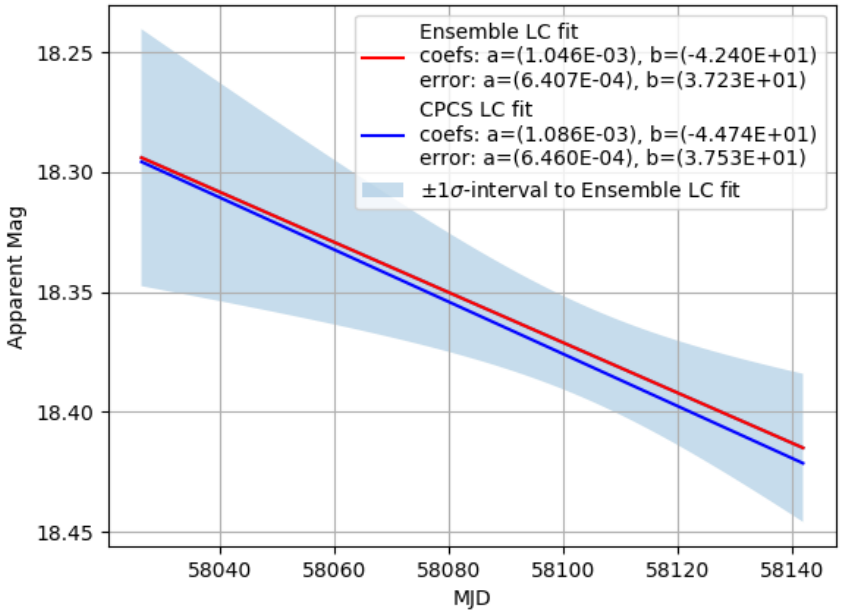

Figure B.1: Ensemble script light curve for Gaia17bts in the Baader G filter (top left) and the CPCS light curve of the same data (top right). Both have been fit with a linear function using the python and sciPy. The two fits are plotted in the bottom figure along with the $\pm 1\sigma$ error for the ensemble script fit.

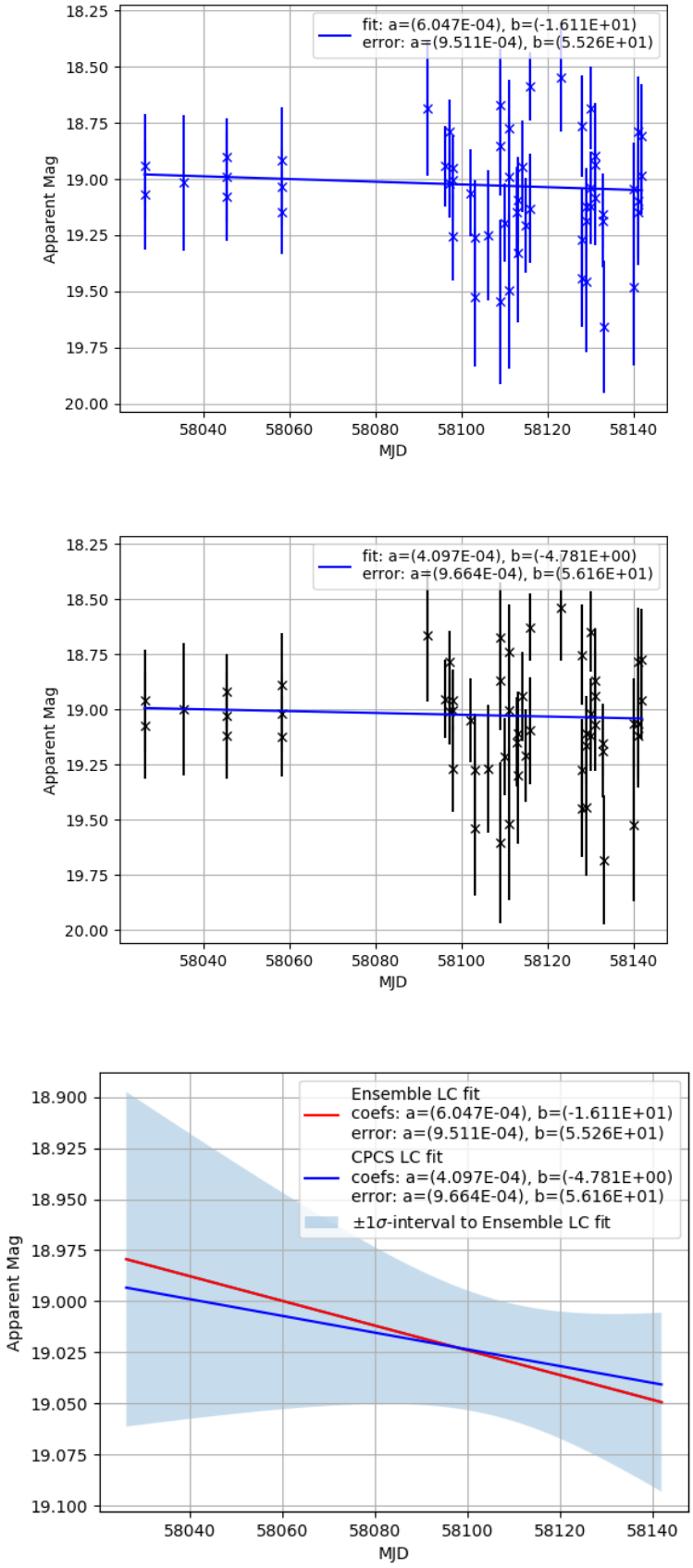

Figure B.2: Ensemble script light curve for Gaia17bts in the Baader B filter (top left) and the CPCS light curve of the same data (top right). Both have been fit with a linear function using the python and sciPy. The two fits are plotted in the bottom figure along with the $\pm 1\sigma$ error for the ensemble script fit.

Gaia17bts - decline section

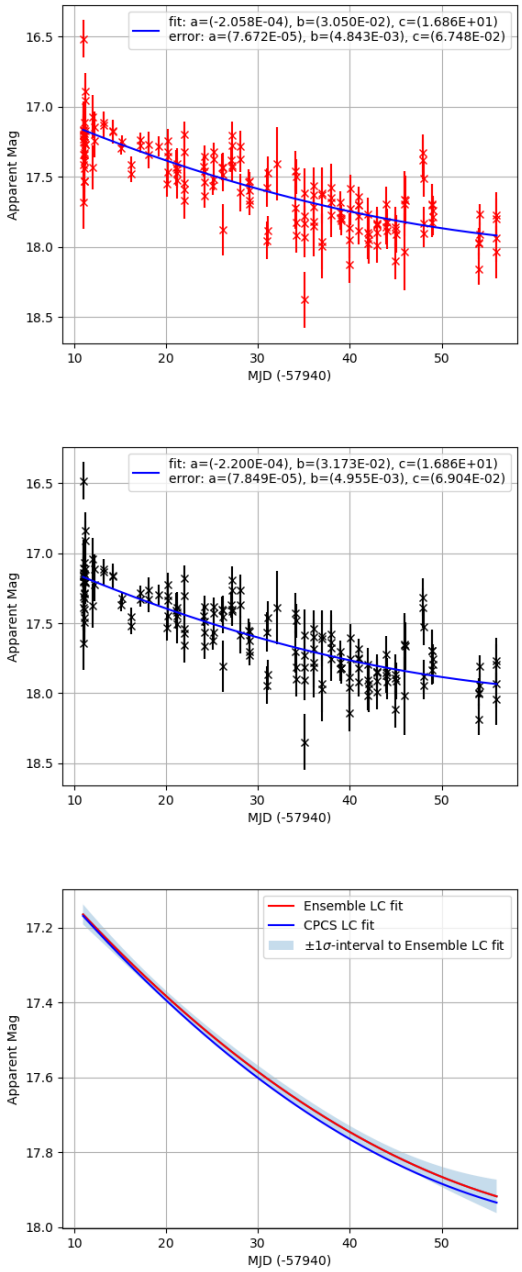

Figure B.3: Ensemble script light curve for Gaia17bts in the Baader R filter (top left) and the CPCS light curve of the same data (top right). Both have been fit with a linear function using the python and sciPy. The two fits are plotted in the bottom figure along with the $\pm 1\sigma$ error for the ensemble script fit.

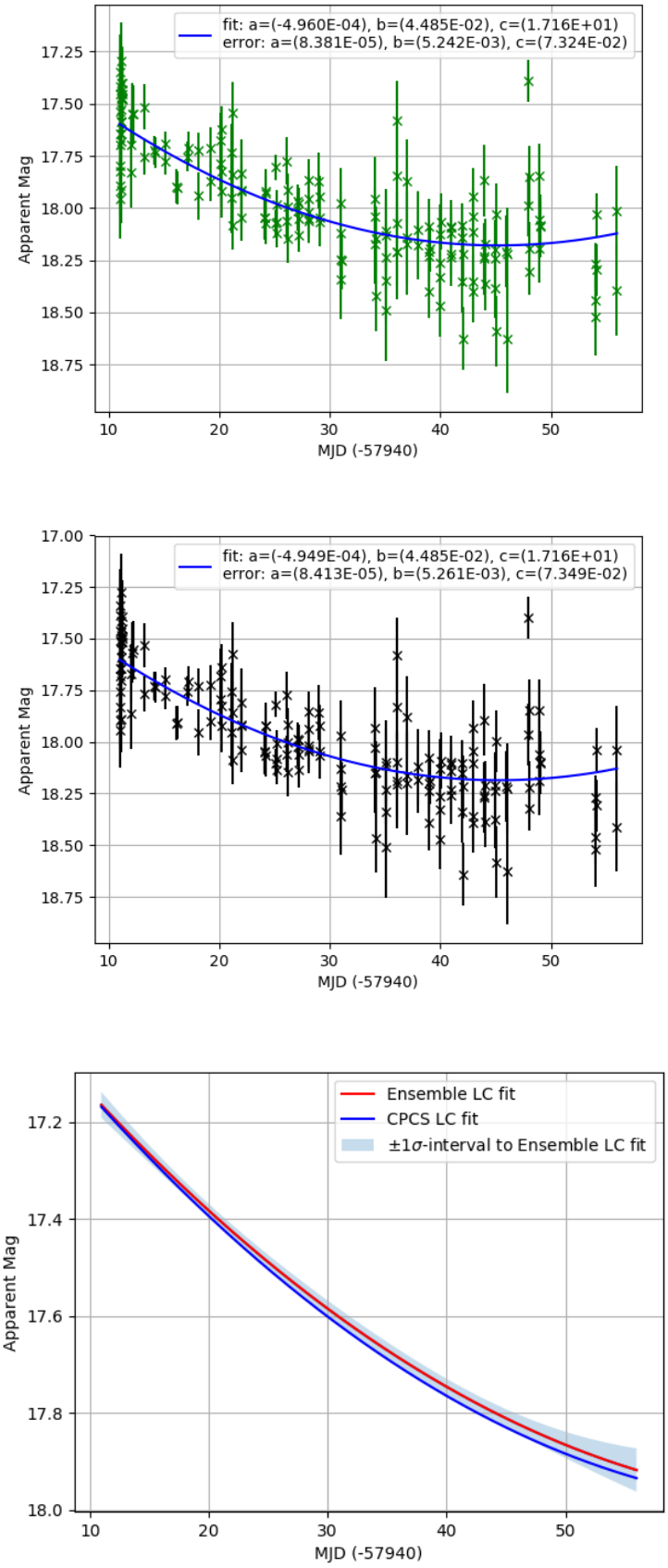

Figure B.4: Ensemble script light curve for Gaia17bts in the Baader G filter (top left) and the CPCS light curve of the same data (top right). Both have been fit with a linear function using the python and sciPy. The two fits are plotted in the bottom figure along with the $\pm 1\sigma$ error for the ensemble script fit.

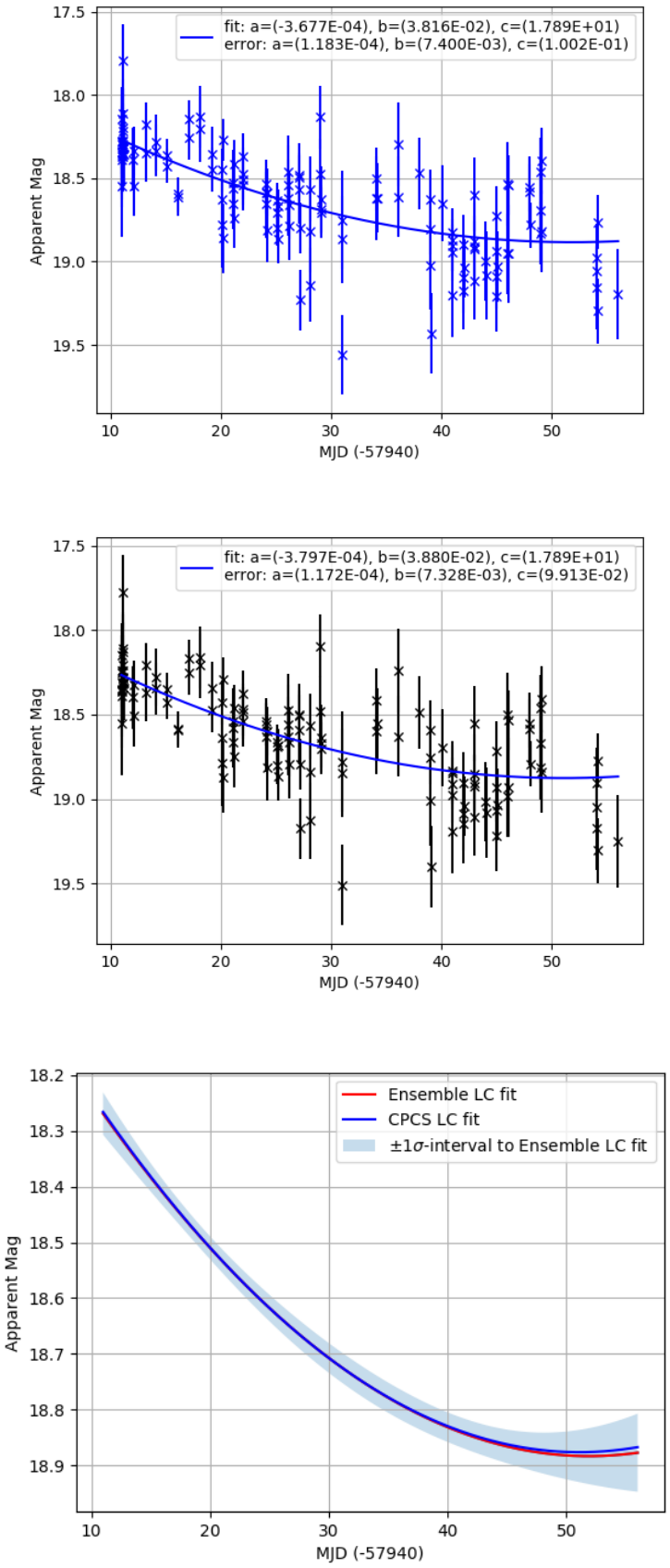

Figure B.5: Ensemble script light curve for Gaia17bts in the Baader B filter (top left) and the CPCS light curve of the same data (top right). Both have been fit with a linear function using the python and sciPy. The two fits are plotted in the bottom figure along with the $\pm 1\sigma$ error for the ensemble script fit.

Gaia18arn

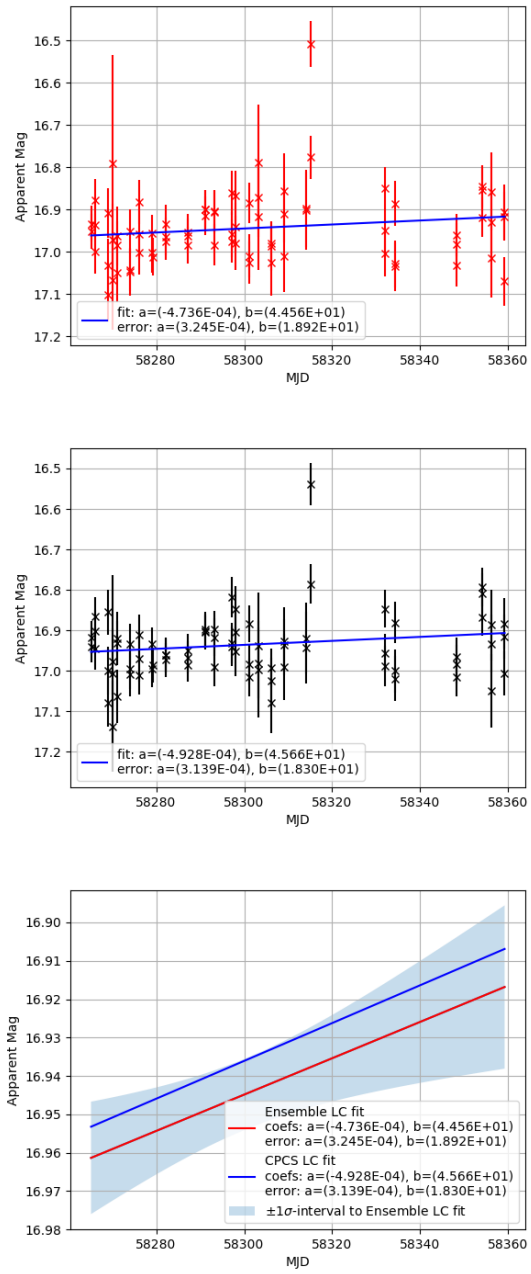

Figure B.6: Ensemble script light curve for Gaia18arn in the Johnson R filter (top left) and the CPCS light curve of the same data (top right). Both have been fit with a linear function using the python and sciPy. The two fits are plotted in the bottom figure along with the $\pm 1\sigma$ error for the ensemble script fit.

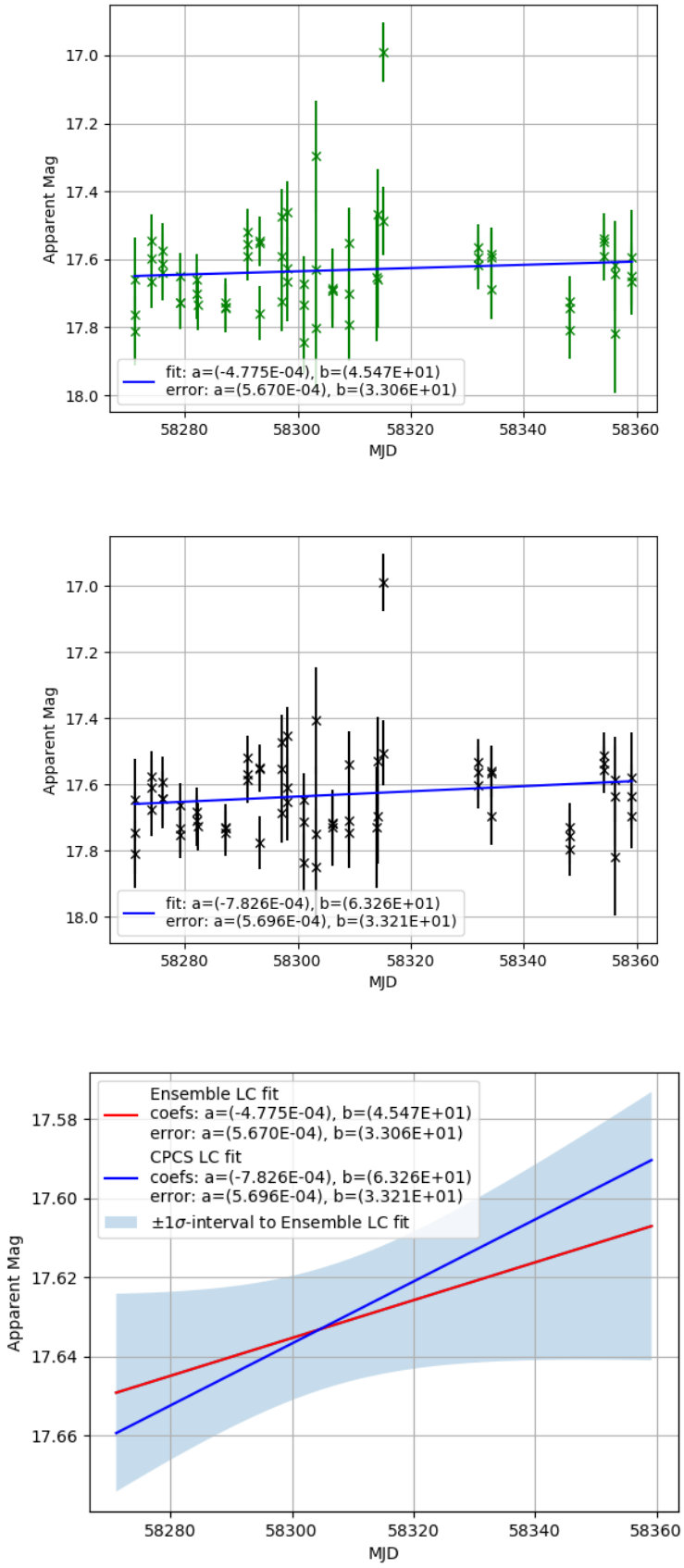

Figure B.7: Ensemble script light curve for Gaia18arn in the Johnson V filter (top left) and the CPCS light curve of the same data (top right). Both have been fit with a linear function using the python and sciPy. The two fits are plotted in the bottom figure along with the $\pm 1\sigma$ error for the ensemble script fit.

Bibliography

Abbott, B. P. et al. (2016). "Localization and Broadband Follow-up of the Gravitational wave Transient GW150914". In: *Astrophysical Journal, Letters* 826, L13, p. L13. DOI: 10.3847/2041-8205/826/1/L13.

Albrecet, R. et al. (1969). "The Sun as a Variable Star". In: *Astronomy and Astrophysics* 3, p. 236.

Alcock, C. et al. (2000). "Binary Microlensing Events from the MACHO Project". In: *The Astrophysical Journal* 541.1, pp. 270–297. DOI: 10.1086/309393.

Alcock, C. et al. (2000). "The MACHO Project: Microlensing Results from 5.7 Years of Large Magellanic Cloud Observations". In: *Astrophysical Journal* 542, pp. 281–307. DOI: 10.1086/309512.

Annunziatella, M. et al. (2013). "Inside Catalogs: A Comparison of Source Extraction Software". In: *PUBLICATIONS OF THE ASTRONOMICAL SOCIETY OF THE PACIFIC* 125.923, p. 68. DOI: 10.1086/669333. arXiv: 1212.0564 [astro-ph.IM].

Antoniadis, J. et al. (2020). "Type Ia supernovae from non-accreting progenitors". In: *Astronomy and Astrophysics* 635, A72, A72. DOI: 10.1051/0004-6361/201936991.

Arbour, R. (2017). "Transient Discovery Report for 2017-05-25". In: *Transient Name Server Discovery Report* 2017-588.

Arcavi, I. et al. (2017). "FLOYDS Classification of ASASSN-17jz/AT 2017fro as an AGN". In: *The Astronomer's Telegram* 10668.

Astropy Collaboration et al. (2013). "Astropy: A community Python package for astronomy". In: *Astronomy and Astrophysics* 558, A33, A33. DOI: 10.1051/0004-6361/201322068. arXiv: 1307.6212 [astro-ph.IM].

Baade, D. et al. (2018). "Short-term variability and mass loss in Be stars. IV. Two groups of closely spaced, approximately equidistant frequencies in three decades of space photometry of ν Puppis (B7-8 IIIe)". In: *Astronomy and Astrophysics* 620, A145, A145. DOI: 10.1051/0004-6361/201834161. arXiv: 1808.10254 [astro-ph.SR].

Bakis, V. et al. (2016). "ATel 9376: Gaia16aye: a flaring object of uncertain nature in Cygnus". In: *Astronomers Telegram*.

Baruch, J. et al. (2007). "Journey into space". In: *Astronomy & Geophysics* 48.4, pp. 4.27–4.28. ISSN: 1468-4004. DOI: 10.1111/j.1468-4004.2007.48427.x. URL: http://dx.doi.org/10.1111/j.1468-4004.2007.48427.x.

Beaulieu, J. P. et al. (1998). "Some results based on the EROS microlensing survey". In: *ArXiv Astrophysics e-prints*. eprint: astro-ph/9811363.

Bersier, D. (2017). "Classification of ASASSN-17em/AT2017cts". In: *The Astronomer's Telegram* 10242.

Bertin, E. et al. (1996). "SExtractor: Software for source extraction." In: *Astronomy and Astrophysics, Supplement* 117, pp. 393–404. DOI: 10.1051/aas:1996164.

Birney, D.S. et al. (2006). *Observational Astronomy*. Cambridge University Press. ISBN: 9780521853705.

Blagorodnova, N. (2017). "Transient Classification Report for 2017-10-03". In: *Transient Name Server Classification Report* 2017-1064.

Blagorodnova, N et al. (2014). "GS-TEC: the Gaia spectrophotometry transient events classifier". In: *Monthly Notices of the RAS* 442.1, pp. 327–342. DOI: 10.1093/mnras/stu837. arXiv: 1404.7150 [astro-ph.IM].

Blagorodnova, N. et al. (2018). "Palomar 60-inch SEDM classification of optical transients". In: *The Astronomer's Telegram* 11493.

Bond, I. A. et al. (2004). "OGLE 2003-BLG-235/MOA 2003-BLG-53: A Planetary Microlensing Event". In: *The Astrophysical Journal Letters* 606.2, p. L155. URL: http://stacks.iop.org/1538-4357/606/i=2/a=L155.

Bopp, B. W. et al. (1981). "The FK Comae stars". In: *Astrophysical Journal, Letters* 247, pp. L131–L134. DOI: 10.1086/183606.

Bose, S. et al. (2018a). "ASAS-SN Transient Classification Report for 2018-04-18". In: *Transient Name Server Classification Report* 2018-509.

Bose, S. et al. (2018b). "Spectroscopic Classification of Three ASAS-SN Supernovae". In: *The Astronomer's Telegram* 11530.

Bourassa, R. R. et al. (1973). "The Spheroidal Gravitational Lens". In: *Astrophysical Journal* 185, pp. 747–756. DOI: 10.1086/152452.

Brimacombe et al. (2017a). "ASASSN-17cz: Discovery of A Probable Supernova in 2MASX J17503055-0148023". In: *The Astronomer's Telegram* 10125.

Brimacombe, J. et al. (2017b). "ASASSN-17ea and ASASSN-17eb: Discovery of Two Probable Supernovae". In: *The Astronomer's Telegram* 10206.

Bruch, A (2016). "Photometry of the long period dwarf nova MU Centauri". In: *New Astronomy* 46, pp. 60–72. DOI: 10.1016/j.newast.2015.12.005. arXiv: 1601.05722 [astro-ph.SR].

Budding, E. et al. (2007). *Introduction to Astronomical Photometry*. Cambridge Observing Handbooks for Research Astronomers. Cambridge University Press. ISBN: 9780521847117.

Burke, C. J. et al. (2006). "Survey for Transiting Extrasolar Planets in Stellar Systems. III. A Limit on the Fraction of Stars with Planets in the Open Cluster NGC 1245". In: *Astronomical Journal* 132, pp. 210–230. DOI: 10.1086/504468. eprint: astro-ph/0512207.

Cartier, R. et al. (2017). "ePESSTO spectroscopic classification of optical transients". In: *The Astronomer's Telegram* 10334.

Catelan, M. et al. (2004). "The RR Lyrae Period-Luminosity Relation. I. Theoretical Calibration". In: *Astrophysical Journal, Supplement* 154.2, pp. 633–649. DOI: 10.1086/422916.

Chambers, K. C. et al. (2017). "Pan-STARRS1 Transient Discovery Report for 2017-05-11". In: *Transient Name Server Discovery Report* 2017-542.

Chevalier, R. A. et al. (2003). "Supernova Interaction with a Circumstellar Medium". In: *Supernovae and Gamma-Ray Bursters. Edited by K. Weiler., Lecture Notes in Physics, vol. 598, p.171-194*. Ed. by K. Weiler. Vol. 598, pp. 171–194. DOI: 10.1007/3-540-45863-8_10.

Clark, J. S. et al. (2003). "Long term disc variability in the Be star <ASTROBJ>o Andromedae</ASTROBJ>". In: *Astronomy and Astrophysics* 403, pp. 239–246. DOI: 10.1051/0004-6361:20030248.

Clayton, G. C. (1996). "The R Coronae Borealis Stars". In: *Publications of the ASP* 108, p. 225. DOI: 10.1086/133715.

Colgate and Moore and Carlson (1975). "A fully automated digitally controlled 30-inch telescope". In: *Publications of the Astronomical Society of the Pacific* 87.518, p. 565. DOI: http://stacks.iop.org/1538-3873/87/i=518/a=565.

Collins, K. et al. (2017). "AstroImageJ: Image Processing and Photometric Extraction for Ultra-precise Astronomical Light Curves". In: *The Astronomical Journal* 153.2, p. 77.

Coulter, D. A. et al. (2017). "Spectroscopic Classifications of Optical Transients with the Lick Shane telescope". In: *The Astronomer's Telegram* 10429.

Daniel, V. (2017). "Transient Classification Report for 2017-09-10". In: *Transient Name Server Classification Report* 2017-988.

De-Paolis, F. et al. (2016). "The Scales of Gravitational Lensing". In: *Universe* 2.1.

Delgado, A. et al. (2017a). "GaiaAlerts Transient Discovery Report for 2017-04-24". In: *Transient Name Server Discovery Report* 2017-470.

— (2017b). "GaiaAlerts Transient Discovery Report for 2017-05-06". In: *Transient Name Server Discovery Report* 2017-527.

— (2017c). "GaiaAlerts Transient Discovery Report for 2017-05-13". In: *Transient Name Server Discovery Report* 2017-547.

— (2017d). "GaiaAlerts Transient Discovery Report for 2017-05-24". In: *Transient Name Server Discovery Report* 2017-587.

— (2017e). "GaiaAlerts Transient Discovery Report for 2017-05-25". In: *Transient Name Server Discovery Report* 2017-591.

— (2017f). "GaiaAlerts Transient Discovery Report for 2017-05-25". In: *Transient Name Server Discovery Report* 2017-591.

— (2017g). "GaiaAlerts Transient Discovery Report for 2017-05-27". In: *Transient Name Server Discovery Report* 2017-600.

— (2017h). "GaiaAlerts Transient Discovery Report for 2017-05-27". In: *Transient Name Server Discovery Report* 2017-600.

— (2017i). "GaiaAlerts Transient Discovery Report for 2017-05-28". In: *Transient Name Server Discovery Report* 2017-604.

— (2017j). "GaiaAlerts Transient Discovery Report for 2017-06-18". In: *Transient Name Server Discovery Report* 2017-666.

— (2017k). "GaiaAlerts Transient Discovery Report for 2017-07-21". In: *Transient Name Server Discovery Report* 2017-788.

— (2017l). "GaiaAlerts Transient Discovery Report for 2017-07-31". In: *Transient Name Server Discovery Report* 2017-823.

— (2017m). "GaiaAlerts Transient Discovery Report for 2017-08-02". In: *Transient Name Server Discovery Report* 2017-830.

— (2017n). "GaiaAlerts Transient Discovery Report for 2017-09-01". In: *Transient Name Server Discovery Report* 2017-949.

— (2017o). "GaiaAlerts Transient Discovery Report for 2017-09-07". In: *Transient Name Server Discovery Report* 2017-976.

— (2017p). "GaiaAlerts Transient Discovery Report for 2017-09-11". In: *Transient Name Server Discovery Report* 2017-990.

— (2017q). "GaiaAlerts Transient Discovery Report for 2017-10-02". In: *Transient Name Server Discovery Report* 2017-1058.

Delgado, A. et al. (2017r). "GaiaAlerts Transient Discovery Report for 2017-10-13". In: *Transient Name Server Discovery Report* 2017-1109.

— (2017s). "GaiaAlerts Transient Discovery Report for 2017-11-15". In: *Transient Name Server Discovery Report* 2017-1261.

— (2017t). "GaiaAlerts Transient Discovery Report for 2017-11-29". In: *Transient Name Server Discovery Report* 2017-1350.

— (2017u). "GaiaAlerts Transient Discovery Report for 2017-11-29". In: *Transient Name Server Discovery Report* 2017-1350.

— (2018a). "GaiaAlerts Transient Discovery Report for 2018-01-11". In: *Transient Name Server Discovery Report* 2018-40.

— (2018b). "GaiaAlerts Transient Discovery Report for 2018-01-18". In: *Transient Name Server Discovery Report* 2018-84.

— (2018c). "GaiaAlerts Transient Discovery Report for 2018-02-14". In: *Transient Name Server Discovery Report* 2018-218.

— (2018d). "GaiaAlerts Transient Discovery Report for 2018-02-15". In: *Transient Name Server Discovery Report* 2018-224.

— (2018e). "GaiaAlerts Transient Discovery Report for 2018-03-14". In: *Transient Name Server Discovery Report* 2018-345.

— (2018f). "GaiaAlerts Transient Discovery Report for 2018-03-16". In: *Transient Name Server Discovery Report* 2018-351.

— (2018g). "GaiaAlerts Transient Discovery Report for 2018-03-21". In: *Transient Name Server Discovery Report* 2018-375.

— (2018h). "GaiaAlerts Transient Discovery Report for 2018-04-09". In: *Transient Name Server Discovery Report* 2018-464.

— (2018i). "GaiaAlerts Transient Discovery Report for 2018-04-11". In: *Transient Name Server Discovery Report* 2018-474.

— (2018j). "GaiaAlerts Transient Discovery Report for 2018-04-11". In: *Transient Name Server Discovery Report* 2018-474.

— (2018k). "GaiaAlerts Transient Discovery Report for 2018-04-30". In: *Transient Name Server Discovery Report* 2018-565.

— (2018l). "GaiaAlerts Transient Discovery Report for 2018-04-30". In: *Transient Name Server Discovery Report* 2018-565.

— (2018m). "GaiaAlerts Transient Discovery Report for 2018-05-08". In: *Transient Name Server Discovery Report* 2018-599.

— (2018n). "GaiaAlerts Transient Discovery Report for 2018-05-09". In: *Transient Name Server Discovery Report* 2018-605.

— (2018o). "GaiaAlerts Transient Discovery Report for 2018-08-22". In: *Transient Name Server Discovery Report* 2018-1229.

— (2018p). "GaiaAlerts Transient Discovery Report for 2018-08-22". In: *Transient Name Server Discovery Report* 2018-1229.

— (2018q). "GaiaAlerts Transient Discovery Report for 2018-08-29". In: *Transient Name Server Discovery Report* 2018-1255.

— (2018r). "GaiaAlerts Transient Discovery Report for 2018-08-29". In: *Transient Name Server Discovery Report* 2018-1255.

— (2018s). "GaiaAlerts Transient Discovery Report for 2018-09-27". In: *Transient Name Server Discovery Report* 2018-1454.

— (2018t). "GaiaAlerts Transient Discovery Report for 2018-10-24". In: *Transient Name Server Discovery Report* 2018-1630.

— (2018u). "GaiaAlerts Transient Discovery Report for 2018-10-24". In: *Transient Name Server Discovery Report* 2018-1630.

Delgado, A. et al. (2019a). "Gaia Photometric Science Alerts Data Flow". In: *Astronomical Data Analysis Software and Systems XXVII*. Vol. 523.

Delgado, A. et al. (2019b). "GaiaAlerts Transient Discovery Report for 2019-01-03". In: *Transient Name Server Discovery Report* 2019-17.

Dessart, Luc et al. (2012). "On the nature of supernovae Ib and Ic". In: *Monthly Notices of the RAS* 424.3, pp. 2139–2159. DOI: 10.1111/j.1365-2966.2012.21374.x.

Dexter, Jason et al. (2013). "SUPERNOVA LIGHT CURVES POWERED BY FALLBACK ACCRETION". In: *The Astrophysical Journal* 772.1, p. 30. DOI: 10.1088/0004-637x/772/1/30. URL: https://doi.org/10.1088\%2F0004-637x\%2F772\%2F1\%2F30.

Dong, S. et al. (2017). "Re-classification of Gaia17biu/SN 2017egm: the closest hydrogen-poor superluminous supernova yet found, located in a massive host galaxy". In: *The Astronomer's Telegram* 10498.

Drake, A. J. et al. (2009). "First Results from the Catalina Real-Time Transient Survey". In: *Astrophysical Journal* 696.1, pp. 870–884. DOI: 10.1088/0004-637X/696/1/870. arXiv: 0809.1394 [astro-ph].

Draper, P. W. et al. (2011). "CCDPACK – CCD data reduction package". In: *Starlink User Note* 139.

Dyson, F. W. et al. (1920). "A Determination of the Deflection of Light by the Sun's Gravitational Field, from Observations Made at the Total Eclipse of May 29, 1919". In: *Philosophical Transactions of the Royal Society of London Series A* 220, pp. 291–333. DOI: 10.1098/rsta.1920.0009.

Einstein, A. (1936). "Lens-Like Action of a Star by the Deviation of Light in the Gravitational Field". In: *Science* 84, pp. 506–507. DOI: 10.1126/science.84.2188.506.

Falco, E. et al. (2017). "ASAS-SN Transient Classification Report for 2017-05-23". In: *Transient Name Server Classification Report* 2017-584.

Fausnaugh, M. M. et al. (2016). "Space Telescope and Optical Reverberation Mapping Project. III. Optical Continuum Emission and Broadband Time Delays in NGC 5548". In: *Astrophysical Journal* 821.1, 56, p. 56. DOI: 10.3847/0004-637X/821/1/56. arXiv: 1510.05648 [astro-ph.GA].

Figer, Donald F. et al. (2020). "A New Candidate Luminous Blue Variable". In: *Astrophysical Journal, Letters* 901.1, L15, p. L15. DOI: 10.3847/2041-8213/abb704. arXiv: 2009.11122 [astro-ph.SR].

Filippenko, A. V. et al. (2001). "The Lick Observatory Supernova Search with the Katzman Automatic Imaging Telescope". In: *IAU Colloq. 183: Small Telescope Astronomy on Global Scales*. Ed. by B. Paczynski et al. Vol. 246. Astronomical Society of the Pacific Conference Series, p. 121.

Folatelli, Gastón et al. (2010). "The Carnegie Supernova Project: Analysis of the First Sample of Low-Redshift Type-Ia Supernovae". In: *Astronomical Journal* 139.1, pp. 120–144. DOI: 10.1088/0004-6256/139/1/120. arXiv: 0910.3317 [astro-ph.CO].

Fraser, M. et al. (2017). "PESSTO spectroscopic classification of optical transients". In: *The Astronomer's Telegram* 10212.

Fraser, M. et al. (2018). "NUTS Transient Classification Report for 2018-05-01". In: *Transient Name Server Classification Report* 2018-568.

Gagliano, R. et al. (2017). "POSS Transient Discovery Report for 2017-09-09". In: *Transient Name Server Discovery Report* 2017-982.

Gaia Collaboration et al. (2016). "The Gaia mission". In: *Astronomy and Astrophysics* 595, A1, A1. DOI: 10.1051/0004-6361/201629272. arXiv: 1609.04153 [astro-ph.IM].

Gallaway, M. (2015). *An Introduction to Observational Astrophysics*. Undergraduate Lecture Notes in Physics. Springer International Publishing. ISBN: 9783319233772.

Genet (1986). "Introduction to Automatic Photoelectric Telescopes (APT's)". In: *International Amateur-Professional Photoelectric Photometry Communications* 25.

Genet, David R. et al. (1987). *The photoelectric photometry handbook*.

Georgy, C. et al. (2009). "The different progenitors of type Ib, Ic SNe, and of GRB". In: *Astronomy and Astrophysics* 502.2, pp. 611–622. DOI: 10.1051/0004-6361/200811339. arXiv: 0906.2284 [astro-ph.SR].

Gillon, M. et al. (2011). "TRAPPIST: a robotic telescope dedicated to the study of planetary systems". In: *European Physical Journal Web of Conferences*. Vol. 11. European Physical Journal Web of Conferences, p. 06002. DOI: 10.1051/epjconf/20101106002. arXiv: 1101.5807 [astro-ph.EP].

Gillon, M. et al. (2017). "Seven temperate terrestrial planets around the nearby ultracool dwarf star TRAPPIST-1". In: *Nature* 542, pp. 456–460. DOI: 10.1038/nature21360. arXiv: 1703.01424 [astro-ph.EP].

Good, G.A. (2003). *Observing Variable Stars*. The Patrick Moore Practical Astronomy Series. Springer London. ISBN: 9781852334987. URL: https://books.google.co.uk/books?id=k9ViYKvKRz0C.

Gould, Andrew (1992). "Extending the MACHO Search to approximately 10 6 M sub sun". In: *The Astrophysical Journal* 392, p. 442. DOI: 10.1086/171443.

— (1994). "MACHO Velocities from Satellite-based Parallaxes". In: *The Astrophysical Journal, Letters* 421, p. L75. DOI: 10.1086/187191.

Graham, M. et al. (2019). "The Zwicky Transient Facility: Science Objectives". In: *Publications of the Astronomical Society of the Pacific* 131.1001, p. 078001. DOI: 10.1088/1538-3873/ab006c.

Greenstein, G. (2013). *Understanding the Universe: An Inquiry Approach to Astronomy and the Nature of Scientific Research*. Cambridge University Press. ISBN: 9781139618878.

Grzegorzek, J. (2017). "Transient Discovery Report for 2017-04-30". In: *Transient Name Server Discovery Report* 2017-494.

GSA (2020a). *Gaia16aye*. URL: http://gsaweb.ast.cam.ac.uk/alerts/alert/Gaia16aye/followup (visited on 08/20/2020).

— (2020b). *Gaia20cil*. URL: http://gsaweb.ast.cam.ac.uk/alerts/alert/Gaia20cil/ (visited on 05/20/2020).

Hamolli, Lindita et al. (2015). "Estimating Finite Source Effects in Microlensing Events due to Free-Floating Planets with the Euclid Survey". In: *Advances in Astron-*

omy 2015, 402303, p. 402303. DOI: 10.1155/2015/402303. arXiv: 1508.07018 [astro-ph.EP].

Han, Cheongho et al. (1999). "Astrometric Properties of Gravitational Binary-Microlens Events and Their Applications". In: *The Astrophysical Journal* 526.1, p. 405. URL: http://stacks.iop.org/0004-637X/526/i=1/a=405.

Hardy, L. K. et al. (2015). "pt5m - a 0.5 m robotic telescope on La Palma". In: *Monthly Notices of the RAS* 454.4, pp. 4316–4325. DOI: 10.1093/mnras/stv2279. arXiv: 1509.08839 [astro-ph.IM].

Hartmann, L. et al. (1996). "The FU Orionis Phenomenon". In: *Annual Review of Astron and Astrophys* 34, pp. 207–240. DOI: 10.1146/annurev.astro.34.1.207.

Hellier, C. (2001). *Cataclysmic Variable Stars - How and Why They Vary*. Praxis Books in Astronomy and Space. Springer. ISBN: 9781852332112.

Helmer, L. et al. (1985). "Carlsberg Automatic Meridian Circle". In: *Vistas in Astronomy* 28, pp. 505–518. DOI: 10.1016/0083-6656(85)90072-8.

Herbig, G. H. (1977). "Eruptive phenomena in early stellar evolution". In: *Astrophysical Journal* 217, pp. 693–715. DOI: 10.1086/155615.

Hessman, F.V. (2016). *Robotic Telescope Projects*. URL: http://www.astro.physik.uni-goettingen.de/\~hessman/MONET/links.html.

Hewish, A. et al. (1968). "Observation of a Rapidly Pulsating Radio Source". In: *NATURE* 217, pp. 709–713. DOI: 10.1038/217709a0.

Hillier, D. John et al. (2021). "BAT99-9 - a WC4 Wolf-Rayet star with nitrogen emission: evidence for binary evolution?" In: *Monthly Notices of the Royal Astronomical Society* 503.2, pp. 2726–2732. DOI: 10.1093/mnras/stab580. arXiv: 2103.01981 [astro-ph.SR].

Holl (2012). *GAIA Scanning-law Movie*. URL: www.cosmos.esa.int/web/gaia/iow_20120312 (visited on 05/15/2020).

Holmes, S. et al. (2011). "PIRATE: A Remotely Operable Telescope Facility for Research and Education". In: *Publications of the Astronomical Society of the Pacific* 123.908, p. 1177. URL: http://stacks.iop.org/1538-3873/123/i=908/a=1177.

Holoien, T. W. S. et al. (2019). "The ASAS-SN bright supernova catalogue - IV. 2017". In: *Monthly Notices of the Royal Astronomical Society* 484.2, pp. 1899–1911. DOI: 10.1093/mnras/stz073. arXiv: 1811.08904 [astro-ph.HE].

Holwerda, B. W. (2005). "Source Extractor for Dummies v5". In: *ArXiv Astrophysics e-prints*. eprint: astro-ph/0512139.

Honeycutt, R. K. (1992). "CCD ensemble photometry on an inhomogeneous set of exposures". In: *Publications of the ASP* 104, pp. 435–440. DOI: 10.1086/133015.

Honeycutt, R. K. et al. (2014). "The Long-term Light Curve of the Cataclysmic Variable V794 Aquilae". In: *Astronomical Journal* 147.1, 10, p. 10. DOI: 10.1088/0004-6256/147/1/10.

Hosseinzadeh, G. et al. (2017). "FLOYDS Classification of AT 2017czd as a Young Type II Supernova". In: *The Astronomer's Telegram* 10266.

Howell, Steve B. (2006). *Handbook of CCD Astronomy*. 2nd ed. Cambridge Observing Handbooks for Research Astronomers. Cambridge University Press. DOI: 10.1017/CBO9780511807909.

Howell, Steve B. et al. (2013). "Optical Spectroscopy at Deep Light Minimum of R Coronae Borealis". In: *Publications of the Astronomical Society of the Pacific* 125.930, p. 879. URL: http://stacks.iop.org/1538-3873/125/i=930/a=879.

Idan, I. et al. (2010). "Accretion-disc model spectra for dwarf-nova stars". In: *Astronomy and Astrophysics* 519, A117, A117. DOI: 10.1051/0004-6361/200810896. arXiv: 0809.0432 [astro-ph].

Im, M. et al. (2017). "IMSNG: Light curve analysis suggests SN 2017ein as a young SN at the time of the discovery". In: *The Astronomer's Telegram* 10481.

Inserra, C. et al. (2017). "Complexity in the light curves and spectra of slow-evolving superluminous supernovae". In: *Monthly Notices of the RAS* 468.4, pp. 4642–4662. DOI: 10.1093/mnras/stx834. arXiv: 1701.00941 [astro-ph.HE].

Itagaki, K. (2017a). "Transient Discovery Report for 2017-04-12". In: *Transient Name Server Discovery Report* 2017-420.

— (2017b). "Transient Discovery Report for 2017-05-11". In: *Transient Name Server Discovery Report* 2017-541.

Jaki, S. L. (1978). "Johann Georg von Soldner and the gravitational bending of light, with an English translation of his essay on it published in 1801". In: *Foundations of Physics* 8, pp. 927–950. DOI: 10.1007/BF00715064.

Janka, Hans-Thomas (2012). "Explosion Mechanisms of Core-Collapse Supernovae". In: *Annual Review of Nuclear and Particle Science* 62.1, pp. 407–451. DOI: 10.1146/annurev-nucl-102711-094901.

Jayasinghe, T. et al. (2019). "The ASAS-SN catalogue of variable stars III: variables in the southern TESS continuous viewing zone". In: *Monthly Notices of the Royal*

Astronomical Society 485.1, pp. 961–971. DOI: 10.1093/mnras/stz444. arXiv: 1901.00009 [astro-ph.SR].

Jetsu, L. et al. (1993). "SPOT and flare activity of FK Comae Berenices: Long-term photometry". In: *Astronomy and Astrophysics* 278, pp. 449–462.

Kankare, E. (2017). "NUTS Transient Classification Report for 2017-05-19". In: *Transient Name Server Classification Report* 2017-569.

Kato, Taichi et al. (2019). "CS Indi: SU UMa-type dwarf nova with long precursor outburst". In: *Publications of the ASJ* 71.6, L4, p. L4. DOI: 10.1093/pasj/psz108. arXiv: 1909.00910 [astro-ph.SR].

Kawabata, M. (2017). "Transient Classification Report for 2017-05-25". In: *Transient Name Server Classification Report* 2017-596.

Khokhlov, A. et al. (1993). "Light curves of type IA supernova models with different explosion mechanisms." In: *Astronomy and Astrophysics* 270, pp. 223–248.

Kopal, Zdeněk (1989). "The Roche Model". In: *The Roche Problem: And Its Significance for Double-Star Astronomy*. Dordrecht: Springer Netherlands, pp. 7–36. ISBN: 978-94-009-2291-4. DOI: 10.1007/978-94-009-2291-4_2. URL: https://doi.org/10.1007/978-94-009-2291-4_2.

Kruszynska, K. et al. (2018). "VLT/X-Shooter spectroscopic classification of candidates for microlensing events". In: *The Astronomer's Telegram* 11634.

Kulkarni, S. R. (2016). "Top Argelander Stars: Pedagogy & Prize". In: *ArXiv e-prints*. arXiv: 1610.06285 [astro-ph.SR].

Kuncarayakti, H. et al. (2018). "Spectroscopic observation of SN 2017jzp and SN 2018bf by NUTS (NOT Un-biased Transient Survey)". In: *The Astronomer's Telegram* 11164.

Labadie-Bartz, Jonathan et al. (2021). "Short-term variability and mass loss in Be stars - VI. Frequency groups in γ Cas detected by TESS". In: *Monthly Notices of the Royal Astronomical Society* 502.1, pp. 242–259. DOI: 10.1093/mnras/staa3913. arXiv: 2012.06454 [astro-ph.SR].

Lambourne, R.J. (2010). *Relativity, Gravitation and Cosmology*. Relativity, Gravitation and Cosmology. Cambridge University Press. ISBN: 9780521131384.

Lang, Dustin et al. (2010). "Astrometry.net: Blind Astrometric Calibration of Arbitrary Astronomical Images". In: *The Astronomical Journal* 139.5, p. 1782. URL: http://stacks.iop.org/1538-3881/139/i=5/a=1782.

Leavitt, H. S. et al. (1912). "Periods of 25 Variable Stars in the Small Magellanic Cloud." In: *Harvard College Observatory Circular* 173, pp. 1–3.

Lefèvre, L. et al. (2005). "Oscillations in the Massive Wolf-Rayet Star WR 123 with the MOST Satellite". In: *Astrophysical Journal, Letters* 634.1, pp. L109–L112. DOI: 10.1086/498393.

Leibowitz, Elia M. (1993). "The Optical Light Curve of Nova Herculis 1991 and of Other Classical Novae". In: *Astrophysical Journal, Letters* 411, p. L29. DOI: 10.1086/186904.

Li, W et al. (2011a). "Nearby supernova rates from the Lick Observatory Supernova Search - II. The observed luminosity functions and fractions of supernovae in a complete sample". In: *Monthly Notices of the RAS* 412.3, pp. 1441–1472. DOI: 10.1111/j.1365-2966.2011.18160.x. arXiv: 1006.4612 [astro-ph.SR].

Li, Weidong et al. (2011b). "Nearby supernova rates from the Lick Observatory Supernova Search - II. The observed luminosity functions and fractions of supernovae in a complete sample". In: *Monthly Notices of the Royal Astronomical Society* 412.3, pp. 1441–1472. DOI: 10.1111/j.1365-2966.2011.18160.x. arXiv: 1006.4612 [astro-ph.SR].

Lipunov, V. et al. (2012). "MASTER global robotic net". In: *Astronomical Society of India Conference Series*. Vol. 7. Astronomical Society of India Conference Series, p. 275.

Longair, M. (2007). *Galaxy Formation*. Astronomy and Astrophysics Library. Springer Berlin Heidelberg. ISBN: 9783540734772.

Maehara, H (2017). "High-dispersion spectroscopy of the probable microlensing event TCP J05074264+2447555". In: *The Astronomer's Telegram* 10919.

Mao, S. et al. (1991). "Gravitational microlensing by double stars and planetary systems". In: *Astrophysical Journal, Letters* 374, pp. L37–L40. DOI: 10.1086/186066.

Matsunaga, N et al. (2013). "Cepheids and other short-period variables near the Galactic Centre". In: *Monthly Notices of the RAS* 429.1, pp. 385–397. DOI: 10.1093/mnras/sts343. arXiv: 1211.0151 [astro-ph.SR].

McBrien, O. et al. (2018). "ePESSTO spectroscopic classification of optical transients". In: *The Astronomer's Telegram* 11635.

McKinney, Wes (2010). "Data Structures for Statistical Computing in Python". In: *Proceedings of the 9th Python in Science Conference*. Ed. by Stéfan van der Walt et al., pp. 51 –56.

McNall, J. et al. (1968). "A Computer-Controlled Photometric Telescope". In: *Astronomical Journal* 73, p. 756. DOI: 10.1086/110694.

Merc, J. et al. (2020). "Gaia18aen: First symbiotic star discovered by Gaia". In: *arXiv e-prints*, arXiv:2009.14709, arXiv:2009.14709. arXiv: 2009.14709 [astro-ph.SR].

Meylan, G. et al., eds. (2006). *Gravitational Lensing: Strong, Weak and Micro*. eprint: astro-ph/0407232.

Montegriffo et al. (2018). *GAIA DR2 Passbands*. URL: https://www.cosmos.esa.int/web/gaia/iow_20180316.

Moreno-Raya, M. et al. (2016). "On the Dependence of Type Ia SNe Luminosities on the Metallicity of Their Host Galaxies". In: *The Astrophysical Journal* 818.1, p. L19. DOI: 10.3847/2041-8205/818/1/l19. URL: https://doi.org/10.3847\%2F2041-8205%2F818%2F1%2Fl19.

Moriya, Takashi J. et al. (2018). "Superluminous Supernovae". In: *Space Science Reviews* 214.2, 59, p. 59. DOI: 10.1007/s11214-018-0493-6. arXiv: 1803.01875 [astro-ph.HE].

Mróz, Przemek et al. (2020). "Microlensing Optical Depth and Event Rate in the OGLE-IV Galactic Plane Fields". In: *The Astrophysical Journal Supplement Series* 249.1, p. 16. DOI: 10.3847/1538-4365/ab9366. URL: https://doi.org/10.3847\%2F1538-4365\%2Fab9366.

Nemiroff, Robert J. et al. (1994). "Finite Source Sizes and the Information Content of Macho-Type Lens Search Light Curves". In: *The Astrophysical Journal, Letters* 424, p. L21. DOI: 10.1086/187265. arXiv: astro-ph/9401005 [astro-ph].

Nomoto, K. et al. (1984). "Accreting white dwarf models for type I supern. III. Carbon deflagration supernovae." In: *Astrophysical Journal* 286, pp. 644–658. DOI: 10.1086/162639.

North, G. (1997). *Advanced Amateur Astronomy*. Cambridge University Press. ISBN: 9780521574303.

North, G. et al. (2014). *Observing Variable Stars, Novae and Supernovae*. Cambridge University Press. ISBN: 9781107636125.

Norton, A.J. et al. (2004). *Observing the Universe: A Guide to Observational Astronomy and Planetary Science*. Cambridge University Press. ISBN: 9780521603935.

Paczynski, B. (1986). "Gravitational microlensing by the galactic halo". In: *Astrophysical Journal* 304, pp. 1–5. DOI: 10.1086/164140.

Padovani, P. et al. (2017). "Active galactic nuclei: what's in a name?" In: *Astronomy and Astrophysics Reviews* 25.1, 2, p. 2. DOI: 10.1007/s00159-017-0102-9. arXiv: 1707.07134 [astro-ph.GA].

Pashchenko, Ilya N. et al. (2018). "Machine learning search for variable stars". In: *Monthly Notices of the RAS* 475.2, pp. 2326–2343. DOI: 10.1093/mnras/stx3222. arXiv: 1710.07290 [astro-ph.IM].

Patterson, J. (1984). "The evolution of cataclysmic and low-mass X-ray binaries." In: *Astrophysical Journal, Supplement* 54, pp. 443–493. DOI: 10.1086/190940.

Pence, W. D. et al. (2010). "Definition of the Flexible Image Transport System (FITS), version 3.0". In: *Astronomy and Astrophysics* 524, A42, A42. DOI: 10.1051/0004-6361/201015362.

Percy (1978). "Rotating variable stars". In: *Journal of the RAS of Canada* 72, pp. 162–166.

Percy (2007). *Understanding Variable Stars*. Cambridge University Press. ISBN: 9781139463287.

Percy et al. (2010). "Photometric Variability Properties of 21 T Tauri and Related Stars from AAVSO Visual Observations". In: *Journal of the American Association of Variable Star Observers (JAAVSO)* 38.2, p. 151.

Perlmutter, S. et al. (1999). "Measurements of Ω and Λ from 42 High-Redshift Supernovae". In: *Astrophysical Journal* 517.2, pp. 565–586. DOI: 10.1086/307221. arXiv: astro-ph/9812133 [astro-ph].

Peterson, Bradley M. (2001). "Variability of Active Galactic Nuclei". In: *Advanced Lectures on the Starburst-AGN*. Ed. by Itziar Aretxaga et al., p. 3. DOI: 10.1142/9789812811318_0002. arXiv: astro-ph/0109495 [astro-ph].

Phillips, Mark M. et al. (2017). "The Peak Luminosity - Decline Rate Relationship for Type Ia Supernovae". In: *Handbook of Supernovae*. Ed. by Athem W. Alsabti et al., p. 2543. DOI: 10.1007/978-3-319-21846-5_100.

Pollacco, D. L. et al. (2006). "The WASP Project and the SuperWASP Cameras". In: *Publications of the ASP* 118, pp. 1407–1418. DOI: 10.1086/508556. eprint: astro-ph/0608454.

Prieto, J. L. et al. (2017). "ASAS-SN Transient Classification Report for 2017-02-27". In: *Transient Name Server Classification Report* 2017-259.

Rahal, Y. R. et al. (2009). "The EROS2 search for microlensing events towards the spiral arms: the complete seven season results". In: *Astronomy and Astrophysics*

500.3, pp. 1027–1044. DOI: 10.1051/0004-6361/200811515. arXiv: 0901.1325 [astro-ph.GA].

Reichart, D. et al. (2005). "PROMPT: Panchromatic Robotic Optical Monitoring and Polarimetry Telescopes". In: *Nuovo Cimento C Geophysics Space Physics C* 28.4, p. 767. DOI: 10.1393/ncc/i2005-10149-6. arXiv: astro-ph/0502429 [astro-ph].

Rodrigo et al. (2012). *The SVO Filter Profile Service*. URL: http://ivoa.net/documents/Notes/SVOFPS/NOTE-SVOFPS-1.0.20121015.pdf.

Rodrigo et al. (2013). *The Filter Profile Service Access Protocol*. URL: http://ivoa.net/documents/Notes/SVOFPSDAL/20130510/NOTE-SVOFPSDAL-v2-1.0-20130510.pdf.

Rossum, G. (1995). *Python Reference Manual*. Tech. rep. Amsterdam, The Netherlands, The Netherlands: python.

Salisbury, M. A. et al. (2021). "Monitoring of transiting exoplanets and their host stars with small aperture telescopes". In: *New Astronomy* 83, 101477, p. 101477. DOI: 10.1016/j.newast.2020.101477. arXiv: 2008.08379 [astro-ph.EP].

Samus, N. and Kazarovets, E. and Durlevich, O. and Kireeva, N. and Pastukhova, E. (2017). "General catalogue of variable stars: Version GCVS 5.1". In: *Astronomy Reports* 61.1, pp. 80–88. ISSN: 1562-6881. DOI: 10.1134/S1063772917010085. URL: http://dx.doi.org/10.1134/S1063772917010085.

Scaringi, S (2014). "A physical model for the flickering variability in cataclysmic variables". In: *Monthly Notices of the RAS* 438.2, pp. 1233–1241. DOI: 10.1093/mnras/stt2270. arXiv: 1311.6814 [astro-ph.GA].

Schneider, P. et al. (1986). "The two-point-mass lens - Detailed investigation of a special asymmetric gravitational lens". In: *Astronomy and Astrophysics* 164, pp. 237–259.

Semiconductor, ON (1995). *KAF-16803: 4096 (H) x 4096 (V) Full Frame CCD Image Sensor*. Tech. rep. onsemiconductor.

Shappee, B. J. et al. (2014). "The Man behind the Curtain: X-Rays Drive the UV through NIR Variability in the 2013 Active Galactic Nucleus Outburst in NGC 2617". In: *Astrophysical Journal* 788.1, 48, p. 48. DOI: 10.1088/0004-637X/788/1/48.

Shin, M.-S. et al. (2018). "Spectroscopic classification of Gaia18ddp: Type Ia Supernova in the extended halo of the brightest cluster galaxy". In: *The Astronomer's Telegram* 12233.

Siebert, M. R. et al. (2017). "Spectroscopic Classifications of Optical Transients with Shane". In: *The Astronomer's Telegram* 10294.

Skrutskie, M. F. et al. (2006). "The Two Micron All Sky Survey (2MASS)". In: *The Astronomical Journal* 131.2, p. 1163. URL: http://stacks.iop.org/1538-3881/131/i=2/a=1163.

Sokolovsky, K. et al. (2017). "Swift X-ray detection and VLT/FORS2 spectroscopy of the nuclear transient Gaia17cmd/AT2017har". In: *The Astronomer's Telegram* 10901.

Sokolovsky, K. V. et al. (2018). "VaST: A variability search toolkit". In: *Astronomy and Computing* 22, pp. 28–47. DOI: 10.1016/j.ascom.2017.12.001. arXiv: 1702.07715 [astro-ph.IM].

Southworth, J. (2012). "Eclipsing Binary Stars: the Royal Road to Stellar Astrophysics". In: *Orbital Couples: Pas de Deux in the Solar System and the Milky Way*. Ed. by F. Arenou et al., pp. 51–58. arXiv: 1201.1388 [astro-ph.SR].

Sproats (2019). *Baader Johnson/Bessel Filter Profiles*. URL: baader-planetarium.co.uk/2019/09/12/baader-ubvri-photometric-filters/ (visited on 08/20/2020).

Stanek, K. Z. (2017). "ASAS-SN Transient Discovery Report for 2017-07-27". In: *Transient Name Server Discovery Report* 2017-809.

— (2018a). "ASAS-SN Transient Discovery Report for 2018-04-04". In: *Transient Name Server Discovery Report* 2018-438.

— (2018b). "ASAS-SN Transient Discovery Report for 2018-04-05". In: *Transient Name Server Discovery Report* 2018-443.

Starrfield, S. et al. (2016). "The Thermonuclear Runaway and the Classical Nova Outburst". In: *Publications of the ASP* 128.963, p. 051001. DOI: 10.1088/1538-3873/128/963/051001. arXiv: 1605.04294 [astro-ph.SR].

Steele, I. A. et al. (2004). "The Liverpool Telescope: performance and first results". In: *Ground-based Telescopes*. Ed. by J. M. Oschmann Jr. Vol. 5489. Proceedings of the SPIE, pp. 679–692. DOI: 10.1117/12.551456.

Stetson, Peter B. (1987). "DAOPHOT: A Computer Program for Crowded-Field Stellar Photometry". In: *Publications of the ASP* 99, p. 191. DOI: 10.1086/131977.

Stone, G. et al. (2017a). "ASAS-SN Transient Discovery Report for 2017-05-22". In: *Transient Name Server Discovery Report* 2017-575.

Stone, G. et al. (2017b). "ASASSN-17ej and ASASSN-17em: Discovery of Two Probable Supernovae". In: *The Astronomer's Telegram* 10241.

Sukhbold, T et al. (2016). "Core-collapse Supernovae from 9 to 120 Solar Masses Based on Neutrino-powered Explosions". In: *Astrophysical Journal* 821.1, 38, p. 38. DOI: 10.3847/0004-637X/821/1/38.

Sumi, T. et al. (2006). "Microlensing Optical Depth toward the Galactic Bulge Using Bright Sources from OGLE-II". In: *The Astrophysical Journal* 636.1, pp. 240–260. DOI: 10.1086/497951. URL: https://doi.org/10.1086\%2F497951.

Surma, P. (1993). "Shutter-free flatfielding for CCD detectors". In: *Astronomy and Astrophysics* 278, pp. 654–658.

Süveges, M. et al. (2017). "Gaia eclipsing binary and multiple systems. Supervised classification and self-organizing maps". In: *ArXiv e-prints*. arXiv: 1702.06296 [astro-ph.IM].

SVO (2020). *APASS Filter Profiles*. URL: http://svo2.cab.inta-csic.es/theory/fps3/index.php?mode=browse&gname=Misc&gname2=APASS&ftypes= (visited on 08/20/2020).

Sybilski, P. et al. (2014). "Software for autonomous astronomical observatories: challenges and opportunities in the age of big data". In: *Proceedings of the SPIE*. Vol. 9152. Society of Photo-Optical Instrumentation Engineers (SPIE) Conference Series, p. 91521C. DOI: 10.1117/12.2055836.

Taddia, F. et al. (2017). "PESSTO spectroscopic classification of optical transients". In: *The Astronomer's Telegram* 10148.

Tanaka, Y. (2018). "Transient Discovery Report for 2018-04-10". In: *Transient Name Server Discovery Report* 2018-469.

Tassoul, J (2000). *Stellar Rotation*. Cambridge Astrophysics. Cambridge University Press. DOI: 10.1017/CBO9780511546044.

Team Baader Planetarium (2016). *The Baader L-RGB-C CCD Filters*. URL: https://www.baader-planetarium.com/en/blog/the-baader-l-rgb-c-ccd-filters/.

Tody, D. (1986). "The IRAF Data Reduction and Analysis System". In: *Instrumentation in astronomy VI*. Ed. by D. L. Crawford. Vol. 627. Proceedings of the SPIE, p. 733. DOI: 10.1117/12.968154.

Tonry, J. et al. (2017a). "ATLAS Transient Discovery Report for 2017-03-07". In: *Transient Name Server Discovery Report* 2017-278.

— (2017b). "ATLAS Transient Discovery Report for 2017-04-15". In: *Transient Name Server Discovery Report* 2017-436.

— (2017c). "ATLAS Transient Discovery Report for 2017-05-19". In: *Transient Name Server Discovery Report* 2017-566.

— (2017d). "ATLAS Transient Discovery Report for 2017-05-23". In: *Transient Name Server Discovery Report* 2017-580.

— (2017e). "ATLAS Transient Discovery Report for 2017-06-13". In: *Transient Name Server Discovery Report* 2017-649.

Tonry, J. et al. (2018). "ATLAS Transient Discovery Report for 2018-03-28". In: *Transient Name Server Discovery Report* 2018-408.

Tsapras, Y. (2018). "Microlensing Searches for Exoplanets". In: *Geosciences* 8.10, p. 365. DOI: 10.3390/geosciences8100365. arXiv: 1810.02691 [astro-ph.EP].

Udalski, A. et al. (1994). "The optical gravitational lensing experiment: OGLE no. 7: Binary microlens or a new unusual variable?" In: *Astrophysical Journal, Letters* 436, pp. L103–L106. DOI: 10.1086/187643. eprint: astro-ph/9407084.

Udalski, A. et al. (2015). "OGLE-IV: Fourth Phase of the Optical Gravitational Lensing Experiment". In: *Acta Astronomica* 65.1, pp. 1–38. arXiv: 1504.05966.

Urry, C. et al. (1995). "Unified Schemes for Radio-Loud Active Galactic Nuclei". In: *Publications of the Astronomical Society of the Pacific* 107, p. 803. DOI: 10.1086/133630. URL: https://doi.org/10.1086\%2F133630.

Van Der Walt, S. et al. (2011). "The NumPy array: a structure for efficient numerical computation". In: *ArXiv e-prints*. arXiv: 1102.1523 [cs.MS].

Van Dyk, S. D. et al. (2017). "A Progenitor Candidate for SN 2017ein in NGC 3938". In: *The Astronomer's Telegram* 10485.

Van Dyk, S D. et al. (2018). "SN 2017ein and the Possible First Identification of a Type Ic Supernova Progenitor". In: *Astrophysical Journal* 860.2, 90, p. 90. DOI: 10.3847/1538-4357/aac32c. arXiv: 1803.01050 [astro-ph.SR].

Varela, A. M. et al. (2002). "Site-testing results at the Teide Observatory". In: *Astronomical Site Evaluation in the Visible and Radio Range*. Ed. by Jean Vernin et al. Vol. 266. Astronomical Society of the Pacific Conference Series, p. 454.

Verbunt, F. (1993). "Origin and evolution of X-ray binaries and binary radio pulsars." In: *Annual Review of Astron and Astrophys* 31, pp. 93–127. DOI: 10.1146/annurev.aa.31.090193.000521.

Wang, B. et al. (2017). "The core-degenerate scenario for the progenitors of Type Ia supernovae". In: *Monthly Notices of the RAS* 464.4, pp. 3965–3971. DOI: 10.1093/mnras/stw2646.

Watson, C. L. et al. (2006). "The International Variable Star Index (VSX)". In: *Society for Astronomical Sciences Annual Symposium* 25, p. 47.

Weis, Kerstin et al. (2020). "Luminous Blue Variables". In: *Galaxies* 8.1, p. 20. DOI: 10.3390/galaxies8010020. arXiv: 2009.03144 [astro-ph.SR].

Williams, Kurtis A. et al. (2013). "Time-resolved Spectroscopy of the Polar EU Cancri in the Open Cluster Messier 67". In: *Astronomical Journal* 145.5, 129, p. 129. DOI: 10.1088/0004-6256/145/5/129. arXiv: 1301.5936 [astro-ph.SR].

Williams, S. C. et al. (2017). "Spectroscopic classification of M31N 2017-05a (Gaia17biq) as a classical nova". In: *The Astronomer's Telegram* 10432.

Wyrzykowski, L. et al. (2012a). "Photometric Science Alerts from Gaia". In: *ArXiv e-prints*. arXiv: 1210.5007 [astro-ph.IM].

Wyrzykowski, Ł. et al. (2015). "OGLE-III Microlensing Events and the Structure of the Galactic Bulge". In: *Astrophysical Journal, Supplement* 216, 12, p. 12. DOI: 10.1088/0067-0049/216/1/12. arXiv: 1405.3134 [astro-ph.SR].

Wyrzykowski, L. et al. (2016). "ATel 9507;Gaia16aye is a binary microlensing event and is crossing the caustic again". In: *Astronomers Telegram*.

Wyrzykowski, Ł. et al. (2020). "Full orbital solution for the binary system in the northern Galactic disc microlensing event Gaia16aye". In: *Astronomy and Astrophysics* 633, A98, A98. DOI: 10.1051/0004-6361/201935097. arXiv: 1901.07281 [astro-ph.SR].

Wyrzykowski, Łukasz et al. (2012b). "Photometric Science Alerts from Gaia". In: *2nd Gaia Follow-up Network for Solar System Objects*, p. 21.

Xhakaj, E. et al. (2017). "Spectroscopic Classifications of Optical Transients with the Lick Shane telescope". In: *The Astronomer's Telegram* 10620.

Xiang, D. et al. (2017a). "Spectroscopic Classification of SN 2017ein as a Possibly Peculiar Type Ic Supernova". In: *The Astronomer's Telegram* 10434.

Xiang, D. et al. (2017b). "Transient Classification Report for 2017-05-07". In: *Transient Name Server Classification Report* 2017-531.

Xu, C et al. (2018). "Determination of angle of light deflection in higher-derivative gravity theories". In: *Journal of Mathematical Physics* 59.3, 032501, p. 032501. DOI: 10.1063/1.5009911. arXiv: 1709.04127 [gr-qc].

Yao, Y. et al. (2019). "ZTF Early Observations of Type Ia Supernovae. I. Properties of the 2018 Sample". In: *The Astrophysical Journal* 886.2, p. 152. DOI: 10.3847/1538-4357/ab4cf5. URL: https://doi.org/10.3847\%2F1538-4357\%2Fab4cf5.

Zang, W et al. (2019). "Spitzer + VLTI-GRAVITY Measure the Lens Mass of a Nearby Microlensing Event". In: *arXiv e-prints*, arXiv:1912.00038, arXiv:1912.00038. arXiv: 1912.00038 [astro-ph.IM].

Zeilik, M. et al. (1998). *Introductory Astronomy & Astrophysics*. Saunders golden sunburst series. Saunders College Pub. ISBN: 9780030062285.